



HAL
open science

Detailed numerical characterization of the separation-induced transition, including bursting, in a low-pressure turbine environment

Jayson Babajee

► **To cite this version:**

Jayson Babajee. Detailed numerical characterization of the separation-induced transition, including bursting, in a low-pressure turbine environment. Other. Ecole Centrale de Lyon; Institut von Karman de dynamique des fluides (Rhode-Saint-Genèse, Belgique), 2013. English. NNT : 2013ECDL0035 . tel-00984351

HAL Id: tel-00984351

<https://theses.hal.science/tel-00984351>

Submitted on 28 Apr 2014

HAL is a multi-disciplinary open access archive for the deposit and dissemination of scientific research documents, whether they are published or not. The documents may come from teaching and research institutions in France or abroad, or from public or private research centers.

L'archive ouverte pluridisciplinaire **HAL**, est destinée au dépôt et à la diffusion de documents scientifiques de niveau recherche, publiés ou non, émanant des établissements d'enseignement et de recherche français ou étrangers, des laboratoires publics ou privés.



ECOLE CENTRALE DE LYON
ECOLE DOCTORALE MEGA



VON KARMAN INSTITUTE FOR FLUID DYNAMICS
TURBOMACHINERY AND PROPULSION DEPARTMENT

Detailed Numerical Characterization of the Separation-Induced Transition, Including Bursting, in a Low-Pressure Turbine Environment

Front Cover Art: T106C low-pressure turbine blade contours of the total pressure and with the recirculation bubble at $Re_{2, is} = 80000$ and $Tu_{l.e.} = 0.9\%$ - Smooth suction side (left) - Local roughness on the suction side (right).

Back Cover Art: TX, T108, T106C, T2, HIVK_LS and HIVK_HS low-pressure turbine blade profiles.

Thesis presented by **Jayson Babajee**, MSc in Aerospace Dynamics and MSc in Mechanical Engineering and Energetics, in order to obtain the degree of “Docteur de l’Ecole Centrale de Lyon”, Ecole Centrale de Lyon, France, November 2013.

Promoter: Prof. Francis Leboeuf (Ecole Centrale de Lyon, France)

Supervisor: Prof. Tony Arts (von Karman Institute for Fluid Dynamics, Belgium)

Doctoral Committee:

Dr. Rémy Dénos (European Commission - DG Research and Innovation, Belgium)

Prof. Eva Dorignac (ENSMA Université de Poitiers, France)

Dr. Pierre Ginibre (SNECMA Villaroche, France)

Prof. Gérard Bois (ENSAM - LML, France)

Prof. Tony Arts (von Karman Institute for Fluid Dynamics, Belgium)

Prof. Isabelle Trébinjac (Ecole Centrale de Lyon, France)

A selection of doctoral theses published by the von Karman Institute:

Multi-dimensional upwind discretization and application to compressible flows
(K. Sermeus, Université Libre de Bruxelles, Belgium, January 2014)

Multiphase fluid hammer: modeling, experiments and simulations
(M. Léma Rodríguez, Université Libre de Bruxelles, Belgium / Universidade da Coruña, Spain, October 2013)

Multiscale modeling of atmospheric flows: towards improving the representation of boundary layer physics
(D. Muñoz-Esparza, Université Libre de Bruxelles, Belgium, September 2013)

Ground testing investigation of hypersonic transition phenomena for a re-entry vehicle
(D. Masutti, TU Delft, The Netherlands, June 2013)

Experimental study of the performance and stability of a low pressure axial compressor for a contra-rotating turbofan engine architecture
(N. Van de Wyer, Université Catholique de Louvain, Belgium, December 2012)

A full catalogue of publications is available from the library.

Detailed Numerical Characterization of the Separation-Induced Transition, Including Bursting, in a Low-Pressure Turbine Environment

Keywords: Low-Pressure Turbine, Boundary Layer, Separation, Bursting, Transition, Turbulence, Reynolds Number, Correlation, Local Roughness, Computational Fluid Dynamics (CFD), γ - $\tilde{Re}_{\theta t}$ model, Chimera Technique.

© 2014 by Jayson Babajee

D/2014/0238/632, T. Magin, Editor-in-Chief

Published by the von Karman Institute for Fluid Dynamics with permission.

All rights reserved. Permission to use a maximum of two figures or tables and brief excerpts in scientific and educational works is hereby granted, provided the source is acknowledged. This consent does not extend to other kinds of copying and reproduction, for which permission requests should be addressed to the Director of the von Karman Institute.

ISBN 978-2-87516-068-3



UNIVERSITÉ DE LYON
ÉCOLE CENTRALE DE LYON
ÉCOLE DOCTORALE
MÉCANIQUE, ENERGÉTIQUE, GÉNIE CIVIL ET ACOUSTIQUE
LABORATOIRE DE MÉCANIQUE DES FLUIDES ET D'ACOUSTIQUE

N° ordre : 2013-35

Année 2013

Thèse présentée par
Jayson Babajee
en vue de l'obtention du grade de Docteur de l'Ecole Centrale de Lyon

Detailed Numerical Characterization of the Separation-Induced Transition, Including Bursting, in a Low-Pressure Turbine Environment

Thèse dirigée par
Francis Leboeuf (Professeur à l'Ecole Centrale de Lyon, France)
et
soutenue le 8 Novembre 2013 à l'Ecole Centrale de Lyon, France

Composition du jury :

Dr. Rémy Dénos (European Commission - DG Research and Innovation, Belgique)	Rapporteur
Prof. Eva Dorignac (ENSMA Université de Poitiers, France)	Rapporteur
Dr. Pierre Ginibre (SNECMA Villaroche, France)	Examinateur
Prof. Gérard Bois (ENSAM - LML, France)	Président
Prof. Tony Arts (von Karman Institute for Fluid Dynamics, Belgique)	Superviseur
Prof. Isabelle Trébinjac (Ecole Centrale de Lyon, France)	Co-directeur

To the people who have always believed in me...

“Scientists discover the world that exists; Engineers create the world that never was.”

Theodore von Kármán

“Strive for perfection in everything you do. Take the best that exists and make it better. When it does not exist, design it.”

Sir Henry Royce

“The results, the scoreboard, the outcomes are totally superseded by the journeys that took me to them. Winning and losing don't last. What do are friendships, the team, giving all you've got, memories, embracing the moment.”

Jonny Wilkinson

Abstract

The Low-Pressure Turbine is a critical component of an Aero-Engine as it drives the Fan which produces most of the thrust in the current turbofan configuration. In order to increase the efficiency in terms of fuel consumption, there is a continuous research for blade count reduction (i.e. mass reduction) which entails a higher loading per rotor blade. It is well-known that this environment is characterised by a low Reynolds number flow condition associated with high diffusion along the aft region of the suction side. Consequently, the flow along this surface is prone to laminar separation which, depending on the status of the separation bubble, would lead to detrimental decrease in the aerodynamic performance (larger and deeper wake).

The present PhD thesis focuses on the investigation of the separation-induced transition phenomenon occurring in a Low-Pressure Turbine environment. The emphasis is put on the numerical predictions based on a CFD RANS approach using the innovative γ - $\widetilde{Re}_{\theta t}$ transition model based on transport equations for the numerical intermittency (γ) and the transition onset momentum thickness Reynolds number ($\widetilde{Re}_{\theta t}$). Nine Low-Pressure Turbine rotor blades form a comprehensive experimental reference database and cover a significant range of different isentropic outlet Reynolds numbers, isentropic outlet Mach numbers, inlet turbulence intensity levels, with or without incoming wakes and with two local roughness configurations. A first analysis of this database stresses the effect of the separation on the transition onset and on the performance. A correlation definition is attempted and allows to link the diffusion rate of a blade to the isentropic outlet Reynolds number at bursting. A reliable and robust numerical methodology is established to predict the transition in the case of uniform upstream flow. The results are in good agreement with the experiments even though it was necessary to adapt the boundary conditions to predict the laminar separation numerically for highly-loaded and strong diffusion rate blades only. The resolution of the boundary layer velocity profiles allows to have an in-depth examination of the flow topology parameters. This gives proper information on the momentum thickness which is the main driving parameter of transition correlations. The Chimera technique for overlapping meshes is used to ease the modelling of passive control devices to trigger transition. It is a decent technique to implement standard geometries or more elaborate designs.

Keywords: Low-Pressure Turbine, Boundary Layer, Separation, Bursting, Transition, Turbulence, Reynolds Number, Correlation, Local Roughness, Computa-

tional Fluid Dynamics (CFD), γ - $\widetilde{Re}_{\theta t}$ model, Chimera Technique.

Résumé

La turbine basse-pression est un composant essentiel d'un turboréacteur car elle entraîne la soufflante qui génère la plus grande partie de la poussée dans la configuration actuelle des turboréacteurs à double flux. Dans la perspective d'accroître son rendement en termes de consommation de carburant, il y a une recherche permanente dans la réduction du nombre d'aubage (c'est-à-dire la réduction de la masse) qui implique un chargement plus élevé par aube de rotor. Cet environnement est caractérisé par un écoulement dont le nombre de Reynolds est faible ainsi qu'une large diffusion le long de la partie aval de l'extrados. Par conséquent, l'écoulement le long de cette surface est potentiellement sujet à une séparation laminaire qui, suivant le statut de la bulle de recirculation, pourrait causer une diminution de la performance aérodynamique (sillages plus larges et plus profonds).

La présente thèse de doctorat se concentre sur l'investigation du phénomène de la transition induite par séparation dans les écoulements de turbines basse-pression. L'accent est mis sur les prédictions numériques basées sur une approche CFD RANS utilisant le modèle innovant de transition γ - $\widetilde{Re}_{\theta t}$ à deux équations de transport (la première équation pour l'intermittence numérique γ et la seconde équation pour le nombre de Reynolds dont la longueur caractéristique est l'épaisseur de quantité de mouvement au début de transition $\widetilde{Re}_{\theta t}$). Neuf aubes différentes de rotor de turbine basse-pression constituent une base de données de référence et couvrent les plages de fonctionnement de différents nombres de Reynolds de sortie isentropique, de nombres de Mach de sortie isentropique, d'intensités de turbulence d'entrée, avec ou sans sillage provenant d'une rangée d'aubes amont et avec deux configurations de rugosité locale. Une première analyse de cette base de données met en évidence l'effet de la séparation sur le début de la transition et sur les performances. La définition d'une corrélation a été tentée et permet de lier le taux de diffusion d'un aubage au nombre de Reynolds de sortie isentropique à la condition de "Bursting". Une méthodologie numérique fiable et robuste a été établie afin de prédire la transition dans le cas d'un écoulement amont uniforme. Les résultats sont en bon accord avec les mesures expérimentales même si il a été nécessaire d'adapter les conditions limites dans le but de prédire une séparation laminaire numériquement pour des aubages fortement chargés et à fort taux de diffusion uniquement. La résolution des profils de vitesse de la couche limite permet d'obtenir une évaluation détaillée des paramètres de la topologie de l'écoulement. Cela fournit une information sur l'épaisseur de quantité de mouvement qui est le paramètre principal définissant les corrélations de transition.

La technique “Chimère” des maillages recouvrants est utilisée pour faciliter la modélisation des moyens de contrôle passif pour déclencher la transition. C’est une technique appropriée pour l’implémentation de géométries simples ou plus élaborées.

Mots-clés: Turbine basse-pression, Couche limite, Séparation, “Bursting”, Transition, Turbulence, Nombre de Reynolds, Corrélacion, Rugosité locale, “Computational Fluid Dynamics (CFD)”, Modèle $\gamma\text{-}\widetilde{Re}_{\theta t}$, Technique Chimère.

Acknowledgements

This section is intended to give an expression of my gratitude to the people I met and helped me during this journey and who contributed to make it such a nice, interesting and rewarding experience.

First of all, working in the field of Aerodynamics is what was driving me since my youth. Fascinated by sports cars and aircraft, I knew I wanted to work and to contribute in these fields which have produced such amazing machines, part of our day-to-day life. In addition, I am not surprised to see myself becoming a specialist in curling shots when I play football.

That is why, I have a thought for my first supervisors during my studies: Dr Christophe Noger, from the IAT (Institut AéroTechnique), who gave me the opportunity to “feel” the Aerodynamic environment when I was responsible for the commissioning and the tests in a wind tunnel and Dr Nicholas Lawson, from Cranfield University, who gave me valuable advices for doing a PhD.

I want to express my sincere appreciation to the members of the doctoral committee for their meticulous review of my work as well as their constructive comments: Dr Rémy Dénos, Prof. Eva Dorignac, Dr Pierre Ginibre, Prof. Gérard Bois, Prof. Tony Arts and Prof. Isabelle Trébinjac.

This project would not have been feasible without the sponsoring of SNECMA and the French organisation for research and technology ANRT.

I want to thank Dr Michel Dumas, from SNECMA, for following my project until the end.

Likewise, I am grateful to the Ecole Centrale de Lyon for hosting me as a PhD candidate and particularly the Turbomachinery team under the supervision of Prof. Francis Leboeuf. Even though, I was on detachment at the von Karman Institute for Fluid Dynamics, Francis was a great professional as he reviewed and commented my work until the very end. He seemed to be a great person from the email and telephone exchanges we had. I was looking forward to thank him in person for his contribution but unfortunately, the destiny decided differently. That is why, part of my work is dedicated to his last fight and his memory...

This leads me to thank Prof. Isabelle Trébinjac who took over the supervision of my project and helped me during the last months.

In this tripartite agreement, I am immeasurably thankful to the von Karman Institute for Fluid Dynamics which hosted me, physically, during my PhD project. I met incredible people who contributed to make me learn both professionally and

personally.

The librarians, Christelle D. and Evelyne C., were a great help and particularly when they found rare articles from the archive room. I thought it was a good way to challenge them but I was losing most of the time.

I worked alongside and mixed with many fellow PhD candidates and Research Master students as we were all from different cultures. I believe this is the legacy of Prof. Theodore von Kármán and his assistants who proposed the establishment of this institution devoted to training and research in aerodynamics and with the objective of fostering fruitful exchanges between the participating nations of the NATO.

The interactions with the members of the faculty were a valuable source of knowledge.

The help of the IT Master, Raimondo G., was greatly appreciated and particularly for setting up and debugging the *elsA* environment at the VKI. In addition, the *elsA* user experience of Péter Vass (VKI) as well as the discussions with Abdelkader Benyahia (ONERA) and Lionel Castillon (ONERA) were helpful for me to start with this CFD package. This package was kindly upgraded to an unreleased development version by the *elsA* team and this was very appreciated as it allowed to investigate new features necessary for the *elsA* community.

The discussions regarding the T106C and the T108 experimental results with Jan Michálek are widely acknowledged.

My work involved mainly numerical investigations but I had the chance to put my hands “in the dust”. Indeed, I designed a unique liquid column manometer directly fitted to the ceiling of my office. It put a smile on any face entering the office...

I had the opportunity to mentor a Research Master student, Juan Ramón Llobet Gómez. This was an enriching experience to pass on to a student what other people passed on to me earlier in my career. I thank him for his valuable work and his concern.

I have a thought for Pierre L. for his great kindness and his availability.

Last but not least, there is obviously my supervisor, Prof. Tony Arts. Without him, all of this would not have been possible. I am deeply grateful to Tony for welcoming me in his team back in 2009. I really appreciated his kindness and his faculties for transmitting his knowledge and advising. Even though, he seems to support the terrestrial globe on his shoulders (only to picture the idea), he would find more than often time to discuss any kind of topic.

I believe being surrounded by great people is the key to success in order to be, somehow, in a sane environment.

This starts with the people you face everyday in the office. I had the chance of sharing this office with five different people. Their common point, they were Italian. The first period with Francesco P. and Michelangelo M. was critical. They know how grateful I am to them as they were the first persons to welcome me outside of the work environment. We had the chance to learn the “basics” of

each other language. The second period with Stefano V. was short but still was good to welcome this new comer. The last one with the “Piccole”, Laura P. and Alessia S., was very significant, particularly during the last months.

I appreciated the talks with Fabrizio F. during his smoking breaks. If he could smoke while sleeping, I am pretty sure he would do it.

I don’t forget Sergio L. and Davide M. for welcoming me as well. I will soon get a membership in their exclusive “P. club”.

There was the French connection with Boris C. and Rémi B. as well as the Spanish connection with Laura V.R. and Victor F.V..

I was pleased to see the state of mind of S.E. Christophe S. and the presence of Clara G.S., Jorge S. and Giulia D..

The remote support of my hometown friends was appreciated: Jérôme B., Nicolas B., Fabian S., Romain B. and Darko M..

I cannot end these acknowledgements without mentioning the other great parallel achievement during this PhD period. I am infinitely thankful to the Royal Brussels British Football Club and particularly to the 3rd Team a.k.a. “the Mighty Thirds”. This activity was my “safety valve”. I was so devoted and eager to play alongside my “comrades in arms” every Saturday whether or not it was raining, snowing, freezing...

The usual suspects: Simon F., Jean-Baptiste C., Ian D., Enric J.P., Jan D., Quentin W., Paul S., Guzman G., Luc T., Divine E., Tim M., Charlie D., Blaise B., Malte C., Diego C., Daniel Y., Romain E., Robert S. and Daniele M..

Being awarded at the end of the season was a great honour as it made me understand that I put everything I have got on and outside the pitch. We were a great team with a team spirit that led us to recover from unlikely situations and to win crucial fixtures.

I cannot fail to remember the many other friends and my family from all places. I believe they know my appreciation.

To finish, this achievement is dedicated to my parents for their unreserved support.

Jayson Babajee
In between the Island and the Continent
In between 2013 and 2014

Contents

Abstract	ix
Résumé	xi
Acknowledgements	xiii
List of Figures	xxi
List of Tables	xxxii
Nomenclature	xxxiii
1. Introduction	1
1.1. The contribution of jet engine to the aircraft expansion	1
1.2. General flow characteristics inside a jet engine	1
1.3. Current jet engine trends	2
1.4. Expectations for the low-pressure turbine (LPT) component design	4
1.5. Objectives and structure of the thesis	8
2. Literature review	11
2.1. Transition and separation phenomena	11
2.1.1. Overview of the concept of transition	11
2.1.1.1. Natural transition	11
2.1.1.2. By-pass transition	12
2.1.1.3. Reverse transition	15
2.1.2. Transition concept applied to a LPT environment	15
2.1.2.1. Separated-flow transition with uniform upstream boundary conditions	16
2.1.2.2. Multimode transition	19
2.1.3. Synthesis of the parameters affecting transition	22
2.2. Control devices to trigger transition and/or remove separation . .	25
2.2.1. Passive control devices	25
2.2.2. Active control devices	28
2.3. Turbulence modelling	29
2.3.1. Introduction to turbulence modelling	29
2.3.2. RANS-equation models	30
2.3.3. Two-equation model	31

2.3.4.	The path to the SST $k\text{-}\omega$ model	32
2.4.	Transition modelling	34
2.4.1.	Transition criteria - Correlation-based models	34
2.4.2.	Transport equation models for transition	36
2.4.2.1.	Empirical approach model	36
2.4.2.2.	Phenomenological approach model	40
2.5.	Summary	41
3.	Description of the database	43
3.1.	Database	43
3.2.	Facilities	45
3.2.1.	S1 facility	45
3.2.2.	CT2 facility	48
3.2.3.	C1 facility	49
3.2.4.	General considerations about the setting of the isentropic outlet Reynolds and Mach numbers	50
3.3.	Effect of the parameters of the database	50
3.4.	Summary	60
4.	Database correlations	63
4.1.	The need for performance models or correlations in a design prospect	63
4.1.1.	Different types of modelling process	63
4.1.2.	AMDCKO correlation for axial turbine	64
4.1.3.	Conclusions on the search for prediction models with a design prospect	68
4.2.	Evaluation of the database information with correlations	70
4.3.	Summary	86
5.	Tools and methodology	87
5.1.	CFD approach with the elsA code	87
5.2.	Methodology	91
5.3.	Summary	101
6.	Evaluation of the $\gamma\text{-}\widetilde{Re}_{\theta t}$ transition model with the database	103
6.1.	T108 LPT blade test case	104
6.2.	T106C LPT blade test case	109
6.2.1.	T106C LPT blade test case: Natural freestream turbulence intensity (0.9%)	111
6.2.2.	T106C LPT blade test case: Turbulence generated by a grid (1.8%)	119
6.3.	T2 LPT blade test case	122
6.4.	HIVK_LS LPT blade test case	128
6.5.	HIVK_HS LPT blade test case	131

6.6.	TX LPT blade test case	135
6.6.1.	TX LPT blade test case: Natural freestream turbulence intensity (0.9%)	137
6.6.2.	TX LPT blade test case: Turbulence generated by a grid (3.2%)	139
6.7.	Summary	143
7.	Investigation of the flow topology with the $\gamma\text{-}\widetilde{Re}_{\theta t}$ transition model	145
7.1.	Separated-flow transition at the natural (low) freestream turbulence intensity	146
7.1.1.	T108 LPT blade test case	146
7.1.2.	T106C LPT blade test case	146
7.1.3.	T2 LPT blade test case	148
7.1.4.	HIVK_LS LPT blade test case	151
7.1.5.	HIVK_HS LPT blade test case	152
7.1.6.	TX LPT blade test case	153
7.1.7.	TD LPT blade test case	154
7.1.8.	TF LPT blade test case	156
7.1.9.	TG LPT blade test case	157
7.1.10.	Bursting characterization	159
7.2.	Transition at the freestream turbulence intensity generated by a turbulence grid	161
7.2.1.	T106C LPT blade test case	163
7.2.2.	TX LPT blade test case	163
7.3.	Summary	165
8.	Investigation of the local roughness-induced transition with the Chimera technique	167
8.1.	Incorporation of the local roughness geometry with the Chimera technique	169
8.2.	Evaluation of the Chimera technique methodology	175
8.2.1.	Comparison between the implicit hole cutting and the patch assembly automatic blanking algorithms	175
8.2.2.	Evaluation of the Chimera technique with a smooth blade suction side overlapping mesh	179
8.2.3.	Evaluation of the overlapping mesh extensions upstream and downstream of the straight forward-backward facing step	180
8.3.	Straight forward-backward facing step investigations	182
8.3.1.	Evaluation of the $\gamma\text{-}\widetilde{Re}_{\theta t}$ transition model on the straight forward-backward facing step configuration	182
8.3.2.	Investigation of the flow topology parameters with the $\gamma\text{-}\widetilde{Re}_{\theta t}$ transition model on the straight forward-backward facing step configuration	187
8.4.	Cylindrical wire investigations	188

8.5. Summary	192
9. Conclusions and recommendations	193
9.1. Conclusions and contributions	193
9.2. Recommendations and prospects	195
A. Evaluation of the $\gamma\text{-}\widetilde{Re}_{\theta t}$ transition model: Additional LPT blade test cases	199
A.1. TD LPT blade test case	199
A.2. TF LPT blade test case	202
A.3. TG LPT blade test case	205
A.4. Comments about the numerical predictions at a turbulence intensity generated by a grid (3.5%)	207
Bibliography	211
List of Publications	219
Curriculum vitæ	221

List of Figures

1.1. Cut-off of the CFM56-7 (Courtesy of CFM International)	3
1.2. Sfc of conventional and geared turbofans at different by-pass ratios - (Kurzke [42])	5
1.3. Stage velocity triangle and station definitions (de la Calzada [18]) .	5
1.4. Commercial aircraft engine flight envelope and the associated LPT operating range Reynolds number (Hourmouziadis [35])	6
1.5. Turbine cascade performance with different flow topologies (Hour- mouziadis [35])	7
1.6. Alternative turbine design losses (Hourmouziadis [35])	8
2.1. Stages of transition (White [77])	12
2.2. Turbulent spot description (Schubauer and Klebanoff [67])	13
2.3. Time-space distribution of the turbulent spots during natural tran- sition (Pfeil et al. [61])	14
2.4. a) Propagation of a turbulent spot in (x,y,t), b) Dependence volume of point P(x,y,t) (Emmons [24])	15
2.5. Sectional view of a two-dimensional short laminar separation bubble (Roberts [65])	16
2.6. Separation bubble types illustration with their corresponding pres- sure distributions from Gaster [26] (Roberts [65])	17
2.7. Wake passing effect on the rotor blades (Dietz and Ainsworth [21])	20
2.8. Time-space diagram of the turbulent spots during forced transition (Pfeil et al. [61])	21
2.9. Turbulent spot production rate as a function of the freestream tur- bulence level for zero-pressure gradient flows (Mayle [52])	22
2.10. Momentum thickness Reynolds number as a function of the free- stream turbulence level for zero-pressure gradient flows (Mayle [52])	23
2.11. Illustration of the momentum thickness Reynolds number at tran- sition onset in function of the acceleration parameter and the tur- bulence level (Mayle [52])	23
2.12. Passive flow control devices (Himmel and Hodson [31])	25
2.13. Mixed-out total pressure loss coefficient for smooth and modified surface cases (LS-T106C, $f_r=0.57$, $Tu=4.0\%$) (Himmel and Hod- son [31])	26
2.14. Passive transition elements (Sieverding et al. [69])	27

2.15. Momentum thickness Reynolds number at transition onset (Abu-Ghannam and Shaw [1])	36
3.1. Effect of the isentropic outlet Reynolds number - Uniform upstream conditions and natural freestream turbulence level of the facility - Cascade losses (a) and outlet flow angle (b) - Area-averaged - HIVK_HS	53
3.2. Effect of the isentropic outlet Reynolds number - Uniform upstream conditions and natural freestream turbulence level of the facility - Cascade losses (a) and outlet flow angle (b) - Mass-averaged - T108, T106C, T2 and HIVK_LS	54
3.3. Effect of the isentropic outlet Mach number - T106C - Uniform upstream conditions and natural freestream turbulence level of the facility (0.9%)	55
3.4. Effect of the turbulence intensity - T106C - Uniform upstream conditions at $M_{2, is} = 0.65$	56
3.5. Effect of the turbulence intensity - HIVK_HS - Uniform upstream conditions at $M_{2, is} \approx 0.75$	56
3.6. Effect of the incoming wakes - HIVK_HS - Wake generator disk rotating speed = 6000 rpm with two different rotating bar diameters d (1.5 mm and 2 mm) at two different $Re_{2, is}$ (130000 and 300000), natural freestream turbulence level (0.8%) and $M_{2, is} \approx 0.75$	57
3.7. Effect of the incoming wakes - T106C - Natural freestream turbulence level (0.9%) and $M_{2, is} = 0.65$	58
3.8. Effect of the incoming wakes - T108 - Natural freestream turbulence level (0.9%)	59
3.9. Effect of the local roughness - T106C - Uniform upstream conditions, natural freestream turbulence level of the facility (0.9%) and $M_{2, is} = 0.65$	60
3.10. Effect of the local roughness - T2 - Uniform upstream conditions, natural freestream turbulence level of the facility (0.9%) and $M_{2, is} = 0.65$	61
4.1. AMDCKO investigations - Cascade total pressure losses - a) T108 at $Tu = 0.9\%$, b) T106C at $Tu = 0.9\%$, c) T2 at $Tu = 0.9\%$, d) T106C at $Tu = 3.2\%$	66
4.2. Examples of power laws representative of the losses evolution with the isentropic outlet Reynolds number	69
4.3. Illustration of the power law coefficients (A and B) variations	69
4.4. Correlation of $Re_{s, reat}$ and $Re_{s, sep}$ - a) Full scale, b) Zoom at low Re	72
4.5. s_{reat}/s_0 against s_{sep}/s_0	72
4.6. Correlation of $Re_{s, end}$ and $Re_{s, onset}$ - a) Full scale, b) Zoom at low Re	72
4.7. s_{end}/s_0 against s_{onset}/s_0	73

4.8. Correlation of $Re_{s,onset}$ and $Re_{s,sep}$ - a) Full scale, b) Zoom at low Re	73
4.9. s_{onset}/s_0 against s_{sep}/s_0	73
4.10. L_B/s_0 against $Re_{2,is}$	76
4.11. ζ against L_B/s_0	76
4.12. L_{lam}/s_0 against $Re_{2,is}$	77
4.13. L_{turb}/s_0 against $Re_{2,is}$	78
4.14. s_{reat}/s_0 against s_{sep}/s_0 - Turbulence intensity effect	78
4.15. s_{end}/s_0 against s_{onset}/s_0 - Turbulence intensity effect	79
4.16. s_{onset}/s_0 against s_{sep}/s_0 - Turbulence intensity effect	79
4.17. L_B/s_0 against $Re_{2,is}$ - Turbulence intensity effect	80
4.18. L_{lam}/s_0 against $Re_{2,is}$ - Turbulence intensity effect	81
4.19. L_{turb}/s_0 against $Re_{2,is}$ - Turbulence intensity effect	81
4.20. s_{reat}/s_0 against s_{sep}/s_0 - $M_{2,is}$ effect - T106C - $\Psi = 1.24$ - $Tu = 0.9\%$	82
4.21. s_{end}/s_0 against s_{onset}/s_0 - $M_{2,is}$ effect - T106C - $\Psi = 1.24$ - $Tu = 0.9\%$	82
4.22. s_{onset}/s_0 against s_{sep}/s_0 - $M_{2,is}$ effect - T106C - $\Psi = 1.24$ - $Tu = 0.9\%$	83
4.23. L_B/s_0 against $Re_{2,is}$ - $M_{2,is}$ effect - T106C - $\Psi = 1.24$ - $Tu = 0.9\%$	83
4.24. ζ against L_B/s_0 - $M_{2,is}$ effect - T106C - $\Psi = 1.24$ - $Tu = 0.9\%$. .	84
4.25. Re_{2,is_B} against D_R - Bursting correlation	85
5.1. Mesh topology of T106C ($\Psi = 1.24$)	92
5.2. "S1" Decay of turbulence ahead of the cascade - T108 CFD predictions	94
5.3. T108 mesh topologies for the mesh independency investigation (not scaled)	96
5.4. T108 isentropic Mach number distribution at $Re_{2,is} = 160000$, $M_{2,is} = 0.6$ and $Tu_{l.e.} = 0.9\%$ - Mesh independency investigation .	97
5.5. T108 wake profile at $Re_{2,is} = 160000$, $M_{2,is} = 0.6$ and $Tu_{l.e.} = 0.9\%$ - Mesh independency investigation - $\Delta P_0 = P_{01} - P_{02}$	97
5.6. T108 pseudo-wall-shear stress ($\tau_{ps,w}$ from experiment) and wall-shear stress (τ_w from CFD calculation) distributions on the SS at $Re_{2,is} = 160000$, $M_{2,is} = 0.6$ and $Tu_{l.e.} = 0.9\%$ - Mesh independency investigation	98
5.7. T108 y^+ distribution on the SS and PS at $Re_{2,is} = 160000$, $M_{2,is} = 0.6$, $Tu_{l.e.} = 0.9\%$ and $Re_{2,is} = 60000$, $M_{2,is} = 0.5$, $Tu_{l.e.} = 0.9\%$.	98
5.8. T108 isentropic Mach number distribution at $Re_{2,is} = 160000$, $M_{2,is} = 0.6$ and $Tu_{l.e.} = 0.9\%$ - Transition model assessment . . .	99
5.9. T108 momentum thickness Reynolds number on the SS at $Re_{2,is} = 160000$, $M_{2,is} = 0.6$ and $Tu_{l.e.} = 0.9\%$ - Transition model assessment	100
5.10. Intermittency function (Abu-Ghannam and Shaw [1])	101
6.1. T108 cascade (not scaled)	104
6.2. T108 isentropic Mach number distribution at $Re_{2,is} = 140000$ and $Tu_{l.e.} = 0.9\%$ - a) Full scale, b) Zoom in the aft region	106

6.3.	T108 pseudo-wall-shear stress ($\tau_{ps,w}$ from experiment) and wall-shear stress (τ_w from CFD calculation) distributions on the SS at $Re_{2,is} = 140000$ and $Tu_{l,e.} = 0.9\%$	106
6.4.	T108 wake profile at $Re_{2,is} = 140000$ and $Tu_{l,e.} = 0.9\%$	107
6.5.	T108 isentropic Mach number distribution at $Re_{2,is} = 70000$ and $Tu_{l,e.} = 0.9\%$ - a) Full scale, b) Zoom in the aft region	107
6.6.	T108 pseudo-wall-shear stress ($\tau_{ps,w}$ from experiment) and wall-shear stress (τ_w from CFD calculation) distributions on the SS at $Re_{2,is} = 70000$ and $Tu_{l,e.} = 0.9\%$	108
6.7.	T108 wake profile at $Re_{2,is} = 70000$ and $Tu_{l,e.} = 0.9\%$	108
6.8.	T108 mass-averaged kinetic losses at $Tu_{l,e.} = 0.9\%$	109
6.9.	T108 mass-averaged outlet flow angle at $Tu_{l,e.} = 0.9\%$	110
6.10.	T106C cascade	110
6.11.	T106C mass-averaged kinetic losses at $Tu_{l,e.} = 0.9\%$	112
6.12.	T106C mass-averaged outlet flow angle at $Tu_{l,e.} = 0.9\%$	112
6.13.	Turbulence across the T106C cascade at $Re_{2,is} = 80000$ with the influence of the turbulent Reynolds number (Re_t)	113
6.14.	Extraction line across the T106C cascade for the investigation of the turbulent Reynolds number influence	114
6.15.	T106C mass-averaged kinetic losses at $Tu_{l,e.} = 0.9\%$ - Re_t effect	115
6.16.	T106C mass-averaged outlet flow angle at $Tu_{l,e.} = 0.9\%$ - Re_t effect	115
6.17.	T106C isentropic Mach number distribution at $Re_{2,is} = 80000$ and $Tu_{l,e.} = 0.9\%$ - a) Full scale, b) Zoom in the aft region	116
6.18.	T106C pseudo-wall-shear stress ($\tau_{ps,w}$ from experiment) and wall-shear stress (τ_w from CFD calculation) distributions on the SS at $Re_{2,is} = 80000$ and $Tu_{l,e.} = 0.9\%$	116
6.19.	T106C wake profile at $Re_{2,is} = 80000$ and $Tu_{l,e.} = 0.9\%$	117
6.20.	T106C turbulence intensity contours at $Re_{2,is} = 80000$ - a) $Re_t = TD$, b) $Re_t = 0.01$	117
6.21.	T106C isentropic Mach number distribution at $Re_{2,is} = 160000$ and $Tu_{l,e.} = 0.9\%$ - a) Full scale, b) Zoom in the aft region	118
6.22.	T106C pseudo-wall-shear stress ($\tau_{ps,w}$ from experiment) and wall-shear stress (τ_w from CFD calculation) distributions on the SS at $Re_{2,is} = 160000$ and $Tu_{l,e.} = 0.9\%$	118
6.23.	T106C wake profile at $Re_{2,is} = 160000$ and $Tu_{l,e.} = 0.9\%$	119
6.24.	T106C mass-averaged kinetic losses at $Tu_{l,e.} = 1.8\%$	120
6.25.	T106C mass-averaged outlet flow angle at $Tu_{l,e.} = 1.8\%$	120
6.26.	T106C isentropic Mach number distribution at $Re_{2,is} = 80000$ and $Tu_{l,e.} = 1.8\%$ - a) Full scale, b) Zoom in the aft region	121
6.27.	T106C pseudo-wall-shear stress ($\tau_{ps,w}$ from experiment) and wall-shear stress (τ_w from CFD calculation) distributions on the SS at $Re_{2,is} = 80000$ and $Tu_{l,e.} = 1.8\%$	121
6.28.	T106C wake profile at $Re_{2,is} = 80000$ and $Tu_{l,e.} = 1.8\%$	122
6.29.	T2 cascade	122

6.30. T2 mass-averaged kinetic losses at $Tu_{l.e.} = 0.9\%$	124
6.31. T2 mass-averaged outlet flow angle at $Tu_{l.e.} = 0.9\%$	125
6.32. T2 isentropic Mach number distribution at $Re_{2,is} = 210000$ and $Tu_{l.e.} = 0.9\%$ - a) Full scale, b) Zoom in the aft region	125
6.33. T2 wake profile at $Re_{2,is} = 210000$ and $Tu_{l.e.} = 0.9\%$	126
6.34. T2 isentropic Mach number distribution at $Re_{2,is} = 120000$ and $Tu_{l.e.} = 0.9\%$ - a) Full scale, b) Zoom in the aft region	126
6.35. T2 pseudo-wall-shear stress ($\tau_{ps,w}$ from experiment) and wall-shear stress (τ_w from CFD calculation) distributions on the SS at $Re_{2,is} =$ 120000 and $Tu_{l.e.} = 0.9\%$	127
6.36. T2 wake profile at $Re_{2,is} = 120000$ and $Tu_{l.e.} = 0.9\%$	127
6.37. HIVK_LS cascade	128
6.38. HIVK_LS mass-averaged kinetic losses at $Tu_{l.e.} = 0.6\%$	129
6.39. HIVK_LS mass-averaged outlet flow angle at $Tu_{l.e.} = 0.6\%$	130
6.40. HIVK_LS pressure coefficient on the blade suction side at $Tu_{l.e.} =$ 0.6% - a) $Re_{2,is} = 130000$ and b) $Re_{2,is} = 50000$	131
6.41. HIVK_HS cascade	131
6.42. HIVK_HS area-averaged kinetic losses at $Tu_{l.e.} = 0.8\%$	133
6.43. HIVK_HS area-averaged outlet flow angle at $Tu_{l.e.} = 0.8\%$	133
6.44. HIVK_HS heat transfer coefficient on the blade suction side (a) and isentropic Mach number distribution (b) at $Re_{2,is} = 450000$ and $Tu_{l.e.} = 0.8\%$	135
6.45. HIVK_HS heat transfer coefficient on the blade suction side (a) and isentropic Mach number distribution (b) at $Re_{2,is} = 90000$ and $Tu_{l.e.} = 0.8\%$	136
6.46. TX cascade	136
6.47. TX area-averaged kinetic losses at $Tu_{l.e.} = 0.9\%$	138
6.48. TX area-averaged outlet flow angle at $Tu_{l.e.} = 0.9\%$	138
6.49. TX wake profile (a) and outlet flow angle profile (b) at $Re_{2,is} =$ 103000 and $Tu_{l.e.} = 0.9\%$	139
6.50. TX wake profile (a) and outlet flow angle profile (b) at $Re_{2,is} =$ 22000 and $Tu_{l.e.} = 0.9\%$	140
6.51. TX area-averaged kinetic losses at $Tu_{l.e.} = 3.2\%$	141
6.52. TX area-averaged outlet flow angle at $Tu_{l.e.} = 3.2\%$	141
6.53. TX wake profile (a) and outlet flow angle profile (b) at $Re_{2,is} =$ 104000 and $Tu_{l.e.} = 3.2\%$	142
6.54. TX wake profile (a) and outlet flow angle profile (b) at $Re_{2,is} =$ 30000 and $Tu_{l.e.} = 3.2\%$	142
7.1. T108 transition onset (s_{onset}/s_0) and separation (s_{sep}/s_0) positions through the $Re_{2,is}$ range at $Tu_{l.e.} = 0.9\%$	147

7.2.	T108 momentum thickness Reynolds number at separation ($Re_{\theta,sep}$) through the $Re_{2,is}$ range at $Tu_{l.e.} = 0.9\%$ - A: Laminar separation - Long bubble region ($Re_{\theta,sep} < 240$) ; B: Laminar separation - Short bubble region ($240 < Re_{\theta,sep} < 320$) ; C: Laminar separation - Dominant transitional / Transitional separation region ($Re_{\theta,sep} > 320$)	147
7.3.	T106C transition onset (s_{onset}/s_0) and separation (s_{sep}/s_0) positions through the $Re_{2,is}$ range at $Tu_{l.e.} = 0.9\%$	148
7.4.	T106C momentum thickness Reynolds number at separation ($Re_{\theta,sep}$) through the $Re_{2,is}$ range at $Tu_{l.e.} = 0.9\%$ - A: Laminar separation - Long bubble region ($Re_{\theta,sep} < 240$) ; B: Laminar separation - Short bubble region ($240 < Re_{\theta,sep} < 320$) ; C: Laminar separation - Dominant transitional / Transitional separation region ($Re_{\theta,sep} > 320$)	149
7.5.	T2 transition onset (s_{onset}/s_0) and separation (s_{sep}/s_0) positions through the $Re_{2,is}$ range at $Tu_{l.e.} = 0.9\%$	150
7.6.	T2 momentum thickness Reynolds number at separation ($Re_{\theta,sep}$) through the $Re_{2,is}$ range at $Tu_{l.e.} = 0.9\%$ - A: Laminar separation - Long bubble region ($Re_{\theta,sep} < 240$) ; B: Laminar separation - Short bubble region ($240 < Re_{\theta,sep} < 320$) ; C: Laminar separation - Dominant transitional / Transitional separation region ($Re_{\theta,sep} > 320$)	150
7.7.	HIVK_LS transition onset (s_{onset}/s_0) and separation (s_{sep}/s_0) positions through the $Re_{2,is}$ range at $Tu_{l.e.} = 0.6\%$	151
7.8.	HIVK_LS momentum thickness Reynolds number at separation ($Re_{\theta,sep}$) through the $Re_{2,is}$ range at $Tu_{l.e.} = 0.6\%$ - A: Laminar separation - Long bubble region ($Re_{\theta,sep} < 240$) ; B: Laminar separation - Short bubble region ($240 < Re_{\theta,sep} < 320$) ; C: Laminar separation - Dominant transitional / Transitional separation region ($Re_{\theta,sep} > 320$)	152
7.9.	HIVK_HS transition onset (s_{onset}/s_0) and separation (s_{sep}/s_0) positions through the $Re_{2,is}$ range at $Tu_{l.e.} = 0.8\%$	153
7.10.	HIVK_HS momentum thickness Reynolds number at separation ($Re_{\theta,sep}$) through the $Re_{2,is}$ range at $Tu_{l.e.} = 0.8\%$ - A: Laminar separation - Long bubble region ($Re_{\theta,sep} < 240$) ; B: Laminar separation - Short bubble region ($240 < Re_{\theta,sep} < 320$) ; C: Laminar separation - Dominant transitional / Transitional separation region ($Re_{\theta,sep} > 320$)	154
7.11.	TX transition onset (s_{onset}/s_0) and separation (s_{sep}/s_0) positions through the $Re_{2,is}$ range at $Tu_{l.e.} = 0.9\%$	155
7.12.	TX momentum thickness Reynolds number at separation ($Re_{\theta,sep}$) through the $Re_{2,is}$ range at $Tu_{l.e.} = 0.9\%$ - A: Laminar separation - Long bubble region ($Re_{\theta,sep} < 240$) ; B: Laminar separation - Short bubble region ($240 < Re_{\theta,sep} < 320$) ; C: Laminar separation - Dominant transitional / Transitional separation region ($Re_{\theta,sep} > 320$)	155
7.13.	TD transition onset (s_{onset}/s_0) and separation (s_{sep}/s_0) positions through the $Re_{2,is}$ range at $Tu_{l.e.} = 0.8\%$	156

7.14. TD momentum thickness Reynolds number at separation ($Re_{\theta,sep}$) through the $Re_{2,is}$ range at $T_{u.l.e.} = 0.8\%$ - A: Laminar separation - Long bubble region ($Re_{\theta,sep} < 240$) ; B: Laminar separation - Short bubble region ($240 < Re_{\theta,sep} < 320$) ; C: Laminar separation - Dominant transitional / Transitional separation region ($Re_{\theta,sep} > 320$)	157
7.15. TF transition onset (s_{onset}/s_0) and separation (s_{sep}/s_0) positions through the $Re_{2,is}$ range at $T_{u.l.e.} = 0.8\%$	158
7.16. TF momentum thickness Reynolds number at separation ($Re_{\theta,sep}$) through the $Re_{2,is}$ range at $T_{u.l.e.} = 0.8\%$ - A: Laminar separation - Long bubble region ($Re_{\theta,sep} < 240$) ; B: Laminar separation - Short bubble region ($240 < Re_{\theta,sep} < 320$) ; C: Laminar separation - Dominant transitional / Transitional separation region ($Re_{\theta,sep} > 320$)	158
7.17. TG transition onset (s_{onset}/s_0) and separation (s_{sep}/s_0) positions through the $Re_{2,is}$ range at $T_{u.l.e.} = 0.8\%$	159
7.18. TG momentum thickness Reynolds number at separation ($Re_{\theta,sep}$) through the $Re_{2,is}$ range at $T_{u.l.e.} = 0.8\%$ - A: Laminar separation - Long bubble region ($Re_{\theta,sep} < 240$) ; B: Laminar separation - Short bubble region ($240 < Re_{\theta,sep} < 320$) ; C: Laminar separation - Dominant transitional / Transitional separation region ($Re_{\theta,sep} > 320$)	160
7.19. Re_{2,is_B} against D_R at the natural (low) freestream turbulence intensity - Bursting correlation updated with the CFD predictions used with the Hatman and Wang correlation [30]	161
7.20. T106C momentum thickness Reynolds number at transition onset ($Re_{\theta,onset}$) through the $Re_{2,is}$ range at $T_{u.l.e.} = 3.2\%$	164
7.21. TX momentum thickness Reynolds number at transition onset ($Re_{\theta,onset}$) through the $Re_{2,is}$ range at $T_{u.l.e.} = 3.2\%$	164
8.1. T106C blade suction side with wavy wire passive control device - UTAT programme - a) View from the top of the blade suction side, b) Zoom of the view from the top of the blade suction side, c) Transversal view from the edge of the blade suction side, d) Straight FB geometry used for the mesh generation	168
8.2. T106C blade suction side with cylindrical wire passive control device - TATMo programme - a) View from the top of the blade suction side, b) Zoom of the view from the top of the blade suction side, c) Cylindrical wire geometry used for the mesh generation	169
8.3. T106C original mesh (overlapped mesh) including the overlapping mesh	170
8.4. T106C overlapping mesh: Straight FB	171
8.5. T106C overlapping mesh: Straight FB meshes resolution - a) Standard view and b) zoom	171

8.6. T106C overlapping mesh: Cylindrical wire	172
8.7. T106C overlapping mesh: Cylindrical wire meshes resolution - a) Standard view and b) zoom	172
8.8. Zones status at overlapping - Cylindrical wire with the implicit hole cutting algorithm - a) Overlapping mesh status, b) Overlapped mesh status	174
8.9. Comparison between the Implicit hole cutting and the Patch assembly automatic blanking algorithms - T106C at $Re_{2,is} = 100000$ and at $Tu_{l.e.} = 0.9\%$ - a) Isentropic Mach number distribution, b) Pseudo-wall-shear stress ($\tau_{ps,w}$ from experiment) and wall-shear stress (τ_w from CFD calculation) distributions on the SS, c) Wake profile	177
8.10. Zones status at overlapping - Straight FB with the patch assembly algorithm - a) Overlapping mesh status, b) Overlapped mesh status	178
8.11. Zones status at overlapping - Straight FB with the implicit hole cutting algorithm - a) Overlapping mesh status, b) Overlapped mesh status	178
8.12. Evaluation of the Chimera technique with a smooth blade suction side overlapping mesh - T106C at $Re_{2,is} = 160000$ and at $Tu_{l.e.} = 0.9\%$ - a) Isentropic Mach number distribution, b) Wall-shear stress, c) Wake profile	179
8.13. Recirculation zones upstream and downstream of the straight FB on the T106C suction side at $Re_{2,is} = 100000$ with the patch assembly algorithm	180
8.14. Evaluation of the overlapping mesh extension downstream of the straight FB - T106C at $Re_{2,is} = 100000$ and at $Tu_{l.e.} = 0.9\%$ - a) Isentropic Mach number distribution, b) Pseudo-wall-shear stress ($\tau_{ps,w}$ from experiment) and wall-shear stress (τ_w from CFD calculation) distributions on the SS, c) Wake profile	181
8.15. T106C mass-averaged kinetic losses at $Tu_{l.e.} = 0.9\%$ with the straight FB	183
8.16. T106C mass-averaged outlet flow angle at $Tu_{l.e.} = 0.9\%$ with the straight FB	183
8.17. T106C isentropic Mach number distribution at $Re_{2,is} = 185000$, $Tu_{l.e.} = 0.9\%$ and with the straight FB - a) Full scale, b) Zoom in the aft region	184
8.18. T106C wake profile at $Re_{2,is} = 185000$, $Tu_{l.e.} = 0.9\%$ and with the straight FB	184
8.19. T106C pseudo-wall-shear stress ($\tau_{ps,w}$ from experiment) and wall-shear stress (τ_w from CFD calculation) distributions on the SS at $Re_{2,is} = 185000$, $Tu_{l.e.} = 0.9\%$ and with the straight FB	185
8.20. T106C isentropic Mach number distribution at $Re_{2,is} = 80000$, $Tu_{l.e.} = 0.9\%$ and with the straight FB - a) Full scale, b) Zoom in the aft region	185

8.21. T106C wake profile at $Re_{2,is} = 80000$, $Tu_{l.e.} = 0.9\%$ and with the straight FB	186
8.22. T106C pseudo-wall-shear stress ($\tau_{ps,w}$ from experiment) and wall-shear stress (τ_w from CFD calculation) distributions on the SS at $Re_{2,is} = 80000$, $Tu_{l.e.} = 0.9\%$ and with the straight FB	186
8.23. Transition onset (s_{onset}/s_0) through the $Re_{2,is}$ range for the T106C at $Tu_{l.e.} = 0.9\%$ with the straight FB	188
8.24. T106C mass-averaged kinetic losses at $Tu_{l.e.} = 0.9\%$ with the cylindrical wire	189
8.25. T106C mass-averaged outlet flow angle at $Tu_{l.e.} = 0.9\%$ with the cylindrical wire	189
8.26. T106C isentropic Mach number distribution at $Re_{2,is} = 160000$, $Tu_{l.e.} = 0.9\%$ and with the cylindrical wire - a) Full scale, b) Zoom in the aft region	190
8.27. T106C wake profile at $Re_{2,is} = 160000$, $Tu_{l.e.} = 0.9\%$ and with the cylindrical wire	190
8.28. T106C isentropic Mach number distribution at $Re_{2,is} = 100000$, $Tu_{l.e.} = 0.9\%$ and with the cylindrical wire - a) Full scale, b) Zoom in the aft region	191
8.29. T106C wake profile at $Re_{2,is} = 100000$, $Tu_{l.e.} = 0.9\%$ and with the cylindrical wire	191
A.1. TD area-averaged kinetic losses at $Tu_{l.e.} = 0.8\%$	201
A.2. TD area-averaged outlet flow angle at $Tu_{l.e.} = 0.8\%$	201
A.3. TD heat transfer coefficient on the blade suction side at $Tu_{l.e.} = 0.8\%$ - a) $Re_{2,is} = 650000$ and b) $Re_{2,is} = 190000$	202
A.4. TF area-averaged kinetic losses at $Tu_{l.e.} = 0.8\%$	203
A.5. TF area-averaged outlet flow angle at $Tu_{l.e.} = 0.8\%$	204
A.6. TF heat transfer coefficient on the blade suction side at $Tu_{l.e.} = 0.8\%$ - a) $Re_{2,is} = 650000$ and b) $Re_{2,is} = 190000$	204
A.7. TG area-averaged kinetic losses at $Tu_{l.e.} = 0.8\%$	206
A.8. TG area-averaged outlet flow angle at $Tu_{l.e.} = 0.8\%$	206
A.9. TG heat transfer coefficient on the blade suction side at $Tu_{l.e.} = 0.8\%$ - a) $Re_{2,is} = 650000$ and b) $Re_{2,is} = 190000$	207
A.10. Heat transfer coefficient on two blades suction side at $Re_{2,is} = 190000$ and $Tu_{l.e.} = 3.5\%$ - a) TD and b) TG	208
A.11. HIVK_HS heat transfer coefficient on the blade suction side at $Re_{2,is} = 90000$ and $Tu_{l.e.} = 3.5\%$	208

List of Tables

3.1. Blades characteristics	44
6.1. T108 LPT blade mesh information	104
6.2. T108 LPT blade working conditions at the natural freestream turbulence intensity	105
6.3. T106C LPT blade mesh information	111
6.4. T106C LPT blade working conditions at the natural freestream turbulence intensity	111
6.5. T106C LPT blade working conditions at a turbulence intensity of 1.8%	119
6.6. T2 LPT blade mesh information	123
6.7. T2 LPT blade working conditions at the natural freestream turbulence intensity	124
6.8. HIVK_LS LPT blade mesh information	128
6.9. HIVK_LS LPT blade working conditions at the natural freestream turbulence intensity	129
6.10. HIVK_HS LPT blade mesh information	132
6.11. HIVK_HS LPT blade working conditions at the natural freestream turbulence intensity	132
6.12. TX LPT blade mesh information	136
6.13. TX LPT blade working conditions at the natural freestream turbulence intensity	137
6.14. TX LPT blade working conditions at a turbulence intensity of 3.2%	140
8.1. T106C LPT blade overlapping mesh information	173
8.2. T106C LPT blade working conditions at the natural freestream turbulence intensity and with the local roughness	182
A.1. TD LPT blade mesh information	200
A.2. TD LPT blade working conditions at the natural freestream turbulence intensity	200
A.3. TF LPT blade mesh information	203
A.4. TF LPT blade working conditions at the natural freestream turbulence intensity	203
A.5. TG LPT blade mesh information	205
A.6. TG LPT blade working conditions at the natural freestream turbulence intensity	205

Nomenclature

Acronyms

2D_CW	Two-Dimensional Cylindrical Wire
2D_RG	Two-Dimensional Rectangular Groove
2D_RS	Two-Dimensional Rectangular Step
<i>elsA</i>	Ensemble Logiciel de Simulation en Aérodynamique
AGS	Abu-Ghannam and Shaw
AMDCKO	Ainley and Mathieson - Dunham and Came - Kacker and Okapuu
CFD	Computational Fluid Dynamics
CFL	Courant-Friedrichs-Lewy
CPU	Computer Processing Unit
DNS	Direct Numerical Simulation
FB	Forward-backward facing step
H&W	Hatman and Wang
HL	High-Lift
HP	High-Pressure
IHC	Implicit Hole Cutting
IP	Intermediate-Pressure
K-H	Kelvin-Helmholtz
LES	Large Eddy Simulation
LP	Low-Pressure

Nomenclature

LPT	Low-Pressure Turbine
ONERA	Office National d'Etudes et de Recherches Aéronautiques
PA	Patch Assembly
PS	Pressure Side
RANS	Reynolds-Averaged Navier-Stokes
RMS	Root Mean Square
RPM	Revolution Per Minute
SS	Suction Side
SST	Shear-Stress Transport model
T-S	Tollmien-Schlichting
TATMo	Turbulence And Transition Modelling for special turbomachinery applications (AST5-CT-2006-030939)
TE	Trailing Edge
UTAT	Unsteady Transitional flows in Axial Turbomachines (GRD1-2001-40192)
VKI	von Karman Institute for Fluid Dynamics
WC	Wake Control

Greek Symbols

ΔH	Total enthalpy variation across the rotor blade	$[J.kg^{-1}]$
ΔV_θ	Tangential velocity variation across the rotor blade	$[m.s^{-1}]$
ϵ	Dissipation rate	$[m^2.s^{-3}]$
η	Non-dimensional distance in the transition region	
η_o	Overall efficiency	
η_{prop}	Propulsive efficiency	
η_{th}	Thermal efficiency	

γ	Intermittency	
κ	Wavenumber	$[m^{-1}]$
λ_θ	Pressure gradient coefficient	
μ_t	Eddy viscosity	$[kg.m^{-1}.s^{-1}]$
ν	Kinematic viscosity	$[m^2.s^{-1}]$
Ω	Rotational speed	$[rad.s^{-1}]$
Ω	Vorticity magnitude	$[s^{-1}]$
ω	Specific dissipation rate	$[s^{-1}]$
Ψ	Compressible Zweifel loading coefficient	
σ	Diffusion coefficient of transport equation	
$\tau_{ps,w}$	Pseudo-wall-shear stress	$[N.m^{-2}]$
τ_w	Wall-shear stress	$[N.m^{-2}]$
θ	Momentum thickness	$[m]$
ζ	Kinetic losses [%]	

Roman Symbols

\dot{m}_f	Mass-flow	$[kg.s^{-1}]$
$\widetilde{Re}_{\theta t}$	Local transition onset momentum thickness Reynolds number (transported variable)	
A	Coefficient used in the power law model	
B	Coefficient used in the power law model	
c	Chord	$[m]$
C_p	Pressure coefficient	
D	Destruction term of transport equation	
d	Bar diameter of the wake generator	$[m]$
D_R	Diffusion rate	

Nomenclature

F	Force	[N]
f_r	Reduced frequency	
g	Pitch	[m]
h	Heat transfer coefficient	[$W.m^{-2}.K^{-1}$]
h_r	Straight FB height or cylindrical wire diameter	[m]
k	Turbulence kinetic energy	[$m^2.s^{-2}$]
l	Length scale	[m]
L_B	Length of the separation bubble: $s_{reat} - s_{sep}$	[m]
L_{lam}	Laminar extent of the separation bubble: $s_{onset} - s_{sep}$	[m]
L_{turb}	Turbulent extent of the separation bubble: $s_{reat} - s_{onset}$	[m]
M	Mach number	
ms	Mesh spacing of the turbulence grid	[m]
N_b	Number of bars in the wake generator system	
P	Production term of transport equation	
P	Static pressure	[Pa]
P_0	Total pressure	[Pa]
Q	Thermal energy	[J]
R	Radius	[m]
$Re_{2,isB}$	Isentropic outlet Reynolds number at bursting	
Re_ν	Vorticity Reynolds number	
$Re_{\theta c}$	Critical momentum thickness Reynolds number	
$Re_{\theta t}$	Transition onset momentum thickness Reynolds number (from the empirical correlation)	
Re_θ	Momentum thickness Reynolds number: $(\theta U_\infty)/\nu_\infty$	
Re_t	Turbulent Reynolds number	

S	Strain rate magnitude	$[s^{-1}]$
s	Curvilinear abscissa	$[m]$
s_0	Suction side TE curvilinear abscissa	$[m]$
sfc	Specific fuel consumption	$[g.N^{-1}.s^{-1}]$
t	Time	$[s]$
Tu	Turbulence level [%]	
U	Velocity	$[m.s^{-1}]$
u'	Fluctuating component of velocity	$[m.s^{-1}]$
V	Velocity	$[m.s^{-1}]$
x	Axial coordinate	$[m]$
Y	Total pressure loss coefficient	
y	Pitch-wise coordinate	$[m]$
y^+	Dimensionless wall distance: $(y\sqrt{\tau_w})/(\nu\sqrt{\rho})$	
$Y_{cascade}$	Total loss coefficient for a blade row	
$Y_{profile}$	Profile loss coefficient	
Y_p	Mixed-out total pressure loss coefficient	
$Y_{secondary}$	Secondary loss coefficient	
Y_{TE}	Trailing edge loss coefficient	
Y_{tip}	Tip clearance loss coefficient	

Subscripts

1	Inlet flow conditions
2	Outlet conditions
γ	Numerical intermittency transport equation
∞	Free-stream condition

Nomenclature

θt	Transition onset momentum thickness Reynolds number transport equation
atm	Atmospheric conditions
ax	Axial flow conditions
$comp$	With Mach number effect
eff	Effective
end	Transition end
f	Fuel
$incomp$	Incompressible
is	Isentropic
k	Turbulence kinetic energy quantity
$l.e.$	Leading edge
$onset$	Transition onset
$peak$	Information at the velocity peak position over the SS
$reat$	Reattachment
sep	Separation
t	Turbulent quantity
$wall$	Conditions at the blade surface

Superscripts

-	Mean component
---	----------------

Chapter 1.

Introduction

1.1. The contribution of jet engine to the aircraft expansion

The idea of jet engine was related to the gas turbine design as illustrated by the well-known thermodynamic Brayton cycle. Several engineers focused on that kind of design in the 1930s. The first patented works are those of Sir Frank Whittle from the United Kingdom in 1930 and Hans-Joachim Pabst von Ohain from Germany in 1936. They share the credit of this design, although they were unaware of the other's work. Concerning the work of Whittle, he built a prototype which was bench-tested in 1937. This design was a single-stage centrifugal compressor coupled to a single-stage turbine. However, von Ohain was the first to implement this propulsion system on an aircraft, the Heinkel He178, which successfully flew in 1939 [25].

In the years following the World War II, the aircraft manufacturers were conscious of the advantages of the jet engine over the piston engine. Those are the possibility to fly at higher speeds, climb faster and fly at higher altitudes in a less vibrating and quieter environment. Moreover, some studies suggest that the core of a gas turbine can be about twenty times as powerful as the same size piston engine [66]. Considering the fact that the current commercial aircraft engine state-of-the-art is still based on the jet engine design, one can say that jet engine has revolutionised air transport and besides it has allowed breaking the "sound barrier". Nowadays, the tendency is to improve this existing configuration by reducing the losses induced aerodynamically, thermodynamically, mechanically . . .

1.2. General flow characteristics inside a jet engine

However, one has to point that turbomachinery flows are among the most complex flows encountered in fluid dynamics. Thus, the flow is subjected to several strong pressure gradients in the compressor stages as well as in the turbine stages due to the deceleration and the acceleration of the flow. There are temperature gradients

as well due to the combustion of the gas and some stresses on the profiles due to the peculiar shapes of some blades. Moreover, the flow is by definition three-dimensional because it is confined in a duct where some 3D structures like vortices appear. Mainly, this flow is considered as unsteady due to the interactions of the numerous rotor and stator blade rows. In that environment, the flow is either laminar or transitional or turbulent. Then, it is prone to separate leading in the worst case to open separation. The flow regime may be incompressible, subsonic, transonic and even supersonic in certain designs. The main parameters governing the behaviour of the machine are the Reynolds number, the Mach number, the Strouhal number, the Prandtl number and the turbulence scales. Some of them are geometrical parameters such as the angular deviation across a stage, the pitch-to-chord ratio and the roughness of the blades.

One can define the performance of an aircraft engine in several ways. The standard one is to take into account the thermal efficiency η_{th} and the propulsive efficiency η_{prop} . The thermal efficiency is the rate of addition of kinetic energy divided by the rate of fuel energy supplied, whereas the propulsive efficiency is the useful power produced divided by the kinetic energy supplied [66]. The overall efficiency is thereafter the product of the propulsive and thermal efficiencies and also the ratio of the useful work over the rate of energy supplied in fuel:

$$\eta_o = \eta_{th} \cdot \eta_{prop} = \frac{F \cdot V_\infty}{Q \cdot \dot{m}_f} = \frac{V_\infty}{sfc \cdot Q_f} \quad (1.1)$$

with sfc , the specific fuel consumption.

Because thrust increases with increasing jet velocity and even more rapidly with fuel consumption [66], one can understand that simple turbojets could be improved particularly for fuel consumption and noise constraints.

1.3. Current jet engine trends

Nowadays, the aircraft engine designs are still turbojets but characterised by high by-pass ratio (8:1 to 10:1 such as the GE90) in order to fulfil the more severe consumption, performance and noise constraints. Then, they are called turbofans where more than 80% of the flow entering the nacelle is passing through the by-pass duct (figure 1.1). A large fan is able to produce the thrust via this by-pass duct (from 19500 to 27300 lb for a CFM56-7B turbofan). This architecture arises due to the need of reducing the fuel consumption and the noise. To achieve these goals, the specific fuel consumption has to be decreased. The common ways to do this are to improve the gas turbine cycle thermodynamic efficiency or to improve the propulsive efficiency. Improved cycle efficiency can be achieved by the increase of the overall pressure ratio or the peak cycle temperature. However,

they are usually limited by the materials and aerodynamics constraints as well as the cooling techniques. The propulsive efficiency is mostly dependent on the by-pass jet velocity for a given flight condition. The propulsive efficiency is high when the by-pass jet velocity difference with respect to the flight speed is low. Low by-pass jet velocity can be achieved by low fan pressure ratio which requires a large fan diameter for a given thrust demand [79]. Consequently, it implies a reduction of the fan rotational speed which prevents shock development at the tip of the fan blades. Considering it is driven by the low-pressure turbine (LPT) via a shaft, it seems quite obvious that this former component is of interest in order to get the maximum efficiency. This means for the LPT higher work to be extracted with lower shaft speed, which entails either an increase in stage loading, if the number of stages is maintained, or an increase in the number of stages for frozen stage loading with the associate penalty in component length and weight [18]. Therefore, one will prefer the first solution which leads to an increase of the flow turning. In addition, the high altitude cruise condition and the low jet velocity ensure the low Reynolds number working conditions encountered in a LPT environment. That is why the LPT is a critical part of the design in a turbofan configuration.

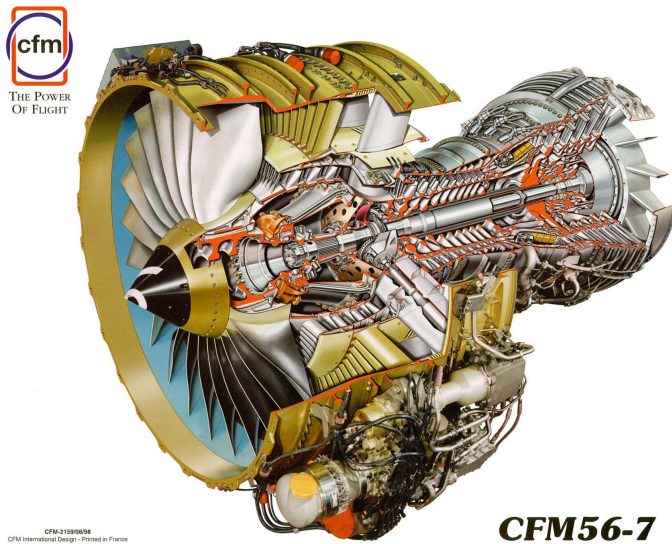


Figure 1.1.: Cut-off of the CFM56-7 (Courtesy of CFM International)

It is common to see turbojet design where both the compressor and the turbine are split in two shafts. Indeed, for small turbojets or simple configurations, only a single compressor and a single turbine are required. But for more complex layout, a multi-shaft or multi-spool is necessary. For an efficiency interest, the smallest

blades of the high-pressure (HP) compressor need to rotate at a higher speed. An illustration of a two-shaft turbofan is given in figure 1.1 where the LP turbine drives the corresponding LP compressor and fan whereas the HP turbine drives the corresponding HP compressor. For larger turbofans (high by-pass ratio), even a three-shaft configuration is possible. This time the LP turbine only drives the fan and there is the introduction of intermediate pressure (IP) compressor and turbine. Consequently, the different components can be optimised to the ideal conditions of each stage. This configuration allows to extract high thrust from a shorter and lighter engine than an equivalently rated two-shaft configuration [66]. Other promising concepts exist to cope with the weight of a conventional high by-pass ratio turbofan. One solution is the geared fan where a speed reduction gear is mounted on the LP shaft between the fan on one side and the LP turbine and LP compressor on the other side. The advantage of this architecture is to de-couple the fan rotational speed from the LP shaft rotational speed. Then, one can optimise the components separately by decreasing the number of LP stages and having a higher LPT rotational speed. The geared configuration allows to further increase the by-pass ratio in comparison to current designs in order to improve the propulsive efficiency and consequently the specific fuel consumption. Another advantage is to decrease the noise and the weight [79]. However, one needs to pay attention at the additional weight of the gear system as well as its operation. Otherwise, the contra rotating fan engine architecture is interesting in the scope of reducing the perceived noise while improving the fuel consumption in the same amount as advanced conventional turbofans. In this configuration, two counter-rotating fans (contrafan) substitute the conventional fan and leads to a reduction of the engine diameter. Moreover, when the contrafan is associated to a statorless LPT with counter-rotating blades, the advantage in terms of mass is obvious.

A summary of the sfc against the by-pass ratio of the different types of turbofans is depicted in figure 1.2. The decrease in sfc is visible when increasing the by-pass ratio and particularly when choosing the geared configuration.

1.4. Expectations for the low-pressure turbine (LPT) component design

The main topic of this PhD thesis is to analyse the laminar to turbulent mechanisms that occur in the LPT. For this purpose, one can evaluate the work done on the rotor in a pure axial machine with the turning of the flow from the Euler's momentum equation:

$$\Delta H = \Omega \cdot R \cdot \Delta V_\theta \quad (1.2)$$

where ΔH and ΔV_θ are the differences between H_2 and H_3 in one hand and V_{θ_2} and V_{θ_3} on the other hand as described by figure 1.3. Ω is the rotational speed

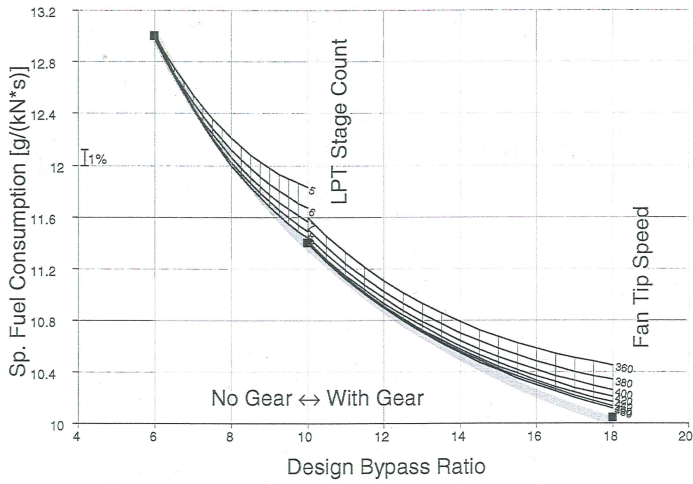


Figure 1.2.: Sfc of conventional and geared turbofans at different by-pass ratios - (Kurzke [42])

and R is the radius.

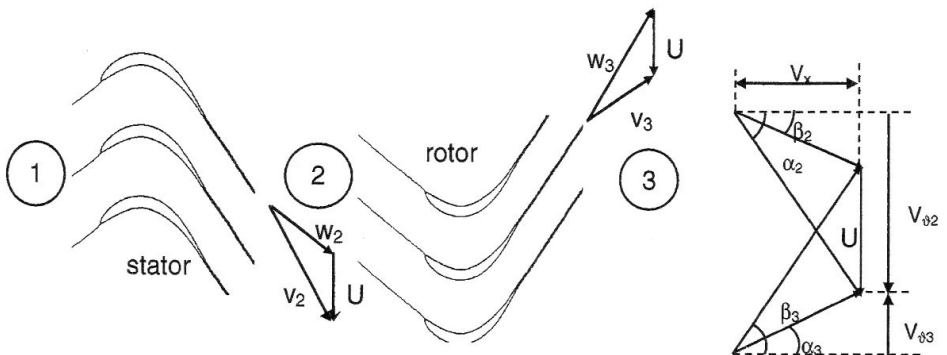


Figure 1.3.: Stage velocity triangle and station definitions (de la Calzada [18])

That is why the study of the transition mechanism is of interest because in the case of open separation, the flow does not behave like it should and the turning is less than expected. A standard LPT is usually made of several stages (4 stages in the case of the CFM56-7B). LPTs commonly operate at an outlet Mach number in the range from 0.6 to 0.9 and weight 20% to 30% of the overall mass of the engine [34]. This latter figure is not negligible when you know that the airplane is lifted

thanks to air and as a consequence, the gravity is its major enemy. Thus, the aim is not to manufacture more powerful and heavier aero-engines such as an industrial gas turbine dedicated to electrical generation but to get the most efficient one in terms of power with respect to weight and losses mainly.

At a first sight, one solution is inevitably to reduce the weight of the LPT component by reducing the number of blades. Then, this would imply an increase of the pitch-to-chord ratio (g/c). In the meantime, this entails a more important loading per blade in order to compensate for the lower number of working blades for a given stage loading. As a consequence, the angular deviation and/or the velocity peak will be higher as well as the diffusion over the rear part of the suction side (SS).

Then, the purpose is to maximise the turbine efficiency, which is already high (about 90%) according to Hodson and Howell [34]. Nevertheless, one has to be aware for this study of the separation and transition phenomena.

To understand this last point, one has to focus on the flight envelope of a typical commercial aircraft. Typically, aircraft fly at 35000 to 40000 feet in cruise configuration. Hourmouziadis [35] illustrated this flight envelope and the LPT Reynolds number operating range in figure 1.4.

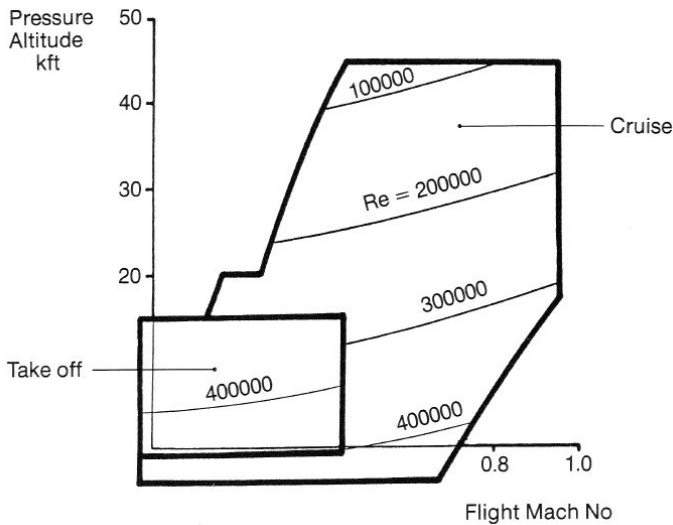


Figure 1.4.: Commercial aircraft engine flight envelope and the associated LPT operating range Reynolds number (Hourmouziadis [35])

One can see that at cruise condition and at mid Mach number (between 0.6 and 0.8), the LPT operating range Reynolds number is below 200000 whereas at take-

where the highest losses are reduced at the low Reynolds number range whereas the lowest losses slightly increase at mid Reynolds numbers. This alternative design was the trend at the time of the study. As one can see, it is really a difficult point to find a good trade-off in terms of configuration to minimise the losses on the overall Reynolds range.

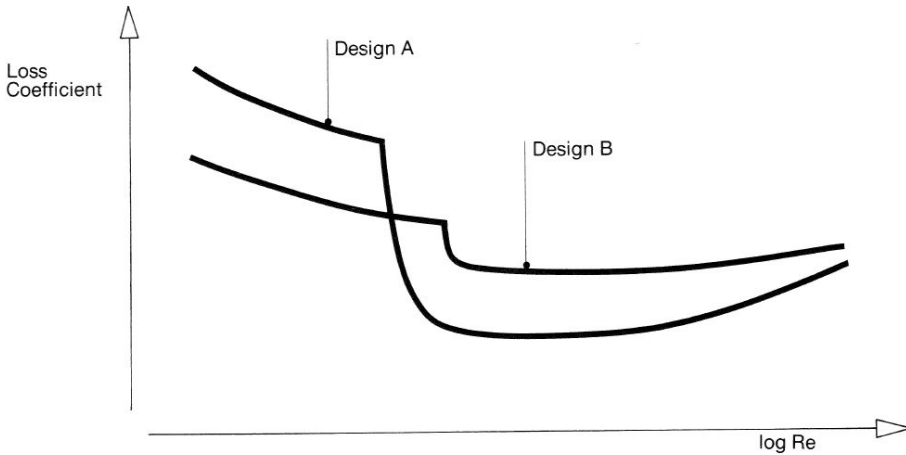


Figure 1.6.: Alternative turbine design losses (Hourmouziadis [35])

As pointed out by Wisler [80], 1% of loss reduction corresponds to a cost reduction of \$200000 per aircraft per year. Likewise, Curtis et al. [17] highlighted that 60% of the losses generated by a blade are due to the suction side. To complete this study, Howell et al. [37] estimated that among these 60% of losses, 60% are related to the boundary layer.

1.5. Objectives and structure of the thesis

The introduction highlighted the main flow behaviours in a LPT as well as the problem of this study which is to reduce the losses of the LPT blades.

In more details, it is a matter of dealing with some economical and environmental concerns that leads to a reduction of the number of blades per row and then to consider what is called “High-Lift (HL) blade”. These blades run at a low Reynolds number and then are prone to separation which has, in terms of performance, a detrimental effect.

That is why one can focus on the internal environment of the turbofan to cope with this separation phenomenon. The interactions between a blade and the upstream row of blades are still the most promising factor due to the unsteady environment of a turbofan. Thus, one can manage to take advantage of the “calming effect”. Several PhD works focused on those topics during the past decade [72, 16]. Moreover, the turbulence intensity is also an important factor to keep in mind. Nowadays, the trend is to take into consideration the roughness either with a spanwise local roughness or with a distributed roughness. Of course a simple design is required in terms of manufacturing cost.

The main aim of this work is to analyse a solution to keep the flow attached and/or to reduce the separation extension over the suction side by triggering the transition and besides by choosing the best trade-off between high Reynolds number regime (take-off configuration) and low Reynolds number regime (cruise configuration). An understanding of the flow behaviour and particularly the separation and transition interactions are of interest in order to get more insight into the physics of this phenomenon. Couple of experimental investigations were carried out at the von Karman Institute for Fluid Dynamics in the framework of partnerships with SNECMA and other European programmes (UTAT and TATMo) on several types of LPT blades with different working conditions. However, data from experimental investigations do not provide all the information needed to understand the flow behaviour over the blade. That is why a numerical approach is used during this work to get more information. It is based on a RANS two-equation turbulence approach coupled with a transition criterion. The numerical predictions are used to support the experimental results. Besides its complementary use, the numerical approach consists in assessing and validating a new transition model based on the transport of two quantities (the numerical intermittency γ and the local transition onset momentum thickness Reynolds number $\widetilde{Re}_{\theta t}$) which was released in the transition community by Langtry and Menter [44]. It constitutes an innovative approach to treat locally the transition process numerically and establishes a framework for future development and improvement for more dedicated applications. Indeed, this model has a universal scope in terms of transition prediction.

Chapter 2.

Literature review

2.1. Transition and separation phenomena

The flow in a LPT environment is prone to transition since the cruise Reynolds numbers are below 100000. It means that most of the boundary layer might be laminar. The LPT environment is significantly disturbed (mid turbulence level of around 4%, upstream row incoming wakes are sources of high disturbances). The transition process results from the amplification of disturbances in the laminar boundary layer. That is why, it is necessary to identify the several modes of transition. It is important to understand and predict the type of boundary layer on a LPT blade since it conditions the separation process and consequently affects the performance. First, an overview of the concept of transition will be presented with a description of the natural transition and the by-pass transition modes. After, an insight into the transition process in a LPT environment will be highlighted.

2.1.1. Overview of the concept of transition

2.1.1.1. Natural transition

Natural transition occurs at low turbulence level (well below 1%). This kind of transition happens generally in external aerodynamics applications such as aircraft wings. As a laminar boundary layer develops, it is subjected to several disturbances. Some of them are damped which leads to a laminar flow whereas some others are amplified which leads to a turbulent flow. This process is known as transition. At a first sight, the practical results of transition are an increase in wall-shear stress as well as in the heat transfer rate and it helps delaying the separation of the boundary layer due to the fuller profile of the turbulent boundary layer. It has been shown that above a certain value of Reynolds number, disturbances, within a certain band of frequencies, will grow with time. This process is referred as the Tollmien-Schlichting (T-S) instability. As they travel downstream, the amplitude of the T-S waves grows and spanwise distortions of the flow vortical structure develop in an increasingly three-dimensional and non-linear manner.

These structures will “burst” into turbulent spots. These turbulent spots will grow while travelling downstream and due to their peculiar shape and propagation velocity, they will merge together to form a fully turbulent boundary layer. An illustration of this natural transition process is given in figure 2.1.

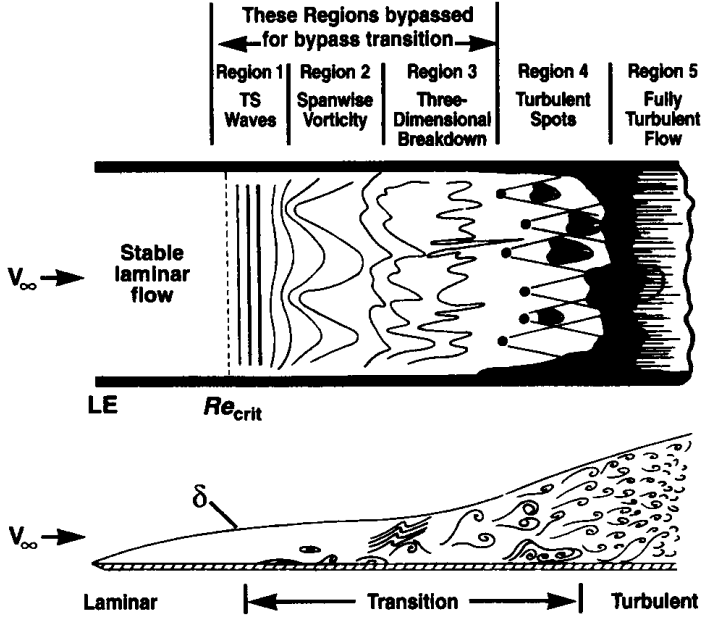


Figure 2.1.: Stages of transition (White [77])

2.1.1.2. By-pass transition

When freestream turbulence is of the order of 1% or more, the transition occurs rapidly, “by-passing” the standard route of the transition process highlighted before and particularly the growth of the T-S waves and their subsequent three-dimensional spanwise distortion. Then, it leads to a direct generation of turbulent spots (figure 2.1). This case happens mainly in turbomachinery applications where the turbulence affects the boundary layer directly. Indeed, the fluctuations of the boundary layer are forced and do not come from the natural growth of the flow instabilities. This phenomenon promotes a sooner transition in comparison to the natural transition process. However, this applies only to attached flows. As highlighted from the former descriptions, turbulent spots constitute the cornerstone of the transition process.

The path to turbulent spots It is quite common to define turbulent spots by: “*Islands of turbulence in a laminar ocean*”. Their peculiar shape and their propagation velocity ensure the birth of the turbulent boundary layer. The general concept of turbulent spot was first observed by Emmons [24]. Schubauer and Klebanoff [67] described the turbulent spot pattern in a zero pressure gradient flow thanks to an electric spark to initiate a turbulent spot. A good illustration of this turbulent spot pattern is depicted in figure 2.2.

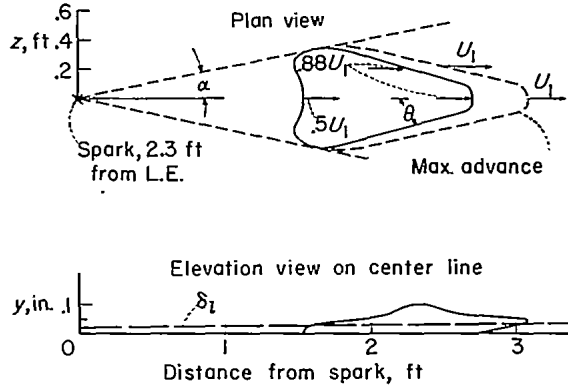


Figure 2.2.: Turbulent spot description (Schubauer and Klebanoff [67])

The turbulent spot has a triangular shape with a half-angle (α) of around 11 degrees. They found that the leading edge and trailing edge velocities are respectively $0.88.U_\infty$ and $0.5.U_\infty$. Due to the velocity difference, the spot can grow longitudinally and transversally. This ensures that spots originating from different locations will merge to form a turbulent boundary layer somehow downstream. They noticed as well that a region unreceptive to disturbances trails behind the turbulent part of each spot. For that reason, they are called “calmed region”. In fact, at the trailing edge of receding turbulence, the flow tends towards laminar condition. The calmed region benefits from a fuller velocity profile which prevents the formation of new instabilities. Moreover, it was found that the trailing edge velocity of the calmed region is $0.3.U_\infty$, which ensures again a stretching of this region behind the turbulent spot. Another feature of this calmed region is the gradually decrease of the wall-shear stress from turbulent level towards laminar level because there should be a continuity between the turbulent pattern and the laminar pattern.

Another good illustration of the turbulent spot growth and extension is given in figure 2.3. The parallel lines to the x-axis reproduce the instantaneous flow conditions along the plate, while the vertical lines describe the change of the flow conditions over the time at a fixed place [61]. From this time-space diagram, one can see the amplification of the T-S wave from the position of neutral stability

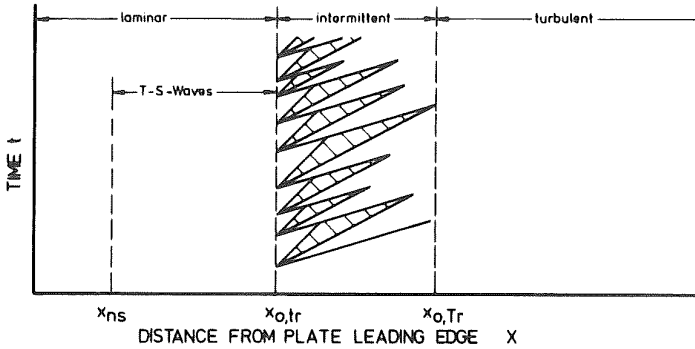


Figure 2.3.: Time-space distribution of the turbulent spots during natural transition (Pfeil et al. [61])

(x_{ns}) to the birth of the turbulent spot at the position of natural transition start ($x_{o,tr}$). The turbulent spots propagate until they merge at the position of natural transition end ($x_{o,Tr}$). The hatched regions correspond to the calmed regions described before and they trail behind the turbulent spot until they are covered by another turbulent spot initiated at a later moment but having a faster propagation velocity. Moreover, the calmed region cannot affect any T-S waves originating upstream of the turbulent spot since the T-S wave velocity is lower than the trailing edge velocity of the calmed region. However, one interesting feature of the calmed region, in a separated-flow configuration with incoming wakes impinging on the suction side of a LPT blade, will be presented later in section 2.1.2.2.

At any position in the transition region, the boundary layer is permanently evolving between a laminar and a turbulent state. That defines the inherent intermittent character of the transition process. Laminar flow corresponds to an intermittency equals to zero whereas a turbulent flow corresponds to an intermittency equals to one. Despite this intermittent behaviour, it is quite common to define a smooth transition process from laminar to turbulent boundary layer with a time averaged value of the intermittency. That is why, it is quite usual to find gradually increasing intermittency factor while going towards the trailing edge. As expected, the probability to get turbulent patterns increases towards the end of the transition region.

This probabilistic approach is illustrated by Emmons [24] in figure 2.4. From his observation of the transition phenomenon (turbulent spots), he derived a phenomenological formula to take into account the fraction of time the flow is turbulent at each position during transition. For that, he defined the “propagation cone”, which is the volume originating from a turbulent spot at $P_0(x_0, z_0, t_0)$ and describing its propagation in time. The turbulent spot shape was previously defined as a triangle (according to a projection on the surface). One can understand

that the three-dimensional extension of the turbulent spot is a cone. Then, Emmons defined a “dependence volume” which is the retrograde cone originating from the point of interest $P(x, z, t)$, containing all the points which could have been the origin of a turbulent spot and subsequently passed over point $P(x, z, t)$. The intermittency at point $P(x, z, t)$ is the fraction of time turbulent spots produced at P_0 pass over P .

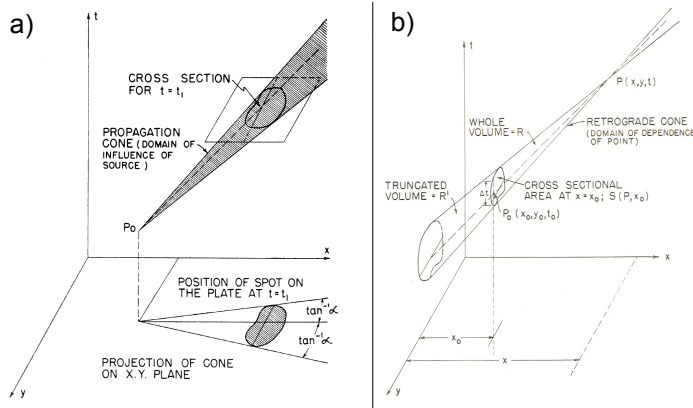


Figure 2.4.: a) Propagation of a turbulent spot in (x,y,t) , b) Dependence volume of point $P(x,y,t)$ (Emmons [24])

2.1.1.3. Reverse transition

So far, the standard path of transition was described, that is to say from laminar to turbulent flow. But, it exists a transition process from turbulent to laminar flow called reverse transition or relaminarization. This process happens in strong favorable pressure gradient flow. In a turbomachinery environment, one can find this type of flow in nozzles, in the exit ducts of combustors, on the front part of turbine blade suction side and generally on the aft part of turbine blade pressure side [52].

2.1.2. Transition concept applied to a LPT environment

After reviewing the general concept of transition, a focus on the typical transition processes occurring in a LPT will be presented. Since the LPT blade pressure side experiences a separation bubble on the front part, followed by a reverse transition on the aft part, only the suction side of the blade is of interest in this study. In a LPT environment, the flow is subjected to mid level of turbulence and strong

adverse pressure gradient on the aft part of the blade suction side. This latter feature induces a flow separation on the aft part of the blade suction side due to the low Reynolds number operating conditions at cruise. Moreover, the flow experiences a strong acceleration on the front part of the suction side leading to laminar flow up to the peak Mach number at least. First, an insight into the separation coupled to the transition effect with uniform upstream boundary conditions will be shown. After, a more realistic flow behaviour with upstream incoming wakes will be illustrated.

2.1.2.1. Separated-flow transition with uniform upstream boundary conditions

Roberts [65] gave a schematic view of the separation-induced transition in the low-speed operating range of an axial compressor or turbine cascade in figure 2.5. The points defined by 'S' correspond to the streamwise location of separation point, the ones defined by 'T' correspond to the streamwise location of the transition onset point and the ones defined by 'R' correspond to the streamwise location of the reattachment point. Under strong adverse pressure gradients, the flow

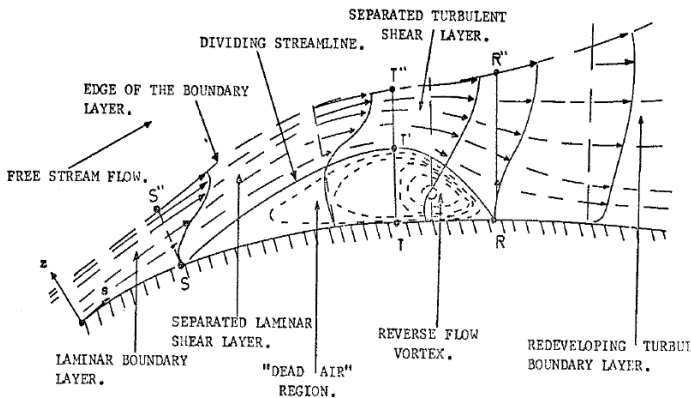


Figure 2.5.: Sectional view of a two-dimensional short laminar separation bubble (Roberts [65])

is prone to separation. Then, the transition takes place in the separated shear layer. Eventually, it reattaches as a turbulent flow. However, in the case of low Reynolds numbers with low level of turbulence, the transition might be too slow and consequently the turbulent entrainment effect cannot make the flow to reattach. As highlighted already, this leads to a dramatic increase of the losses. In the separated shear layer, the main source affecting the transition process is the Kelvin-Helmholtz (K-H) instability [50]. This leads to the growth of fluctuations

in the separated shear layer. As they move downstream, they are amplified and finally trigger transition. Once the transition has started, the momentum exchange in the shear layer by a turbulent mixing reduces the vertical extent of the reverse flow layer and consequently the displacement effect of the bubble. The shear layer entrains more fluid and contributes to the reattachment of the free shear layer.

Roberts [65] presented the pressure distribution of different bubble types, compiling the experimental results of Gaster [26]. These experimental results were made over a range of speeds for the bubbles to pass from the highest Reynolds number short bubble regime to the critical bursting regime that leads to long bubble type. Indeed, they are three types of separation bubble. The first one is the short bubble

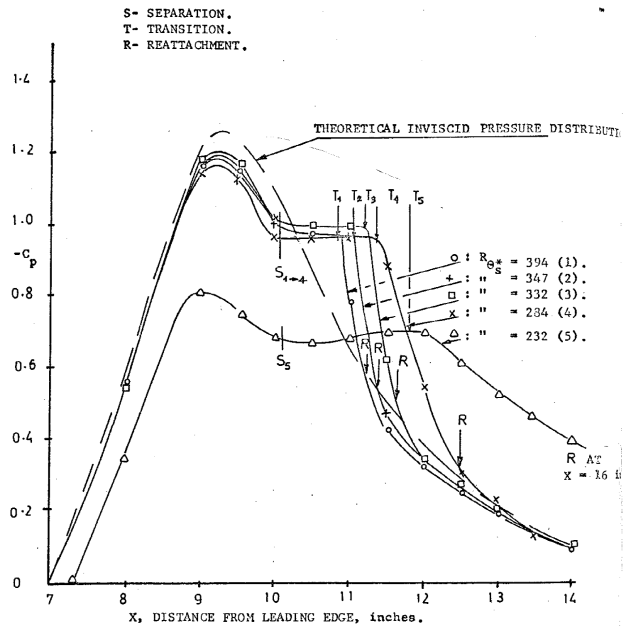


Figure 2.6.: Separation bubble types illustration with their corresponding pressure distributions from Gaster [26] (Roberts [65])

type that does not affect the pressure distribution and is sometimes of interest to trigger the transition process (see configurations 1 to 4 in figure 2.6). The second one is the long bubble type. This kind of separation occurs below a critical Reynolds number where the short bubble “bursts” in a long bubble. The pressure distribution is dramatically affected and particularly the peak Mach number (see configuration 5 in figure 2.6). Besides, the bubble extension can cover a great part of the aft part of the blade suction side and eventually leads to an open separation (i.e. without any reattachment). Again, the peak Mach number is tremendously

decreased and the consequences on the wake are a wider extension in the suction side part and a more axial outlet flow angle for the velocity vector in the frame of the blade.

Those phenomena were studied more than forty years ago. In the past decade, a comprehensive study carried out by Hatman and Wang [27, 28, 29, 30] gave more insights into the bubble types structures over a flat plate at low freestream turbulence and adverse pressure gradients. They stressed the fact that the conventional definitions for long and short bubbles are ambiguous because they are mainly based on the extent of the bubble or the deviation effect from the inviscid pressure distribution [30]. Instead, they based their distinction on the separated flow structures and the vortex shedding dynamics. Indeed, it is commonly accepted that the separated laminar shear layer is inherently unstable and promotes the growth of disturbances [30]. They identified three kinds of separated-flow transition which are conditioned by the superposition of two types of instability (K-H and T-S instabilities). They are the transitional separation, the laminar separation / short bubble mode and the laminar separation / long bubble mode.

Transitional separation bubble The transitional separation occurs when the transition position is ahead of the separation position. It generally happens at high Reynolds number and low adverse pressure gradient, which is not in the context of the present study. The transition process is similar to the natural transition already described previously (see section 2.1.1.1). Hatman and Wang defined a limit where this kind of separation is likely to happen: $Re_{\theta,sep} > 320$.

Laminar separation / short bubble mode The laminar separation / short bubble mode occurs at moderate Reynolds number and mild adverse pressure gradient. This time the transition process takes place in the free shear layer. After the separation of the laminar shear layer, the K-H instability sets in. Then, the roll-up vortex periodically forms, grows, pairs and interacts with the wall. This vortex-wall interaction is the source of the ejection of near wall fluid into the freestream and consequently eddies are released in the shear layer. Because of this ejection, the turbulence develops faster, leading to a shorter transition region and an enhanced turbulent mixing that forces the free shear layer to reattach. In addition to this turbulent mixing, a distinctive vortex shedding signature contributes to the reattachment. The range of this laminar separation / short bubble mode is defined by: $240 < Re_{\theta,sep} < 320$.

Laminar separation / long bubble mode The laminar separation / long bubble mode occurs at low Reynolds number and strong adverse pressure gradient. The process is similar to the laminar separation / short bubble mode except that the ejection process is no longer coupled to the distinctive vortex shedding. Instead

of being shed, this vortex constitutes an extended near-wall region of slow moving fluid. Moreover, the low Reynolds number effect affects the turbulent mixing. Because of these aspects, the shear layer cannot reattach and the separation bubble “bursts” in a long bubble type. Then, the separation bubble extension is dramatically increased and the transition completion is delayed until the turbulence is fully developed which eventually leads to a reattachment of the shear layer. The range of this laminar separation / long bubble mode is defined by: $Re_{\theta,sep} < 240$.

Open separation At last, the worst case encountered in terms of separation is the open separation or massive separation mode. This happens at low Reynolds number with very strong adverse pressure gradient when the separation bubble of the laminar separation / long bubble mode never reattaches because of the reduced turbulent mixing.

2.1.2.2. Multimode transition

Multimode transition is the type of transition which is the more likely to occur in a LPT. In fact, it is characterised by the impingement of wakes from the upstream stator row on the suction side of rotor blades. These upstream wakes are patches of turbulent fluid traveling at a lower velocity than the freestream velocity. The wake is often depicted as a negative jet in the relative frame of reference of the rotor blade. In the rotating frame of reference, the wake slip velocity makes the wake appear as a jet directed from the blade pressure side to the suction side inside one channel [21]. An illustration of this phenomenon is given in figure 2.7.

Due to the velocity defect inside the wake, the wake relative flow angle inside the rotor channel is greater than the relative flow angle in the surrounding freestream flow. It means that there is an overturning of the flow in the wake whereas there is an underturning of the flow outside of the wake. This leads to two circulating flow regions inside the rotor channel on each side of the wake. Consequently, this deforms the wake and there is an accumulation of wake material on the suction side whereas a diminution is experienced on the pressure side [9]. Hence, this results in a jet impinging on the suction side.

As described by Pfeil et al. [61], the forced start of transition is induced by the wake jet. The wake jet is a source of turbulent spots that spread and form on the blade suction side. As discussed before (see section 2.1.1), this leads to an intermittent laminar-turbulent boundary layer where a calmed region trails behind a turbulent spot. Depending on the spacing between two stators (or cylinder bars in an experimental configuration), the natural transition process could be encountered in the undisturbed region between two forced transition onsets induced by impinging wake jets. This is illustrated in figure 2.8.a. x_{ns} is the position of neutral stability. $x_{o,tr}$ and $x_{o,Tr}$ are the positions of natural transition start and

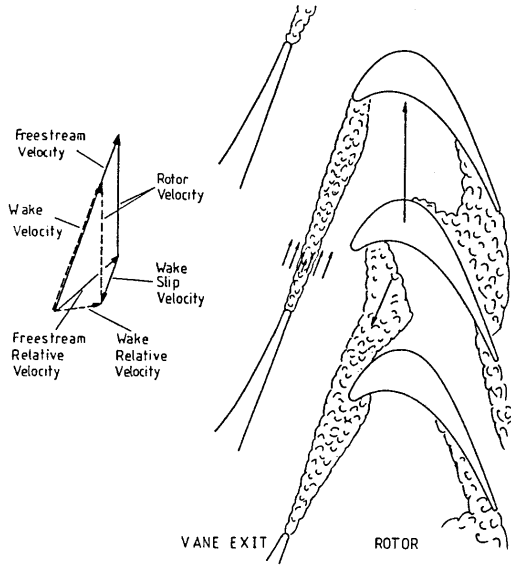


Figure 2.7.: Wake passing effect on the rotor blades (Dietz and Ainsworth [21])

end. $x_{f,tr}$ and x_{f,T_r} are the positions of forced transition start and end. However, it is possible to define an optimum smaller spacing where the creation of turbulent spots of the natural transition type is totally prevented by the calmed regions of the forced turbulent spots (figure 2.8.b). Likewise, it is possible, by decreasing the spacing, to merge earlier the turbulent spots and therefore to reduce the transition length.

The frequency of the wake impingement is made non-dimensional and is similar to a Strouhal number (see equation (3.9)). Coton [16] widely studied the unsteady wake-boundary layer interaction. He concluded that the evolution of the profile losses as a function of reduced frequency presents an optimum. This value of reduced frequency is around 0.7 (with his reduced frequency definition where the reference velocity is the inlet axial velocity $V_{ax,1}$ - this is equivalent to a reduced frequency of 0.28 when the reference velocity is the isentropic outlet velocity $V_{2,is}$, see section 3.3). Moreover, he pointed out that the condition at which the facility was run to simulate a realistic aero-engine working condition matched a reduced frequency of 0.88 (with his reduced frequency definition - this is equivalent to a reduced frequency of 0.34 when the reference velocity is the isentropic outlet velocity $V_{2,is}$). The corresponding rotational speed of the bar rotating system was set at 6000 rpm, which is in the range of LP shaft rotational speed of 2-shaft aero-engine.

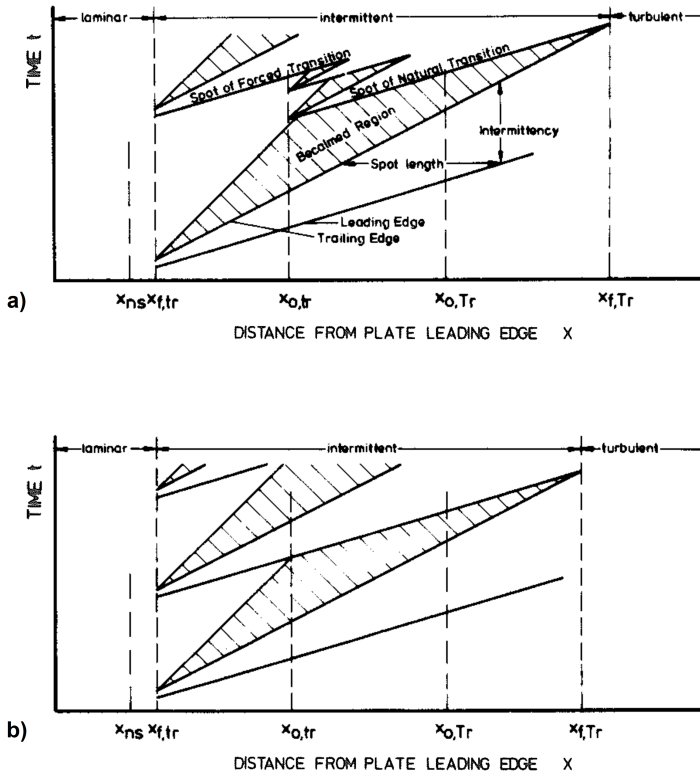


Figure 2.8.: Time-space diagram of the turbulent spots during forced transition (Pfeil et al. [61])

2.1.3. Synthesis of the parameters affecting transition

Main parameters The main parameters affecting the transition process were highlighted before. The Reynolds number is by definition the scale that conditions the range where the flow is more likely to be laminar, transitional or turbulent. But, it does not give the strength of the transition process. In contrast, due to its non-dimensional character, it is a tool used to quantify the start of the transition process, mainly based on boundary layer information, such as the momentum thickness. The main source affecting the transition process is the turbulence spot production. Consequently, their production rate is critical as pointed out by Mayle [52] in figure 2.9 and figure 2.10 from a compilation of data. In figure 2.9, the production rate of turbulent spots for zero pressure gradient flows increases with the turbulence level as expected. Likewise, the momentum thickness Reynolds number at transition onset reduces as the turbulence level increases (figure 2.10).

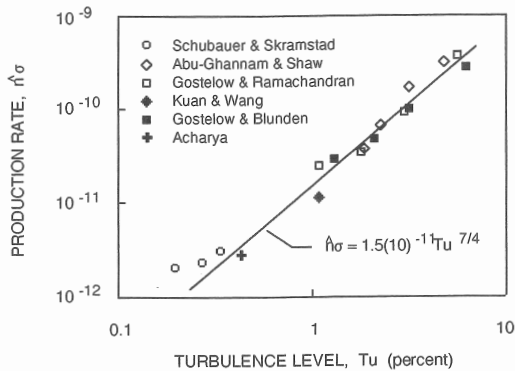


Figure 2.9.: Turbulent spot production rate as a function of the freestream turbulence level for zero-pressure gradient flows (Mayle [52])

The pressure gradient is another parameter that influences the turbulent spot production. Mayle [52] suggested a representation (figure 2.11) where the momentum thickness Reynolds number at transition is a function of the pressure gradient and turbulence level. Three regions are depicted. The separated-flow region is when laminar separation occurs before transition. The natural region is when the transition may be induced by T-S waves, but an influence of the turbulence intensity and the acceleration parameter may also be felt. The bypass region is when the transition is only managed by the turbulence level and happens at high level of turbulence (above 5%). What is defined as the stability criterion is the line above which a T-S instability is possible. What is defined as the separation criterion is the line above which a laminar separation might occur. As expected from these

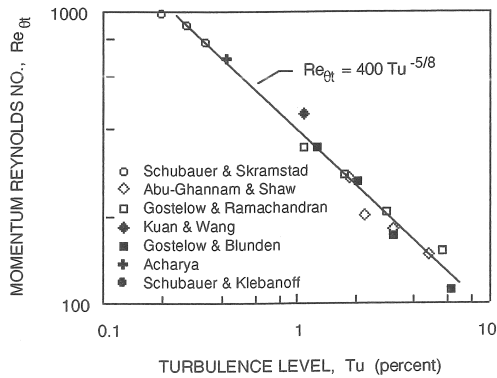


Figure 2.10.: Momentum thickness Reynolds number as a function of the free-stream turbulence level for zero-pressure gradient flows (Mayle [52])

trends, for favorable pressure gradient flows, the transition process is only conditioned by by-pass transition mechanism and consequently depends only on the freestream turbulence. For adverse pressure gradient flows, there is an influence of the pressure gradient in addition to the turbulence level. The general conclusion is that the momentum thickness Reynolds number at the beginning of transition increases with either an increase in acceleration (favorable pressure gradient) or a decrease in the freestream turbulence level. This coupling between turbulence level and pressure gradient was comprehensively studied by Abu-Ghannam and Shaw [1] and is presented later on in the scope of transition modelling (see section 2.4.1).

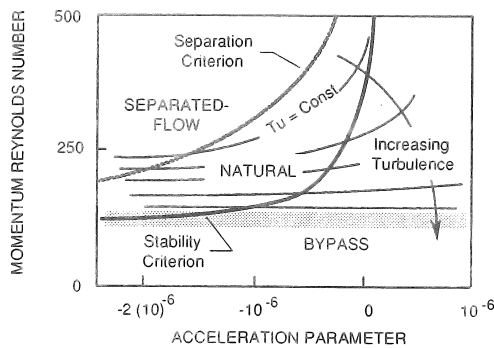


Figure 2.11.: Illustration of the momentum thickness Reynolds number at transition onset in function of the acceleration parameter and the turbulence level (Mayle [52])

The wake-induced transition process is a concrete illustration of the turbulent spot production influence on the boundary layer transition as shown previously.

Secondary parameters In gas turbine, the transition process is conditioned by the free-stream turbulence, the pressure gradient and the unsteadiness. Otherwise, Mayle [52] depicted other parameters which have a secondary effect on the turbulent spot production. That is to say that they have a minor impact on the turbulent spot production (five to ten times less than that of the pressure gradient [51]). However, the surface trip might be an exception since it is intrusive and induces a separation of the boundary layer. The surface distributed roughness can affect the transition process only under low level of turbulence. It hastens the transition process since it gives rise to additional disturbances in the laminar boundary layer. Then, its influence could be spotted for LPT under the worse conditions. A study of Vera et al. [74] will be presented in section 2.2.1 illustrating this latter aspect. Concerning surface trips, they constitute a good approach to trigger transition locally due to the forced separation bubble developing downstream. Then, it is similar to a transitional separation bubble type or a laminar separation / short bubble type. This approach will be illustrated along this work since it constitutes part of the investigation. The streamwise curvature is well known to affect the stability of a boundary layer. The present work focuses on the LPT environment with highly curved blade. A convex curvature (such as the blade suction side) has the tendency to stabilise the boundary layer from transitioning. A fluid particle from an outer layer opposes a tendency to move inwards because its centrifugal force is higher than the one of a fluid particle closer to the convex surface. That is why outwards motion is prevented and consequently the vertical mixing between layers (characteristic of turbulent flows) is reduced. Therefore, a convex curvature has a stabilising effect, in response to disturbances, in comparison to a concave curvature (blade pressure side). However, the scope of this work is the boundary layer evolution on the suction side and therefore on a convex curvature. The effect of heat transfer is known to affect the transition process and particularly when the surface is hotter than the fluid because it promotes small disturbance instabilities and hastens transition. However, in the present work, LPT operates far downstream the combustor, so the fluid temperature is still higher than the blade one and then the flow is less sensible to small disturbances. At last, the compressibility effect can be mentioned but it has a real effect at Mach numbers exceeding one, particularly when there is a shock boundary layer interaction.

2.2. Control devices to trigger transition and/or remove separation

Removing separation by triggering transition is a solution to get rid of the detrimental effects of the massive separation occurring at low Reynolds numbers and consequently the loss of efficiency. That is why the need for control devices seems promising for future LPT design trends. Indeed, the aim is to introduce disturbances in the flow before the separation position in order to make the boundary layer more stable by energising it. The first type of control device is the passive one. The effort to implement and set them up is less important compared to active control devices. They are generally geometrical extensions such as transition wires, roughness strips or other kinds of disturbance generators. In contrary to those, the active control devices are still promising despite an actuation for some of them or a complicated geometrical shape. However, their great interest is to take advantage of their actuation for the whole Reynolds number range.

2.2.1. Passive control devices

Passive control devices are typically wires or roughness strips and even a surface roughness defined during the manufacturing process of the blade with the machine tool. To characterise this type of control device, a study from the University of Cambridge by Himmel and Hodson [31] is highlighted. They presented the results of different kinds of passive flow control devices. They cover three groups: elevated blunt element (two-dimensional cylindrical wire, 2D_CW), elevated element with sharp edges (a two-dimensional rectangular step, 2D_RS) and depression-type element (a two-dimensional rectangular groove, 2D_RG). They are illustrated in figure 2.12.

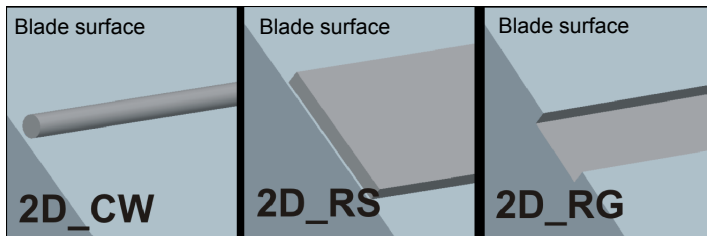


Figure 2.12.: Passive flow control devices (Himmel and Hodson [31])

These devices are typically examples of the geometries that could be encountered in the research environment. They were tested in the low-speed low-pressure turbine linear cascade facility at the University of Cambridge on a low-speed version of

the T106C. They were part of a series of designs studied in the frame of the EU-funded TATMo programme. The other designs were not published in the open literature. However, Himmel and Hodson published the three aforementioned designs which have the easiest-to-implement geometry of each group. One can see in figure 2.13, the improvement in reducing the losses at low Reynolds numbers but there is still a slight increase of the losses at high Reynolds numbers, except for the rectangular groove (2D_RG). This latter design seems to be the good trade-off in terms of loss reduction and blade implementation. Apparently, the better results of the rectangular groove are due to its absence of blockage in contrary to elevated control devices. However, one has to point out that those results were assessed at a turbulence intensity of 4.0% and with a moving bar mechanism where the reduced frequency was 0.57. Indeed, these latter flow characteristics may bias the judgement of the effectiveness of the rectangular groove but still, those conditions are closer to what a LPT experiences during operating conditions.

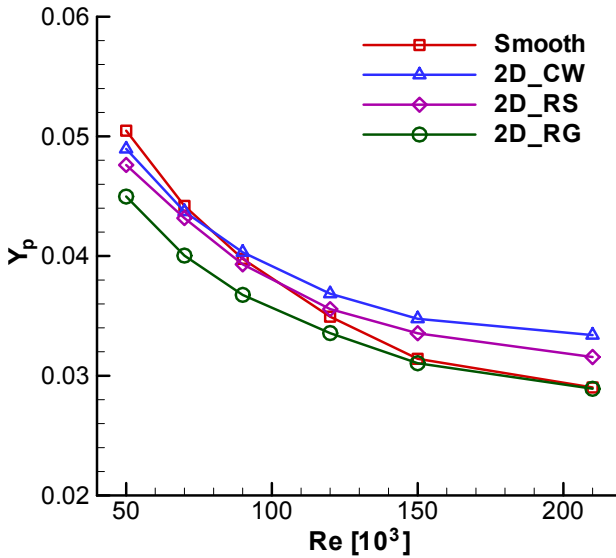


Figure 2.13.: Mixed-out total pressure loss coefficient for smooth and modified surface cases (LS-T106C, $f_r=0.57$, $Tu=4.0\%$) (Himmel and Hodson [31])

In addition to those located transition wires and roughness strips, Himmel and Hodson [32] described their work on another kind of passive flow control device. This investigation was performed under the TATMo programme as well and introduced blowing channels connecting the pressure side and the suction side. The aim is to take advantage of the large pressure difference between the pressure side and the suction side of HL-LPT blades. Typically, it reproduces a forced jet (like an active control device where the blowing mechanism is embedded in the blade) but without any actuation.

Another study of the effectiveness of various types of boundary layer transition elements was carried out by Sieverding et al. [69]. The passive transition elements will only be presented. They are a trip wire, spherical elements and partial slots (figure 2.14).

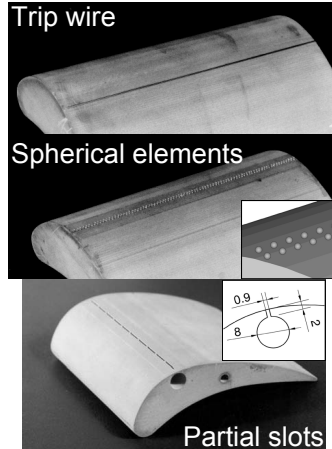


Figure 2.14.: Passive transition elements (Sieverding et al. [69])

The trip wire was assessed at different chord-wise positions and with different wire diameters. The spherical elements were investigated in a single-row and double-row configuration. The partial spanwise slots are connected to an underlying spanwise cavity inside the blade. It came out that the optimum position for the trip wire is slightly ahead of the blade suction side velocity peak. As expected, the losses increase at high Reynolds numbers with this configuration. The spherical elements do not seem to add any improvement in comparison to the optimum trip wire configuration. Concerning the partial slots, they show a small improvement at low Reynolds numbers but what is more interesting is the absence of detrimental effects at high Reynolds numbers. That is why this latter passive control device seems promising because it takes into account the gap in the blade suction side surface (similar to the groove configuration highlighted previously [31]). Moreover, there is a natural blowing effect due to the difference in the blade pressure at mid-span and near the endwalls.

During the manufacturing of the blade, one might take into account the roughness induced by this process. There is a study made by Vera et al. [74] describing it. They examined the effect of different surface finishes on an aft-loaded ultra-HL-LPT profile at Mach and Reynolds numbers representative of LPT engine conditions. Two different kinds of manufacturing process were used to mold the blades. The first one produces a standard “as cast” finish and the second one leaves small spanwise ribs of $\sim 15 \mu\text{m}$ in depth. Moreover, for each casting process,

different post casting finishing processes were applied. The more rough of the finish is defined as “as-cast”, then barreling more this surface, one obtains a less rough surface and barreling more leads to a polished surface. They concluded that the rough surface finish plays a secondary role in the reduction of the losses in comparison to a smoother surface finish. In fact, they found that the presence of spanwise ribs left on the surface of the blade by a specific manufacturing process could lead to a large reduction of the profile losses. Indeed, they defined the presence of these small ribs between the suction peak and the separation point as negative steps and determined this effect as of first order in comparison to the roughness characterising the surface finish [74].

At last, a comprehensive study of Zhang et al. [82] illustrates the interaction between incoming wakes, shed from the upstream row, with surface trips on one side and with air jets on the other side in a ultra HL-LPT environment. They pointed out the effects of suppressing the separation underneath the wakes, the strengthened calmed region (as already described previously) and the reduced separated region between wakes. In fact, they highlighted the effect of the surface trips in the transition process both underneath the wakes and in between them. Although, the calmed region that follows an impinging wake is known to be the main source of loss reduction, any separation and transition control that prevents the formation of these calmed region should be avoided. That is why control devices that add mass-flow in the near wall region, such as air jets are not recommended. However, surface finishes [74] are more recommended than surface trips because surface trips are optimised for a defined design Reynolds number [82].

2.2.2. Active control devices

Nowadays, the search for active control devices is topical. Indeed, in the field of LPT, the design is going towards highly-loaded blade with a strong diffusion at the rear part of the blade (see section 1.4). These designs trends make the flow prone to strong separation that leads to a massive deterioration of the losses. The previous subsection (see section 2.2.1) illustrates the awareness of the designers to cope with this separation issue with passive control devices. Unfortunately, the advantages one gains at low Reynolds numbers turn out to be detrimental at mid or high Reynolds numbers. That is why, if one can adjust the potential of a control device for the whole Reynolds number range, then the efficiency of the machine could be improved at all regimes. In that perspective, research groups focused on the investigations of straightforward designs (such as blowing channels [75]) whereas other prefer fancier designs (such as adjustable membranes and/or plates [69], pressure pulsations [7] and plasma actuators [38, 14]). However, one has to pay attention that the implementation of these active control devices necessitates to be embedded inside the LPT rotor blades with its actuation mechanism.

2.3. Turbulence modelling

The aim of this study is to analyse the aerodynamic behaviour of the flow around LPT blades and particularly the separation and transition processes. For that purpose, the basic equations describing these phenomenon are the fluid dynamics ones which are the Navier-Stokes equations. They define the conservation of mass, momentum and energy.

2.3.1. Introduction to turbulence modelling

Turbulent flow is probably the most challenging topic in the field of fluid dynamics since it is inherent in our environment. The smoke of a cigarette, the water stream downstream bridge piers, the floating flag and more other examples illustrate that. O. Reynolds, cited by Jackson and Launder [39], studied the nature of the flow in the late ninetieth century. His experiment of a thin filament of dye injected in the flow of a fluid in a pipe made him famous and will leave his name for ever related to turbulence. Turbulent flow is defined by a broad range of excited length and time scales. It is characterised by random fluctuations which leads to a non-deterministic behaviour. Thus, the irregular, rotational and time-dependent natures of turbulent motion highlight the contrast with laminar motion because the latter one was imagined to flow in smooth laminae or layers [78]. Turbulent motion is the result of the instability of large vortical structures in the flow which break down into smaller parts [20]. The process associated to the transfer of kinetic energy from the largest structures towards the smallest ones is called the “energy cascade”. At the smallest structures, the kinetic energy is dissipated into heat due to the molecular viscosity. One important feature of turbulence is its enhanced diffusivity which enhances the transfer of mass, momentum and energy [78].

The smallest scale where the kinetic energy is dissipated into heat is commonly referred as the Kolmogorov length scale (η). To get an insight into this scale, A.N. Kolmogorov, cited by Wilcox [78], defined an assumption called the “universal equilibrium theory”. In fact, the smaller eddies should be in a state where the rate of receiving energy from the larger eddies is very nearly equal to the rate at which the smallest eddies dissipate energy to heat [78]. The only dimensional parameters determining the conditions at the dissipative scales are the rate at which the larger eddies supply energy (ϵ) and the kinematic viscosity (ν). From a dimensional analysis, one can get the following Kolmogorov length scale (η).

$$\eta \equiv (\nu^3/\epsilon)^{1/4} \quad (2.1)$$

At last, to understand the energy cascade phenomenon, one can focus on the energy spectral distribution of turbulent properties such as the turbulence kinetic

energy k because the turbulence contains a continuous spectrum of scales. This energy spectral distribution ($E(\kappa)$) can be defined with κ as a wavenumber and $E(\kappa)d\kappa$ as the turbulence kinetic energy contained between wavenumbers κ and $\kappa + d\kappa$:

$$k = \frac{1}{2} \overline{u_i' u_i'} = \int_0^\infty E(\kappa) d\kappa \quad (2.2)$$

Resolving all the scales in time and space of the Navier-Stokes equations may require a lot of computer resources. This approach is defined as a direct numerical simulation (DNS). This technique gives an understanding of the turbulent structures and associated turbulent processes. They can be viewed as an additional source of experimental data where unmeasurable information can be obtained [78]. Another option is to use large eddy simulation (LES). As it states, the largest eddies are only resolved while the smallest eddies are modelled. In fact, since the largest eddies are primarily affected by the boundary conditions, they need to be simulated. Still, this approach requires subsequent computer resources for a design purpose but may be of interest for an academic approach in comparison to DNS. However, for a design purpose, a mean value is generally of interest. It means that the information of DNS and LES, at a design level, will be averaged at a certain point after the resolution of the equations. That is why, Reynolds-averaged Navier-Stokes (RANS) equations are of interest at a design level because the equations are averaged statistically before solving them [20].

2.3.2. RANS-equation models

The Reynolds averaging concept suggested by O. Reynolds, cited by Wilcox [78], consists in time-averaging the Navier-Stokes equations. An instantaneous field is defined as the sum of a mean component and a fluctuating one whose average quantity is null:

$$U(x, t) = \overline{U(x)} + u'(x, t) \quad \text{with} \quad \overline{u'(x, t)} = 0 \quad (2.3)$$

With this concept, one can get rid of the turbulent fluctuations. However, time-averaging the Navier-Stokes equations leaves unknown terms which make the system of equations not close. This is known as the “closure problem”. Indeed, the unknown terms comes from the momentum equation where the “Reynolds shear stress” tensor appears due to the non-linearity of the convective terms and from the energy equation where the turbulent heat flux vector appears. These unknown have to be modelled somehow in order to close the system. Boussinesq drew an analogy with the Newton’s law for describing the turbulent stresses. It is possible

to connect the Reynolds stresses to the strain rate with the eddy viscosity (μ_t). Likewise for the turbulent heat flux, one can determine the turbulent thermal conductivity with a constant turbulent Prandtl number (0.9) and the eddy viscosity introduced before from the Boussinesq hypothesis. The aim of the turbulence modelling is to define the Reynolds stresses and consequently the eddy viscosity. One can define the class of the model according to the number of equations associated to close the system. Thus, only models of two equations will be discussed.

2.3.3. Two-equation model

These models have been developed to incorporate nonlocal and flow history effects in the definition of the eddy viscosity. Indeed, in this RANS approach, the only link to the turbulence phenomenon is the eddy viscosity as highlighted before with the Boussinesq hypothesis. In fact, those models still retain this hypothesis. L. Prandtl, cited by Wilcox [78], postulated a model in which the eddy viscosity depends upon the kinetic energy of the turbulent fluctuations or turbulence kinetic energy (k see equation 2.2). With a dimensional analysis, one can relate the density (ρ), a turbulence length scale (l_t) and the turbulence kinetic energy (k) to the eddy viscosity (μ_t):

$$\mu_t = \text{constant} \cdot \rho k^{1/2} l_t \quad (2.4)$$

He proposed a modelled differential equation approximating the exact equation for k . However, the need to specify a length scale remains. Algebraic approach is used for that purpose. In that prospect, A.N. Kolmogorov, cited by Wilcox [78], was the first to introduce a second transported variable which is the “rate of dissipation of energy in unit volume and time” or the specific dissipation rate (ω). According to dimensional analysis, one can arrange the turbulence kinetic energy, the specific dissipation rate, the eddy viscosity and a turbulence length scale.

$$\mu_t \sim \frac{\rho k}{\omega}, \quad l_t \sim \frac{k^{1/2}}{\omega}, \quad \epsilon \sim \omega k \quad (2.5)$$

Then, the eddy viscosity is affected by where the flow has been and consequently by the flow history [78]. One key comment to remind here is that the specific dissipation rate (ω) is the reciprocal of the time scale on which dissipation of turbulence kinetic energy occurs. However, the actual process of dissipation occurs in small eddies (see section 2.3.1) whereas the specific dissipation rate is the rate of transfer of turbulence kinetic energy to the smallest eddies. Then, one can understand that the specific dissipation rate is indirectly associated to dissipative processes because it depends on the large eddies scales [78].

2.3.4. The path to the SST k - ω model

The most famous two-equation models are the k - ϵ and the k - ω families. The “standard k - ϵ model” developed by W.P. Jones and B.E. Launder, cited by Wilcox [78], is an illustration of the first family. This kind of model has shown a great interest for engineering problems. However, it is inaccurate for complex flows such as flow under adverse pressure gradient and experiences problem to be extended for integration through the viscous sublayer. Despite these highlighted drawbacks, the model can provide substantial qualitative results at the expenses of a fine tuning for each application. In comparison, the k - ω model, as the one of Wilcox [78], is regarded as a more accurate and robust modelling framework of the boundary layer. It performs well under variable pressure gradient (both adverse and favorable) and can be integrated through the viscous sublayer without any viscous corrections. However, the model drawback is its sensitivity to the freestream boundary conditions for free shear flows. In contrast, the k - ϵ does not suffer from this deficiency. That is why, those considerations led Menter [54] to combine the advantages of the k - ω model robustness and accurate formulation in the near wall region and the k - ϵ model freestream independence in the outer part of the boundary layer. The resulting model comes from the blending of the original k - ω model and a k - ϵ model transformed into a k - ω formulation [54]. The original k - ω model is multiplied by a blending function (F_1) and the transformed k - ϵ model is multiplied by $(1-F_1)$. Then, the two expressions are added together. The blending will take place in the wake region of the boundary layer. F_1 equals to zero activates the transformed k - ϵ model away from the wall whereas F_1 equals to one activates the k - ω model in the near wall region. This is, so far, described as the baseline model [54]. Another correction added by Menter [54] is the shear-stress transport model (SST). It introduces a limiter in the eddy viscosity definition. This limiter prevents the shear stress to be overpredicted under adverse pressure gradient flows with the two-equation model. Indeed, it was found that the ratio of the production over the dissipation of k can be higher than one in adverse pressure gradient flows. Thus, it was leading to an underestimation of the adverse pressure gradient effects.

The SST k - ω transport equations are:

$$\frac{D\rho k}{Dt} = P_k - D_k + \frac{\partial}{\partial x_j} \left[(\mu + \sigma_k \mu_t) \frac{\partial k}{\partial x_j} \right] \quad (2.6)$$

$$\frac{D\rho\omega}{Dt} = \frac{\gamma}{\nu_t} P_k - \beta\rho\omega^2 + \frac{\partial}{\partial x_j} \left[(\mu + \sigma_\omega \mu_t) \frac{\partial \omega}{\partial x_j} \right] + 2(1 - F_1) \frac{\rho\sigma_{\omega 2}}{\omega} \frac{\partial k}{\partial x_j} \frac{\partial \omega}{\partial x_j} \quad (2.7)$$

with:

$$\frac{D\cdot}{Dt} = \frac{\partial \cdot}{\partial t} + u_j \frac{\partial \cdot}{\partial x_j} \quad (2.8)$$

and with the destruction (D_k) and production (P_k) terms of the k-equation:

$$D_k = \beta^* \rho \omega k \quad (2.9)$$

$$P_k = \min(\mu_t S^2, 10D_k) \quad (2.10)$$

The blending function F_1 is calculated from:

$$F_1 = \tanh(\arg_1^4) \quad (2.11)$$

$$\arg_1 = \min \left[\max \left(\frac{\sqrt{k}}{\beta^* \omega y}; \frac{500\nu}{y^2 \omega} \right); \frac{4\rho\sigma_{\omega 2} k}{CD_{k\omega} y^2} \right] \quad (2.12)$$

$$CD_{k\omega} = \max \left(2\rho\sigma_{\omega 2} \frac{1}{\omega} \frac{\partial k}{\partial x_j} \frac{\partial \omega}{\partial x_j}; 10^{-20} \right) \quad (2.13)$$

The turbulent viscosity is calculated from:

$$\mu_t = \min \left(\frac{\rho k}{\omega}; \frac{a_1 \rho k}{S \cdot F_2} \right) \quad (2.14)$$

with $a_1=0.31$ and the blending function F_2 :

$$F_2 = \tanh(\arg_2^2) \quad (2.15)$$

$$\arg_2 = \max \left(2 \frac{\sqrt{k}}{\beta^* \omega y}; \frac{500\nu}{y^2 \omega} \right) \quad (2.16)$$

The coefficients $\Phi(\sigma_k, \dots)$ of this model are functions of F_1 :

$$\Phi = F_1 \Phi_1 + F_1 (1 - \Phi) \quad (2.17)$$

where $\Phi_1(\sigma_{k1}, \dots)$ and $\Phi_2(\sigma_{k2}, \dots)$ are respectively the coefficients of the k - ω and the transformed k - ϵ models.

The values of the model coefficients implemented in the *elsA* CFD code from ONERA are presented below [59]. All the calculations made during this thesis were done with those coefficients. The coefficients of $\Phi_1(\sigma_{k1}, \dots)$ (k - ω Wilcox) and $\Phi_2(\sigma_{k2}, \dots)$ (k - ϵ Launder-Sharma) are:

$$\begin{aligned} \sigma_{k1} &= 0.85 & ; & & \sigma_{\omega 1} &= 0.5 & ; & & \beta 1 &= 0.075 \\ \sigma_{k2} &= 1.0 & ; & & \sigma_{\omega 2} &= 0.856 & ; & & \beta 2 &= 0.0828 \\ \beta^* &= 0.09 & ; & & \mathcal{K} &= 0.41 & ; & & \gamma_i &= \frac{\beta_i}{\beta^*} - \frac{\sigma_{\omega i} \mathcal{K}^2}{\sqrt{\beta^*}} & ; & & a_1 &= 0.31 \end{aligned} \quad (2.18)$$

2.4. Transition modelling

Two-equation model can predict transition but they generally predict them too early [78]. Indeed, Wilcox [78] illustrated that on an incompressible flat plate configuration, using the k - ω model, the transition is predicted one order of magnitude too low in terms of Reynolds number. That is why on LPT blades, the skin friction will exhibit a local minimum in the front part of the blade.

A solution to trigger the transition is to affect a weighting factor to the production term of the turbulence kinetic energy, that will be called the “intermittency weighting factor”. This factor has to be controlled somehow. For that purpose, one can use transition criteria based upon experimental investigations.

Most of the transition criteria are based upon empirical correlations [52, 1]. When the transition criterion is met, the so-called intermittency weighting factor is switched on from 0 to 1 (like a step) and consequently triggers the production of the turbulence kinetic energy. However, despite its numerical definition, it still keeps the same qualitative meaning of the intermittency coefficient which is the fraction of time during transition for which the flow is turbulent. Besides, this kind of methodology implies the need for the boundary layer thickness calculation from the integration of the velocity profiles. This is to define the edge of the boundary layer to retrieve the freestream information.

Instead of triggering transition by a switch (via the intermittency weighting factor), the transition process should be handled locally with a gradually evolving intermittency weighting function. That is why, new methods for the computation of transition founded on transport equations (using local quantities) are of interest such as the γ - $\widetilde{Re}_{\theta t}$ model of Langtry and Menter [44]. This approach is widely discussed in this thesis since it was the model chosen to assess the transition phenomenon in LPT. Another transport equation transition model based on the laminar kinetic energy approach [76, 46] seems promising.

2.4.1. Transition criteria - Correlation-based models

Correlation-based transition criteria are widely used in the field of turbomachinery because the flow is mainly characterised by by-pass transition which occurs at mid turbulence levels. A comprehensive study of transition investigation in the LPT environment is the one of Abu-Ghannam and Shaw [1]. It dates back 1980 but it is still widely used by the LPT designers and is still implemented in CFD code [59]. It even constitutes part of the framework of new transport equation models [44].

This investigation was done in a low-speed wind-tunnel on a flat plate with free-stream turbulence ranging from 0.5% to 5% and with pressure gradient histories

typical of turbomachinery blades without separation [1]. Even though, they stated they investigate natural transition, some of their test cases were assessed at mid turbulence levels. The robustness of this model relies on the fact that they linked the boundary layer quantities to external information. In addition, they assessed several configurations covering both the turbulence level and the pressure gradient (positive and negative) ranges.

They defined a correlation for the transition onset. This correlation encompasses both the turbulence level and the pressure gradient information. The output of the correlation is the momentum thickness Reynolds number from the following set of equations:

$$Re_{\theta t} = 163 + \exp \left[F(\lambda_{\theta}) - \frac{F(\lambda_{\theta}) \cdot Tu}{6.91} \right] \quad (2.19)$$

$$F(\lambda_{\theta}) = 6.91 + 12.75 \lambda_{\theta} + 63.64 \lambda_{\theta}^2 \quad ; \quad \lambda_{\theta} < 0 \quad (2.20)$$

$$F(\lambda_{\theta}) = 6.91 + 2.48 \lambda_{\theta} - 12.27 \lambda_{\theta}^2 \quad ; \quad \lambda_{\theta} > 0 \quad (2.21)$$

$$\lambda_{\theta} = \left(\frac{\theta^2}{\nu} \right) \left(\frac{dU_{\infty}}{ds} \right) \quad (2.22)$$

Moreover, they derived a couple of boundary layer parameters during transition in function of a non-dimensional distance η from the start of transition over the transition length.

$$\eta = \frac{s - s_{onset}}{s_{end} - s_{onset}} \quad (2.23)$$

Here is the relationship between the intermittency coefficient γ , which defines the fraction of time during transition for which the flow is turbulent, and η .

$$\gamma = 1 - \exp(-5\eta^3) \quad (2.24)$$

The illustration of the Abu-Ghannam and Shaw (AGS) correlation (equations 2.19 to 2.21) is depicted on figure 2.15. One feature is the quasi non-dependency of the momentum thickness Reynolds number with the turbulence level in the favorable pressure gradient region. In contrast, one can see this dependency in the adverse pressure gradient region and particularly at low turbulence level.

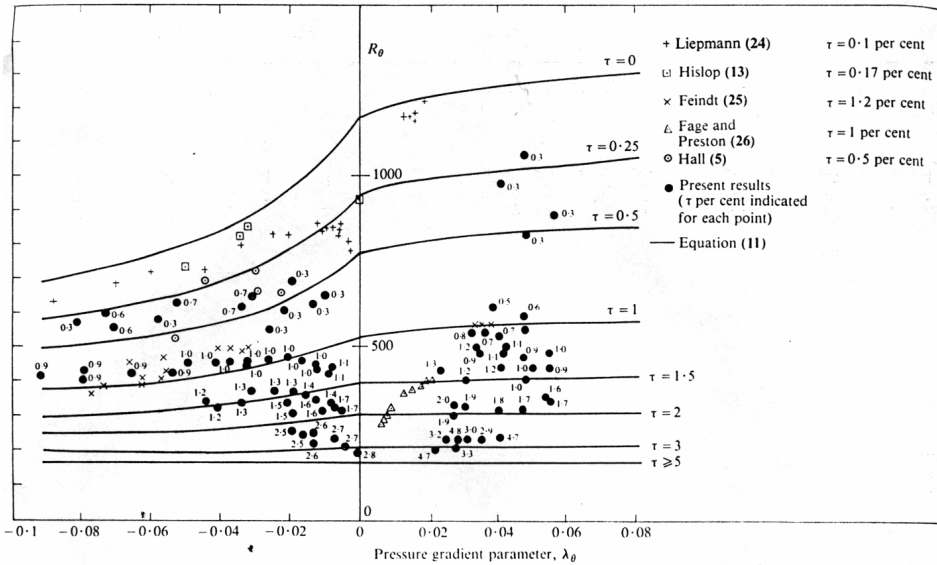


Figure 2.15.: Momentum thickness Reynolds number at transition onset (Abu-Ghannam and Shaw [1])

2.4.2. Transport equation models for transition

As highlighted before, one drawback of the transition triggered at a defined stream-wise location is the non-gradual evolution of the intermittency weighting factor inside the boundary layer. To cope with this and take into account the history of the flow, transport equation is the solution to transport the intermittency weighting factor. One of the illustration of this technique is the model of Langtry and Menter [44], as known as the $\gamma\text{-}\widetilde{Re}_{\theta t}$ model. This model will be used and assessed in this thesis in the framework of LPT blades.

2.4.2.1. Empirical approach model

The $\gamma\text{-}\widetilde{Re}_{\theta t}$ model description is based upon the works of Langtry and co-workers [43, 44, 55, 45]. The model central idea is the van Driest and Blumer’s vorticity Reynolds number concept [73]. It allows to link the transition onset momentum thickness Reynolds number to the local boundary layer quantities. The concept is depicted in equation 2.25 and equation 2.26.

$$Re_\nu = \frac{\rho y^2}{\mu} \left| \frac{\partial u}{\partial y} \right| \tag{2.25}$$

$$Re_{\theta} = \frac{\max(Re_{\nu})}{2.193} \quad (2.26)$$

In fact, this model gets rid of the integration of the boundary layer velocity profile along “computation lines” based on the wall mesh lines. Those velocity profiles were used to determine the onset of transition according to transition criteria (such as the Abu-Ghannam and Shaw correlation [1]), since they are based on the turbulence intensity and the pressure gradient parameter estimated at the edge of the boundary layer.

The transport equation for the numerical intermittency (γ) is:

$$\frac{\partial(\rho\gamma)}{\partial t} + \frac{\partial(\rho U_j \gamma)}{\partial x_j} = P_{\gamma} - D_{\gamma} + \frac{\partial}{\partial x_j} \left[\left(\mu + \frac{\mu_t}{\sigma_f} \right) \frac{\partial \gamma}{\partial x_j} \right] \quad (2.27)$$

The source term (P_{γ}) of the numerical intermittency equation is triggered by the ratio of the vorticity Reynolds number (Re_{ν}) and the critical momentum thickness Reynolds number (Re_{θ_c}) via the F_{onset} function (see equation 2.28 to equation 2.33). Basically, this source term is designed to be inactive (equal to zero) in the laminar boundary layer and active everywhere the local transition criterion is met. Moreover, the F_{length} function controls the magnitude of this source term in order to take into account the extent of the transitional region.

$$P_{\gamma} = F_{length} c_{a1} \rho S [\gamma F_{onset}]^{0.5} [1 - c_{e1} \gamma] \quad (2.28)$$

The F_{onset} function is defined as follows:

$$F_{onset_1} = \frac{Re_{\nu}}{2.193 Re_{\theta_c}} \quad (2.29)$$

$$F_{onset_2} = \min [\max (F_{onset_1}, F_{onset_1}^4), 2.0] \quad (2.30)$$

$$F_{onset_3} = \max \left[1 - \left(\frac{Re_t}{2.5} \right)^3, 0.0 \right] \quad (2.31)$$

$$Re_t = \frac{\rho k}{\mu \omega} \quad (2.32)$$

$$F_{onset} = \max [F_{onset_2} - F_{onset_3}, 0.0] \quad (2.33)$$

The destruction/relaminarization term (D_{γ}) ensures the numerical intermittency remains close to zero in the laminar boundary layer and even predicts relaminarization.

$$D_{\gamma} = c_{a2} \rho \Omega \gamma F_{turb} [c_{e2} \gamma - 1] \quad (2.34)$$

The constants for the numerical intermittency equation are:

$$c_{e_1} = 1.0 \quad ; \quad c_{a_1} = 2.0 \quad ; \quad c_{e_2} = 50.0 \quad ; \quad c_{a_2} = 0.06 \quad ; \quad \sigma_f = 1.0 \quad (2.35)$$

The function F_{turb} is used to disable the destruction/relaminarization source outside of a laminar boundary layer or in the viscous sublayer:

$$F_{turb} = e^{-\left(\frac{Re_t}{4}\right)^4} \quad (2.36)$$

In their first publication, Menter et al. [55] did not disclose all their functions and particularly the F_{length} and the $Re_{\theta c}$ functions. At this time, it was known they were both function of the transition onset momentum thickness Reynolds number ($\widetilde{Re}_{\theta t}$). That is why several groups throughout the world focused on the determination of these functions [62, 49, 23, 13]. At last, the originators of this transition model published their own version of these missing functions [44]. However, in this study, the CFD code *elsA* relies on the calibrations of those functions performed by Content and Houdeville [13].

The transport equation for the transition onset momentum thickness Reynolds number ($\widetilde{Re}_{\theta t}$) is:

$$\frac{\partial(\rho \widetilde{Re}_{\theta t})}{\partial t} + \frac{\partial(\rho U_j \widetilde{Re}_{\theta t})}{\partial x_j} = P_{\theta t} + \frac{\partial}{\partial x_j} \left[\sigma_{\theta t} (\mu + \mu_t) \frac{\partial \widetilde{Re}_{\theta t}}{\partial x_j} \right] \quad (2.37)$$

The purpose of this equation is to transform the non-local empirical correlation into a local quantity in order to compute the transition length function (F_{length}) and the critical momentum thickness Reynolds number ($Re_{\theta c}$), necessary for the numerical intermittency equation (see equation 2.27).

Then, when Re_{θ} (see equation 2.26) exceeds locally $Re_{\theta c}$ (which is a function of $\widetilde{Re}_{\theta t}$), γ equals one due to the activation of P_{γ} in equation 2.27. After, a function defines the effective intermittency γ_{eff} by the maximum value between γ and γ_{sep} . This latter separation intermittency coefficient (γ_{sep}) is part of a separation-induced transition correction that allows the local intermittency to exceed one. At last, γ_{eff} imposes laminar regions locally and triggers the transition mechanism by turning on the production term of the turbulence kinetic energy transport equation, since this transition model is coupled to the SST $k-\omega$ turbulence model. Besides, γ_{eff} affects the destruction term of the turbulence kinetic energy transport equation. The mentioned separation-induced transition correction is to let k grow more rapidly once the boundary layer separates. This is the reason why it exceeds one.

The source term ($P_{\theta t}$) is designed to force the transported variable $\widetilde{Re}_{\theta t}$ to be equal to $Re_{\theta t}$ in the freestream and to diffuse this value into the boundary layer by means of the blending function ($F_{\theta t}$) which turns off this source term in the boundary layer. This $Re_{\theta t}$ comes from an empirical correlation ($Re_{\theta t}=f(Tu, \lambda_{\theta})$) similar to the one of Abu-Ghannam and Shaw (see equation 2.19) [44].

$$P_{\theta t} = c_{\theta t} \frac{\rho}{t} \left(Re_{\theta t} - \widetilde{Re}_{\theta t} \right) (1.0 - F_{\theta t}) \quad (2.38)$$

$$t = \frac{500\mu}{\rho U^2} \quad ; \quad c_{\theta t} = 0.03 \quad ; \quad \sigma_{\theta t} = 2.0 \quad (2.39)$$

$$F_{\theta t} = \min \left\{ \max \left[F_{wake} e^{-\left(\frac{y}{\delta}\right)^4}, 1 - \left(\frac{\gamma - 1/c_{e2}}{1 - 1/c_{e2}} \right)^2 \right], 1 \right\} \quad (2.40)$$

This approach implies the existence of a lag between the freestream value of $\widetilde{Re}_{\theta t}$ and the one inside the boundary layer. The reason is related to Abu-Ghannam and Shaw's conclusion about the predominant effect of the past history of the pressure gradient on transition over the effect of the local history at transition [1]. That lag could be controlled by the diffusion coefficient ($\sigma_{\theta t}$). This coefficient was tested at two values $\sigma_{\theta t} = 2$ (Langtry and Menter [44]) and $\sigma_{\theta t} = 10$ (Menter et al. [55] and Content and Houdeville [13]). However, in their latest publications Langtry and Menter [44] used and recommended the value of $\sigma_{\theta t} = 2$ (this value has been implemented in the CFD code *elsA*). This choice is due to the fact that smaller the value of $\sigma_{\theta t}$ and more sensitive the model is to history effects [43]. In contrary to standard transition onset correlation [1], Langtry and Menter [44] introduced a correction to take into account separation-induced transition as briefly introduced couple of lines above. The main difference is on the relation between the vorticity Reynolds number Re_{ν} and the critical momentum thickness Reynolds number ($Re_{\theta c}$) where they changed the value of a constant based on a Blasius boundary layer profile to the one corresponding to the value at separation when the shape factor is 3.5. Moreover, this function emerged due to the under-production of turbulence downstream the transition onset for separation-induced transition configuration while using the SST $k-\omega$ turbulence model. It leads to the non-reattachment of the boundary layer. That is why the γ_{sep} function was introduced in order to allow an over-production of turbulence kinetic energy which will enhance the reattachment process.

$$\gamma_{sep} = \min \left\{ s_1 \max \left[0, \left(\frac{Re_{\nu}}{3.235 Re_{\theta c}} - 1 \right) \right] F_{reattach}, 2 \right\} F_{\theta t} \quad (2.41)$$

$$F_{reattach} = e^{-\left(\frac{Re_{\nu}}{20}\right)^4} \quad ; \quad s_1 = 2.0 \quad (2.42)$$

$$\gamma_{eff} = \max(\gamma, \gamma_{sep}) \quad (2.43)$$

According to Langtry [43], the s_1 constant controls the reattachment location and the larger the value of s_1 is and the shorter the reattachment length. This explains why couple of researchers worked on this parameter such as Corral and Gisbert [15] who introduced a $\widetilde{Re}_{\theta t}$ -dependency of s_1 .

The modified SST k - ω turbulence model is:

$$\frac{\partial(\rho k)}{\partial t} + \frac{\partial(\rho U_j k)}{\partial x_j} = \tilde{P}_k - \tilde{D}_k + \frac{\partial}{\partial x_j} \left[(\mu + \sigma_k \mu_t) \frac{\partial k}{\partial x_j} \right] \quad (2.44)$$

$$\tilde{P}_k = \gamma_{eff} P_k \quad ; \quad \tilde{D}_k = \min [\max(\gamma_{eff}, 0.1), 1.0] D_k \quad (2.45)$$

with P_k (see equation 2.10) and D_k (see equation 2.9).

2.4.2.2. Phenomenological approach model

A phenomenological model is a physics-based model where one wants to describe the fundamental mechanism of a phenomenon. An illustration of this phenomenological type of model is the laminar kinetic energy (k_l) model. This model is based on the laminar fluctuation energy in the pre-transitional region of the boundary layer as first introduced by Mayle and Schulz [53]. Their starting point was the fact that the laminar fluctuations preceding transition are primarily caused by the work of the imposed fluctuating freestream pressure forces on the flow in the boundary layer. This framework has led several research groups to focus on this concept [76, 46]. Lardeau et al. [46] highlighted that the pre-transitional fluctuations leading to bypass transition are due to the presence of low-frequency/low amplitude streamwise vortices in the boundary layer. These vortices are assimilated as “streaky structures” from their large eddy simulations. Then, they showed that the generation of these “streaky structures” is due to a production mechanism such as the production of turbulence in a turbulent flow. It turned out that the kinetic energy of the laminar fluctuations (k_l) can be described by a transport equation similar to the transport equation for the turbulence kinetic energy (k). Then, they are able to address the rise of pre-transitional fluctuations in boundary layers and subsequent breakdown to turbulence since they are formulated in terms of local flow quantities. This k_l -equation can be incorporated in different turbulence models, but seems more reliable with the k - ω model form since it has been adopted by the two research groups previously cited. The objective is to model the pre-transitional fluctuations with the k_l -equation. Once a parameter including the kinetic energy is greater than some threshold level, the energy from the streamwise fluctuations k_l is transferred to the turbulent fluctuations [20]. Besides, the transition process is defined by a transfer of energy from k_l to k via the pressure-strain mechanism [76]. It is called “energy redistribution”.

2.5. Summary

This chapter reviewed the phenomena of transition and separation occurring in a LPT environment looking at the detrimental effect of open separation on the performance of LPT blades. Realistic solutions to cope with this harmful effect are provided.

Even though the calming effect is seen in a real machine (due to incoming wakes), there is still a large time window during which no wake impinges on the suction side. This time window might even increase in the case of HL configurations where the pitch is longer. That is why roughness-induced transition seems a reasonable approach for HL configurations.

A reliable flow prediction is critical for the designer. Consequently, the latest transition models have to be evaluated, particularly when modelling the transition process. Indeed, transport equation models show their more realistic treatment of the transition process in comparison to transition algebraic criteria.

Chapter 3.

Description of the database

The investigation of the separation-induced transition phenomenon is topical as the current LPT design trend is to increase the pitch-to-chord ratio (see section 1.4) which consequently hastens the separation process. As a large variety of LPT rotor blades were assessed at the von Karman Institute for Fluid Dynamics (VKI), the idea is to analyse the information from this large database and to understand the flow behaviour affecting the generation of losses.

3.1. Database

The database is composed of nine LPT rotor blades assessed at the VKI during the last fifteen years. They cover a large range of Zweifel loading coefficient (Ψ), standard regime Mach and Reynolds numbers, inlet turbulence intensities (from the natural freestream turbulence intensity of the facility to grid generated turbulence intensity), incoming wakes generated by bars attached to an upstream rotating disk and local roughness.

Table 3.1 sums up the characteristics of each blade used in the VKI/SNECMA database of the project. The information submitted to confidentiality is documented as “N/A”. The blades are arranged from left to right by Zweifel loading coefficient ascending order. The other characteristics are the blade chord (c), the blade axial chord (c_{ax}), the pitch-to-chord ratio (g/c), the inlet flow angle (β_1), the Zweifel loading coefficient (Ψ , see equation 3.1), the type of loading, the diffusion rate (D_R , see equation 3.2), the velocity ratio ($V_{peak}/V_{2,is}$), the isentropic outlet Mach number ($M_{2,is}$), the isentropic outlet Reynolds number ($Re_{2,is}$, see equation 3.3), the turbulence intensity ($Tu_{l.e.}$ (%), see equation 3.4), the presence of upstream incoming wakes and the presence of a local roughness.

$$\Psi = 2 \cdot \frac{g}{c_{ax}} \cdot \frac{|\rho V_\theta V_x|_2 - |\rho V_\theta V_x|_1}{\rho_2 V_2^2} \quad (3.1)$$

Table 3.1.: Blades characteristics

Blade	TX	TD	TF	T108	T106C	TG	T2	HIVK_LS	HIVK_HS
c (mm)	N/A	N/A	N/A	98.42	93.01	N/A	96.35	50.79	48.37
c_{ax} (mm)	N/A	N/A	N/A	81.23	79.97	N/A	80.32	44.98	42.98
g/c	N/A	N/A	N/A	0.90	0.95	N/A	1.05	1.05	1.05
β_1 (deg)	N/A	N/A	N/A	33.2	33.2	N/A	32.7	50	50
Ψ	0.95	1.07	1.19	1.22	1.24	1.35	1.46	1.48	1.50
Loading	Aft	Aft	Aft	Front	Aft	Aft	Aft	Aft	Flat roof top Flat roof top
D_R	0.50	N/A	N/A	0.41	0.58	N/A	0.67	0.74	1.01
Velocity Ratio	N/A	N/A	N/A	1.31	1.30	N/A	1.38	1.36	1.45
$M_{2,iss}$	0.6	0.8	0.8	{0.5 ; 0.6}	{0.6 ; 0.7}	0.8	0.65	LS	~0.75
$Re_{2,iss}$ ($\times 10^3$)	[22 ; 104]	[190 ; 650]	[190 ; 650]	[60 ; 200]	[80 ; 250]	[190 ; 650]	[100 ; 250]	[50 ; 200]	[90 ; 600]
$T_{u_i, e}$ (%)	{0.9 ; 3.2}	{0.8 ; 3.5}	{0.8 ; 3.5}	0.9	[0.9 ; 3.2]	0.8	0.9	0.6	{0.8 ; 3.5}
Incoming wakes	No	Yes/No	Yes/No	Yes/No	Yes/No	Yes/No	Yes/No	No	Yes/No
Local roughness	No	No	No	No	Yes/No	No	Yes/No	No	No
Facility	S1	CT2	CT2	S1	S1	CT2	S1	C1	CT2

$$D_R = \frac{V_{peak} - V_{2,is}}{V_{2,is}} \cdot \frac{s_{peak} - s_0}{s_0} \quad (3.2)$$

$$Re_{2,is} = \frac{\rho_{2,is} \cdot V_{2,is} \cdot c}{\mu_{2,is}} \quad (3.3)$$

$$T_{u,e.}(\%) = 100 \cdot \frac{\sqrt{\frac{2}{3} \cdot k}}{U} \quad ; \quad k = \frac{3}{2} u'^2 \quad \text{assuming the flow is isotropic.} \quad (3.4)$$

3.2. Facilities

3.2.1. S1 facility

The TX, T108, T106C and T2 LPT blades were assessed in the S1 facility of the VKI. This facility is a continuous closed-loop wind tunnel which is driven by an axial compressor. This facility is a supersonic/transonic wind tunnel.

To accommodate the need of LPT investigations, one 90-degree elbow, following the diffuser, is replaced by the LPT linear cascade test section. Honeycombs are set in the settling chamber, upstream, in order to ensure homogeneous flow conditions. Moreover, it is possible to set a turbulence grid ahead of the cascade at several positions to impose a desired level of turbulence in the test section (see section 5.2). A rotating disk with bars can be installed as well in order to reproduce incoming wakes from an upstream blade row. This facility allows to vary the Mach number and the Reynolds number independently by vacuuming the facility and setting the rotational speed of the axial compressor. More details about this facility are documented in Michálek et al. [57].

Measured quantities A downstream total pressure probe gives information about the outlet total pressure and flow angle. This probe was moved pitchwise at several discretised positions. The outer diameter of the probe is 3.2 mm and the total pressure hole is 0.6 mm. Outlet static pressure holes are arranged pitchwise. An upstream total pressure probe gives information about the inlet total pressure and flow angle. Static pressure holes on the blade surface give information about the isentropic Mach number distribution. Surface-mounted hot-film sensors

give information about the pseudo-wall-shear stress. More information about the measurement techniques are documented in Michálek et al. [57].

The TX blade was assessed without any information on the blade surface because this blade was too small to implement any measurement technique on it. Concerning the downstream total pressure probe, it was moved pitchwise and acquiring continuously. The outer diameter of the probe tube is 0.4 mm and the inner diameter is 0.3 mm.

The T108, T106C and T2 blades were investigated with the same techniques and have similar size. Michálek et al. documented their results on the T108 [56] and T106C [57]. The following uncertainty information is given in Michálek et al. [57]. They estimated the uncertainties within the full range of the flow conditions. The values are given for maximum and minimum isentropic outlet Reynolds number. The kinetic losses relative uncertainties range between 10% and 20%. The reason which explains this high level of uncertainty is that the measurements were performed at very low pressure (≈ 0.1 bar). The outlet flow angle absolute uncertainties range between 0.2 degree and 0.3 degree. The relative uncertainties on the isentropic Mach number vary between 0.4% and 1.2%. The relative uncertainties on the Reynolds number are between 0.5% and 1.3%. The uncertainty on the turbulence intensity is estimated at 12%.

The TX blade uncertainty information is provided in Arts and Monaldi [5]. The kinetic losses absolute uncertainty is of the order of 0.2 point. The outlet flow angle absolute uncertainty is of the order of 0.2 to 0.3 degree. The Reynolds number relative uncertainties vary between 3% and 12% for the highest and the lowest values of the corresponding parameter respectively. The Mach number relative uncertainties vary between 1.5% and 9% for the highest and the lowest values of the isentropic outlet Reynolds number respectively.

Assessment of the flow topology parameters From the measured quantities, one can define the flow topology parameters. These flow topology parameters are key positions over the blade surface where the important behaviours condition the boundary layer development. There are the positions of separation, reattachment, transition onset, transition end and pressure recovery. As already highlighted, some of those flow topology parameters cannot be described as a definite position due to the unsteady characteristic of the separation/transition phenomenon. However, since the measurement techniques used allow to define an averaged position and because the CFD approach used is a RANS method, the positions will be taken as definite. Since, there are several measurement techniques, it is possible to cross-check the extracted information.

For the separation point, the mean pseudo-wall-shear stress ($\tau_{ps,w}$) is used. This technique only allows to have the magnitude of the shear stress. Then, to define the position of the separation, one needs to check when $\tau_{ps,w}$ decreases towards

zero. The isentropic Mach number distribution allows to assess the position of separation at the beginning of the pressure plateau [16]. In general the positions match between the two techniques. For consistency, only $\tau_{ps,w}$ information will be used. For the reattachment point, $\tau_{ps,w}$ is used. Since, $\tau_{ps,w}$ information is not sensible to the sign of the shear stress, then when $\tau_{ps,w}$, which is already close to zero because of the separation, increases abruptly to reach a local maximum, this position is considered as the reattachment point. Concerning the transition onset location, the hot-film sensors signal root mean square (RMS) is used. The criterion is defined by the moment the RMS increases after being close to zero. Indeed, in the laminar boundary layer, the chaotic behaviour of turbulence is absent, then the RMS is quasi-null. As soon as the RMS increases, it defines the exchange of momentum between the layers and consequently the associated mixing that disturbs the laminar boundary layer. About the transition end location, the hot-film sensors signal RMS is used again. This time when the RMS decreases, after reaching a maximum defined usually as the mid-transition point [57], and stabilises, it indicates the end of the transition process. Those flow topology parameters determination are illustrated in Zhang et al. [81], Michálek et al. [57] and Pucher and Göhl [63]. At last, the pressure recovery position is defined as the position of maximum displacement of the bubble [36]. Indeed, it corresponds to the position where the separation bubble extension does not affect the pressure gradient and consequently the boundary layer starts its path to reattachment. To assess this pressure recovery point, a method based on the tangents of the pressure distribution before separation, the pressure plateau, the pressure distributions before and after reattachment is used. The flow deceleration from the suction peak, the plateau and the pressure recovery are approximated by straight lines. The successive intersections of these lines provide respectively the positions of separation, pressure recovery and reattachment [16].

To get those flow topology parameters from the CFD predictions, one can rely on the effective intermittency (γ_{eff}), the turbulent/laminar viscosity ratio (μ_t/μ), the shape factor (H) and the wall-shear stress (τ_w). γ_{eff} is the output of the correlation behind the transition model. While scanning the boundary layer from the wall to the edge, one can use this parameter when it suddenly increases to one and then decreases. The sudden increase might be defined as the transition onset. This position is considered as the moment where the intermittency first starts to grow [43]. Besides, there is a correlation between Re_{θ_c} and $\widetilde{Re}_{\theta_t}$ which defines the lag between the first rise of intermittency and the moment where the skin friction starts to increase [43]. For μ_t/μ , one can assess the transition onset when it exceeds one. This criterion is defined by the ratio of the eddy viscosity and the molecular viscosity. Thus, when this ratio exceeds one, it means the turbulence patterns are preponderant. For H , one can assess the transition onset when it is maximum before any sudden decrease. Indeed, it is well-known that the shape factor of a laminar incompressible boundary layer ($H \approx 2.6$) is higher than a turbulent one ($H \approx 1.3$) in a flat plate configuration. Moreover, the shape factor is influenced

by the adverse pressure gradient in those HL-LPT configurations. Thus, it allows to assess the position of a possible separation point when H exceeds 3.5. For τ_w , one will notice a sudden increase of it close to its minimum value defining the transition onset. When τ_w starts to stabilise at a constant value and even to decrease in order to follow the trend of the fully turbulent case, then this position is defined as the transition end. When τ_w is negative, this indicates a separation. When τ_w exceeds zero after being negative, one can define a reattachment.

3.2.2. CT2 facility

The TD, TF, TG and HIVK_HS were assessed in the CT2 facility of the VKI. This facility is a short duration, isentropic compression tube providing full similarity with modern aero engine operating conditions with respect to Mach and Reynolds numbers. A turbulence grid and upstream periodic wakes system can also be installed if needed. More details about this facility can be obtained in Coton [16].

Measured quantities An upstream total pressure probe gives information about the inlet total pressure. A downstream total pressure probe provides information on the total pressure and the flow angle. The inner diameter of the probe is 0.8 mm. Before the beginning of the test, the compressed, hot air in the compression tube is isolated from the test section by a shutter valve. Then, the test section is at the ambient temperature. Due to the short duration of the test, there is a heat flux from the air towards the blade surface. That is why, thin films were used to determine the heat transfer coefficient. More information about the measurement techniques are documented in Coton [16].

Coton [16] documented his measurement uncertainties. The kinetic losses absolute uncertainties range between 0.2 point and 1 point at isentropic outlet Reynolds numbers of respectively 300000 and 130000. The absolute uncertainty on the exit flow angle is estimated a bit more than 0.5 degree. The uncertainty on the heat transfer coefficient is slightly above 5%.

Assessment of the flow topology parameters In CT2 configuration, only the mean heat transfer coefficient (h) along the blade surface is considered. This distribution is then used to assess the flow topology parameters except the pressure recovery position. In the case of no separation of the boundary layer, h gives two indications, the transition onset and the transition end. h decreases monotonically in the laminar region and reaches a minimum. This minimum is the transition onset. Indeed, the first turbulent spots affect the heat balance of the boundary layer and consequently induce an increase in the heat flux. This abrupt increase illustrates the transition region. Then, it reaches a local maximum which corresponds to the transition end because after this local maximum, h decreases. This decrease

corresponds to the growth of a fully turbulent boundary layer where basically, the increasing thickness plays the role of an insulator.

In the case of the presence of a separation bubble, the monotonically decrease of h in the laminar region reaches a minimum where an inflection point is visible. This inflection point is considered as the point of separation. Besides, what illustrates the presence of a separation bubble is a flat evolution of h close to its minimum level. As described previously, the increase of h following the separation point is identified as the transition onset. Likewise, the transition end is considered at the local maximum reached by h . However, depending on the evolution of h and the test conditions, one has to be sceptical about the shape of h and particularly when assessing the reattachment point. According to Rivir et al. [64], they found that the heat transfer rate reaches a maximum slightly downstream of the mean reattachment point. They pointed out that it was in contradiction to previous findings of the backward-facing step flow [64]. In fact, depending on the Reynolds number range, the investigator has to feel if the flow is prone to separation with reattachment and if the transition process is about to end before or after the reattachment point. Usually, for the configurations studied in this project, it is expected to have a laminar separation followed by a transitional reattachment.

Concerning the CFD assessment of the flow topology parameters, the methodology described in section 3.2.1 is used and the heat transfer information is evaluated in the same way as the experimental information depicted above.

3.2.3. C1 facility

The HIVK_LS is the only LPT blade of the database assessed at low-speed conditions in the C1 low-speed linear cascade wind tunnel. This wind tunnel is a continuous flow subsonic facility. The air is supplied by a centrifugal blower. The Reynolds number is varied by adapting the operating point of the blower. More details about this facility are documented in Coton [16].

Measured quantities Upstream and downstream pressures (static and total) were measured by pressure probes. The outlet pressure probe had an outer diameter of 3.2 mm and an inner diameter of 0.71 mm. The outlet flow angle was measured as well. At last, the static pressure over the blade was assessed in order to define the pressure coefficient distribution. More information can be found in Coton [16].

Coton [16] documented his measurement uncertainties. The kinetic losses absolute uncertainties range between 0.2 point and 0.9 point at isentropic outlet Reynolds numbers of respectively 200000 and 50000. The exit flow angle absolute uncertainties range between 0.13 degree and 0.25 degree at isentropic outlet Reynolds

numbers of respectively 200000 and 50000. For the investigated Reynolds numbers, the absolute uncertainty on the pressure coefficient is between 0.003 and 0.02.

Assessment of the flow topology parameters To assess the flow topology parameters, only the pressure coefficient (C_p) distribution is available. Then, the method of the tangents can be used to define the separation, the pressure recovery and the reattachment points. These positions can be found in Coton PhD thesis [16] and are the one used for the comparison with the CFD values.

Still, the methodology described in section 3.2.1 is used to define the CFD flow topology parameters.

3.2.4. General considerations about the setting of the isentropic outlet Reynolds and Mach numbers

For uniform inlet flow conditions (no turbulence grid and no wake generator), the inlet total pressure is determined without any problem as there is no incoming disturbances in the flow upstream. Then, the isentropic outlet Mach number is correctly defined for the cascade. When introducing disturbing devices, such as a turbulence grid, the inlet total pressure is measured downstream of the turbulence grid and upstream of the leading edge plane of the cascade. Then, the isentropic outlet Mach number is still correctly defined. However, when a wake generator system is used, there is no more room to set a total pressure measurement device in front of the cascade. The only measure of inlet total pressure is upstream of the wake generator system. It was observed that the wake generator system induces a total pressure drop. In order to have the correct isentropic outlet Mach number, a corrected inlet total pressure has to be set. Indeed, the new inlet total pressure has to be increased by the total pressure drop value measured across the wake generator system. Consequently, the isentropic outlet Mach number is correctly defined. Otherwise, without taking into account this total pressure drop, the isentropic outlet Mach number would be lower than the expected one.

3.3. Effect of the parameters of the database

The database (see table 3.1) shows the broad range of the LPT blades tested in different wind tunnels and covering the cruise Reynolds number and Mach number ranges. Their loading spreads from mid to very high. What is more of interest is to have a first insight into the behaviour of these designs under the effect of parameters intended to improve their efficiency. In this project, the measure of efficiency is done with the kinetic losses (ζ) resulting from the integration of the

wake profile. For the TX, TD, TF, TG, and HIVK_HS, the kinetic losses are area-averaged. For the T108, T106C, T2 and HIVK_LS, the kinetic losses are mass-averaged. The kinetic losses quantify the profile losses that are due to the boundary layer development over the blade.

The expression of the kinetic losses for compressible flow is given below:

$$\zeta = 1 - \left(\frac{V_2}{V_{2,is}} \right)^2 = 1 - \frac{1 - \left(\frac{P_2}{P_{02}} \right)^{\frac{\gamma-1}{\gamma}}}{1 - \left(\frac{P_2}{P_{01}} \right)^{\frac{\gamma-1}{\gamma}}} \quad (3.5)$$

The expression of the kinetic losses for incompressible flow is given below:

$$\zeta = 1 - \left(\frac{V_2}{V_{2,is}} \right)^2 = \frac{P_{01} - P_{02}}{P_{01} - P_2} \quad (3.6)$$

The area-averaging of a quantity X is defined as:

$$\bar{X} = \frac{\int_0^g X dy}{\int_0^g dy} \quad (3.7)$$

The mass-flow-averaging of a quantity X is defined as:

$$\bar{X} = \frac{\int_0^g \rho V_{2,ax} X dy}{\int_0^g \rho V_{2,ax} dy} \quad (3.8)$$

The parameters of interest are the turbulence intensity and the incoming wakes, which are not negligible in the real LPT environment. Nowadays, the trend is to add on the suction side surface local roughness in order to promote the transition process (see section 2.2.1). The present section aims to provide an understanding of the main results of the database study. Before highlighting the parameters of interest, one has to focus on the effect of the isentropic outlet Reynolds number. This parameter is by default inherent to the performance definition of turbine blade design as it conditions the working environment (from cruise to take-off). Likewise, the isentropic outlet Mach number affects the performance.

Effect of the isentropic outlet Reynolds number According to the data matrix (see table 3.1), the best set of conditions where the maximum information on all the blades could be compared is when the turbulence level is the natural free-stream level of the facility, without any incoming wakes generated by the upstream

rotating bar system and without any local roughness. Indeed, this set of conditions allows to decouple the effects of the different parameters and consequently to understand the fundamental role of the isentropic outlet Reynolds number.

Figures 3.1a and 3.2a gather the area-averaged (see equation 3.7) and the mass-averaged (see equation 3.8) cascade kinetic losses (ζ) respectively. Figures 3.1b and 3.2b gather the area-averaged and the mass-averaged outlet flow angle (β_2) respectively. These two information are typical indicators of a blade performance. Generally, one uses the cascade turning instead of the outlet flow angle even though there are linked. The cascade turning quantifies the turning done by the flow from the leading edge until the trailing edge of the blade. Usually, β_1 is constant and corresponds to the design inlet angle, whereas β_2 is the result of the path around the blade and the working conditions (mainly $Re_{2,is}$) the flow encounters. From equation (1.2) and figure 1.3, one can understand that the turning of the flow is paramount in the definition of performance. Besides, as β_1 is constant, one can assess the turning by looking at the deviation of β_2 in comparison to the design value of β_2 or the one at the highest $Re_{2,is}$. Typically, at high $Re_{2,is}$, β_2 corresponds to the design outlet angle because the losses are minimum.

At first sight, one can see that at low $Re_{2,is}$, the kinetic losses are higher. Likewise, this is visible when looking at the outlet flow angle except that it is lower. Indeed, at low $Re_{2,is}$, the outlet flow angle is less than the design value due to a more axial outlet flow angle when a massive separation of the boundary layer occurs. The impact on the performance was stressed with equation (1.2). Another comment is that the more loaded (high Ψ) and the higher the diffusion rate (D_R) are, the higher the losses are at low $Re_{2,is}$ (T106C, T2, HIVK_LS and HIVK_HS). However, a high loaded and mild diffusion blade (T108) illustrates the low level of losses at low $Re_{2,is}$. For the T108, there is an intentional break in the $Re_{2,is}$ range since the two lowest $Re_{2,is}$ were performed in the facility at a lower isentropic outlet Mach number ($M_{2,is} = 0.5$ instead of 0.6). Figure 3.2 stresses the difference, in terms of performance, between front-loaded configuration (T108) in one hand and aft-loaded (T106C and T2) and roof-top (HIVK_LS) configurations in another hand.

Effect of the isentropic outlet Mach number The isentropic outlet Mach number plays a role in the boundary layer development. Indeed, the higher $M_{2,is}$ is and the higher the adverse pressure gradient on the aft part of the blade is. Moreover, it means that the peak Mach number is higher which might exceed the critical Mach number of 1. Consequently, the development of shock may arise which is source of additional losses. Therefore, a higher $M_{2,is}$ should be sources of higher losses and a loss of performance. To illustrate this, several Mach numbers (0.6, 0.65 and 0.7) were tested at the same $Re_{2,is}$ range on the T106C blade. Figure 3.3 depicts the aforementioned statement.

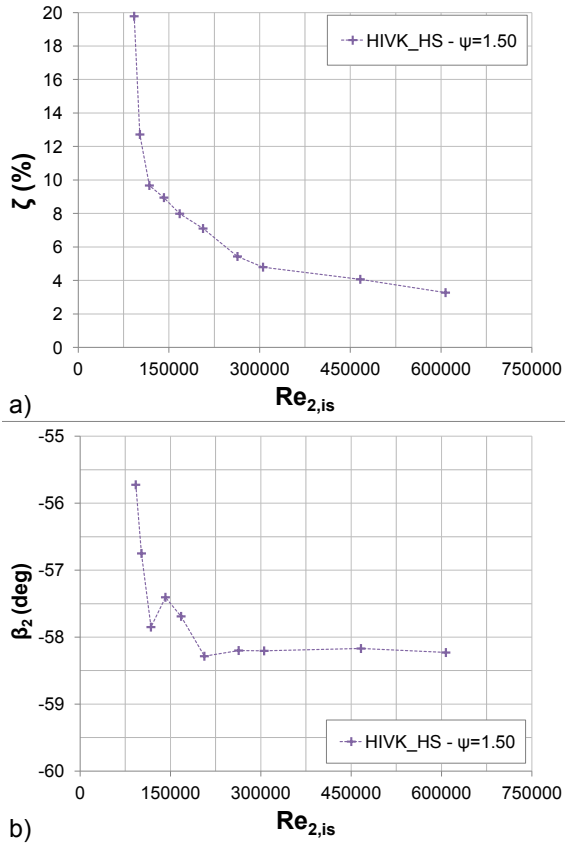


Figure 3.1.: Effect of the isentropic outlet Reynolds number - Uniform upstream conditions and natural freestream turbulence level of the facility - Cascade losses (a) and outlet flow angle (b) - Area-averaged - HIVK.-HS

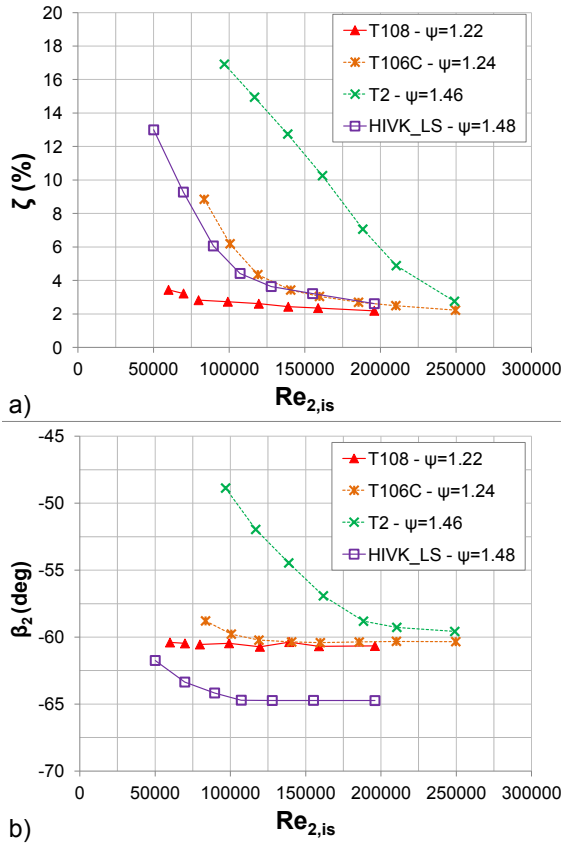


Figure 3.2.: Effect of the isentropic outlet Reynolds number - Uniform upstream conditions and natural freestream turbulence level of the facility - Cascade losses (a) and outlet flow angle (b) - Mass-averaged - T108, T106C, T2 and HIVK_LS

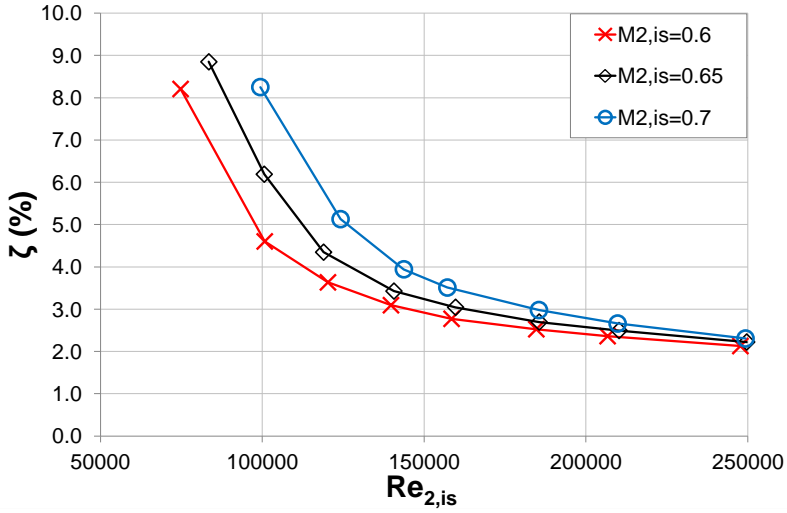


Figure 3.3.: Effect of the isentropic outlet Mach number - T106C - Uniform upstream conditions and natural freestream turbulence level of the facility (0.9%)

Effect of the turbulence intensity To illustrate the effect of turbulence, the T106C LPT blade was assessed at several turbulence intensities. In S1 facility, it was possible to set the turbulence grid at several distances upstream from the leading edge plane. The cases are referred by turbulence intensities at the leading edge plane (Natural freestream turbulence intensity 0.9%, 1.8% and 3.2%). The HIVK_HS LPT blade was assessed as well at the natural freestream turbulence level (0.8%) and at 3.5%. Moreover, these tests were done for the isentropic outlet Reynolds number range corresponding to cruise and take-off conditions.

From figure 3.4 and figure 3.5, the turbulence intensity (when increased from 0.9% to 3.2% on one hand and from 0.8% to 3.5% on the other hand) plays a great role in reducing the losses. As one can see, the effect is visible at low and mid $Re_{2, is}$. However, at higher $Re_{2, is}$ the losses are increased because the boundary layer undergoes transition earlier and consequently the boundary layer is thicker at the trailing edge. This is particularly visible in figure 3.5.

Effect of the incoming wakes Another characteristic of the LPT environment is the presence of incoming wakes from the stator row that impinge on the suction side of the rotor blade (see section 2.1.2.2). Coton [16] extensively studied this phenomenon by varying the parameters affecting the frequency of the incoming wakes. This frequency is made non-dimensional and is similar to a Strouhal number. The

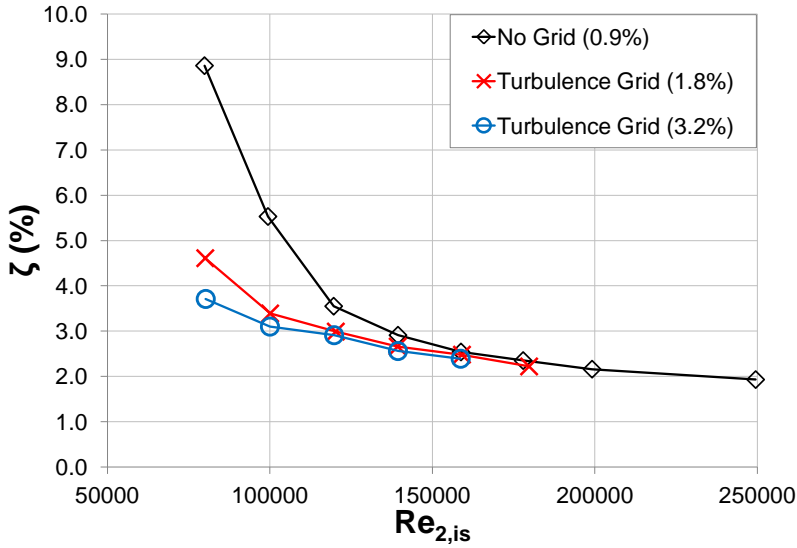


Figure 3.4.: Effect of the turbulence intensity - T106C - Uniform upstream conditions at $M_{2,is} = 0.65$

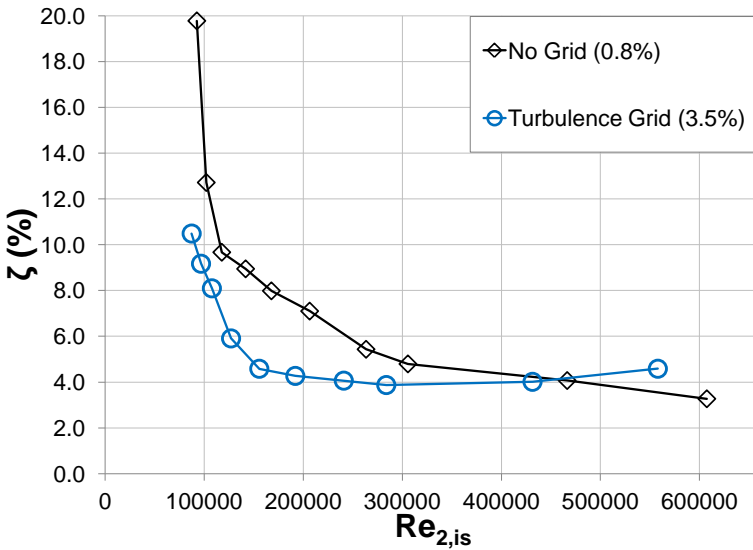


Figure 3.5.: Effect of the turbulence intensity - HIVK_HS - Uniform upstream conditions at $M_{2,is} \approx 0.75$

common way to define it is the following with RPM , the rotational speed, N_b , the number of bars in the wake generator system and a reference velocity V :

$$f_r = \frac{(RPM/60) N_b \cdot c}{V} \quad (3.9)$$

Coton [16] used as a reference velocity the inlet axial velocity $V_{ax,1}$. Incoming wakes studies were carried out as well on the T108, T106C and T2 blades. This time, the reduced frequency is defined as previously except that the velocity scale is taken as the isentropic outlet velocity ($V_{2,is}$). For a comparison reason, the reduced frequencies will be presented with the isentropic outlet velocity ($V_{2,is}$) as a reference velocity.

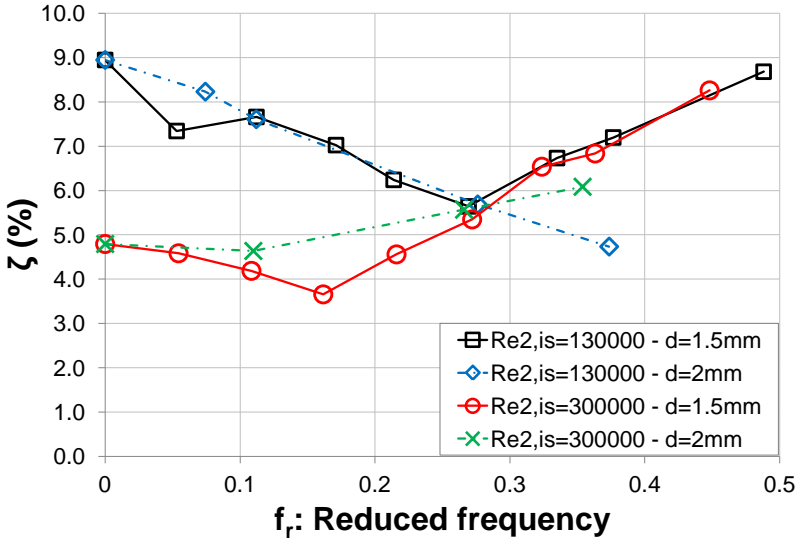


Figure 3.6.: Effect of the incoming wakes - HIVK_HS - Wake generator disk rotating speed = 6000 rpm with two different rotating bar diameters d (1.5 mm and 2 mm) at two different $Re_{2,is}$ (130000 and 300000), natural freestream turbulence level (0.8%) and $M_{2,is} \approx 0.75$

In figure 3.6, one can see the influence of the incoming wakes on the losses. The abscissa $f_r = 0$ corresponds to the case with uniform upstream conditions (i.e. without any incoming wake). When comparing the losses at $f_r = 0$ and the losses at $f_r \neq 0$, one can see the general improvement at low $Re_{2,is}$. However, there is an optimum value of f_r where the losses are the minimum. When increasing this reduced frequency, the losses start to increase. At this low $Re_{2,is}$, laminar separation is expected and consequently the losses are the highest. Thus, the

patches of turbulent spots impinging on the suction surface energise the boundary layer and promote the transition to turbulent boundary layer. However, if the rate of turbulent patches impinging is too high (high reduced frequency), then the transition will be too short and the state of the boundary layer will be fully turbulent leading to a thicker boundary layer at the trailing edge. At a higher $Re_{2, is}$, the conclusion is the same except that the gain in losses is not so important. Indeed, it was expected since the transition to turbulent boundary layer is already ongoing and/or finished. Then, adding turbulent patches will only provide more turbulence in the boundary layer and consequently affect its development and thicken it, leading to higher losses.

Concerning the diameter of the rotating disk bars, they do not show a real influence since they follow the same trend at constant $Re_{2, is}$. Their goal is to mimic the trailing edge of upstream stator blade and to reproduce the associated wakes and vortex shedding.

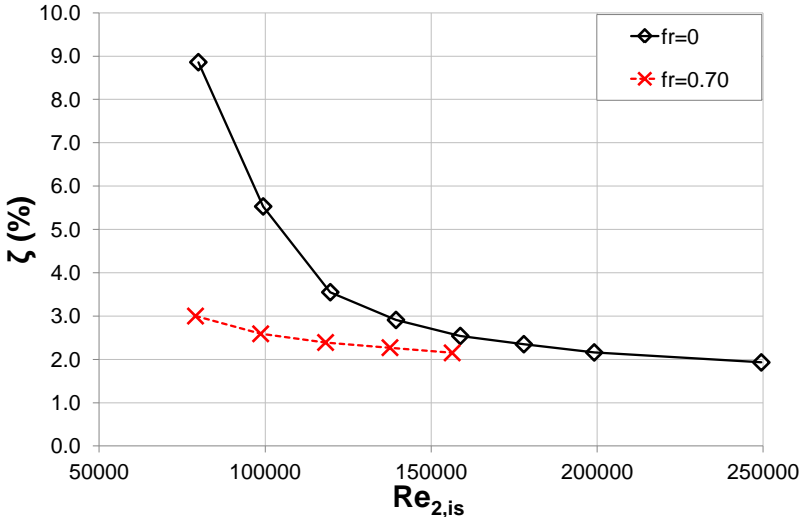


Figure 3.7.: Effect of the incoming wakes - T106C - Natural freestream turbulence level (0.9%) and $M_{2, is} = 0.65$

The T106C LPT blade experiences the same effect when subjected to incoming wakes as depicted in figure 3.7. However, the conclusion is only valid for low and mid $Re_{2, is}$. However, this positive effect of the incoming wakes is not true for all the LPT blade configurations. Indeed, so far only aft-loaded blade with high diffusion rate (D_r) were shown. The T108 LPT blade is a counter-example. It is a front-loaded blade with consequently a mild diffusion rate (see table 3.1). In fact, it turned out the presence of the incoming wakes deteriorates the losses (figure 3.8). The reason is the position of the velocity peak which is in the first

third of the blade suction side. Then, in the diffusion part, the boundary layer experiences separation and transition earlier than a conventional aft-loaded LPT blade. However, the separation process is not as marked as in a higher diffusion blade. That is why, over the long diffusing part, the boundary layer undergoes transition and has a fully developed turbulent profile. Therefore, adding turbulent patches impinging on the surface increases the development of the thick turbulent boundary layer and consequently leads to higher losses.

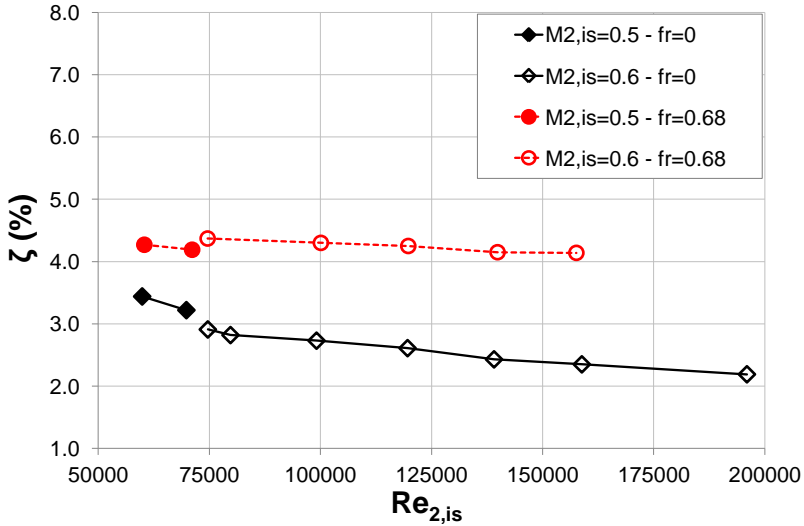


Figure 3.8.: Effect of the incoming wakes - T108 - Natural freestream turbulence level (0.9%)

Effect of the local roughness The last parameter that was used to improve the efficiency of the LPT blades is the local roughness. What is considered as a local roughness is a local spanwise extension of a trip wire for instance. This approach was assessed on the T106C and the T2 LPT blades. The local roughness used is a wavy wire (similar to a sawtooth configuration but with rounded edges, see figure 8.1). This local roughness could be approximated as a forward-backward facing step in a streamwise direction (see chapter 8). Another design was assessed only on the T106C. This time the local roughness is a cylindrical wire (see figure 8.2). The advantages of such devices were already spotted in section 2.2.1.

Figure 3.9 show the positive impact of the local roughness (wavy wire and cylindrical wire) on the losses and particularly at low $Re_{2,is}$. In contrast, at high $Re_{2,is}$, the local roughness slightly increase the losses. The local roughness geometry does not seem to affect so much the improvement of a blade with a local roughness in comparison to a smooth blade at high and mid $Re_{2,is}$. However, at low $Re_{2,is}$,

the cylindrical wire has lower losses in comparison to the wavy wire. The wavy wire has a longer streamwise extension on the suction side in comparison to the cylindrical wire (one order of magnitude more, see geometrical characteristics in figures 8.1 and 8.2). Moreover, its three dimensional shape should induce complex vortical structures that might energise more the boundary layer, leading to a shorter transition region.

In the case of the T2 blade, the diffusion rate is pretty high. A massive separation bubble flow topology is expected at the natural freestream turbulence and uniform upstream flow conditions. In order to cope with this, the local roughness is well appropriated to hasten the transition process close to the separation point and avoid the massive separation. This is illustrated in figure 3.10 where the losses are tremendously reduced thanks to the introduction of the local roughness.

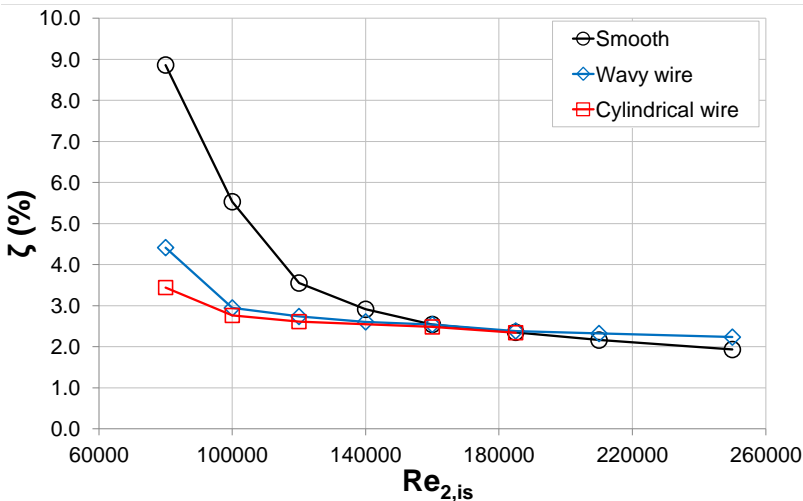


Figure 3.9.: Effect of the local roughness - T106C - Uniform upstream conditions, natural freestream turbulence level of the facility (0.9%) and $M_{2,is} = 0.65$

3.4. Summary

The database description highlighted the geometrical and working condition parameters as well as the quantities measured during the experimental campaigns. A definition of the way to get information out of the data is provided in order to compare consistently the experimental results and the numerical predictions. The performance evaluation was done in order to understand the effects of the database parameters separately.

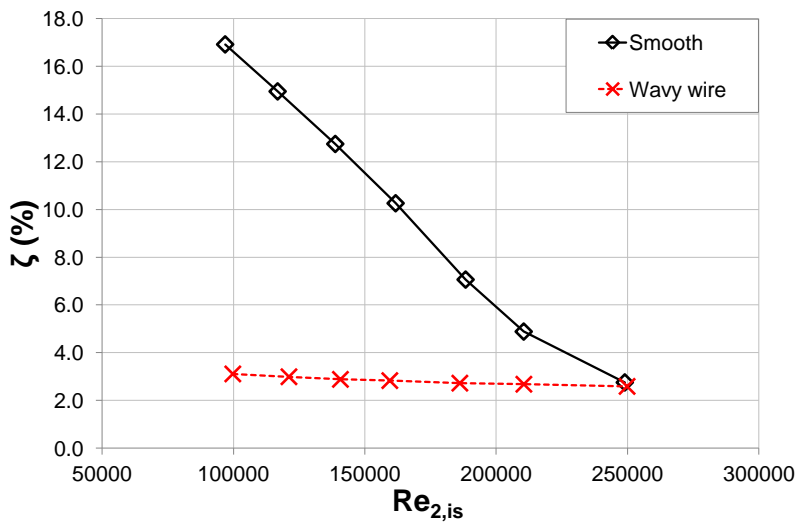


Figure 3.10.: Effect of the local roughness - T2 - Uniform upstream conditions, natural freestream turbulence level of the facility (0.9%) and $M_{2,is} = 0.65$

Chapter 4.

Database correlations

For a designing point of view, a large database is of interest in order to correlate the effects of different parameters on the behaviour of the flow around the blade and consequently predict the performance of a blade under defined working conditions. Usually, these correlating methods rely on statistical approaches. In this chapter, an investigation of the performance models will be provided and a comparison of the database information with existing models of the literature will be given in order to evaluate the present database.

4.1. The need for performance models or correlations in a design prospect

The search for performance models in axial turbines is still relatively tricky. The need for loss prediction models is critical when designing a new turbine. Usually, the performance models are based on experimental data assessed in a cascade configuration. This design process starts with the mean-line (one-dimensional) model of the velocity triangles. However, one has to incorporate the standard expected losses in his mean-line prediction in order to get an estimation of the efficiency of the blade design. These main losses are generally referred as profile losses (contribution of the boundary layer shear), secondary flow losses (which corresponds to the development of vortices due to the presence of the end walls), trailing edge losses (or base pressure losses), tip leakage losses, shock losses and some others [40].

4.1.1. Different types of modelling process

The modelling process is defined by different levels. Indeed, in the search of performance and optimization models, one-dimensional model is the straight-forward solution. It is often referred to a mean-line model and aims at describing the performance of a blade from the inlet and outlet locations in the streamwise direction only. If the spanwise evolution of the flow field is investigated, such as a hub-to-tip

analysis, or the viscous interaction of the boundary layer, then two-dimensional models are of interest to predict the performances. Indeed, the one-dimensional models do not directly investigate the losses generated by the boundary layer viscous interaction for example. At last, the CFD models predict the whole flow field and are an example of three-dimensional models [40].

When a designer or engineer has a need for understanding a phenomenon from a large number of data, the straight-forward solution is to define the inputs and the outputs of the system, try to link the variables with subsequent physics and common senses and set some constants in order to reduce the variance of the distribution. Thus, this approach is based on trials and errors rather than established physics rules. Usually, this approach is defined as a data-driven global model since it describes the overall performance and is based on statistical methods [40].

4.1.2. AMDCKO correlation for axial turbine

The best known and most comprehensive study of performance prediction was carried out by Ainley and Mathieson [3, 2] more than six decades ago and set a framework for the axial turbine flow performance prediction. Indeed, a number of researchers used this framework to implement their findings, improve and revise the correlation by adding new features and corrections. The most known are Dunham and Came [22] and Kacker and Okapuu [41]. This framework correlation is usually cited as AMDCKO (Ainley and Mathieson - Dunham and Came - Kacker and Okapuu) in the literature.

Description of the AMDCKO correlation This AMDCKO correlation is primarily meant for the determination of the losses. In fact, Ainley and Mathieson [2] defined two applications of their model. The first one aims at determining the losses under a wide range of inlet conditions. The second one is intended for building up a complete picture of the flow at all points from one blade row to the next. For the purpose of the present study, only the first application is considered. In their prediction method, they assumed that the flow and consequently the losses were calculated at one diameter only (which is the arithmetic mean of the rotor and stator row inner and outer diameters). The losses computed in this model are total pressure losses (Y , see equation 4.1).

$$Y = \frac{P_{0,inlet} - P_{0,outlet}}{P_{0,outlet} - P_{outlet}} \quad (4.1)$$

They assumed the overall or cascade losses are the simple summation of each individual losses contribution (profile, secondary, trailing edge and tip leakage losses). Moreover, the profile losses expression is built on data from impulse stage blades

and inlet guide vanes. Dunham and Came [22] improved the formulas for secondary and tip clearance losses. Kacker and Okapuu [41] modified the summation assumption of the losses contributions. They introduced acceleration and transonic corrections to the profile losses and add a Reynolds number correction to the profile losses as there is little evidence in the literature that other losses are affected by it.

The resulting correlation is given below and is fully documented in Japikse [40].

$$Y_{cascade} = Y_{profile} \cdot f(Re) + Y_{secondary} + Y_{TE} + Y_{tip} \quad (4.2)$$

$Y_{cascade}$ is the cascade total pressure loss coefficient, $Y_{profile}$ is the profile total pressure loss coefficient, $Y_{secondary}$ is the secondary flows total pressure loss coefficient, Y_{TE} is the trailing edge total pressure loss coefficient and Y_{tip} is the tip leakage total pressure loss coefficient. In the present study, the profile losses and the trailing edge losses are the only ones of interest in order to evaluate the database. Indeed, the investigations were made in a cascade configuration where the cascade losses were assessed downstream of the blade at midspan. Then, the secondary losses as well as the tip clearance losses are neglected.

The profile losses are expressed in terms of blade inlet angle, maximum blade thickness, trailing edge thickness, pitch, chord, gas relative outlet angle, inlet and outlet Mach numbers. The trailing edge losses take into account the blade inlet angle, the gas relative outlet angle, the outlet Mach number and the ratio of the trailing edge thickness to throat opening.

In order to compare appropriately the total pressure loss coefficients determined with the AMDCKO correlation (see equation 4.2) and the kinetic energy loss coefficients of the database, one can use the relationship used by Chen [12] where the kinetic energy loss coefficients are a function of the total pressure loss coefficient and the outlet Mach number. For that, the cascade kinetic energy loss coefficient is converted in total pressure loss coefficient via the Chen's expression (see equation 4.3).

$$\zeta = 1 - \frac{1 - \left(1 + \frac{\gamma-1}{2} M_2^2\right)^{-1}}{1 - \left[\left(1 + \frac{\gamma-1}{2} M_2^2\right)^{\frac{\gamma}{\gamma-1}} (1 + Y) - Y\right]^{\frac{1-\gamma}{\gamma}}} \quad (4.3)$$

Evaluation of the AMDCKO correlation with the database To evaluate the AMDCKO correlation with the available database, only the results of the T108, T106C and T2 blades are presented. The three blades were investigated in the same wind tunnel (S1) and cover the different LPT blade design philosophies (see table 3.1). The turbulence intensity is taken as the natural freestream turbulence level of the facility (around 0.9%). The effect of the turbulence level is investigated as well with the results of the T106C blade where the turbulence level is of 3.2% at

the leading edge plane (see section 5.2). The experimental results are represented by plain symbols while the AMDCKO results are represented by empty symbols in figure 4.1. This figure is split in four sub-figures for clarity due to the different ordinate scales. The sub-figures illustrate one blade each (a. is T108 at $Tu = 0.9\%$, b. is T106C at $Tu = 0.9\%$, c. is T2 at $Tu = 0.9\%$ and d. is T106C at $Tu = 3.2\%$).

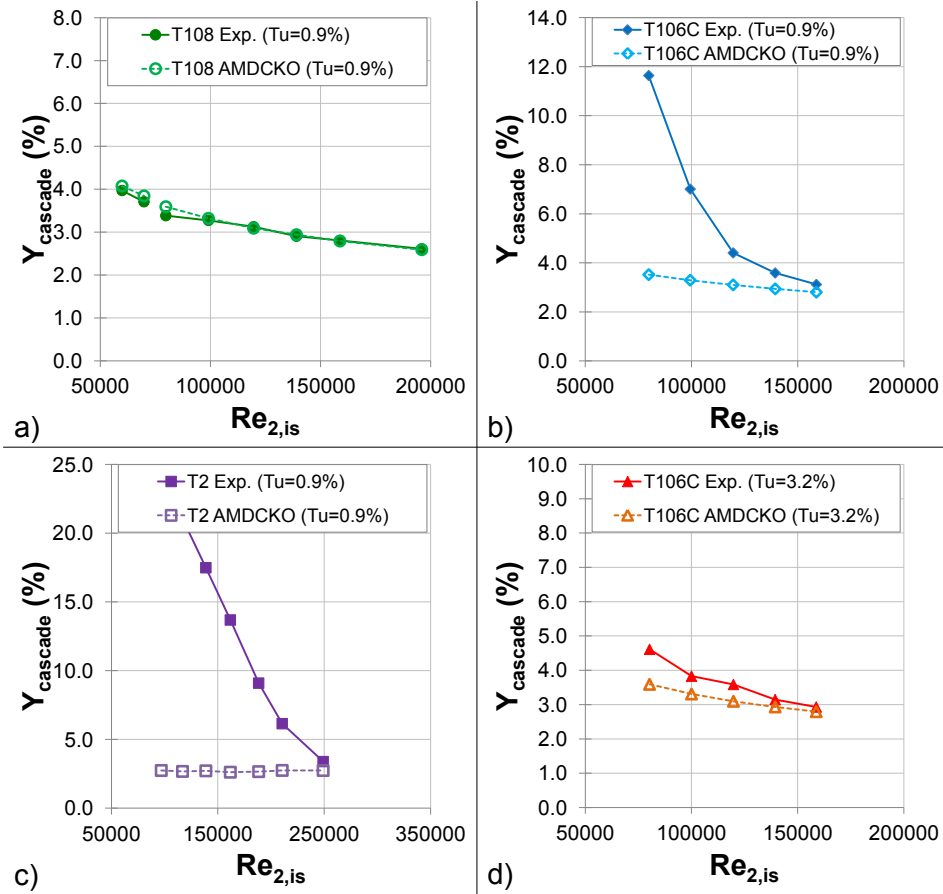


Figure 4.1.: AMDCKO investigations - Cascade total pressure losses - a) T108 at $Tu = 0.9\%$, b) T106C at $Tu = 0.9\%$, c) T2 at $Tu = 0.9\%$, d) T106C at $Tu = 3.2\%$

First of all, the T108 AMDCKO predictions (figure 4.1.a) describe perfectly the experimental results over the whole Reynolds number range. However, for the T106C (figure 4.1.b) and the T2 (figure 4.1.c), the AMDCKO predictions are only good at high Reynolds numbers but dramatically deteriorate at low Reynolds num-

bers. This was expected since the AMDCKO correlation was calibrated on blade designs dated back the 1980s and even before [2, 22, 41]. At high Reynolds numbers, the flow is expected to behave according to the design point conditions. At low Reynolds numbers, one cannot consider that the blade behaves at off-design conditions. Indeed, the reason is the separation process that affects dramatically the flow topology around the blade. Again, this is the purpose of this work. This separation process was not included in the AMDCKO, even though the gas outlet angle is used in the correlation. But it is assumed that the contribution of the outlet angle was not weighted enough to affect the losses accordingly. Moreover, to the best knowledge of the author, the blade designs of that era were not as loaded with such strong diffusion rate as the current designs (such as the T2 blade for instance) even though the AMDCKO at high Reynolds numbers are acceptable. In addition, the turbulence factor was not incorporated in the correlation explicitly. It is believed that the blades used for the AMDCKO correlation were assessed with a turbulence level representative of the machine conditions (higher than 4%). Indeed, from figure 4.1.d, the effects of the turbulence is clearly visible in the experimental predictions where the losses are improved and are closer to the AMDCKO predictions (which are not really different from the AMDCKO predictions of figure 4.1.b because the outlet flow angle influence is not that strong on the AMDCKO predictions).

Drawbacks of the AMDCKO prediction methodology The AMDCKO is a relatively good model for the prediction of the losses at design point conditions and high Reynolds numbers. However, from the former investigation, the predictions at low Reynolds numbers are not accurate for highly loaded and high diffusion rate blades. It should be acknowledged that the methodology used to describe the losses is still opened to improvement, corrections and extensions for current blade design trends and working conditions. Indeed, the effect of separation and particularly long bubble and massive separation cases are not well integrated in the correlation even though a Reynolds number correction exists. Moreover, the turbulence effect is not explicitly defined in the correlation. One drawback is the need of the outlet flow angle as an input of the correlation. The point is there is no need of using the AMDCKO correlation if one input is a measured quantity. In fact, if one knows the outlet flow angle from a total pressure probe, then the losses can be determined. As a consequence, the AMDCKO is not anymore useful. Indeed, the predictive character is lost. In addition, the roots of the physics behind the losses behaviour is not investigated even though, the physics is still embedded in the correlation via statistics.

It is believed that developing such a prediction method might be useful as a design tool for turbine blade designers. However, the determination and the calibration of the model constants as well as the definition of the inputs are critical in order to understand the needs and particularly to rely on accurate findings. One advantage

is that anyone can tune his prediction method according to his proper design philosophy but it will be interested to compile all the data available to generate a “universal prediction model”. This search for prediction model should be the topic of a whole PhD project since it is time-consuming and that it necessitates a lot of investigations. It is even suggested to use optimization tools. At last, the data matrix should be completed in order to understand all the aspects and to incorporate all the interactions between parameters.

4.1.3. Conclusions on the search for prediction models with a design prospect

The need for prediction models was spotted previously and represents a promising topic thanks to the large amount of data available in the literature. Moreover, one needs to be aware of choosing the inputs of the correlation appropriately in order to be independent of the resulting flowfield and particularly the exit flow quantities such as the outlet flow angle.

The present author investigated the possibility of incorporating the Reynolds number parameter inside the correlation by making it silent. What is meant is to get rid of the Reynolds number input but the Reynolds number influence is still embedded inside the correlation. What is suggested is to consider the losses evolution with the isentropic outlet Reynolds number as a power law function (see equation 4.4) where B is expected to be negative.

$$\zeta = f(Re_{2,is}) = A \cdot (Re_{2,is})^B \quad (4.4)$$

Couple of power law representative of the losses evolution with the isentropic outlet Reynolds number are provided in figure 4.2. From this figure, both the effects of the coefficients A and B are illustrated. The coefficient A is an indicator of the level of the losses. The lower the coefficient A , the lower are the losses. The coefficient B is an indicator of the slope evolution of the losses over the isentropic outlet Reynolds number. The coefficient B should be below zero but close as possible to zero. Indeed, a positive coefficient B indicates an increase of the losses with an increase of the Reynolds number (which is not feasible in our Reynolds number range studies). In addition, the coefficient B should be as close as possible to zero in order to have a flat evolution of the losses. However, one has to bear in mind that those two coefficients work in pair and that their common assessment is essential for the classification of the blade. Figure 4.3 depicts typical examples encountered in the LPT environment, such as the effect of the turbulence intensity and the detrimental case of massive separation. Figure 4.3.a shows the effect of the turbulence intensity on the losses. Usually, the turbulence intensity has the tendency to flatten the losses evolution over the isentropic outlet Reynolds number

range. Depending on the blade configuration, it can reduce the level of the losses or increase it (which is seen with the increase or decrease of the coefficient A). Concerning the effect of the coefficient B , its decrease illustrates the rise of losses at low Reynolds numbers typical of massive separation cases (see figure 4.3.b).

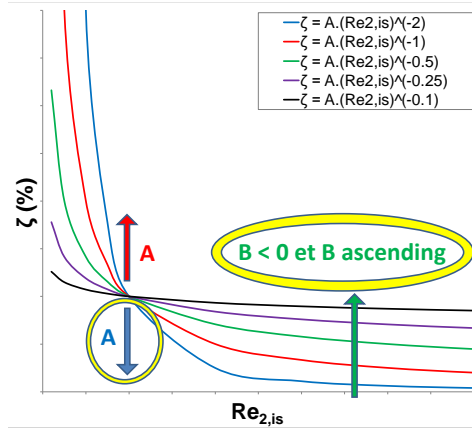


Figure 4.2.: Examples of power laws representative of the losses evolution with the isentropic outlet Reynolds number

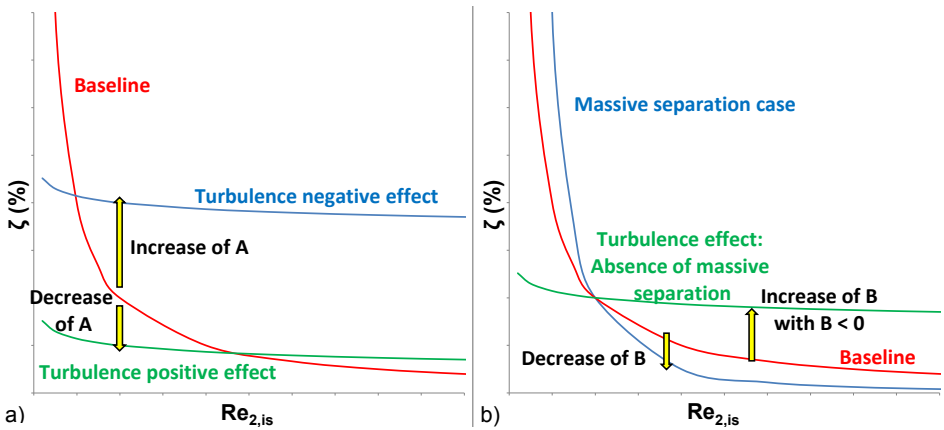


Figure 4.3.: Illustration of the power law coefficients (A and B) variations

It is believed that this method might be of interest in order to predict the losses lapse of a given configuration from abaci based on the coefficients A and B . For that, the database should be made of cases which are assessed with the same type of parameters (turbulence intensity, Mach number, incoming wakes from an upstream rotating bar system, local roughness, ...) in order to build reliable abaci.

Otherwise, the use of one-dimensional model seems straight-forward for a design prospect because only integrated, geometrical, inlet and outlet information are used. Obviously, to understand the physics that is hidden behind the separation and transition phenomena, one has to use three-dimensional model where the whole flowfield is known. It has been widely accepted in the field of transition that the momentum thickness Reynolds number is a key element in understanding the path to transition because it is representative of the boundary layer state and consequently evolution. Indeed, it is based on the momentum thickness which quantifies the portion (in terms of distance away from the wall) of momentum flux loss due to the presence of the wall and consequently the viscous dissipation through viscous stress tensor. In the case of turbulent flow, the instabilities are more important due to the presence of large eddies which interact and break down into smaller eddies. Then, knowing that eddies are really efficient in the mixing process, it means that the momentum thickness will behave differently according to the nature of the flow in the boundary layer.

The problem with the momentum thickness is the difficulty to measure it in a cascade configuration and particularly on LPT blades (high curvature). That is why, only information from CFD simulations can be used to get a measure of the momentum thickness. After describing meanline models based on inlet and outlet information, one can evaluate the flowfield information around the blade (such as the separation and transition onset locations) with appropriate investigations of the literature.

4.2. Evaluation of the database information with correlations

The flowfield information around the blade are of interest in order to understand the behaviour of the boundary layer under certain types of design. The flow topology parameters, already described in chapter 3, have aroused a set of investigations correlating them. The studies carried out by Hatman and Wang [27, 28, 29, 30] is, according to the best knowledge of the author, the only recent comprehensive investigation on boundary layer separation-induced transition applicable to LPT environment. However, this study was carried out at low-speed conditions with uniform inlet freestream turbulence intensity (0.3% to 0.6%) over a flat plate with a varying outer wall, allowing to set different distributions and strengths of adverse pressure gradient [27].

The present database presents a large variety of LPT blades assessed in different environments with different techniques and at different working conditions. The outlet total pressure profile was measured on all the blades in order to calculate the losses. The blades on which more information is available are the T108, T106C

and T2 blades since the isentropic Mach number and the pseudo-wall-shear stress distributions are at disposal. Moreover, these blades cover a Reynolds number range that encompasses the low Reynolds numbers expected during cruise condition. Unfortunately, some T2 pseudo-wall-shear stress information miss at mid and high Reynolds number. The TX blade information features only the outlet total pressure profile but covers the very low Reynolds number regime condition. The HIVK_HS provides information of the blade surface heat transfer, but only the averaged information. It covers a large Reynolds number range from low to high. In comparison, the TD, TF and TG blades have the same kind of information as the HIVK_HS except that they do not cover the low Reynolds number range. At last, the HIVK_LS blade provides the blade pressure distribution and cover the low Reynolds number range. That is why more confidence is granted to the T108, T106C and HIVK_HS blades in the assessment of the flow topology parameters. Besides the other blades information are still relevant in order to complete and corroborate the findings made on the most reliable test cases.

Evaluation of the database at the natural freestream turbulence intensity (without any turbulence grid), with uniform inlet conditions (without incoming wake) and at the design isentropic outlet Mach number. These conditions fit the Hatman and Wang conditions, at least for the turbulence intensity and the inlet flow conditions. Figure 4.4 illustrates a linear correlation between the Reynolds numbers based on the local information (see equation 4.5) at the reattachment and the separation locations.

$$\begin{aligned}
 Re_{s,j} &= \frac{U_j \cdot s_j}{\nu_j} \\
 j &\in \{sep; reat; onset; end\} \\
 U_j &= f(p_{stat,j}, P_{0_1}, T_{0_1}) \\
 \nu_j &= f(p_{stat,j}, P_{0_1}, T_{0_1})
 \end{aligned} \tag{4.5}$$

The proximity between the Hatman and Wang data and the present work data highlights the interest of this correlating method. Indeed, it gets rid of the scaling factor (low-speed data against high-speed data), the wind tunnel factor (Hatman and Wang facility, VKI S1, VK1 CT2 and VKI C1) and the blade configuration (high-loaded against normal-loaded in one hand and front-loaded against aft-loaded in another hand). Likewise, the correlation between the Reynolds numbers based on the local information at the transition end and transition onset locations (figure 4.6) and the correlation between the Reynolds numbers based on the local information at the transition onset and separation locations (figure 4.8) illustrate again the linearity between those parameters and their proximity with Hatman and Wang data.

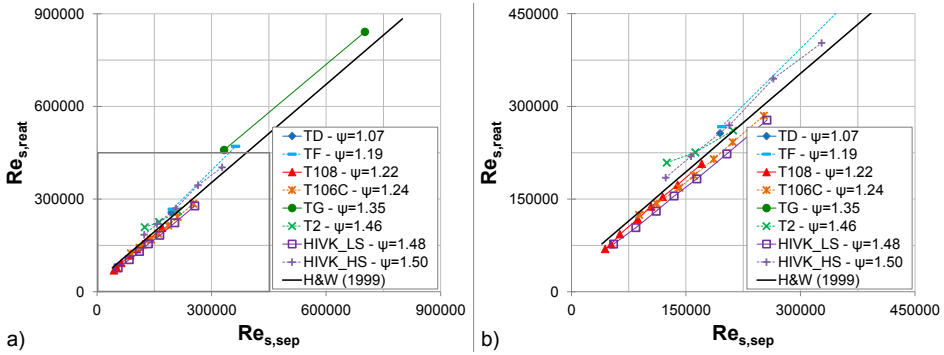


Figure 4.4.: Correlation of $Re_{s,reat}$ and $Re_{s,sep}$ - a) Full scale, b) Zoom at low Re

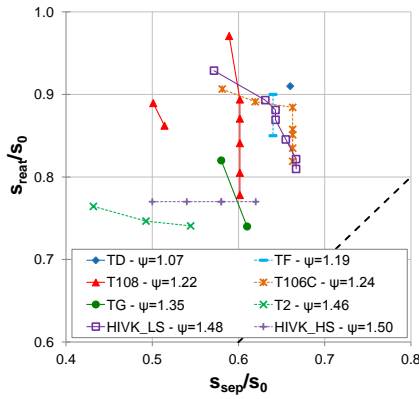


Figure 4.5.: s_{reat}/s_0 against s_{sep}/s_0

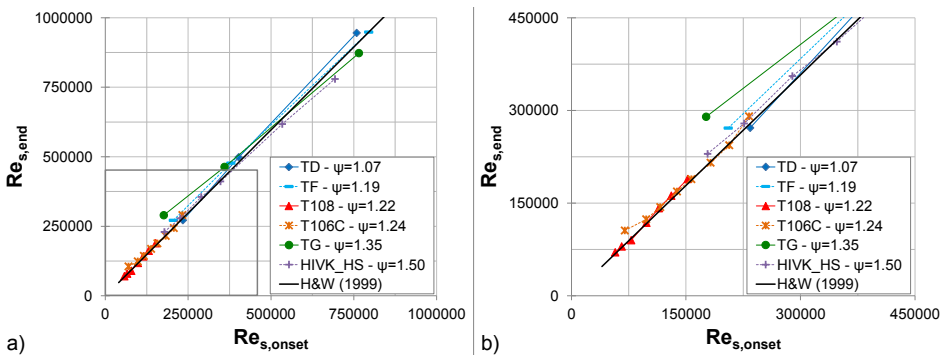


Figure 4.6.: Correlation of $Re_{s,end}$ and $Re_{s,onset}$ - a) Full scale, b) Zoom at low Re

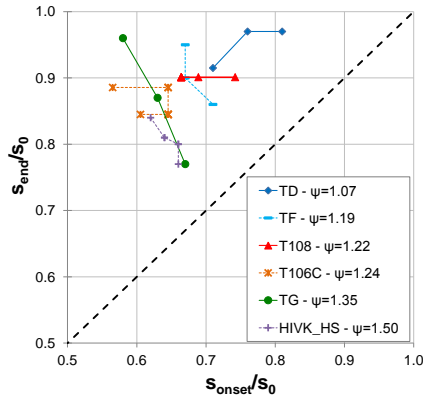


Figure 4.7.: s_{end}/s_0 against s_{onset}/s_0

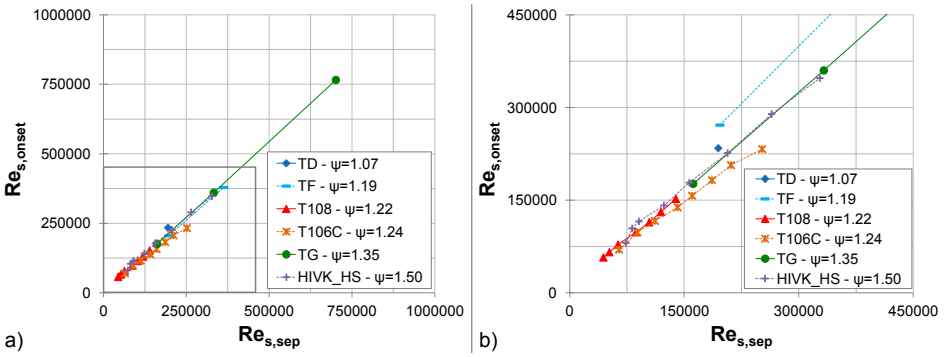


Figure 4.8.: Correlation of $Re_{s,onset}$ and $Re_{s,sep}$ - a) Full scale, b) Zoom at low Re

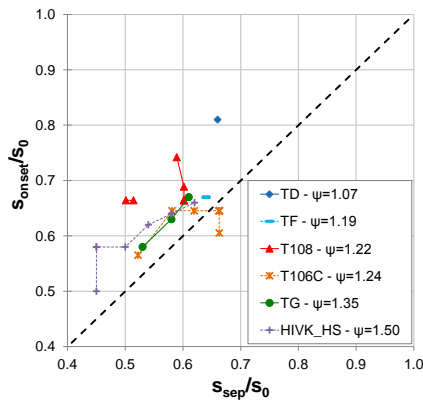


Figure 4.9.: s_{onset}/s_0 against s_{sep}/s_0

However, this correlating method is only a verification tool as it is not possible to determine the flow topology parameters positions. In that sense, it is not intended for prediction purposes. The only piece of information available from the correlations is the Reynolds number associated to them. What is essential in the understanding of figures 4.4, 4.6 and 4.8 is the link between the local pressure condition and the corresponding flow topology parameter location. Indeed, these two pieces of information are embedded in their Reynolds number definition (see equation 4.5). This guarantees the causal relationship between the flow topology parameters such as between the separation and the reattachment of the boundary layer on one side and the transition onset and the transition end of the boundary layer on another side. These causal relationships are due to the linear correlations. In order to better understand the interest of the Reynolds number-based correlating method, the non-dimensionalised flow topology parameters (figures 4.5, 4.7 and 4.9), associated to the aforementioned Reynolds numbers correlations, show the direct effect on the boundary layer of the working conditions and the blade configuration. In those figures, a diagonal black dotted line shows the positions where both the abscissae and ordinates are equal. In those causal relationship, one will expect to have data in the part above this black dotted line. At first sight, there is no obvious trend visible. Indeed, as the data matrix does not cover all the Reynolds number range (and particularly at low Reynolds number for the TD, TF and TG) the expected trends are not visible. In figure 4.5, the expected behaviour is visible for the T108, T106C and HIVK_LS blade where a decrease in $Re_{2, is}$ shows an upstream movement of the separation location which moves the reattachment downstream. Moreover, for highly-loaded blades (T2 and HIVK_HS), the separation process is reasonably tough and the separation bubble does not close at mid and low Reynolds numbers. In figure 4.7, the expected behaviour is visible only for the T106C blade. At low $Re_{2, is}$, the onset of transition appears sooner due to the earlier separation process which brings disturbances into the boundary layer. However, the transition end is still delayed towards the trailing edge. Then, when increasing $Re_{2, is}$, the transition onset moves downstream as the separation process is not as strong as at low $Re_{2, is}$. The transition end moves upstream. A further increase of $Re_{2, is}$ implies an upstream movement of the transition onset and transition end. The TG and HIVK_HS blades experience a similar behaviour since they are concerned by massive separation. Instead, the T108 experiences a flat evolution of the transition end in function of the transition onset. This is due to the fact that the diffusion is smoother on this blade. In figure 4.9, the expected behaviour is visible on the T108, T106C, TG and HIVK_HS blades. Indeed, one can see at low $Re_{2, is}$, the effect of the separation on the transition onset (already mentioned in the description of figure 4.7). The upstream movement of the separation induces an upstream movement of the transition onset. Towards higher $Re_{2, is}$, the separation still moves downstream but, there is a location where the transition onset stops moving downstream and instead starts moving upstream. At a certain point, the transition onset location will be ahead of the separation location (when the data is below the black dotted line). This means that there is

a transitional separation bubble which only occurs at high $Re_{2, is}$ as illustrated in Hatman and Wang studies [27, 28, 29, 30].

To have more insights on the laminar and turbulent contributions of the separated shear layer, the length of the separation bubble ($L_B = s_{reat} - s_{sep}$), the laminar extent of the separation bubble ($L_{lam} = s_{onset} - s_{sep}$) and the turbulent extent of the separation bubble ($L_{turb} = s_{reat} - s_{onset}$) are plotted against $Re_{2, is}$ respectively in figures 4.10, 4.12 and 4.13. Those length are non-dimensionalised by s_0 . The s_0 -non-dimensionalised parameter was made even though it is common to find in the literature investigations with the length of the bubble (L_B) as a non-dimensionalised parameter. In fact, it allows to plot more information on the separation bubble and particularly when it is an open bubble. The bubble length increases in size when $Re_{2, is}$ decreases. It could cover more than one third of the blade suction side in the worst cases of closed bubble. The general trends are pretty similar, particularly when looking at the T108, T106C, T2, HIVK_LS and HIVK_HS blades. However, some of them do not cover the low $Re_{2, is}$ region since they experience massive separation (T106C, T2 and HIVK_LS). The bubble length and the performance of the blades are linked in figure 4.11. As expected from the analysis of figures 3.1, 3.2 and 4.10, the relationships between the bubble length and the cascade losses are pretty linear (except the HIVK_LS and HIVK_HS blades) which means that the bubble length might condition the development of the boundary layer and consequently the wake profile. However, one can see that the linear relationships present different slope coefficients which depend on the blade configuration and particularly its diffusion factor mainly. Indeed, when comparing two blades with similar Ψ (T108 and T106C), one can see that they have a fairly close bubble length evolution (figure 4.10) but their losses evolution is different (figure 4.11). Interestingly, the T108 blade have the longest bubble length at low $Re_{2, is}$. This might be paradoxical, but it turns out that a mild diffusion rate blade (T108) which has a longer bubble extent than a strong diffusion rate blade (T106C), has a lower loss in performance. This allows to conclude that the boundary layer development under separation bubble conditions might be due to the thickness of the bubble rather than its surface extent. Unfortunately, no boundary layer thickness information is available from the set of data as it is not practical to implement the measurement devices in the facility. To assess the bubble thickness effect, the CFD predictions will be used.

After analysing the bubble length effect on the performance of the blades, one can focus on the laminar and turbulent contributions of the separation bubble. Figure 4.12 illustrates the laminar extent of the separation bubble contribution and figure 4.13 shows the turbulent extent of the separation bubble contribution. First, the laminar extent is smaller than the turbulent extent of the separation bubble except for the TD blade. The reason might be the mild diffusion rate that does not contribute as much as a strong diffusion rate blade to the turbulent spot production and propagation. Then, the turbulent extent tends to diminish while increasing $Re_{2, is}$. The reason is the inertial force that damps the viscous force

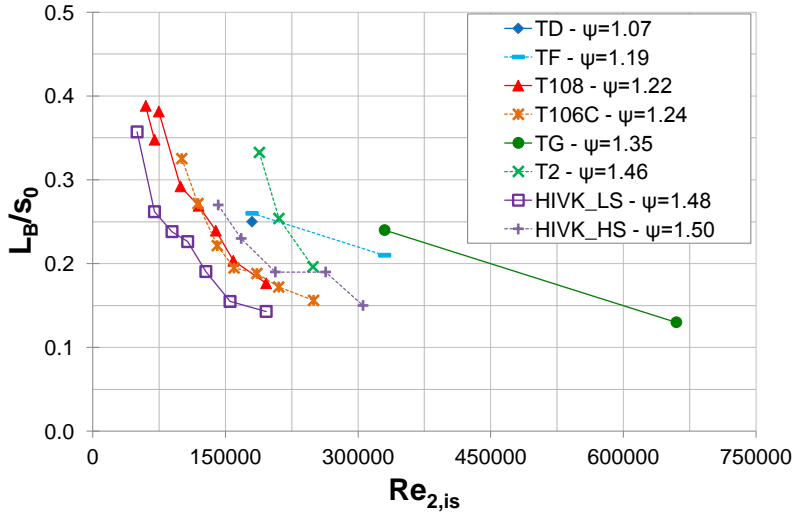


Figure 4.10.: L_B/s_0 against $Re_{2,is}$

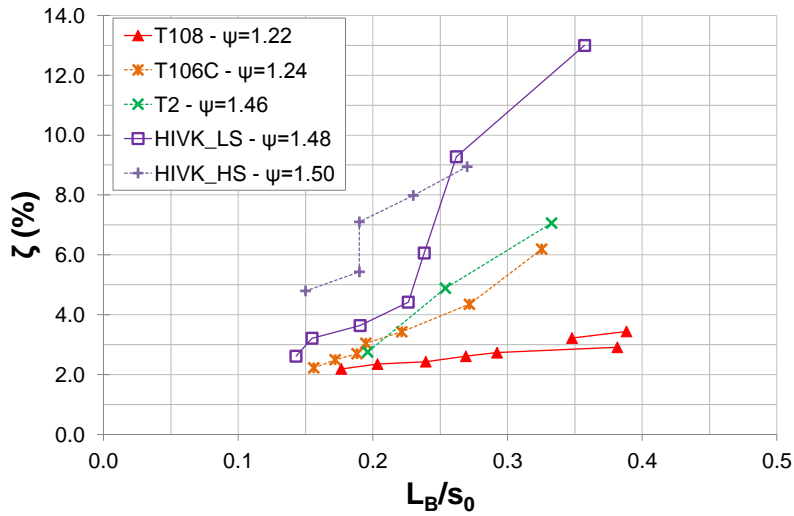


Figure 4.11.: ζ against L_B/s_0

according to the definition of the Reynolds number. Consequently, the transition to turbulence is faster, so as the turbulent spot production and propagation. At low $Re_{2,is}$, the turbulent extent is increased as the path to a full turbulent flow is slowed down because of the viscous dissipation. The laminar extent remains constant at mid and high $Re_{2,is}$ but starts to increase at low $Re_{2,is}$. Usually, the flow will separate while still being laminar, but as soon as the separated shear layer develops, disturbances are created and affect the laminar state. It may happen that the boundary layer is already transitional before separating (see T106C and T2 blades when the laminar extent is negative). Interestingly, at the lowest $Re_{2,is}$ (for the T106C and HIVK_HS blades) where there is massive separation, the laminar extent decreases. This aspect demonstrates the impact of the massive separation on the laminar part of the shear layer. As a remark, the T2 blade pseudo-wall-shear stress information above an isentropic outlet Reynolds number of 160000 are not available and consequently may bias the interpretation.

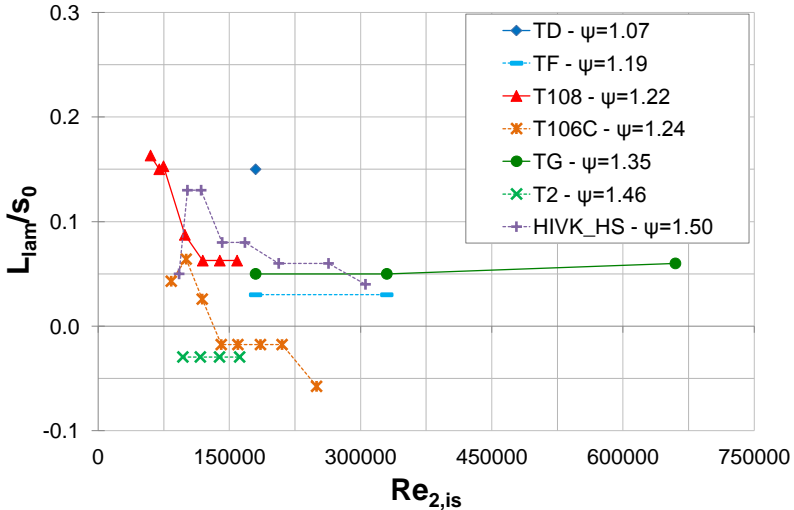


Figure 4.12.: L_{lam}/s_0 against $Re_{2,is}$

Evaluation of the database at different turbulence intensities, with uniform inlet conditions (without incoming wake) and at the design isentropic outlet Mach number. A similar investigation of the relationships between the flow topology parameters can be led at different turbulence intensities. In figure 4.14, the effect of the turbulence level is visible as the separation location is moved downstream, which consequently affects the reattachment position, that is moved downstream as well. Concerning the effect of the transition onset on the transition end, the turbulence intensity plays a great role as it moves further upstream the transition

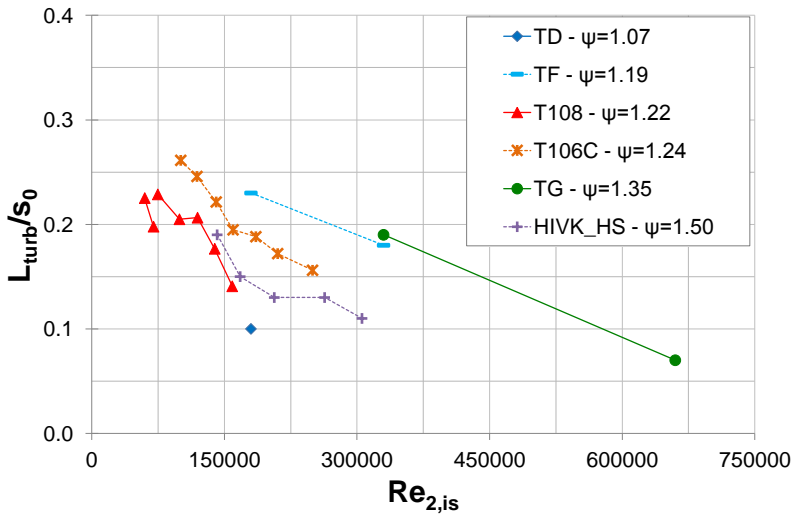


Figure 4.13.: L_{turb}/s_0 against $Re_{2,is}$

onset location (see figure 4.15). Likewise, the transition end location is affected and moves upstream. These conclusions are particularly visible in the HIVK_HS case which covers a large $Re_{2,is}$ range at a high turbulence intensity. Unfortunately, no hot-films information was available on the T106C case at high turbulence intensity (3.2%). In figure 4.16, the effect of the separation location on the transition onset location at high turbulence intensity shows that the transition onset location precedes or is close to the separation location (T106C case).

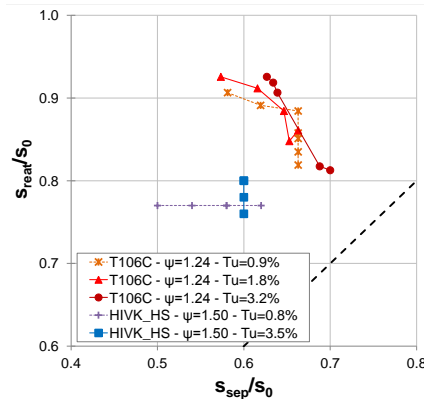


Figure 4.14.: s_{reat}/s_0 against s_{sep}/s_0 - Turbulence intensity effect

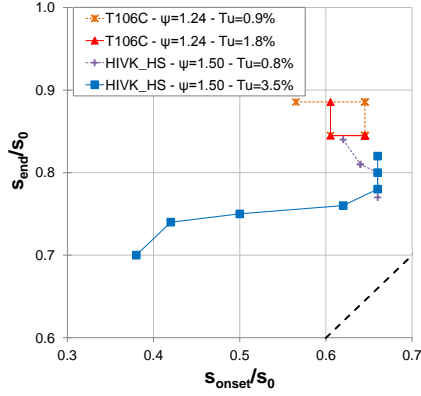


Figure 4.15.: s_{end}/s_0 against s_{onset}/s_0 - Turbulence intensity effect

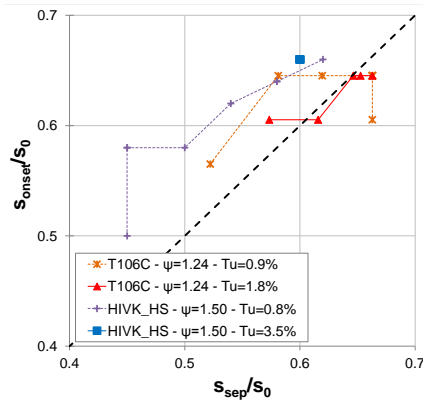


Figure 4.16.: s_{onset}/s_0 against s_{sep}/s_0 - Turbulence intensity effect

Regarding the length of the separation bubble (see figure 4.17), one can notice a general reduction when increasing the turbulence intensity. Indeed, it was expected since the turbulent structures are higher and consequently interact within the boundary layer to enhance the mixing between layers. Then, the boundary layer is more energised and is able to withstand the adverse pressure gradient in order to remain attached. The laminar contribution of the separation bubble (see figure 4.18) is absent (because there is a transitional separation bubble) or smaller at high turbulence intensity. The turbulent contribution of the separation bubble is expected to be shorter at a high turbulence intensity as in the HIVK_HS case (see figure 4.19). This reflects the general trend of the separation bubble length reduction observed previously at high turbulence intensity (see figure 4.17). Nonetheless, the T106C case does not experience this behaviour even though the turbulence intensity is not as high as expected (1.8%).

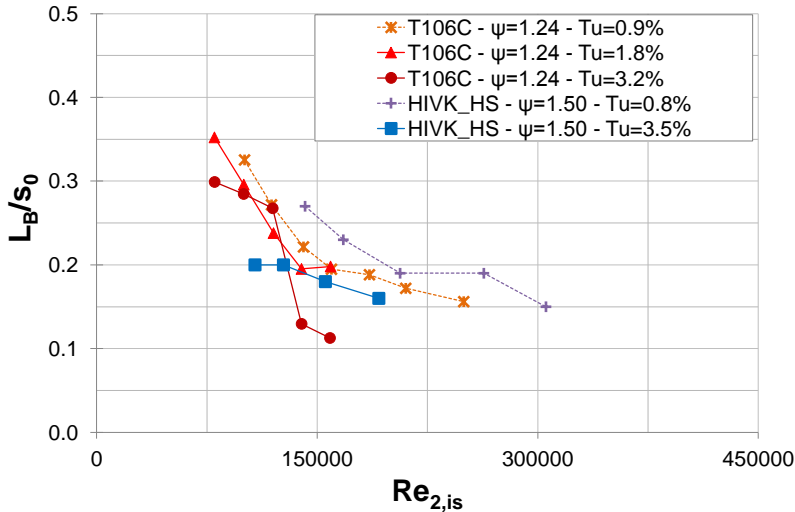


Figure 4.17.: L_B/s_0 against $Re_{2,is}$ - Turbulence intensity effect

Evaluation of the database at different isentropic outlet Mach numbers, with uniform inlet conditions (without incoming wake) and at the natural freestream turbulence intensity. The T106C blade was studied at several isentropic outlet Mach numbers. This allows to have an insight at the effect of $M_{2,is}$ on the flow topology parameters relationships. The effect of the separation location on the reattachment location is not modified as the trends are the same for all the isentropic outlet Mach numbers (see figure 4.20). Moreover, at lower $M_{2,is}$, the bubble length is reduced as the diffusion on the aft part of the blade is reduced at this condition. The transition onset location effect on the transition end is as expected

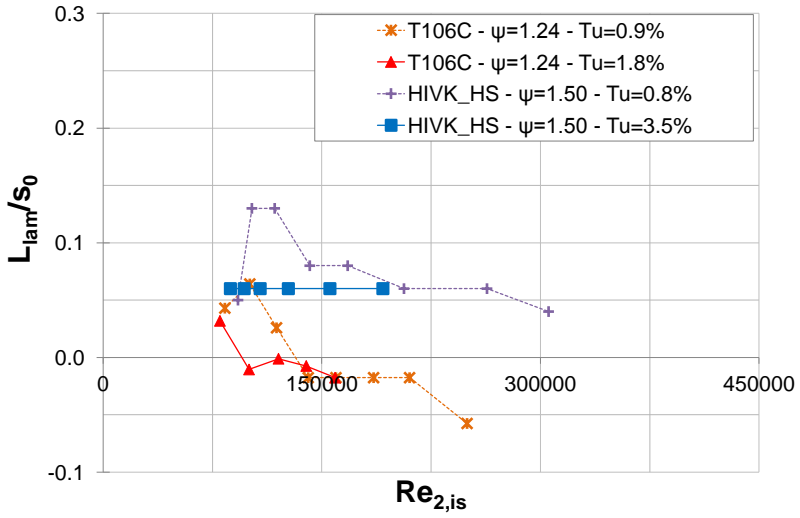


Figure 4.18.: L_{lam}/s_0 against $Re_{2,is}$ - Turbulence intensity effect

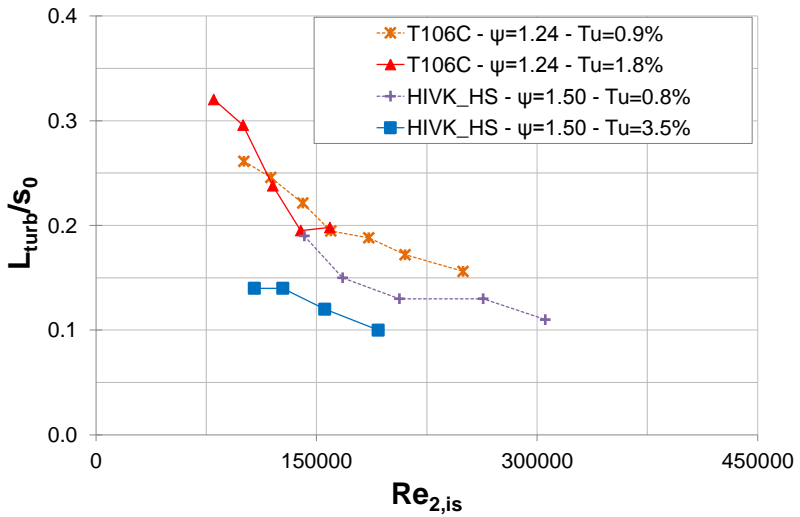


Figure 4.19.: L_{turb}/s_0 against $Re_{2,is}$ - Turbulence intensity effect

with the mirrored “C” shape (see figure 4.21). The separation location affects the transition onset location as already presented before. The trends are the same except that the transition onset location moves more downstream at low $M_{2,is}$ (see figure 4.22).

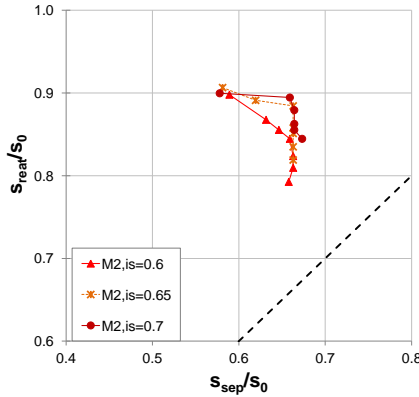


Figure 4.20.: s_{reat}/s_0 against s_{sep}/s_0 - $M_{2,is}$ effect - T106C - $\Psi = 1.24$ - $Tu = 0.9\%$

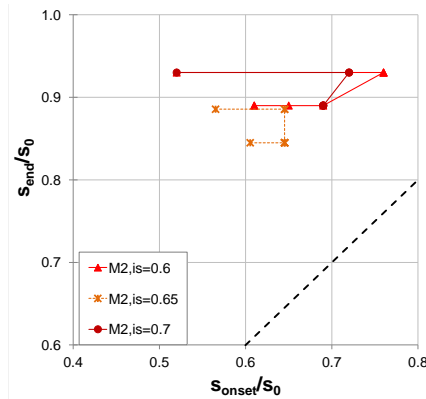


Figure 4.21.: s_{end}/s_0 against s_{onset}/s_0 - $M_{2,is}$ effect - T106C - $\Psi = 1.24$ - $Tu = 0.9\%$

As pointed out before, the trend of the evolution of the separation bubble and consequently the losses is not so affected by the isentropic outlet Mach number (see figures 4.23 and 4.24). However, the higher the isentropic outlet Mach number is and the higher the separation bubble is for a given isentropic outlet Reynolds number. This was observed in figure 3.3 with the losses. Instead, figure 4.24 shows that the separation bubble length affects the losses similarly without regard to the

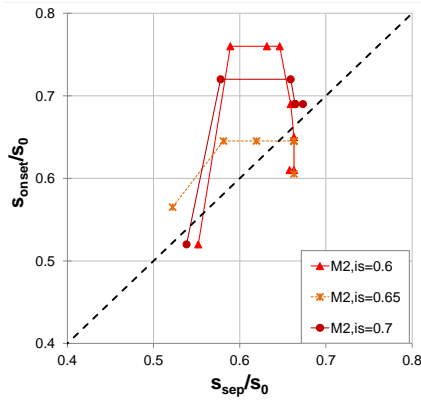


Figure 4.22.: s_{onset}/s_0 against s_{sep}/s_0 - $M_{2, is}$ effect - T106C - $\Psi = 1.24$ - $Tu = 0.9\%$

isentropic outlet Mach number.

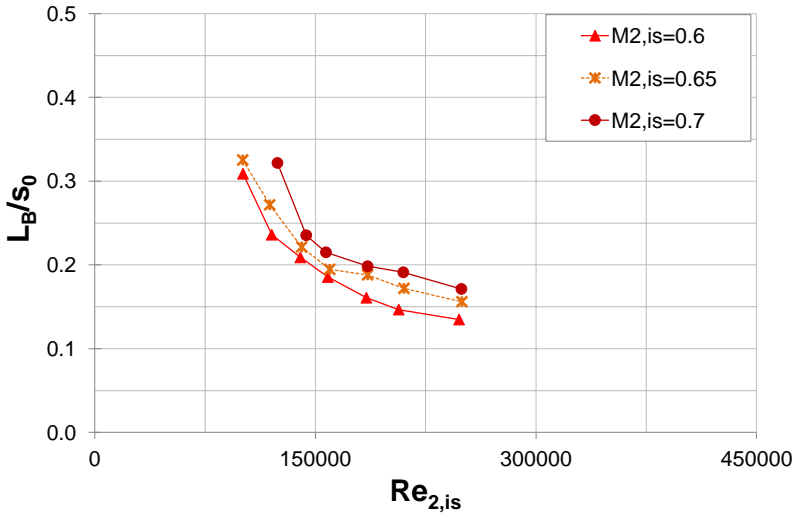


Figure 4.23.: L_B/s_0 against $Re_{2, is}$ - $M_{2, is}$ effect - T106C - $\Psi = 1.24$ - $Tu = 0.9\%$

Evaluation of the database with the isentropic outlet Reynolds number at bursting condition in function of the turbulence intensity. To end this chapter about the database evaluation, one can focus on the bursting condition (see section 2.1.2.1). Indeed, this condition illustrates the deterioration of the losses

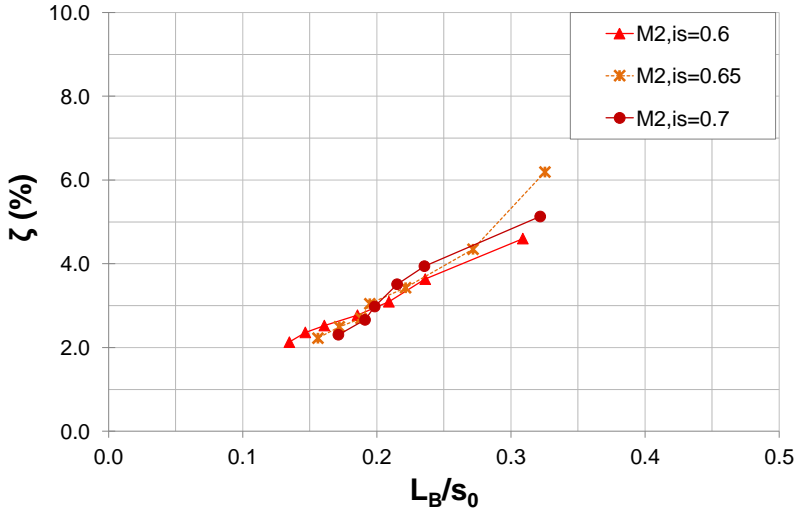
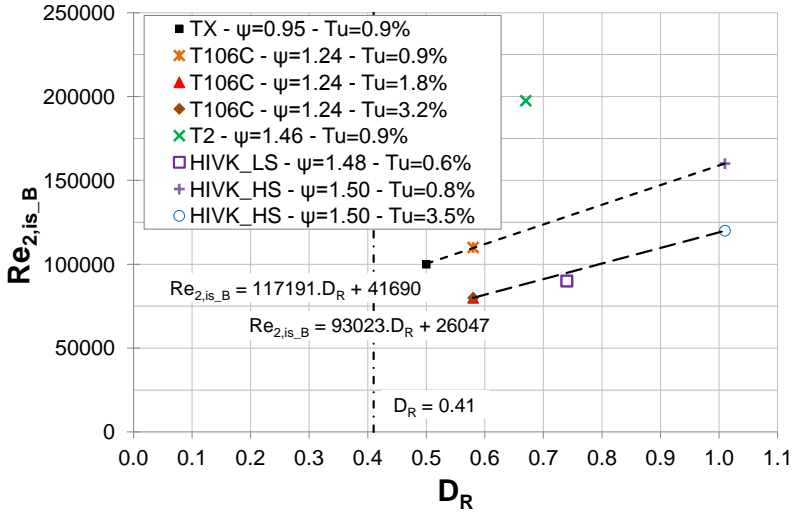


Figure 4.24.: ζ against L_B/s_0 - $M_{2, is}$ effect - T106C - $\Psi = 1.24$ - $Tu = 0.9\%$

and consequently the performances. The effects of the flow topology parameters were reviewed previously to understand their interaction and at different working conditions. Some causal relationships were highlighted. The aim of the bursting condition investigation is to define a correlation that could incorporate different blade designs with a prediction scope. Moreover, the interest of the bursting condition relies on the fact that it is the value of the isentropic outlet Reynolds number for which the separation bubble topology changes from short to long. That is why with one value, one can represent the performance of a blade for a complete Reynolds number range (from cruise to take-off). To represent this bursting condition, one has to choose the way to classify the blades. The first obvious variable is the Zweifel loading coefficient (Ψ , see equation (3.1)). However, it turns out that Ψ might not be a good parameter to characterise the blades because it could be misleading. As an example, the T108 and T106C blades present the same Ψ but they behave differently. One has a smoother diffusion rate ($D_R = 0.41$) that prevents the long and massive separation processes (T108) whereas the other one has a stronger diffusion rate ($D_R = 0.58$) that promotes the long and massive separation processes (T106C). From the available data, the conditions at which the bursting condition can be evaluated are at the design $M_{2, is}$, natural freestream turbulence intensity in one hand and turbulence intensities generated by turbulence grids in another hand. Figure 4.25 illustrates the correlating process between the isentropic outlet Reynolds number at bursting and the diffusion rate.

At first sight, the TX, T106C and HIVK_HS isentropic outlet Reynolds numbers at bursting fall into one linear trend. The TD, TF and TG blades are not repre-

Figure 4.25.: Re_{2,is_B} against D_R - Bursting correlation

sented because the isentropic outlet Reynolds number range was not wide enough (particularly at low $Re_{2,is}$) to conclude on the existence of a bursting condition. The T108 blade is not represented because it was concluded there is no bursting condition. Instead, the T2 and HIVK_LS blades are out of the trend. It was expected for the T2 blade as it is one of the most loaded blade of the database and particularly when looking at the losses evolution. The HIVK_LS was assessed under incompressible conditions. This might be the reason why the bursting prediction is overestimated (lower Re_{2,is_B} than the one that might be expected from the linear trend). Therefore, at an uniform inlet flow condition, with the natural freestream turbulence intensity, without any local roughness on the blade suction side and at the design $M_{2,is}$, one can define a correlation between Re_{2,is_B} and D_R . The resulting equation is given by:

$$Re_{2,is_B} = 117191 \cdot D_R + 41690 \quad (4.6)$$

When considering the turbulence intensity generated by turbulence grids, only the T106C and the HIVK_HS could be considered as they cover a wide $Re_{2,is}$ range. Since they are two points, one can define a correlation between Re_{2,is_B} and D_R . Indeed, the evolution is as expected. The effect of a change in the turbulence intensity is to change the slope of the linear relationships. That is why the slope is smaller in the high turbulence case. The resulting equation is given by:

$$Re_{2,is_B} = 93023 \cdot D_R + 26047 \quad (4.7)$$

Figure 4.25 features a vertical black dashed line corresponding to the diffusion rate limit below which there is no bursting possible. This limit is based on the fact that the T108 blade does not experience any bursting.

The correlation (see equation (4.6)), determined from the database evaluation and analysis, will be used later on, in chapter 7, to assess the CFD predictions in terms of bursting condition.

4.3. Summary

A correlation process was suggested in order to predict the performance of a LPT blade as a function of the isentropic outlet Reynolds number. Indeed, both cruise and take-off conditions do not have to be treated separately. Moreover, this methodology seems promising to define abaci for a quick determination of the losses when using a meanline model.

Other investigations focusing on the flow topology were performed. They stressed that the separation position of a recirculation bubble has an impact on the losses and particularly on the transition onset position.

Finally, a correlation is suggested to predict the isentropic outlet Reynolds number at bursting condition against the diffusion rate.

Chapter 5.

Tools and methodology

Analysing the database information allowed to understand the flow behaviour around LPT blades at different working conditions. Moreover, the definition of a prediction model for the bursting condition was successful. However, to get more insight on the local development of the boundary layer and to corroborate the experimental findings, one has to use a CFD approach. This approach is still the best prediction tool for a design prospect as it should be time- and cost-effective. In spite of these advantages, one should be sceptical and questioning about the predictions and their reliability. That is why, this chapter aims at defining the best and the most reliable solution, in terms of tools and methodology, to predict the flow behaviour around the LPT blades and consequently their performance.

5.1. CFD approach with the elsA code

The aim of this project is to understand the interaction between the separation and the transition phenomena occurring in an LPT environment. As stated before, the experimental investigations already provide interesting insights about the physical behaviour of the flow but still lacks some local boundary layer information, such as the momentum thickness, to be able to go deeper in the understanding and consequently build reliable prediction model. In contrast, CFD tools allow to get information that are not accessible with common measurement techniques. However, there is a price to pay if one wants a complete solution of the problem in terms of computer time and degree of modelling (see section 2.3). In the scope of this project, averaged solutions are satisfactory, particularly when considering the number of test cases. Moreover, as highlighted before, most of the transition models are based on correlations taking into account averaged positions describing the separation/transition phenomenon. In addition, the experimental information is generally presented in an averaged way. That is why, a RANS approach using a two-equation model (SST $k-\omega$) for the turbulence scales coupled to a two-equation model ($\gamma-\widetilde{Re}_{\theta t}$) for the transition process are considered.

The solver used for this project is the in-house CFD code of ONERA *elsA* [10, 59]. This software is dedicated to the numerical simulation of the compressible viscous

mono-species, steady and unsteady flows of fluids, on three-dimensional multi-block structured meshes.

Fluid flows can be modelled by a set of non-linear conservation laws (Navier-Stokes equations). However, in order to solve these equations numerically, one needs to discretise them. The approach used in *elsA* is a finite volume method, in which the unknowns are average values over the discretization cells, which are assigned to the centre of these cells. This defines control volumes where the integral conservation laws are applied and allows to have a conservative discretization. The discretization of space and time are done separately. That is why a first description of space discretization will be followed by the used time integration.

Space discretization The convective and diffusive fluxes are treated separately. In *elsA*, the diffusive fluxes uses a centred discretization. Concerning the convective fluxes, there is the choice between centred and upwind schemes.

To discretise the convective fluxes through the faces of the control volume, one can distinguish between central scheme and upwind scheme. In the present application, the Jameson scheme (central discretization) and the Roe scheme (upwind scheme) are available in *elsA*. Central schemes are based on local flux estimations while upwind schemes determine the cell face fluxes according to the propagation direction of the convection velocity [33].

The Jameson scheme is second order accurate in space. It is defined as the sum of a centred discretization and a numerical/artificial dissipation term. This last term includes a nonlinear second order dissipation term ($k^{(2)}$) to correctly capture flow discontinuities (particularly shock waves) and a linear fourth order dissipation term ($k^{(4)}$). These terms are introduced to ensure the stability of the centred discretization [59]. $k^{(2)}$ is taken as 1 as recommended in [58] but $k^{(4)}$ is more of interest in the current application because it can affect the dissipation process of the scheme and consequently affect the results of the simulation [19].

In contrast, the Roe scheme (which is part of the upwind scheme class) relies on the basic concept of introducing more physics at the discretization level. Indeed, the solution at a certain point depends only on the upwind points. The common Roe scheme is first order accurate in space but introduces excessive numerical dissipation. That is why second order schemes are required for acceptable accuracy [33]. Besides, it is known that the Roe scheme may lead to non-entropic solutions. Then, to prevent entropy violation, the Roe fluxes have to be modified according to the Harten entropy correction. This is characterised by a coefficient defined as “psiroe” in the *elsA* environment. During this project, this coefficient was kept at 0.01 even though a study of this parameter did not show a real influence to the best knowledge and use of the author. The second order extension needs the introduction of a limiter function, which is the van Albada used in the present work.

For high-speed calculation, the Roe scheme suits well since it does not need to tune the dissipation parameter. For low-speed calculation, the Jameson scheme seems more appropriate since the convection velocities are lower and because it is a common practice among *elsA* users. Concerning low-speed calculations, a low-speed preconditioning is necessary and will be described later.

Time integration To deal with the time dependence of the conservation laws, an integration in time is necessary. In the present project, only time asymptotic, pseudo-steady numerical solutions are expected even though the separation/transition phenomenon is known as unsteady. One has to remind that the equations are solved in a RANS way, consequently the solutions are representative of averaged variables. The choice has to be made between explicit and implicit methods. The explicit methods are conditionally stable which means that they are constrained by small time steps and consequently small CFL (Courant-Friedrichs-Lewy) numbers. The advantage is that the CPU (Computer Processing Unit) cost is low. In contrast, implicit scheme are generally unconditionally stable, it means that large time steps can be used which leads to high CFL numbers. However, the CPU cost is higher than the explicit one because matrix inversion has to be done at each iteration.

For this project, the particular single-step case of the Runge-Kutta time integration method, known as the Backward Euler scheme, is used. This scheme is explicit. To accelerate the convergence process, the integration scheme can be modified by introducing an implicit phase. This necessitates an approximate linearization of the system of equations. For that, a LU-SSOR factorization is considered and recommended by the *elsA* development team [58] when coupled to a Backward Euler scheme. Then, a Backward Euler scheme coupled to a LU-SSOR factorization and with a CFL value of 50 were adopted as the time integration method. Concerning the CFL value, it was set with a constant ramp from 0.1 to 50 for the first hundred iterations.

However, if during the convergence evaluation (presented later), the integrated losses or any other tracers of the flow field experience an oscillating (or non-asymptotic) pattern, then the local time-step is switched to a global one where all the cells of the domain progress at the same time step.

Low-speed preconditioning The majority of the test cases are real Mach number investigations. However, there is only one case (HIVK_LS) which was performed at low velocities. Then one needs to apply a preconditioning method for low Mach number flows. The convergence of the pseudo-steady methods is degraded at low velocities because of the very large difference between the fast acoustic modes and the slow convective modes. The method of local preconditioning modifies the considered equations, without modifying their mathematical properties, and thus

makes it possible to decrease the difference between propagation velocities of the various modes and accelerates the procedure of convergence towards the steady solution [59]. In this approach, the Jameson scheme for space discretization seems more appropriate due to its centred approach. In fact, the Roe scheme is also adapted for low-speed flows. But according to the *elsA* user database, there was no application of the Roe scheme with low-speed flows (to the best knowledge of the author). In that configuration, the CFL number is reduced by one order of magnitude in comparison to high speed flows.

Chimera technique The Chimera technique is used to simplify the meshing of complicated objects or the addition of new features in the mesh. This method lies within the scope of the resolution of the equations of Navier-Stokes on overlapping multi-domain 3D grids. Therefore, it allows overlapping different mesh blocks in order to add new features to an already existing meshed geometry. This method consists in transferring the solution from overlapping grids by interpolation [59].

This technique will be described in chapter 8.

Convergence assessment The expected type of solution is a time asymptotic, pseudo-steady numerical one. It means that convergence should be reached somehow to conclude on the dependability of the calculation. That is why several convergence criteria are set.

The residuals based on the net fluxes balance of a variable into a volume due to convection and diffusion and the amount of creation of a variable should reach an error which, with a certain number of iterations, dropped to an acceptable level. Usually, a common rule of thumb is to consider convergence when the residuals dropped by three orders of magnitude. In the present work, the raw residuals were taken into account (no non-dimensionalization).

The evolution of the domain inlet and outlet mass-flow is used to assess the convergence. Usually, they should match to conclude on the convergence. Oscillations may denote the presence of a recirculation area.

Other tracers are included in the domain in order to assess the evolution of the flow field at specific positions. For instance, the static pressure on the aft part of the blade suction side is extracted to track any possible recirculation bubble or simply any oscillating features such as the movement of the bubble over the blade. The same approach is used when non-adiabatic boundary condition is applied on the surface of the blade. Then, the heat flux information can be related to the possible oscillating recirculation process. The inlet total pressure, extracted three nodes downstream of the inlet plane, and the outlet static pressure, extracted couple of nodes upstream of the outlet plane are used to monitor the respect of the boundary conditions.

However, the most interesting parameter to monitor is the loss coefficient corresponding to the integration of the wake profile. Its evolution gives a direct information of the flow field around the blade. Then, when large oscillation of the loss coefficient is detected, the time step is switched from local to global. Then, the solution evolves in time realistically. In order to assess the separation/transition information, the worst case in terms of losses (when the losses are the highest in the oscillations) are taken as representative of the configuration (Reynolds and Mach numbers).

5.2. Methodology

The CFD methodology was defined and assessed on the T108 HL-LPT blade. The broad Reynolds number range (from 60000 to 160000), the mild diffusion rate and the large information measured during the experimental campaign (pressure distribution and pseudo-wall-shear stress around the blade and wake profile) are the reasons why this geometry was chosen and consequently contributed to the validation of the methodology.

The mesh topology is a periodic standard O4H with High Staggered corrections since the geometries are defined by high values of deviation (figure 5.1). It was generated by the Numeca software Autogrid.

The central O-mesh is around the blade and has at least 41 points in the perpendicular direction away from the blade surface. In the streamwise direction around the blade, the number of nodes is above 225 in order to get a good discretization of the suction side of the blade. The extension of the mesh in the spanwise direction is restricted to 5 layers and consequently symmetry boundary conditions are used to define the pseudo-hub and -shroud. This allows to model zero-shear slip walls. This saves a lot of computation time by focusing on the middle of the blade in order to apply convergence acceleration methodologies. Since the study focuses on LPT blades which have high aspect-ratios, it is possible to avoid the calculation of the endwall regions. This is to mimic the experimental configuration where the measurements were taken at midspan. The upper and lower part of the mesh domain in the pitch-wise direction are coupled by periodic boundaries. Depending on the configuration, the blade surface is defined as adiabatic (in the case of S1 facility which is a continuous closed circuit [57] and C1 facility which is a continuous flow, subsonic wind tunnel [16]) and isothermal (in the case of CT2 facility which is a short duration blow down wind tunnel [16]). The inlet plane is set as a subsonic inlet condition where the inflow angle, the total pressure, the total enthalpy, the turbulence kinetic energy, the specific dissipation rate, the numerical intermittency and the momentum thickness Reynolds number at transition are defined. The outlet plane is set as a subsonic outlet condition where the static pressure is defined.

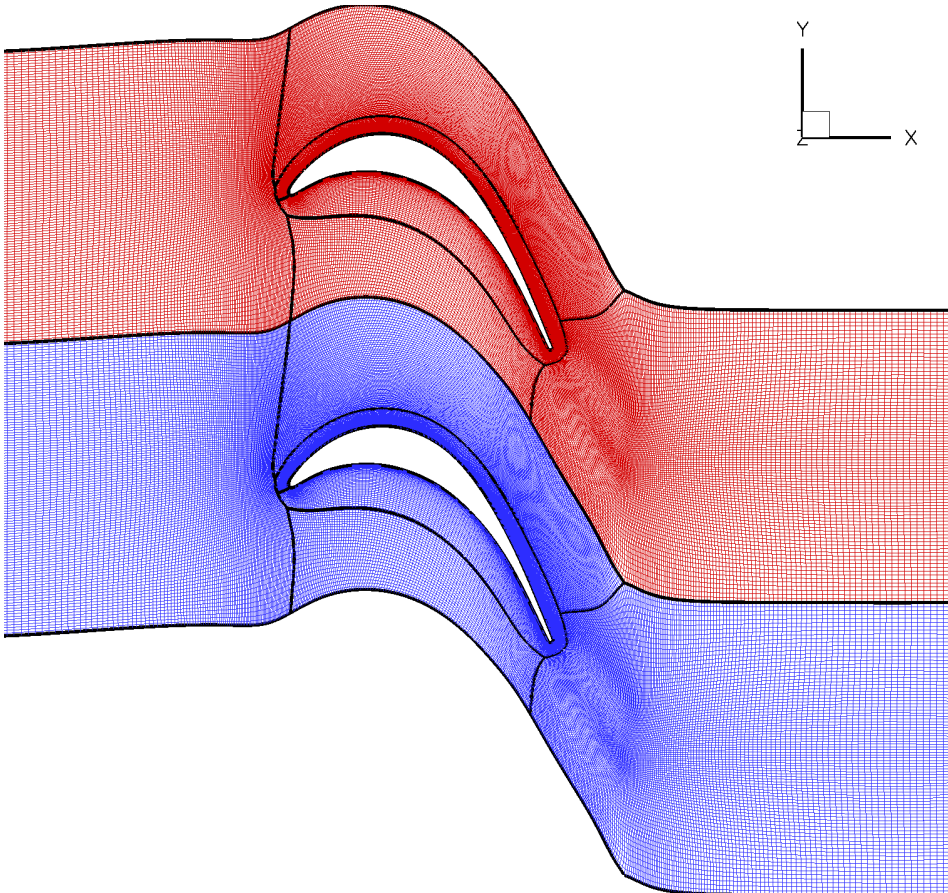


Figure 5.1.: Mesh topology of T106C ($\Psi = 1.24$)

Boundary conditions settings Concerning the computational inlet conditions for distant boundaries, one needs to provide turbulence and transition variables. About the transition ones, γ is set to 1.0 and $\widetilde{Re}_{\theta t}$ is determined by a correlation [44]. The turbulence variables (turbulent kinetic energy k and specific turbulence dissipation rate ω), at those inlet conditions, are incompletely known by the CFD community according to Spalart and Rumsey [70]. However, the decay of turbulence, ahead of the cascade, is available from the test campaign carried out at the von Karman Institute [57] where it was assessed behind a turbulence grid in the S1 facility. The corresponding points are the plain green triangles in figure 5.2. This “S1” decay law was compared to a decay law defined by Chassaing [11]. The assumption made about the turbulence is homogeneity and isotropy. The flow in the wind tunnel is considered to be statistically stationary and statistics vary only in the direction of the flow (the x-direction) at a mean velocity U_0 with time t . Chassaing [11] highlighted two phases of the decay of turbulence.

The initial phase is defined as the prevalence of the eddies in the decay of turbulence (in the region downstream the turbulence grid). He stated a “decay law” for the initial phase resulting from the work of several groups.

$$\frac{u'}{U_0} = 0.21 \left(\frac{U_0}{ms} t - \frac{U_0}{ms} t_0 \right)^{-5/8} = 0.21 \left(\frac{x - x_0}{ms} \right)^{-5/8} \quad (5.1)$$

where $ms = 12mm$ is the mesh spacing of the turbulence grid, x_0 is a virtual origin and considered as $x_0 = 0$

$$Tu = 100 \cdot \frac{u'}{U_0} = 100 \cdot 0.21 \left(\frac{x}{ms} \right)^{-5/8} \quad (5.2)$$

From the VKI S1 facility experimental measurements [57], the corresponding decay law for the initial phase is:

$$Tu = 100 \cdot \frac{u'}{U_0} = 100 \cdot 0.31 \left(\frac{x}{ms} \right)^{-0.71} \quad (5.3)$$

The final phase is defined as the prevalence of the dissipation in the decay of turbulence (far downstream the turbulence grid).

In figure 5.2, one can see the good agreement between the two sets of decay of turbulence (the “S1” one and the initial phase one from Chassaing [11]). Since the turbulence intensity measured without any grid of turbulence (0.9%) is in between the initial and final phases but closer to the initial phase, an extrapolation of the “S1” decay law was done in order to get the input values (and particularly the dissipation rate) for the inlet boundary conditions. Thus, from this extrapolated “S1” decay law (depicted by the empty green symbols in figure 5.2), it is possible to set the inlet boundary conditions in accordance with the desired values at

the leading edge plane. However, it is noticeable that the turbulence drops and then increases close to the leading edge plane. This is due to the proximity with the blade leading edge. When assessing the CFD predictions of the turbulence evolution ahead of the cascade at several $Re_{2,is}$, one can see that the inlet boundary condition inputs enable the CFD predictions to match the experimental trends (figure 5.2). Then, this methodology for imposing the dissipation rate at the inlet boundary condition is adopted for this project.

To give an order of magnitude, the Kolmogorov length scale for the T106C blade at $Re_{2,is} = 120000$, $M_{2,is} = 0.65$ and $Tu_{l.e.} = 0.9\%$ is 4.10^{-4} m for the CFD calculation whereas Michálek et al. [57], who carried out the experimental investigation of this configuration, had 5.10^{-4} m.

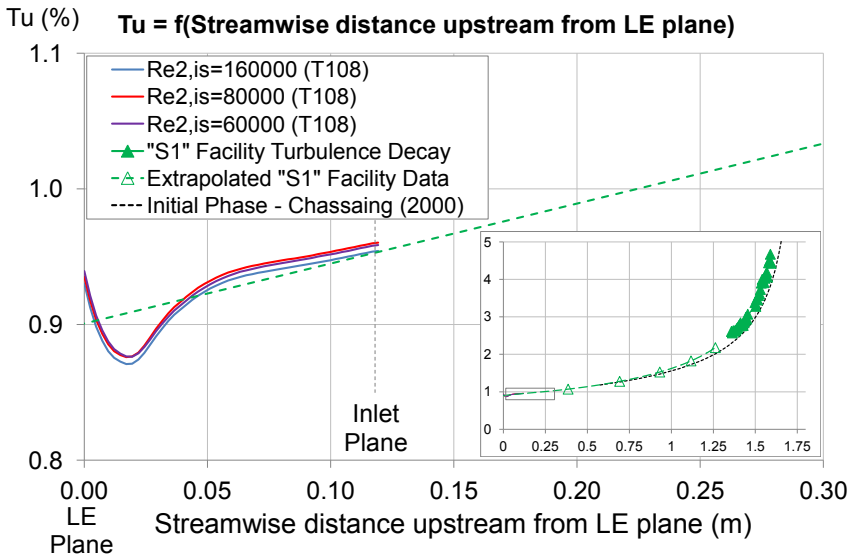


Figure 5.2.: “S1” Decay of turbulence ahead of the cascade - T108 CFD predictions

Mesh independency investigation Before starting the test campaigns, a study of the mesh was carried out in order to assess the influence of the wake treatment. Indeed, the standard mesh methodology (generated by the mesh software) reveals to be too coarse and not taking into account the exit flow angle. It will be referred as “Baseline”. It turned out that the wake prediction could be too wide and not deep enough with respect to the experimental wakes (and consequently the mass-averaged kinetic losses) as depicted in figure 5.5. In fact, the cells downstream of the trailing edge of the blade should follow the flow direction in order to calculate the fluxes appropriately. Moreover, the mesh extension, upstream of the leading

edge, was not sufficient to assess the decay of turbulence suitably. Following these recommendations, other meshes were assessed taking into account the wake treatment and are referred as “WC_1” and “WC_2”.

An illustration of the mesh topologies is given in figure 5.3. The mesh are not scaled since the T108 geometry is not opened to the literature. From left to right, there are the “Baseline”, “WC_1” and “WC_2” meshes. The improvement introduced in the “WC_1” case is a an extension of the mesh upstream of the leading edge and a cell orientation, at the downstream of the trailing edge, following the natural direction of the flow at the outlet. Moreover, a refinement in this area is done to better capture the wake. The “WC_2” mesh is similar to the “WC_1” mesh except that the downstream extension of the mesh stays oriented in the direction of the flow at the outlet. The difference is that more cells are skewed in the downstream region. The orthogonality level is still acceptable but there are more cells below 36 degrees. The meshes are cropped at both the inlet and outlet in purpose but still give an idea of the extension of the meshes in both direction.

To investigate the meshes reliability, the $\gamma\text{-}\widetilde{Re}_{\theta t}$ transition model is used. From figure 5.4 to figure 5.6, the advantage of the wake treatment associated to a refinement of the mesh is visible. Indeed, the pressure plateau and the separation phenomenon are better predicted by the “WC” meshes when comparing the isentropic Mach number distribution and the wall-shear stress. Because the mass-averaged kinetic losses could be the same due to the integration process of the wake, it is better to check the wake profiles in comparison to the experimental one. Indeed, as already spotted, the “Baseline” case predicts a wider and a less deep wake. Instead, the “WC_1” case predicts a wake that matches the experimental measurement. At last, the “WC_2” approach predicts a too narrow and too deep wake.

At the end, the mesh methodology illustrated by the “WC_1” case is adopted for all the test cases of this project. The number of nodes, in the T108 case, is 46605 in one streamwise layer. Moreover, y^+ values are below 1 through the Reynolds number ranges (figure 5.7). The orthogonality is higher than 25.9 degrees and the expansion ratio is lower than 1.78.

Ways to deal with transition in RANS with *elsA* There are three ways to deal with the transition process in RANS with *elsA*. First, one can use a transition criterion coupled to a turbulence model to trigger the production of turbulence (AGS criterion). When the criterion is met, the numerical intermittency around the blade jumps from 0 to 1 as a step function. Second, inspired by a similar approach, one can use a transition model to trigger the production of turbulence locally ($\gamma\text{-}\widetilde{Re}_{\theta t}$ model). The difference is the gradual evolution of numerical intermittency since this variable is made local due to the use of transport equation (see section 2.4.2.1). At last, one can define transition manually with an intermittency profile. With a FORTRAN routine, it was possible to set any kind of intermittency

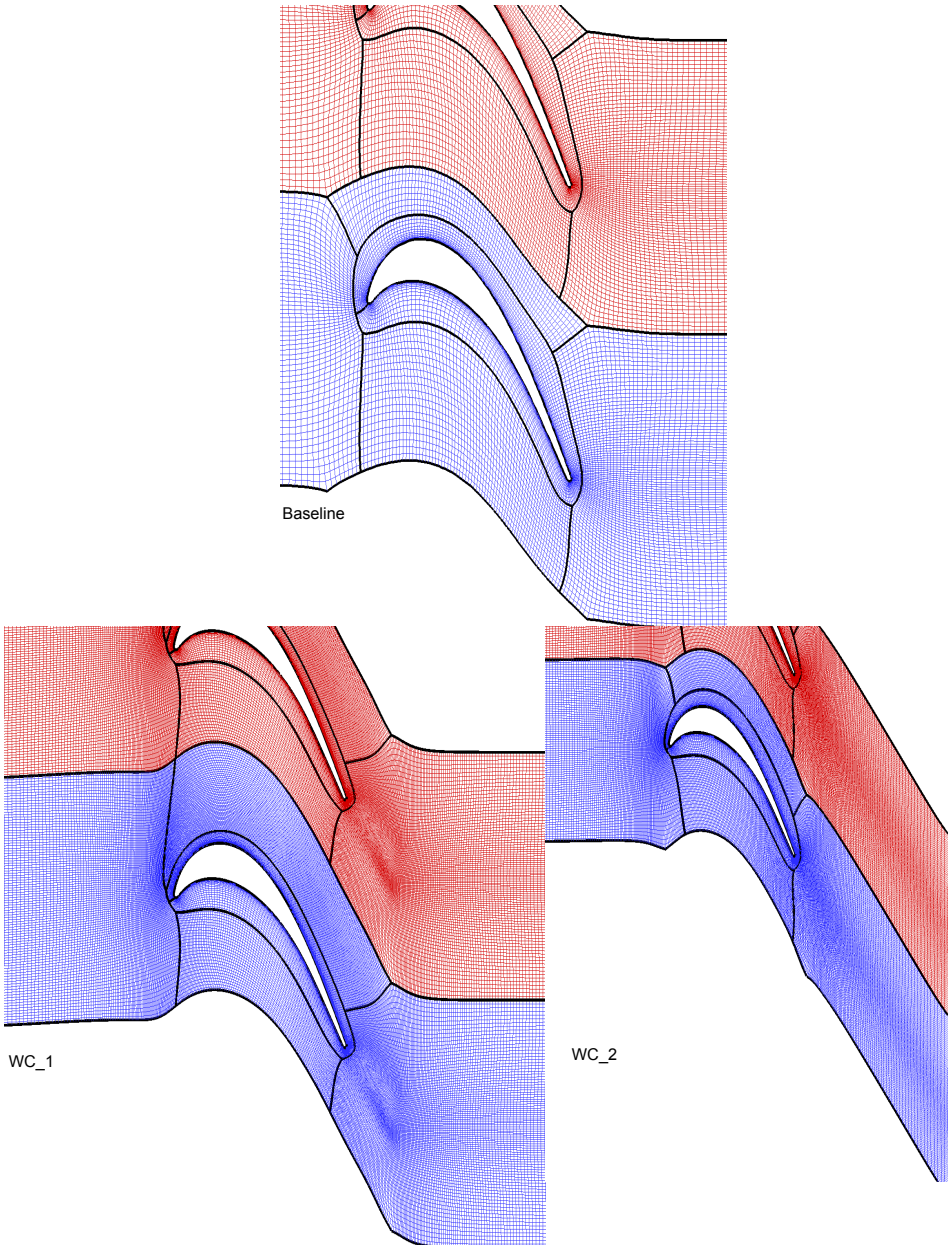


Figure 5.3.: T108 mesh topologies for the mesh independency investigation (not scaled)

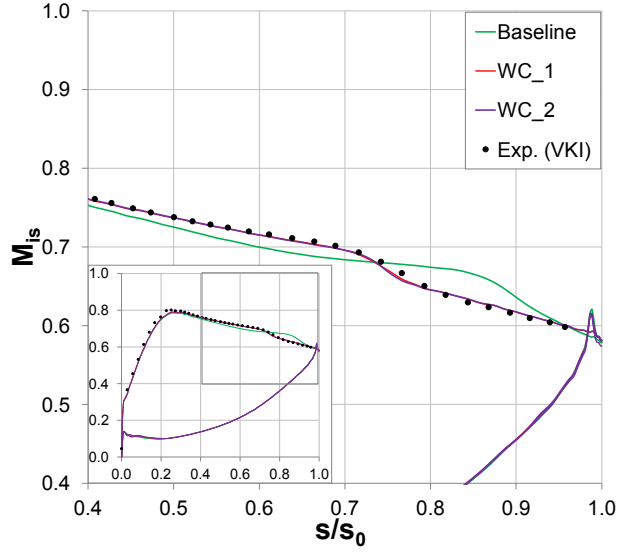


Figure 5.4.: T108 isentropic Mach number distribution at $Re_{2, is} = 160000$, $M_{2, is} = 0.6$ and $T_{u.l.e.} = 0.9\%$ - Mesh independency investigation

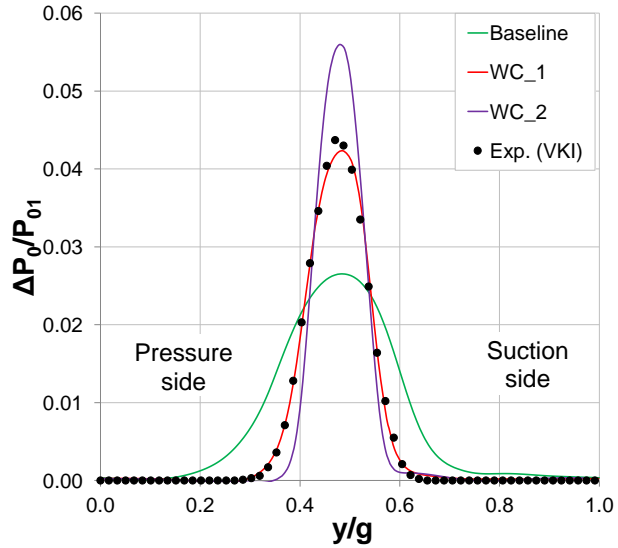


Figure 5.5.: T108 wake profile at $Re_{2, is} = 160000$, $M_{2, is} = 0.6$ and $T_{u.l.e.} = 0.9\%$ - Mesh independency investigation - $\Delta P_0 = P_{01} - P_{02}$

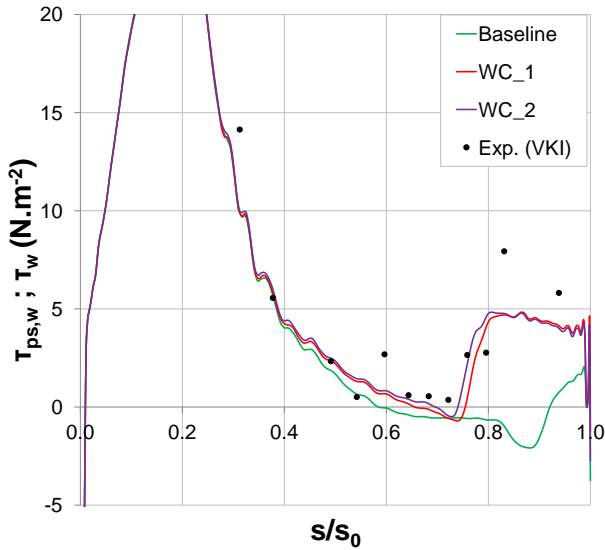


Figure 5.6.: T108 pseudo-wall-shear stress ($\tau_{ps,w}$ from experiment) and wall-shear stress (τ_w from CFD calculation) distributions on the SS at $Re_{2,is} = 160000$, $M_{2,is} = 0.6$ and $Tu_{l.e.} = 0.9\%$ - Mesh independency investigation

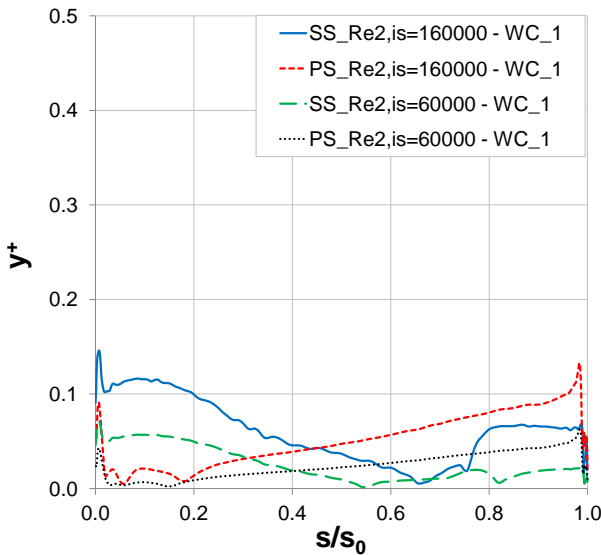


Figure 5.7.: T108 y^+ distribution on the SS and PS at $Re_{2,is} = 160000$, $M_{2,is} = 0.6$, $Tu_{l.e.} = 0.9\%$ and $Re_{2,is} = 60000$, $M_{2,is} = 0.5$, $Tu_{l.e.} = 0.9\%$

function. In fact, this approach gets rid of the search for transition onset since it is imposed.

The first approach constitutes what was the common and state-of-the-art way to deal with transition at the beginning of the project. As it is shown in figure 5.8, the second approach gives better prediction due to its local nature. Indeed, with the same mesh “WC_1” (mesh independency approach explained before), the isentropic Mach number distribution illustrates the difference in the prediction of the pressure plateau and consequently the boundary layer information as depicted in figure 5.9. However, this second approach was not available at the beginning of this project. The author would like to take a brief parenthesis to thank the *elsA* team for providing this transition model ($\gamma\text{-Re}_{\theta t}$) during the course of the project. This model is still under development at ONERA at the time of writing.

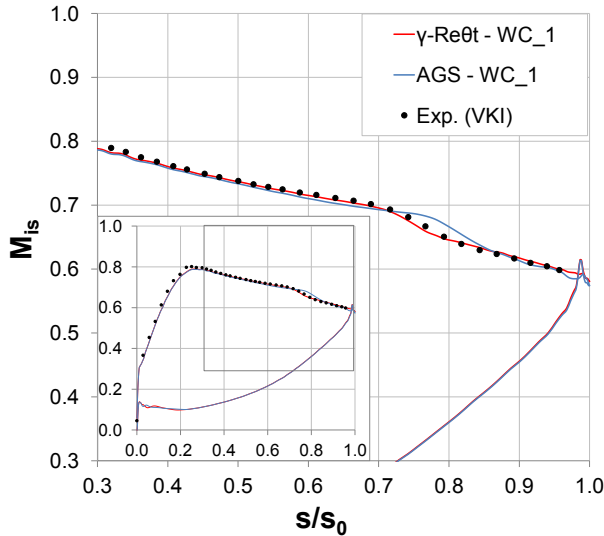


Figure 5.8.: T108 isentropic Mach number distribution at $Re_{2, is} = 160000$, $M_{2, is} = 0.6$ and $T_{u.l.e.} = 0.9\%$ - Transition model assessment

Concerning the third approach, it was widely tested during the project with different intermittency function shapes. The standard one is a step such as the one used in the AGS transition criterion approach. The advantage over the AGS transition criterion is that the step can be defined anywhere in order to try to predict the experimental measurements. Several shapes were tested because it turned out that a step function was certainly too abrupt in the production of k . That is why, functions with a more gradual evolution were considered. Thus, a standard ramp where the numerical intermittency increase from 0 at the transition onset point to 1 at the transition end point seems pertinent. To even add more physical sense,

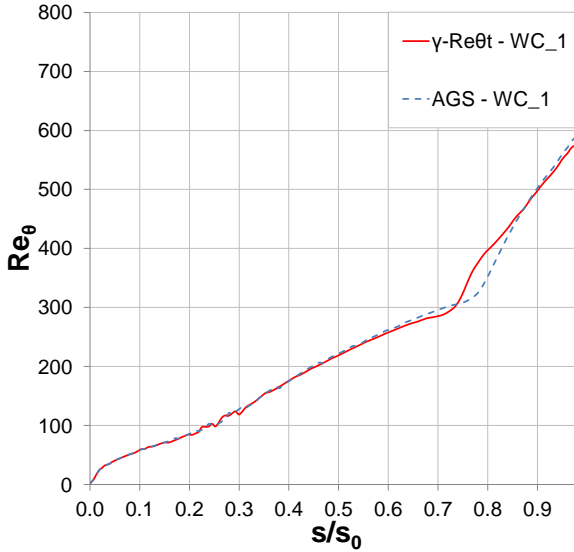


Figure 5.9.: T108 momentum thickness Reynolds number on the SS at $Re_{2, is} = 160000$, $M_{2, is} = 0.6$ and $Tu_{l.e.} = 0.9\%$ - Transition model assessment

the intermittency function was derived as the standard “S” shape defined by Abu-Ghannam and Shaw [1] in equations 2.23 and 2.24 and illustrated in figure 5.10. An illustration of this last intermittency function is documented in Babajee [6].

However, this method loses its prediction characteristics since the user has to set the onset of transition. But, the idea behind it was to get closer to the experimental information in terms of measured variable and consequently conclude on the good boundary layer information predicted from the numerical calculation. It turns out to be really difficult to tune the position of transition onset to get reliable information. Moreover, this approach might be of interest in an optimization strategy.

That is why, the project will focus only on the use of the $\gamma\text{-}\widetilde{Re}_{\theta t}$ transition model in predicting LPT rotor blade flow features such as separation and transition onset and particularly the prediction of the experimental measured quantities. An investigation of the inlet turbulent boundary conditions will be done in order to make the model “dormant” [70] in the aim to reproduce a fake laminar flow. Indeed, the goal is to understand how at low turbulence level (0.9%) the model triggers transition when the flow is considered to be laminar since neither upcoming wakes nor high turbulence scales structures affect the boundary layer.

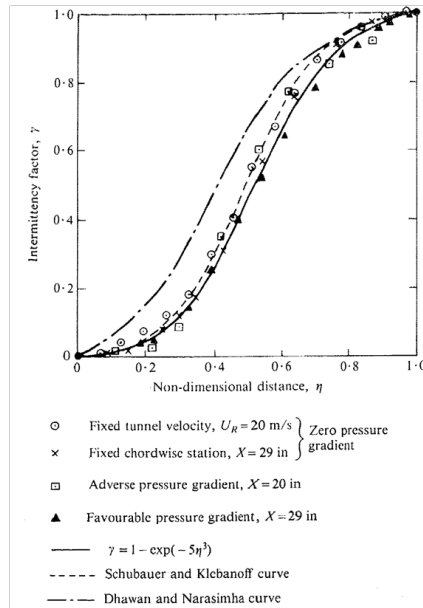


Figure 5.10.: Intermittency function (Abu-Ghannam and Shaw [1])

5.3. Summary

Predicting the flow topology around a LPT blade as well as its performance requires a reliable model. This chapter illustrates the CFD methodology used to tackle the topic and highlights the functionalities chosen to model accordingly the phenomena considered in this work.

Chapter 6.

Evaluation of the γ - $\widetilde{Re}_{\theta t}$ transition model with the database

After reviewing the literature in order to define the framework of the study, the analyses of the large database of LPT blades at disposal allow to better understand the separation-induced transition phenomenon occurring in that environment. To evaluate and verify these findings, a numerical simulation-based approach was undertaken. Investigations of the available tools and techniques were carried out to determine the best and the most reliable methodology to investigate the several test cases. This chapter illustrates the use of a methodology based on the γ - $\widetilde{Re}_{\theta t}$ transition model. The aim is to evaluate the ability of this methodology for predicting the experimental results in terms of blade pressure distribution, total pressure profile (for wake investigation), pseudo-wall-shear stress and heat transfer coefficient. These experimental information are interesting data but they still need to be cross-compared when possible to get the most reliable understanding of the studied phenomenon. However, the aim of the numerical simulation is to evaluate the degree of confidence one can have using this technique by predicting the experimental information and consequently explore more data that cannot be measured in a wind tunnel in order to get more insight into the separation-transition phenomenon. This chapter will present the results of the numerical investigations led to evaluate the reliability of the γ - $\widetilde{Re}_{\theta t}$ transition model in predicting the experimental results. An effort will be done to illustrate the comparison between the available experimental results (designated as “*Exp. (VKI)*” in the plots) and the transition model predictions (designated as “ $\gamma - Re_{\theta t}$ ” in the plots) for two isentropic outlet Reynolds numbers. One will be characteristic of engine cruise condition (low $Re_{2, is}$ where the separation-induced transition phenomenon occurs) and another one will be representative of a milder or higher $Re_{2, is}$ according to the working conditions matrix. In addition, the fully turbulent predictions (designated as “*Turbulent*” in the plots) will be incorporated in the comparisons to understand the improvement made by the use of a transition model.

6.1. T108 LPT blade test case

The T108 blade is a mild diffusion blade which was used as a test case for the determination of the methodology to investigate LPT blades in the present study (see section 5.2). The blade design is illustrated in figure 6.1 in a linear cascade configuration. This is a front-loaded high-lift LPT blade designed by MTU Aero Engines in the frame of the European programme TATMo.

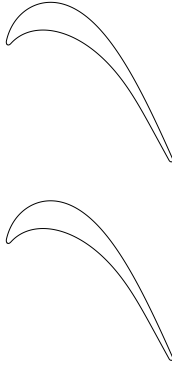


Figure 6.1.: T108 cascade (not scaled)

The mesh information is provided in table 6.1.

Table 6.1.: T108 LPT blade mesh information

Blade	T108
Number of {nodes ; cells} in one streamwise layer	{46605 ; 45488}
Minimum orthogonality (deg)	25.9
Number of cells in orthogonality intervals: {[18 deg ; 27 deg[; [27 deg ; 36 deg[} in one streamwise layer	{77 ; 841}
Maximum expansion ratio	1.78
Maximum y^+ on the blade {SS ; PS}	{0.15 ; 0.13}
Number of nodes around the blade	321
Number of nodes on the blade SS	204

The T108 blade was assessed at the natural freestream turbulence intensity (0.9%) of the facility. The working conditions at which the T108 blade was evaluated are displayed in table 6.2.

The CFD investigations lead us to have a look at the isentropic Mach number distribution and the pseudo-wall-shear stress information on the blade suction side.

Table 6.2.: T108 LPT blade working conditions at the natural freestream turbulence intensity

Blade	T108
Ψ	1.22
g/c	0.90
Loading	Front
D_R	0.41
$M_{2,is}$	{0.5 ; 0.6}
$Re_{2,is}$ ($\times 10^3$)	[60 ; 160]
$Tu_{l.e.}$ (%)	0.9
Re_t	[4.8 ; 12.7]
Facility	S1

These information are critical in understanding the boundary layer development on the suction side.

First, the comparison between the experimental results and the numerical predictions is given for a mild $Re_{2,is}$ (140000). Figure 6.2 shows the isentropic Mach number distribution around the blade. At first sight, the numerical predictions are very satisfactory when using the transition model methodology. One is able to predict the separation and the pressure recovery while the standard turbulent calculation fails. This is corroborated in figure 6.3 where the wall-shear stress matches with the experimental pseudo-wall-shear stress, specially when assessing the qualitative information (which are the positions of separation and reattachment). Concerning the wake profile comparison (figure 6.4), it shows a very good matching in terms of wake depth and width.

Similarly, at a lower $Re_{2,is}$ (70000), the isentropic Mach number distribution around the blade is satisfactory (figure 6.5). Indeed, the separation process is well predicted as it features a short bubble type. This is visible from the level of both the experimental peak isentropic Mach number and the transition prediction which are close to the fully turbulent case (basically without any separation bubble). This is corroborated by the wall-shear stress information where the separation bubble extension is well predicted (figure 6.6). Instead, the wake profile (figure 6.7) is slightly overpredicted in terms of wake depth but still constitutes a reasonable prediction.

The comparisons, in terms of mass-averaged kinetic losses and outlet flow angle are depicted in figures 6.8 and 6.9. From these figures, one can see that the present study predictions are in good agreement with the experimental measurements over the full $Re_{2,is}$ range. As a remark, the break in the $Re_{2,is}$ range is intentional since the two lowest $Re_{2,is}$ were performed in the facility at a lower outlet isentropic Mach number ($M_{2,is}=0.5$ instead of 0.6). Several research groups were involved in

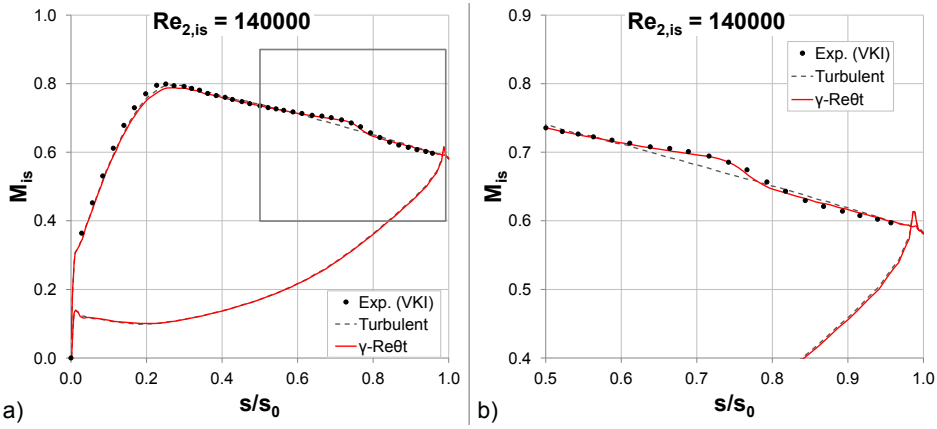


Figure 6.2.: T108 isentropic Mach number distribution at $Re_{2,is} = 140000$ and $Tu_{l.e.} = 0.9\%$ - a) Full scale, b) Zoom in the aft region

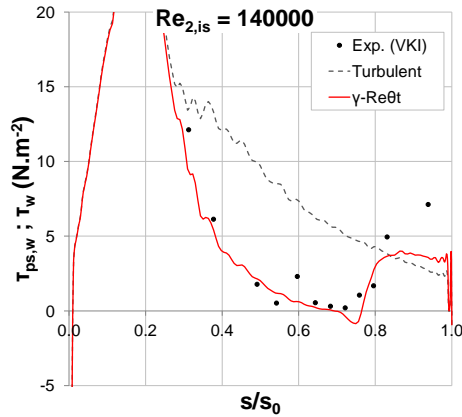


Figure 6.3.: T108 pseudo-wall-shear stress ($\tau_{ps,w}$ from experiment) and wall-shear stress (τ_w from CFD calculation) distributions on the SS at $Re_{2,is} = 140000$ and $Tu_{l.e.} = 0.9\%$

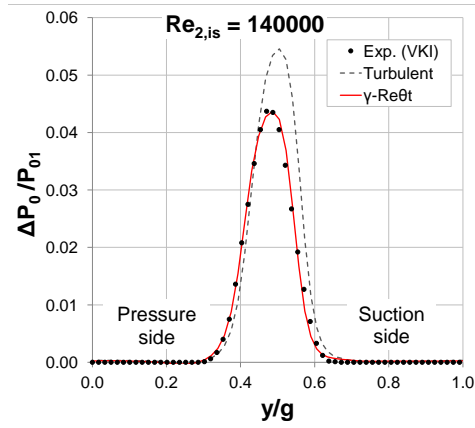


Figure 6.4.: T108 wake profile at $Re_{2,is} = 140000$ and $Tu_{l.e.} = 0.9\%$

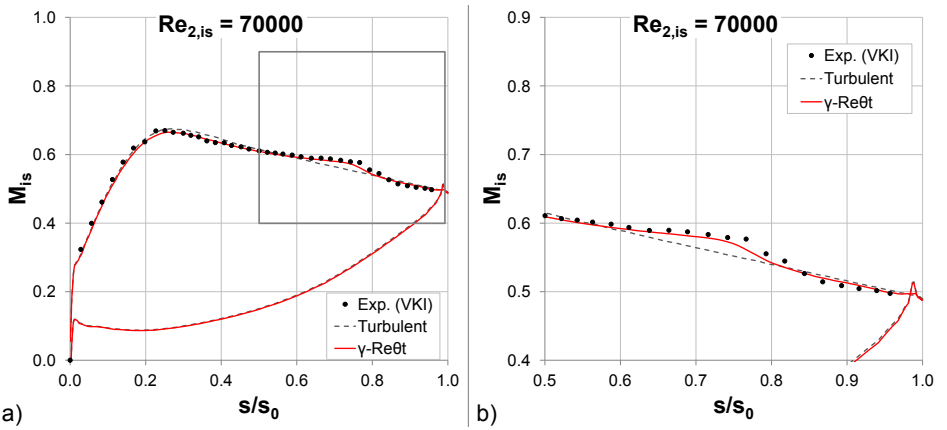


Figure 6.5.: T108 isentropic Mach number distribution at $Re_{2,is} = 70000$ and $Tu_{l.e.} = 0.9\%$ - a) Full scale, b) Zoom in the aft region

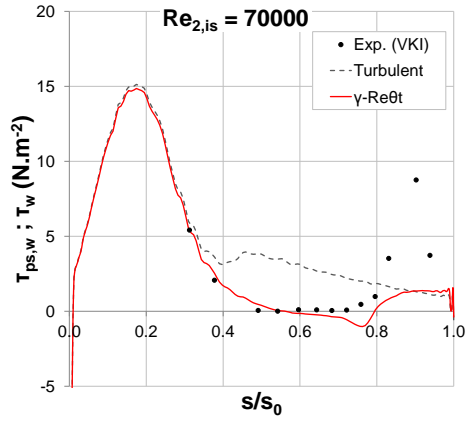


Figure 6.6.: T108 pseudo-wall-shear stress ($\tau_{ps,w}$ from experiment) and wall-shear stress (τ_w from CFD calculation) distributions on the SS at $Re_{2,is} = 70000$ and $Tu_{l.e.} = 0.9\%$

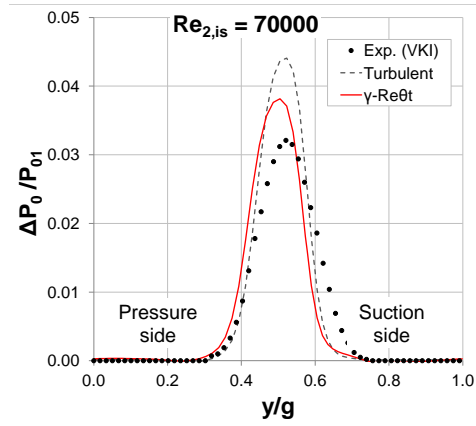


Figure 6.7.: T108 wake profile at $Re_{2,is} = 70000$ and $Tu_{l.e.} = 0.9\%$

the TATMo programme. The comparison with their published results is discussed below.

From those trends, the similarity between the correlation-based transition model (Corral and Gisbert [15] and the present study) is remarkable even though the calibration parameters are not the same (such as $\sigma_{\theta t}$ and s_1). This could be a reason why an offset in the trends is noticeable. However, this might be due to the different values of the turbulent Reynolds number (Re_t) used between the two groups to compute the dissipation rate at the inlet boundary condition. The quality of the mesh in both studies does not seem to imply any mesh dependency. This last point leads to the comparison between the present study predictions with the ones of Benyahia et al. [8]. Their predictions overestimate the experimental results, even though they got good predictions of the isentropic Mach number distribution over the blade suction side. The reason is a question of mesh dependency since they used the coarsest mesh among all the presented studies and there is no apparent wake treatment or refinement in the wake vicinity. At last, the comparison with Pacciani et al. [60] predictions leads to a good matching. Since their laminar kinetic energy approach is intended to be based on more physical models, one can conclude on the reliability of the correlation-based transition model, used in this study, for this HL-LPT blade configuration.

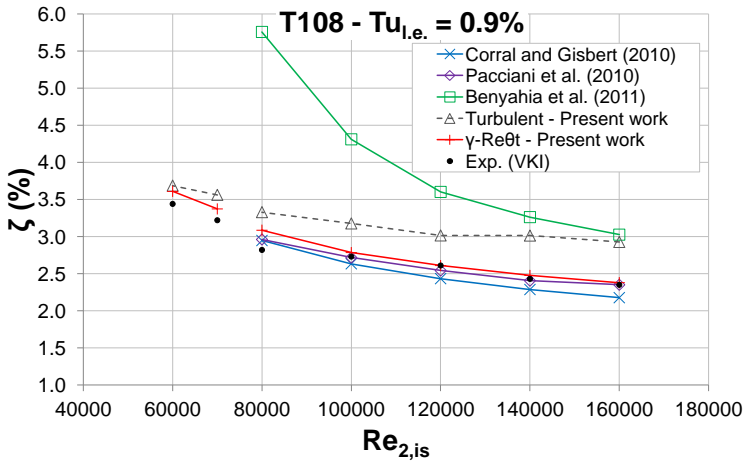


Figure 6.8.: T108 mass-averaged kinetic losses at $Tu_{l,e} = 0.9\%$

6.2. T106C LPT blade test case

The T106C blade is a high diffusion blade. The blade design is illustrated in figure 6.10 in a linear cascade configuration. This is an aft-loaded high-lift LPT

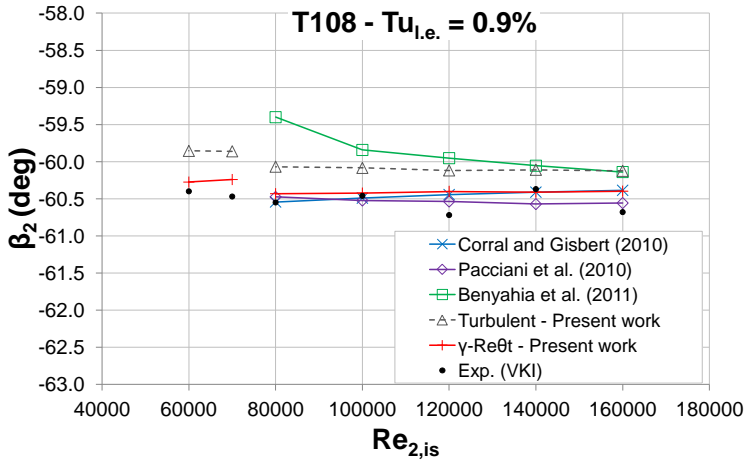


Figure 6.9.: T108 mass-averaged outlet flow angle at $Tu_{l.e.} = 0.9\%$

blade which was assessed in the frame of the European programmes UTAT and TATMo. This blade was tested at several turbulence levels. From the available information, only the investigations carried out at two turbulence levels (0.9%, see section 6.2.1 and 1.8%, see section 6.2.2) are presented.

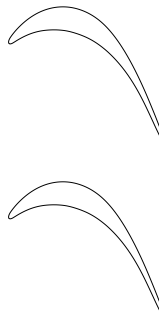


Figure 6.10.: T106C cascade

The mesh information is provided in table 6.3.

Table 6.3.: T106C LPT blade mesh information

Blade	T106C
Number of {nodes ; cells} in one streamwise layer	{46605 ; 45488}
Minimum orthogonality (deg)	31.1
Number of cells in orthogonality interval: [27 deg ; 36 deg[in one streamwise layer	299
Maximum expansion ratio	1.71
Maximum y^+ on the blade {SS ; PS}	{0.27 ; 0.21}
Number of nodes around the blade	321
Number of nodes on the blade SS	204

Table 6.4.: T106C LPT blade working conditions at the natural freestream turbulence intensity

Blade	T106C
Ψ	1.24
g/c	0.95
Loading	Aft
D_R	0.58
$M_{2, is}$	0.65
$Re_{2, is} (\times 10^3)$	[80 ; 250]
$Tu_{l.e.} (\%)$	0.9
Re_t	[6.7 ; 22.2]
Facility	S1

6.2.1. T106C LPT blade test case: Natural freestream turbulence intensity (0.9%)

The T106C blade was tested at the natural freestream turbulence intensity of the facility. The working conditions at which the T106C blade was evaluated are displayed in table 6.4.

The mass-averaged kinetic losses (figure 6.11) and outlet flow angle (figure 6.12) numerical results do not correctly predict the experimental results at low $Re_{2, is}$. However, at mid and high $Re_{2, is}$, the numerical predictions match pretty well with the experimental results. There is an underprediction of the present work “ $Re_t = TD$ ” results (“TD” corresponds to the value of the turbulent Reynolds number extracted from the extrapolated “S1” decay law, see section 5.2). This aspect was expected as the current blade is a high diffusion blade with high adverse pressure gradient level. The correlation for the onset of transition in the adverse pressure gradient region is basically meant for attached flows [1, 55] and ranges

up to $\lambda_\theta = \pm 0.1$ (λ_θ can be lower than -0.1 for the HL-LPT blade cases of the present work ; $\lambda_{\theta,min} = -2.5$ for the T106C case). Consequently, this explains why the model might fail at low $Re_{2,is}$ where laminar separation is encountered.

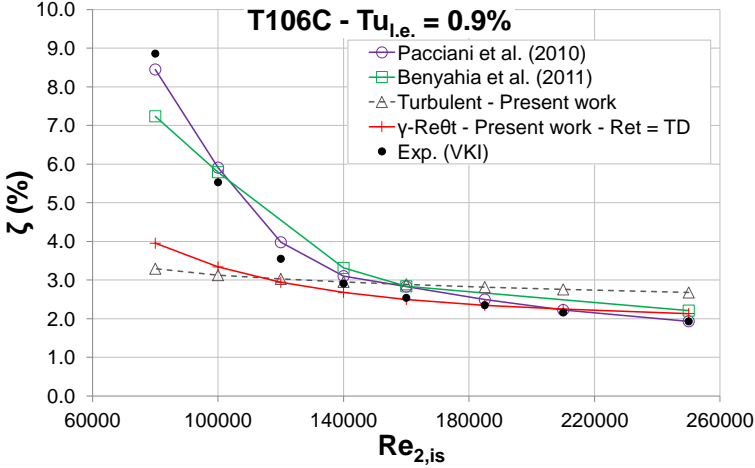


Figure 6.11.: T106C mass-averaged kinetic losses at $Tu_{l.e.} = 0.9\%$

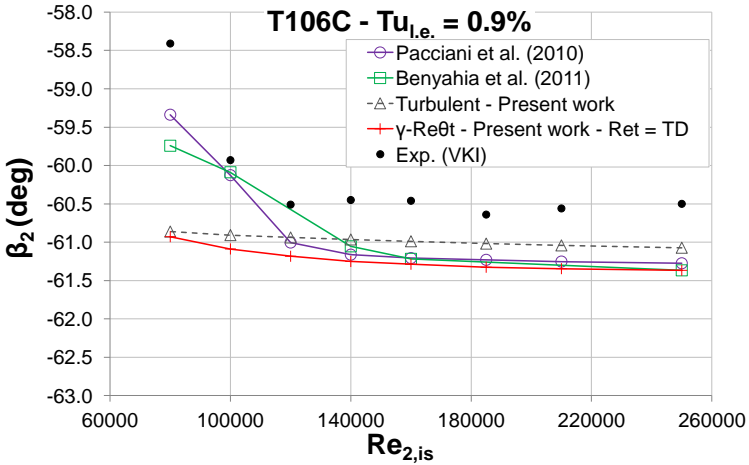


Figure 6.12.: T106C mass-averaged outlet flow angle at $Tu_{l.e.} = 0.9\%$

The same research groups, as in the former section, worked on the T106C blade with the same methodology and numerical approach, except Benyahia et al. [8] who used a finer mesh with a wake treatment. Their results are presented in figures 6.11 and 6.12. Apparently, the values of Re_t used by the other research

groups are lower than the one used in the ‘TD’ trend (see table 6.4). In fact, Pacciani et al. [60] used a ratio of turbulence length scale over the axial chord of 2.5×10^{-3} which represents values of Re_t ranging in the interval $[0.94 ; 2.95]$ for the $Re_{2, is}$ range (see table 6.4). Benyahia et al. [8] used a value of $Re_t = 0.1$. Since the predictions seem to be Re_t -dependent, a study of this turbulent Reynolds number was carried out.

To understand this Re_t dependence, an insight at the turbulence intensity level along a streamline across the cascade (from the inlet plane to the outlet plane) in the ‘freestream’ region (between two blades) is provided in figure 6.13 for $Re_{2, is} = 80000$. The corresponding extraction streamline is shown in figure 6.14. There are two turbulence intensity levels (0.9% and 1.7%). The plain lines correspond to the 0.9%-case and the dashed lines correspond to the 1.7%-case. For the 0.9%-case, one can see that for $Re_t = 0.01$, the level of turbulence is really low (around 0.1%). This behavior is close to a pseudo-laminar case or an external flow configuration. Moreover, it does not follow the extrapolated ‘S1 facility’ decay law. This conclusion is applicable to $Re_t = 0.1$ as well whereas $Re_t = 1$ seems close to the extrapolated ‘S1’ decay law. For the lowest Re_t (0.01 and 0.1), the dissipation of the turbulence, set by the specific dissipation rate (ω), is independent of the turbulence intensity (a fortiori the turbulent kinetic energy, k). Indeed, both turbulence intensity trends fall into the same low level which confirms this low- Re_t independency.

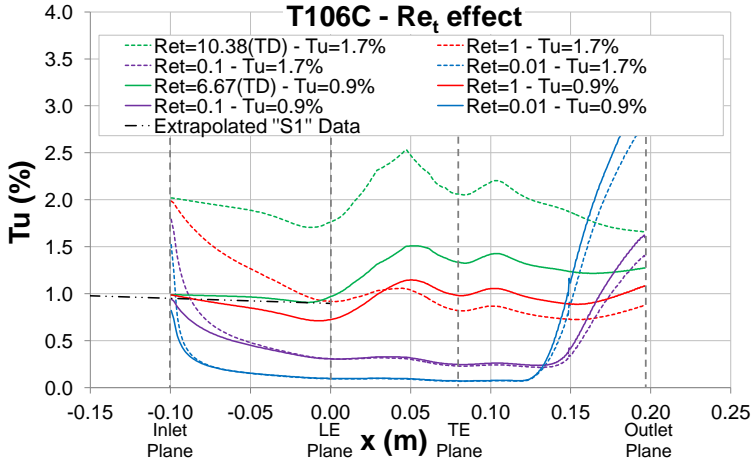


Figure 6.13.: Turbulence across the T106C cascade at $Re_{2, is} = 80000$ with the influence of the turbulent Reynolds number (Re_t)

The introduction of the low- Re_t approaches is illustrated in figures 6.15 and 6.16. The improvement in the prediction is obvious and particularly for the two lowest $Re_{2, is}$. The $Re_t = 0.01$ -cases are able to predict the measured kinetic losses and

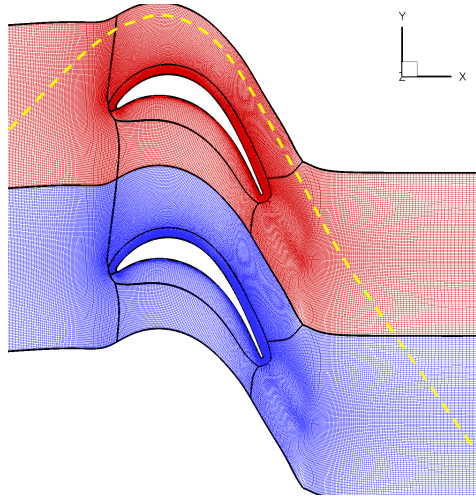
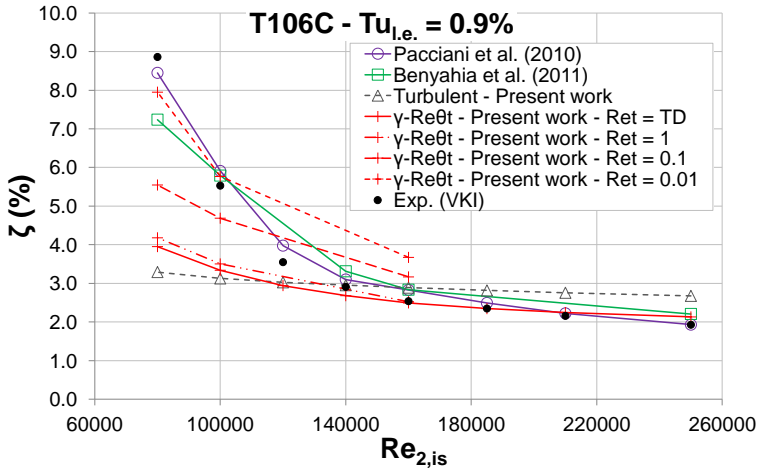
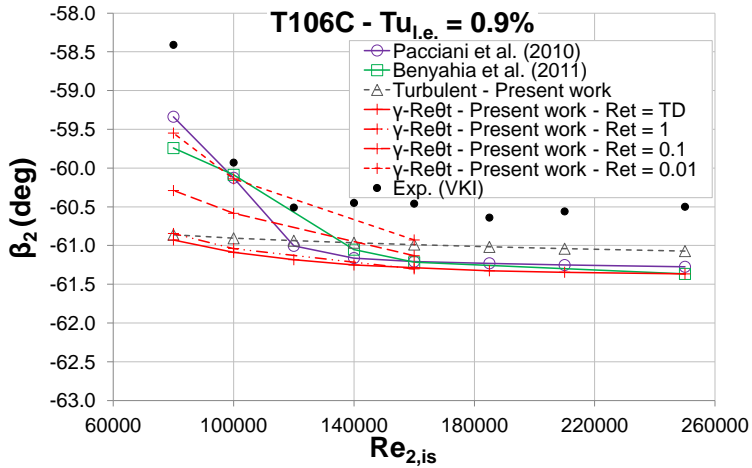


Figure 6.14.: Extraction line across the T106C cascade for the investigation of the turbulent Reynolds number influence

the outlet flow angle. Indeed, the features of a massive separation are visible from the kinetic losses and outlet flow angle trends.

To better understand the Re_t investigations, the isentropic Mach number and wall-shear stress distributions and the wake profile at two isentropic outlet Reynolds numbers (80000 and 160000) are presented in figures 6.17 to 6.23. At $Re_{2,is} = 80000$, the experimental isentropic Mach number distribution shows a long bubble/massive separation pattern which is noticeable from the reduced isentropic Mach number peak, the extended pressure plateau and the incomplete pressure recovery. The gradual decrease of the turbulent Reynolds number induces a flow behaviour which is similar to a pseudo-laminar calculation. Indeed, by lowering the turbulent Reynolds number, one drastically reduces the turbulence intensity level in the freestream region (see figure 6.20). Consequently, the boundary layer is prone to laminar separation, which is expected according to the experimental information. The lowest Re_t isentropic Mach number distribution is able to predict the aft region pressure level as well as the pressure plateau extension (see figure 6.17). This is corroborated by the wall-shear stress information where the separation is moved forward when decreasing the turbulent Reynolds number (see figure 6.18). However, it is expected to have a massive separation bubble since the isentropic Mach number distribution shows an incomplete pressure recovery and the wake profile (see figure 6.19) is wide and deep, characteristic of a massive separation. It is believed that the reattachment position assessed with the hot-film sensors is more delicate than the separation one. Indeed, when the level of the pseudo-wall-shear stress reaches a level close to zero, then the boundary

Figure 6.15.: T106C mass-averaged kinetic losses at $Tu_{l,e} = 0.9\%$ - Re_t effectFigure 6.16.: T106C mass-averaged outlet flow angle at $Tu_{l,e} = 0.9\%$ - Re_t effect

layer is considered to have separated. This is the dead air region (see figure 2.5). In the separation bubble, there is the reverse flow vortex that follows the dead air region and which is associated to friction on the wall and consequently to an increase of the pseudo-wall-shear stress. This reverse flow vortex is still part of the separation bubble (see figure 2.5). That is why the determination of the reattachment position should be defined in concordance with the isentropic Mach number distribution.

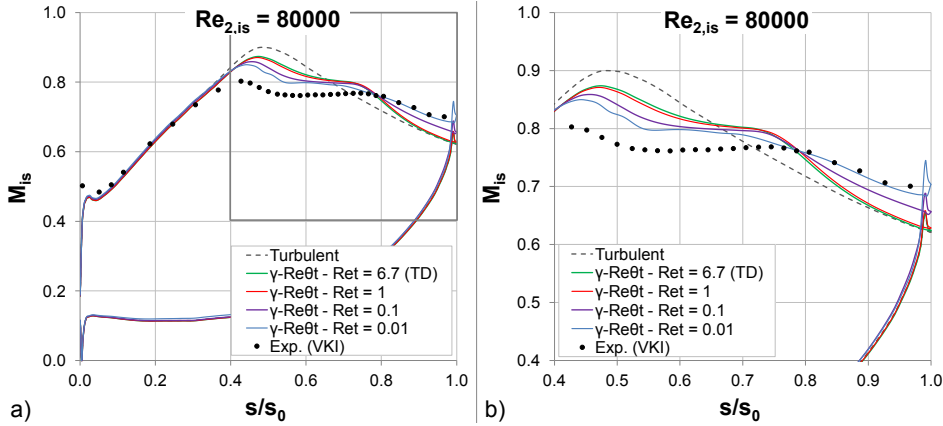


Figure 6.17.: T106C isentropic Mach number distribution at $Re_{2,is} = 80000$ and $Tu_{l,e} = 0.9\%$ - a) Full scale, b) Zoom in the aft region

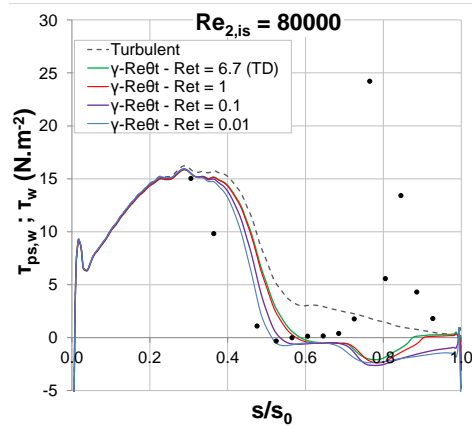


Figure 6.18.: T106C pseudo-wall-shear stress ($\tau_{ps,w}$ from experiment) and wall-shear stress (τ_w from CFD calculation) distributions on the SS at $Re_{2,is} = 80000$ and $Tu_{l,e} = 0.9\%$

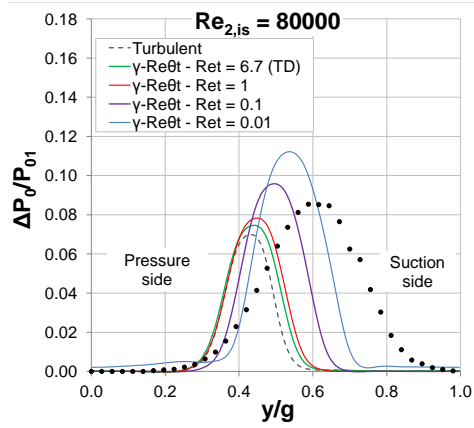


Figure 6.19.: T106C wake profile at $Re_{2,is} = 80000$ and $Tu_{l,e} = 0.9\%$

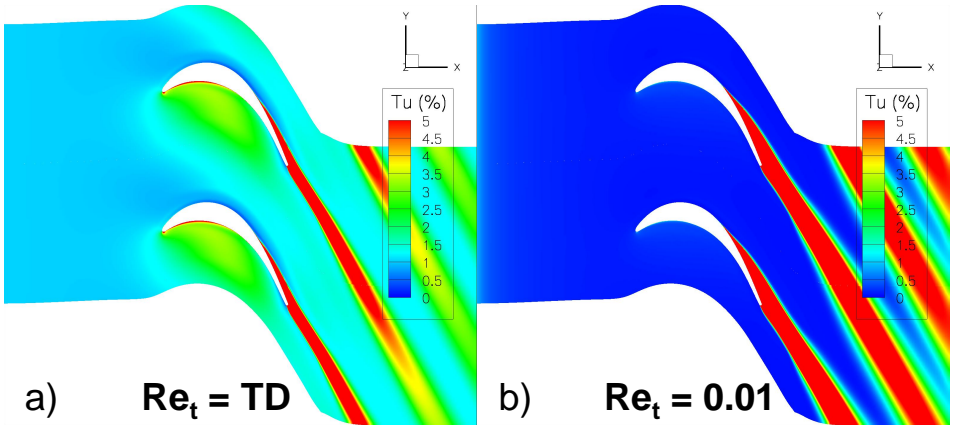


Figure 6.20.: T106C turbulence intensity contours at $Re_{2,is} = 80000$ - a) $Re_t = TD$, b) $Re_t = 0.01$

At $Re_{2,is} = 160000$, the experimental isentropic Mach number distribution features a short bubble type (see figure 6.21). This is retrieved from the $Re_t = TD$ prediction. However, the bubble extension is shorter than expected. This is corroborated by the wall-shear stress information (see figure 6.22). Instead, the wake profile information is well predicted in terms of wake width and depth in comparison to the low turbulent Reynolds number approach (see figure 6.23).

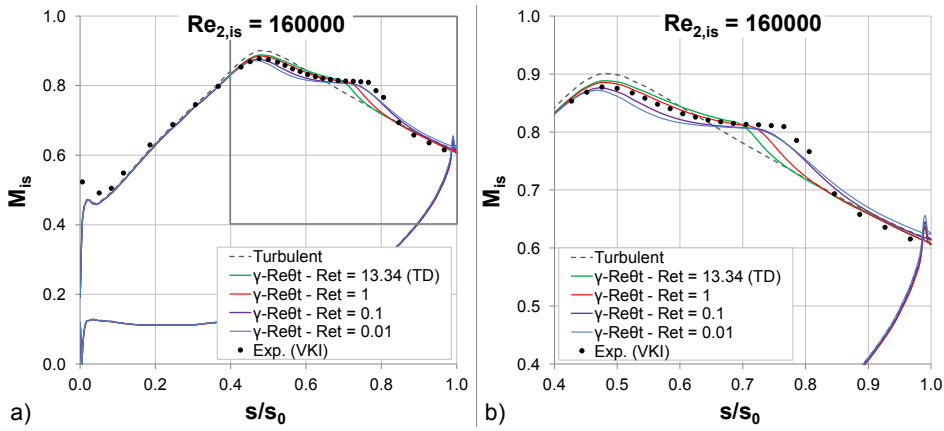


Figure 6.21.: T106C isentropic Mach number distribution at $Re_{2,is} = 160000$ and $Tu_{l.e.} = 0.9\%$ - a) Full scale, b) Zoom in the aft region

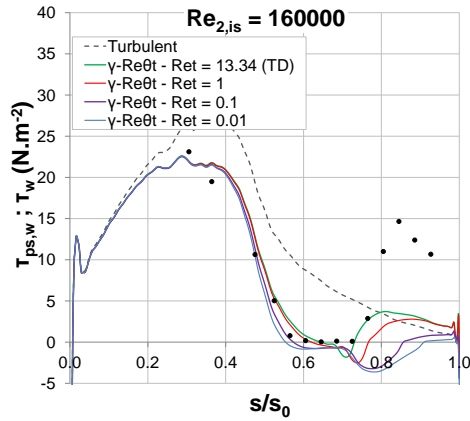


Figure 6.22.: T106C pseudo-wall-shear stress ($\tau_{ps,w}$ from experiment) and wall-shear stress (τ_w from CFD calculation) distributions on the SS at $Re_{2,is} = 160000$ and $Tu_{l.e.} = 0.9\%$

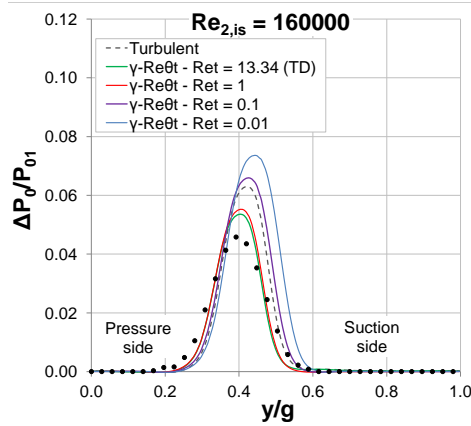


Figure 6.23.: T106C wake profile at $Re_{2,is} = 160000$ and $Tu_{l.e.} = 0.9\%$

Table 6.5.: T106C LPT blade working conditions at a turbulence intensity of 1.8%

Blade	T106C
Ψ	1.24
g/c	0.95
Loading	Aft
D_R	0.58
$M_{2,is}$	0.65
$Re_{2,is} (\times 10^3)$	[80 ; 160]
$Tu_{l.e.}(\%)$	1.8
Re_t	[10.5 ; 21.0]
Facility	S1

6.2.2. T106C LPT blade test case: Turbulence generated by a grid (1.8%)

The introduction of a turbulence grid allows to set different turbulence intensity levels at the leading edge plane of the cascade. The working conditions at a turbulence intensity of 1.8% are displayed in table 6.5.

The mass-averaged kinetic losses and outlet flow angle are displayed in figures 6.24 and 6.25. The numerical predictions are in good agreement down to $Re_{2,is} = 100000$. At $Re_{2,is} = 80000$, the model fails to predict the separation bubble extension (see figures 6.26 and 6.27). Indeed, there is a pressure plateau and a reattachment. Moreover, the predicted wake profile is too narrow which confirms the underprediction of the separation bubble on the suction side (see figure 6.28).

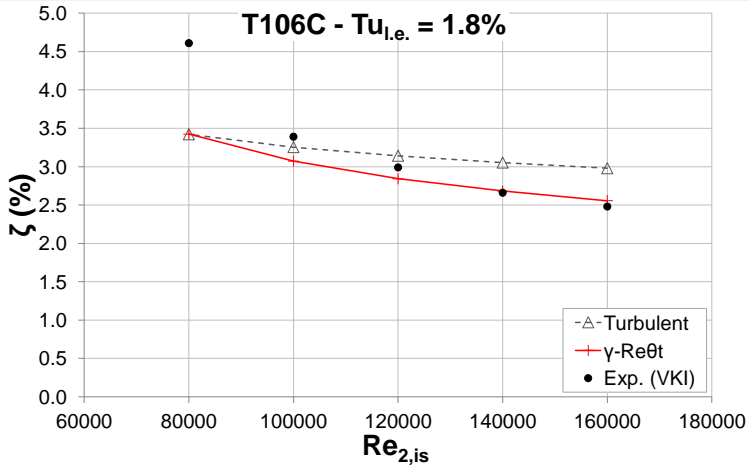


Figure 6.24.: T106C mass-averaged kinetic losses at $Tu_{l.e.} = 1.8\%$

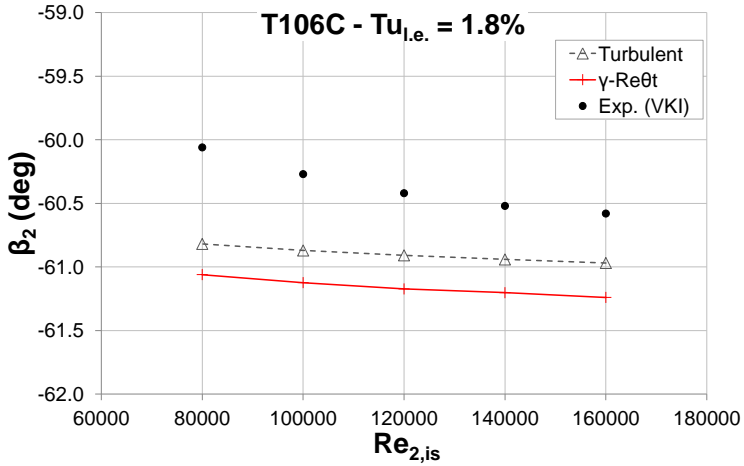


Figure 6.25.: T106C mass-averaged outlet flow angle at $Tu_{l.e.} = 1.8\%$

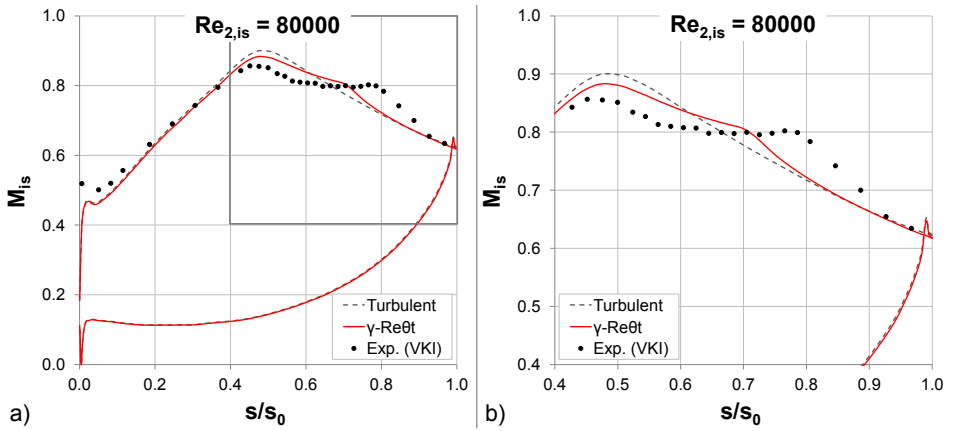


Figure 6.26.: T106C isentropic Mach number distribution at $Re_{2,is} = 80000$ and $Tu_{l.e.} = 1.8\%$ - a) Full scale, b) Zoom in the aft region

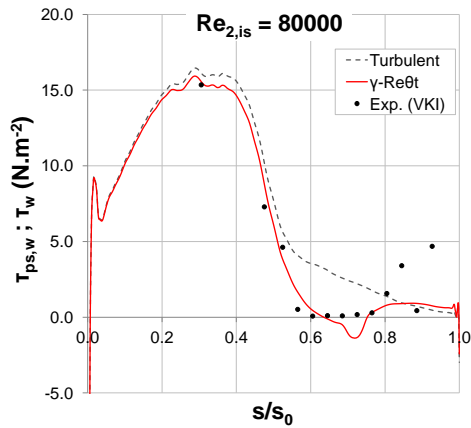


Figure 6.27.: T106C pseudo-wall-shear stress ($\tau_{ps,w}$ from experiment) and wall-shear stress (τ_w from CFD calculation) distributions on the SS at $Re_{2,is} = 80000$ and $Tu_{l.e.} = 1.8\%$

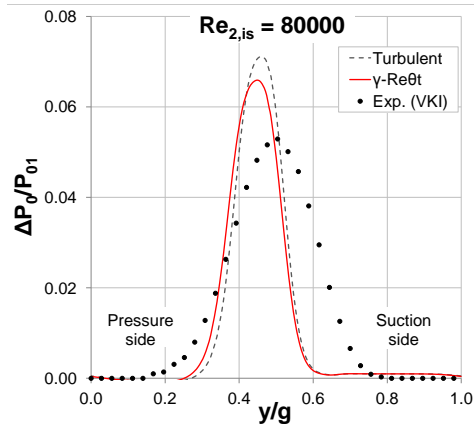


Figure 6.28.: T106C wake profile at $Re_{2,is} = 80000$ and $Tu_{l.e.} = 1.8\%$

6.3. T2 LPT blade test case

The T2 blade is a high diffusion blade. The blade design is illustrated in figure 6.29 in a linear cascade configuration. This is an aft-loaded high-lift LPT blade specifically designed at the von Karman Institute for Fluid Dynamics in the frame of the European programme UTAT [68]. It is based on the same velocity triangles as of the T106C and its design guidelines were to maximise the pitch-to-chord ratio, maintaining the same acceleration along the front suction side but limiting the maximum surface Mach number for subsonic conditions. The main change, in comparison to the T106C, was the increased diffusion rate along the rear suction side [68].

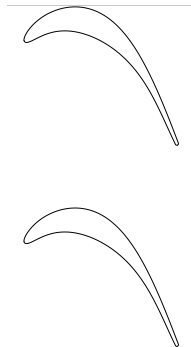


Figure 6.29.: T2 cascade

The mesh information is provided in table 6.6.

Table 6.6.: T2 LPT blade mesh information

Blade	T2
Number of {nodes ; cells} in one streamwise layer	{70601 ; 69280}
Minimum orthogonality (deg)	30.3
Number of cells in orthogonality interval: [27 deg ; 36 deg[in one streamwise layer	771
Maximum expansion ratio	1.72
Maximum y^+ on the blade {SS ; PS}	{0.26 ; 0.23}
Number of nodes around the blade	393
Number of nodes on the blade SS	254

The T2 blade was assessed at the natural freestream turbulence intensity of the facility. The working conditions are displayed in table 6.7.

The T2 blade is among the most difficult blades of the database as it features a high Zweifel loading coefficient and a high diffusion rate. This means that the diffusion on the aft part of the blade is pretty steep.

At first sight, the standard $Re_t = TD$ approach underpredicts the experimental mass-averaged kinetic losses and outlet flow angle (see figures 6.30 and 6.31) and particularly in catching the massive separation occurring at mid and low $Re_{2,is}$. That is why a study of the turbulent Reynolds number was done in order to improve the predictability of the calculation. According to the T106C study, a value of $Re_t = 0.01$ is kept to simulate a pseudo-laminar flow. Indeed, the aim is to set a developing laminar boundary layer which will be influenced by the adverse pressure gradient in order to trigger a laminar separation. It turns out that the trend of both the mass-averaged kinetic losses and outlet flow angle are acceptable at high and mid $Re_{2,is}$ (down to $Re_{2,is} = 160000$). However, at low $Re_{2,is}$, the kinetic losses and the outlet flow angle predictions could not reach the level of the experiment even though open separation is attained and particularly the pressure plateau level.

Those behaviours are illustrated in the isentropic Mach number and wall-shear stress distributions and wake profile at two isentropic outlet Reynolds numbers (210000 and 120000). At $Re_{2,is} = 210000$, the numerical predictions match well for both Re_t approaches (see figure 6.32). There is no pseudo-wall-shear stress information available. Then, the wake profiles are satisfactory, at least their width (see figure 6.33).

At $Re_{2,is} = 120000$, the experimental results illustrate a massive separation that affects the global isentropic Mach number distribution (see figure 6.34). This is corroborated by the pseudo-wall-shear stress that shows a really low level close to

Table 6.7.: T2 LPT blade working conditions at the natural freestream turbulence intensity

Blade	T2
Ψ	1.46
g/c	1.05
Loading	Aft
D_R	0.67
$M_{2,is}$	0.65
$Re_{2,is} (\times 10^3)$	[100 ; 250]
$Tu_{l.e.} (\%)$	0.9
Re_t	[8.8 ; 22.0]
Facility	S1

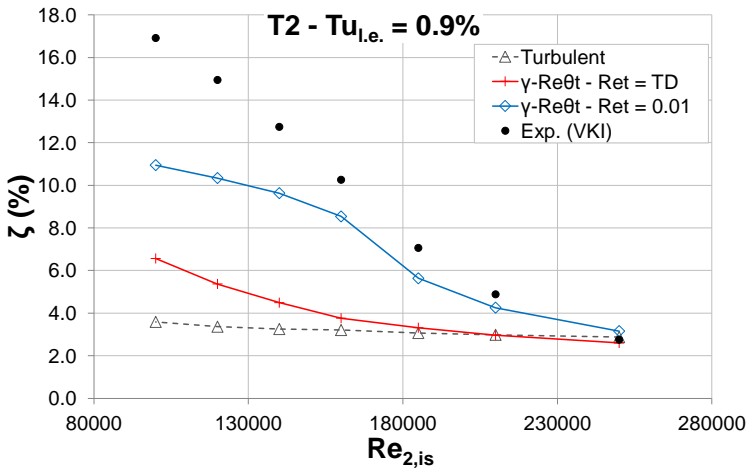
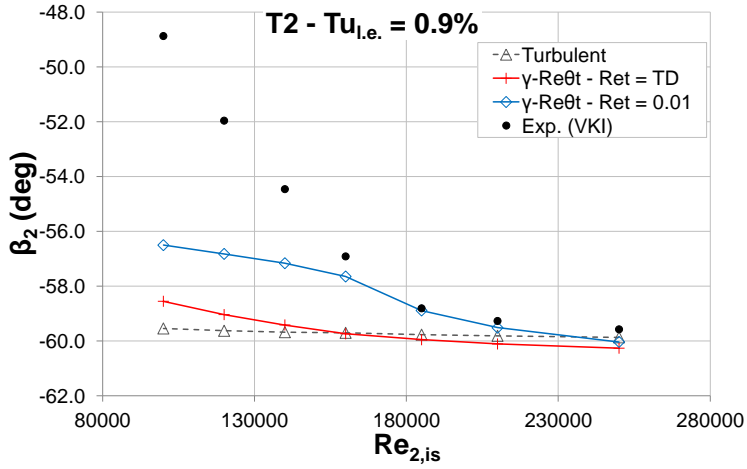
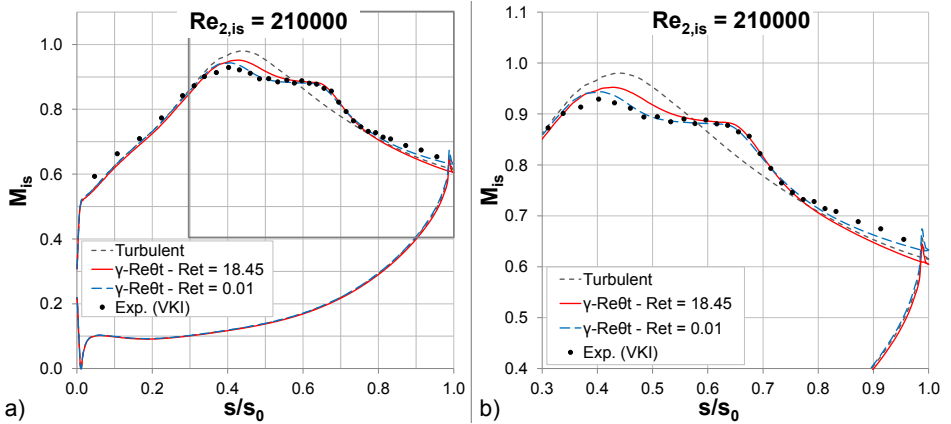


Figure 6.30.: T2 mass-averaged kinetic losses at $Tu_{l.e.} = 0.9\%$

Figure 6.31.: T2 mass-averaged outlet flow angle at $Tu_{l.e.} = 0.9\%$ Figure 6.32.: T2 isentropic Mach number distribution at $Re_{2,is} = 210000$ and $Tu_{l.e.} = 0.9\%$ - a) Full scale, b) Zoom in the aft region

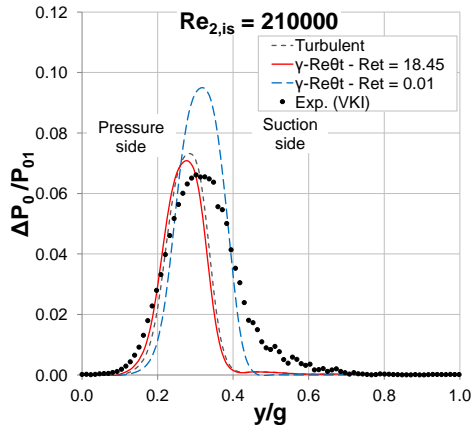


Figure 6.33.: T2 wake profile at $Re_{2,is} = 210000$ and $Tu_{l.e.} = 0.9\%$

zero (see figure 6.35). The numerical $Re_t = 0.01$ isentropic Mach number prediction succeeds to reach the pressure plateau level but could not succeed to predict the level of the peak Mach number. However, the wall-shear stress successfully predicts the separation position. Concerning the wake profile, the under-turning of the flow is well retrieved when the $Re_t = 0.01$ -approach is applied (see figure 6.36). Indeed, the wake is shifted towards the suction side at $Re_t = 0.01$ but still cannot catch the experimental wake shift.

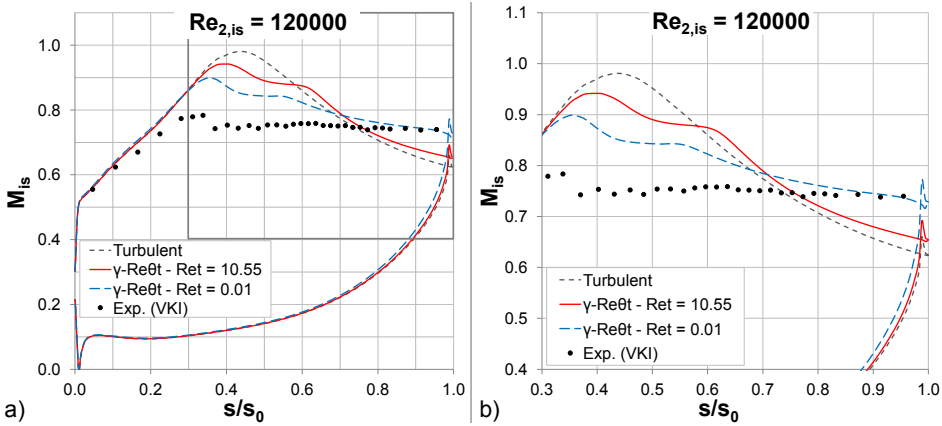


Figure 6.34.: T2 isentropic Mach number distribution at $Re_{2,is} = 120000$ and $Tu_{l.e.} = 0.9\%$ - a) Full scale, b) Zoom in the aft region

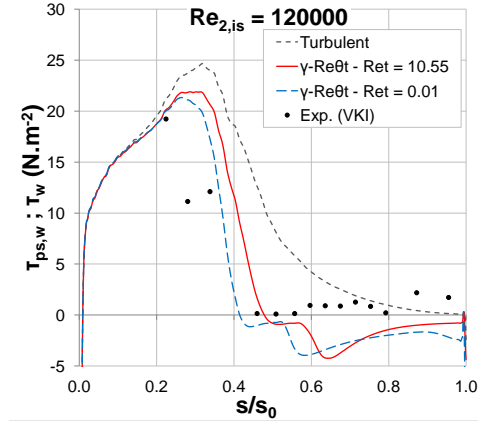


Figure 6.35.: T2 pseudo-wall-shear stress ($\tau_{ps,w}$ from experiment) and wall-shear stress (τ_w from CFD calculation) distributions on the SS at $Re_{2,is} = 120000$ and $Tu_{l.e.} = 0.9\%$

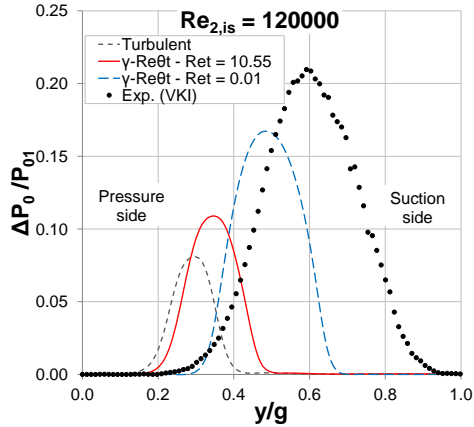


Figure 6.36.: T2 wake profile at $Re_{2,is} = 120000$ and $Tu_{l.e.} = 0.9\%$

6.4. HIVK_LS LPT blade test case

The HIVK_LS blade is a high diffusion blade. The blade design is illustrated in figure 6.37 in a linear cascade configuration. This blade is the low-speed version of the HIVK_HS blade studied by Coton during his PhD thesis [16]. This is a flat roof top ultra-high-lift LPT blade. The low-speed design was commissioned in order to conserve the pressure gradient evolution along the blade suction side. Moreover, the purpose of this low-speed investigation is to assess the incidence effect and the secondary flows in an easier way than in the CT2 facility [16].

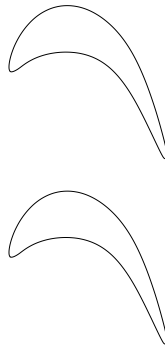


Figure 6.37.: HIVK_LS cascade

The mesh information is provided in table 6.8.

Table 6.8.: HIVK_LS LPT blade mesh information

Blade	HIVK_LS
Number of {nodes ; cells} in one streamwise layer	{59225 ; 58032}
Minimum orthogonality (deg)	15
Number of cells in orthogonality intervals: {[9 deg ; 18 deg] ; [18 deg ; 27 deg] ; [27 deg ; 36 deg]}	{654 ; 1583 ; 2067}
Maximum expansion ratio	1.58
Maximum y^+ on the blade {SS ; PS}	{0.35 ; 0.34}
Number of nodes around the blade	377
Number of nodes on the blade SS	285

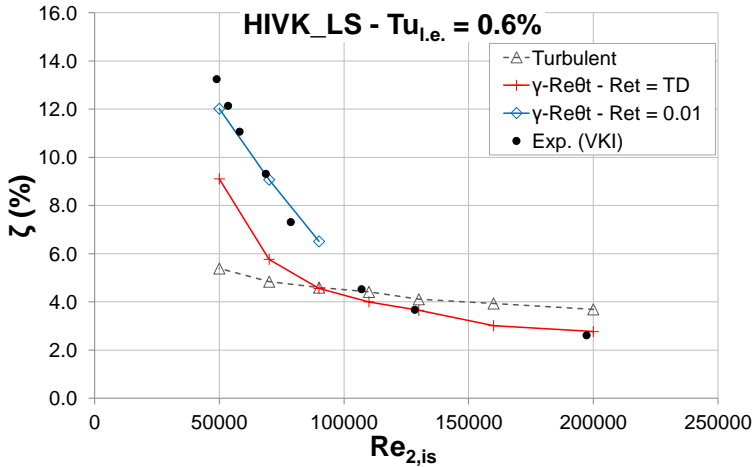
The HIVK_LS blade was assessed at the natural freestream turbulence intensity of the facility. The working conditions at which the HIVK_LS blade was evaluated are displayed in table 6.9.

The HIVK_LS blade is the only low-speed blade investigated in this thesis. The

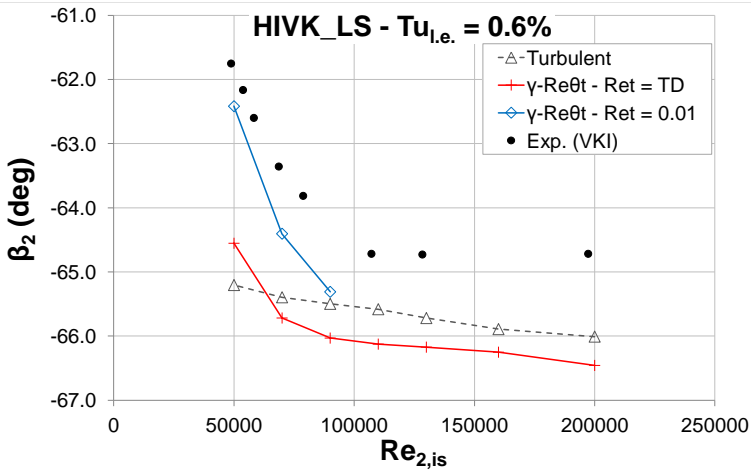
Table 6.9.: HIVK_LS LPT blade working conditions at the natural freestream turbulence intensity

Blade	HIVK_LS
Ψ	1.48
g/c	1.05
Loading	Flat roof top
D_R	0.74
$M_{2,is}$	LS
$Re_{2,is} (\times 10^3)$	[50 ; 200]
$Tu_{l.e.} (%)$	0.6
Re_t	[6.4 ; 25.5]
Facility	C1

Zweifel loading coefficient and the diffusion rate are relatively high. Therefore, a separation phenomenon is expected through the isentropic outlet Reynolds number range. The mass-averaged kinetic losses and outlet flow angle are displayed in figures 6.38 and 6.39. The numerical predictions of the $Re_t = TD$ -approach are within the uncertainty range at high and mid $Re_{2,is}$. Nevertheless, at low $Re_{2,is}$, the increase in the kinetic losses and the outlet flow angle trends is present which illustrates the presence of a long separation/massive separation phenomenon. To improve the prediction, the $Re_t = 0.01$ -approach is used and gives a fairly good agreement with the experimental results.

Figure 6.38.: HIVK_LS mass-averaged kinetic losses at $Tu_{l.e.} = 0.6\%$

The static pressure around the blade was measured during the experimental cam-


 Figure 6.39.: HIVK_LS mass-averaged outlet flow angle at $Tu_{l.e.} = 0.6\%$

paings. This information is presented as a pressure coefficient C_p for two isentropic outlet Reynolds numbers (130000 and 50000) in figure 6.40. The atmospheric pressure P_{atm} is set at the exit of the cascade [16].

$$C_p = \frac{P_{01} - P_{wall}}{P_{01} - P_2} = \frac{P_{01} - P_{wall}}{P_{01} - P_{atm}} \quad (6.1)$$

At $Re_{2,is} = 130000$, the predictions are in good agreement with the measurements. The accelerating part of the suction side as well as the pressure recovery in the aft region are in good agreement. Likewise, the pressure side information is well predicted. The $Re_t = TD$ approach is able to represent correctly the separation phenomenon from the pressure distribution (from the velocity peak until the pressure plateau). The extension of the pressure plateau is not well retrieved at $Re_{2,is} = 50000$. However, the pressure recovery is not totally completed as the experimental result and the transition prediction do not recover the pressure level close to the trailing edge of the fully turbulent calculation. Indeed, from this fully turbulent case, one does not expect any separation bubble. Even though the mass-averaged kinetic losses trend features an increase at low $Re_{2,is}$, the $Re_t = 0.01$ approach is used to extend the pressure plateau. It turns out that the separation phenomenon is over-predicted from the pressure coefficient distribution as the pressure plateau is longer than the experimental result and the separation bubble corresponds to a massive separation. In spite of these facts, the mass-averaged kinetic losses and outlet flow angle are close to the experimental results.

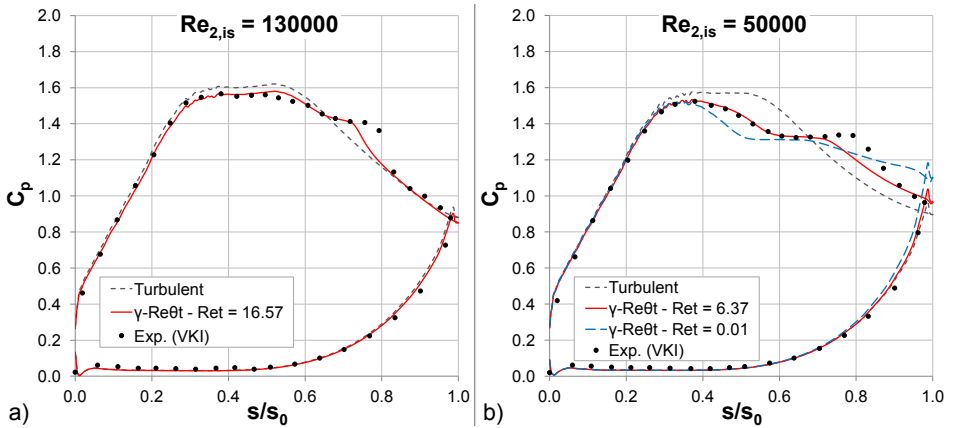


Figure 6.40.: HIVK_LS pressure coefficient on the blade suction side at $Tu_{l.e.} = 0.6\%$ - a) $Re_{2,is} = 130000$ and b) $Re_{2,is} = 50000$

6.5. HIVK_HS LPT blade test case

The HIVK_HS blade is a high diffusion blade. The blade design is illustrated in figure 6.41 in a linear cascade configuration. This is a flat roof top ultra-high-lift LPT blade which was assessed in the frame of Coton's PhD thesis [16]. The CFD investigations were carried out at the natural freestream turbulence intensity of the facility. An investigation at a higher turbulence intensity (3.5%) was carried out and did not show confidence in predicting the flow topology. As a consequence, the high turbulence level predictions are not discussed (see the explanations in appendix A.4).

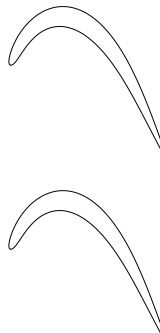


Figure 6.41.: HIVK_HS cascade

The mesh information is provided in table 6.10. The values of the dimensionless

Table 6.10.: HIVK_HS LPT blade mesh information

Blade	HIVK_HS
Number of {nodes ; cells} in one streamwise layer	{70541 ; 69184}
Minimum orthogonality (deg)	21.1
Number of cells in orthogonality intervals: {[18 deg ; 27 deg[; [27 deg ; 36 deg[} in one streamwise layer	{1079 ; 2019}
Maximum expansion ratio	1.55
Maximum y^+ on the blade {SS ; PS}	{1.42 ; 1.01}
Number of nodes around the blade	417
Number of nodes on the blade SS	313

Table 6.11.: HIVK_HS LPT blade working conditions at the natural freestream turbulence intensity

Blade	HIVK_HS
Ψ	1.50
g/c	1.05
Loading	Flat roof top
D_R	1.01
$M_{2,is}$	~ 0.75
$Re_{2,is} (\times 10^3)$	[90 ; 600]
$Tu_{l.e.} (\%)$	0.8
Re_t	[14.7 ; 112.1]
Facility	CT2

wall distance, y^+ , (slightly over 1) correspond to the highest isentropic outlet Reynolds number working conditions. Otherwise, for the other isentropic outlet Reynolds numbers, the y^+ is below 1. The working conditions at which the HIVK_HS blade was evaluated are displayed in table 6.11.

The HIVK_HS blade is the most difficult blade of the database as it features the highest Zweifel loading coefficient and the highest diffusion rate. This means that the diffusion on the aft part of the blade is very steep. Interestingly, this is the only blade which was assessed on a wide $Re_{2,is}$ range, covering cruise and take-off conditions.

At first sight, the standard $Re_t = TD$ approach underpredicts the experimental area-averaged kinetic losses and outlet flow angle (see figures 6.42 and 6.43) and particularly fails in catching the massive separation occurring at mid and low $Re_{2,is}$. That is why the $Re_t = 0.01$ approach is used to improve the predictability. Indeed, the aim is to set a developing laminar boundary layer which will be influ-

enced by the adverse pressure gradient in order to trigger a laminar separation. It turns out that the trend of both the area-averaged kinetic losses and outlet flow angle are acceptable at high and mid $Re_{2, is}$. However, at low $Re_{2, is}$, the kinetic losses and the outlet flow angle predictions could not reach the level of the experiment.

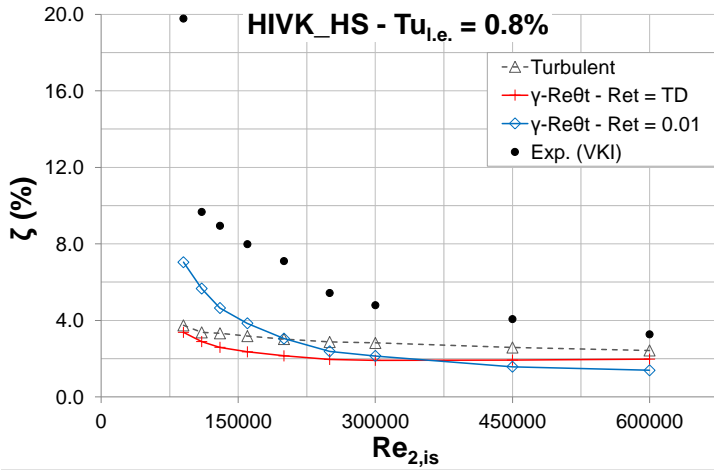


Figure 6.42.: HIVK_HS area-averaged kinetic losses at $Tu_{l.e.} = 0.8\%$

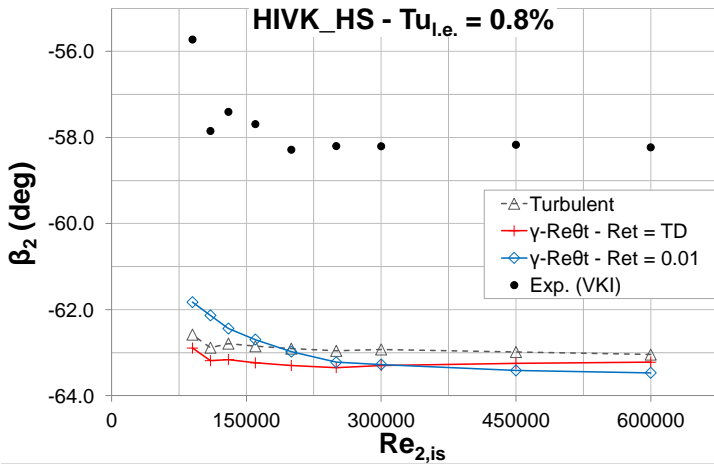


Figure 6.43.: HIVK_HS area-averaged outlet flow angle at $Tu_{l.e.} = 0.8\%$

Coton [16] commented on the higher kinetic losses level and consequently the lower outlet flow angle. Indeed, the desired value that he provided was around -62 de-

grees. This is what is obtained from the present numerical simulations. Instead the experimental values are below -58 degrees. This difference could not be explained by the measurement uncertainty. Coton [16] pointed out that there is a mismatching of the working conditions. The isentropic outlet Mach number is slightly higher than the desired value (0.75 instead of 0.7). It was already stressed that the isentropic outlet Mach number influences the losses for a fixed isentropic outlet Reynolds number (see section 3.3). Knowing this issue, the numerical investigations were set in accordance with the isentropic outlet Mach and Reynolds numbers as reported by the experimentalist during his test campaigns. Nevertheless, it is believed that the kinetic losses and the outlet flow angle experimental values present an offset [4]. Indeed, there is more confidence in their trend than the absolute values [4].

The heat transfer coefficient h for two isentropic outlet Reynolds numbers (450000 and 90000) are presented in figures 6.44 and 6.45 along with the isentropic Mach number distribution around the blade, even though there is no experimental data for the latter. This isentropic Mach number distribution is provided to support and give a better understanding of the heat transfer coefficient information.

At $Re_{2,is} = 450000$, the heat transfer coefficient numerical predictions follow well the laminar extent of the boundary layer in the front part of the blade (see figure 6.44a). Then, the $Re_t = TD$ approach fails to predict the separation as visible from the experiments. Indeed, the transition starts at $s/s_0 = 0.5$ without any separation. This is corroborated by the isentropic Mach number distribution (see figure 6.44b). The $Re_t = 0.01$ approach is able to predict a short separation bubble type (see figure 6.44b) with the characteristic inflection point close to the minimum value of h . However, the separation (from the numerical information) is shifted downstream in comparison to the separation evaluated experimentally. The level of the turbulent heat transfer coefficient is in a fairly good agreement, even though it is delayed. Besides, the gradient of the heat transfer coefficient rise at transition is similar to the experimental one. From this investigation, one can see that the low turbulent Reynolds number approach is able to give a good evolution of the heat transfer coefficient (in terms of level) but fails to predict the separation position.

At $Re_{2,is} = 90000$, both the heat transfer coefficient predictions ($Re_t = TD$ and $Re_t = 0.01$ approaches) show a separation that is shifted downstream in comparison to the experimental result (see figure 6.45). The $Re_t = TD$ approach features a small bubble type (see figure 6.45b) in comparison to the $Re_t = 0.01$ approach which features a long bubble/massive separation type (the pressure recovery is not complete as there is no reattachment of the flow, but the peak Mach number is not so affected by the long bubble). Indeed, the experimental result shows a slightly earlier separation (around $s/s_0 = 0.45$) with a smooth increase of h , depicting a longer transitional zone and a non-reattached boundary layer. From the experimental information (heat transfer coefficient, mass-averaged kinetic losses and

outlet flow angle), it is expected that the boundary layer experiences a massive separation, comparable with the $Re_{2,is} = 120000$ T2 case where the isentropic Mach number distribution was tremendously affected (see figure 6.34). In the HIVK_HS case, the peak Mach number level is not so affected but one has to remember that this blade is a flat roof top configuration. More insight about the interpretation of the heat transfer coefficient distributions is provided in appendix A where other LPT blade investigations in CT2 facility are discussed.

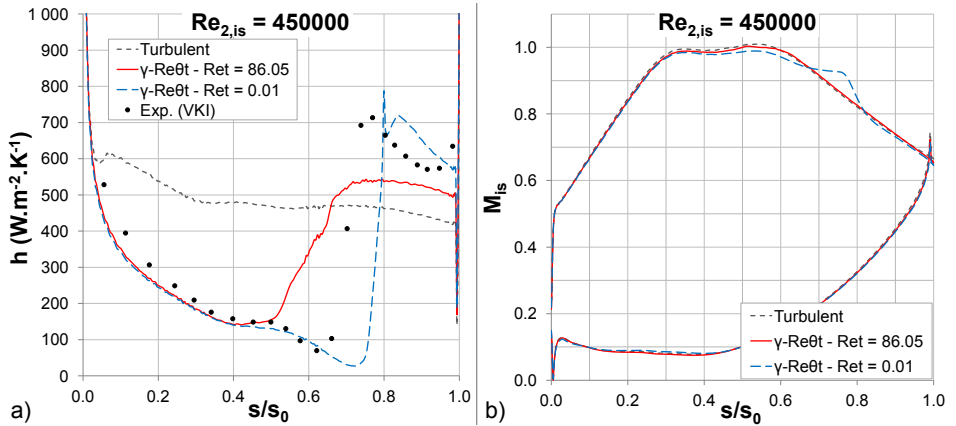


Figure 6.44.: HIVK_HS heat transfer coefficient on the blade suction side (a) and isentropic Mach number distribution (b) at $Re_{2,is} = 450000$ and $Tu_{l.e.} = 0.8\%$

6.6. TX LPT blade test case

The TX blade is a mild diffusion blade. The blade design is illustrated in figure 6.46 in a linear cascade configuration. This is an aft-loaded LPT blade. This blade was assessed at two turbulence levels (0.9%, see section 6.6.1 and 3.2%, see section 6.6.2). The particularity of this test case is the low isentropic outlet Reynolds number that could be set (22000). Indeed, it allows to explore a range where massive separation and long bubble are expected. Moreover, it constitutes challenging working conditions to evaluate the γ - $\tilde{Re}_{\theta t}$ transition model and the methodology presented during this work (see section 5.2).

The mesh information is provided in table 6.12.

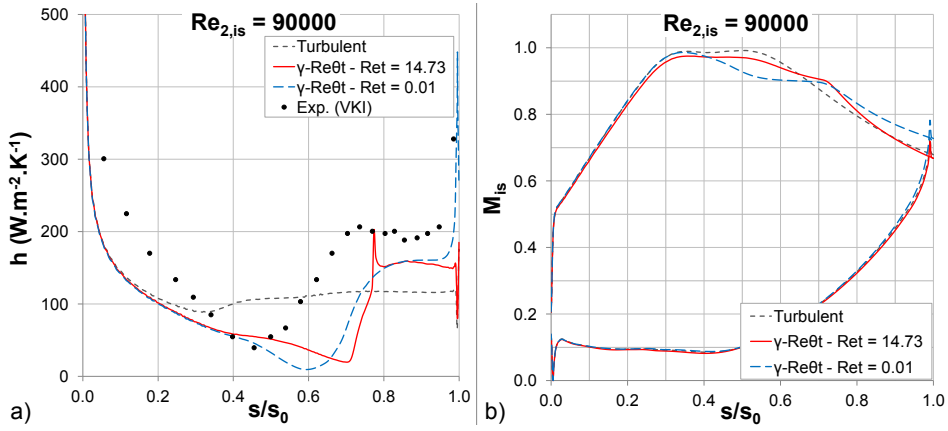


Figure 6.45.: HIVK_HS heat transfer coefficient on the blade suction side (a) and isentropic Mach number distribution (b) at $Re_{2,is} = 90000$ and $Tu_{l.e.} = 0.8\%$

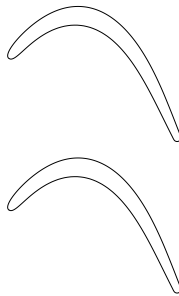


Figure 6.46.: TX cascade

Table 6.12.: TX LPT blade mesh information

Blade	TX
Number of {nodes ; cells} in one streamwise layer	{55061 ; 53888}
Minimum orthogonality (deg)	20.7
Number of cells in orthogonality intervals: {[18 deg ; 27 deg[; [27 deg ; 36 deg[} in one streamwise layer	{1027 ; 2189}
Maximum expansion ratio	1.42
Maximum y^+ on the blade {SS ; PS}	{1.47 ; 1.14}
Number of nodes around the blade	361
Number of nodes on the blade SS	256

Table 6.13.: TX LPT blade working conditions at the natural freestream turbulence intensity

Blade	TX
Ψ	0.95
g/c	N/A
Loading	Aft
D_R	0.50
$M_{2,is}$	0.6
$Re_{2,is} (\times 10^3)$	[22 ; 103]
$Tu_{l.e.}(\%)$	0.9
Re_t	[8.1 ; 40.9]
Facility	S1

6.6.1. TX LPT blade test case: Natural freestream turbulence intensity (0.9%)

The TX blade was assessed at the natural freestream turbulence intensity of the facility. The working conditions at which the TX blade was evaluated are displayed in table 6.13.

The area-averaged kinetic losses (see figure 6.47) and the area-averaged outlet flow angle (see figure 6.48) are non-dimensionalised for confidentiality reasons. The reference is the corresponding experimental value at $Re_{2,is} = 103000$. From those comparisons, one can see the good agreement between the predictions and the experiments. The interesting aspect is the good prediction at very low $Re_{2,is}$. In fact, at those conditions, one might expect a laminar boundary layer which should be prone to massive separation. Since there is no flow information around the blade, the trends of the kinetic losses and the outlet flow angle are important as well as the wake profile to understand the type of separation. That is why an extension of the numerical investigation towards the higher isentropic outlet Reynolds numbers was carried out.

The wake and the outlet flow angle profiles downstream the cascade are provided for two $Re_{2,is}$ (103000, see figure 6.49 and 22000, see figure 6.50). The non-dimensionalization of the wake is done by dividing $\Delta P_0/P_{01}$ by its maximum measured value at $Re_{2,is} = 103000$. The agreement between the experimental results and the predictions is good in terms of wake and outlet flow angle profiles and particularly at $Re_{2,is} = 22000$. In terms of outlet flow angle, both profiles present similar trends with approximately the same mean value but with different levels away from the mean. However, the general trend of the flow angle in a wake is respected. At higher $Re_{2,is}$ (103000), the experimental wake profile seems wider in comparison to the prediction and even less deep. This behaviour is verified to

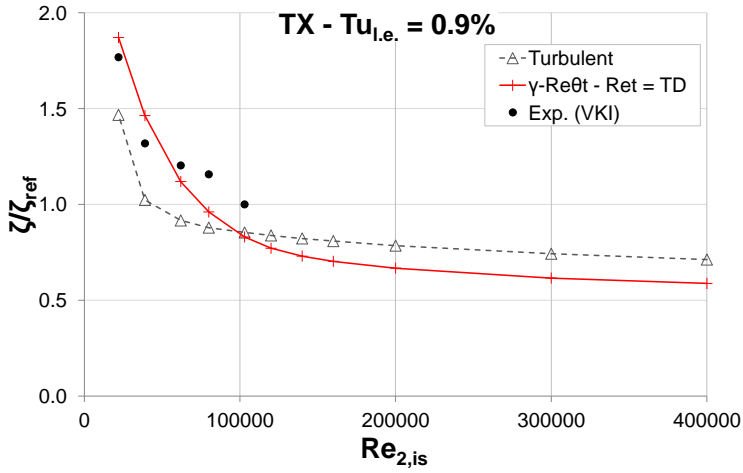


Figure 6.47.: TX area-averaged kinetic losses at $Tu_{l.e.} = 0.9\%$

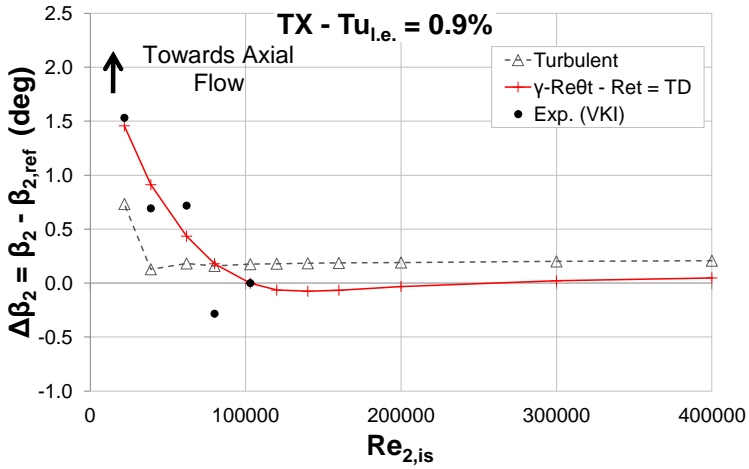


Figure 6.48.: TX area-averaged outlet flow angle at $Tu_{l.e.} = 0.9\%$

be independent of the mesh since a couple of investigations were done to get rid of this dependency. One can explain this aspect by the inherent presence of a large separation bubble on the pressure side. It could extend up to 50% of the pressure side curvilinear abscissa (this was assessed by the numerical wall shear stress, not presented here). The pressure side is defined by a concave surface, which is prone to transition. Thus, from the combination of separation and concave curvature, it was possible to observe from the turbulence intensity and turbulent kinetic energy contours the presence of an extended turbulent region over the whole pressure side for $Re_{2, is} = 103000$. Instead, this turbulent region vanishes for $Re_{2, is} = 22000$ in the rear part of the pressure side. Indeed, the low $Re_{2, is}$ case features a relaminarization due to the low density whereas the higher $Re_{2, is}$ experiences an acceleration as well but seems less prone to a way back to laminar flow. Therefore, a wider wake profile at a high $Re_{2, is}$ could be explained by the presence of a turbulent boundary layer on the pressure side.

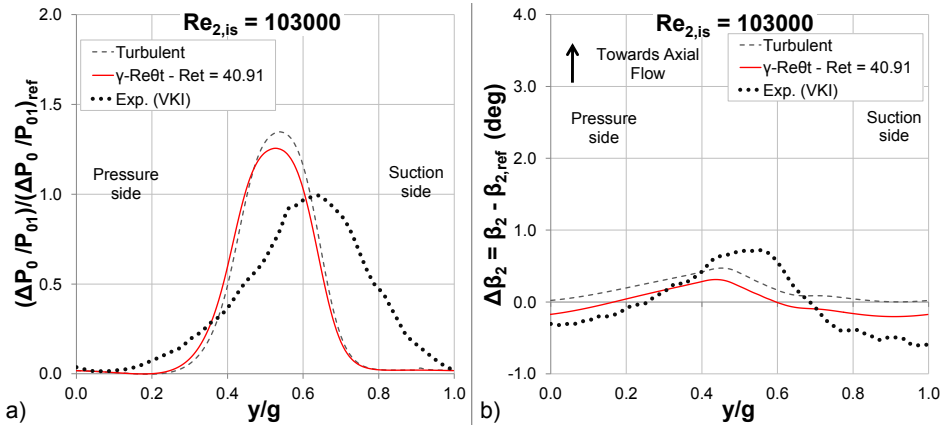


Figure 6.49.: TX wake profile (a) and outlet flow angle profile (b) at $Re_{2, is} = 103000$ and $Tu_{l.e.} = 0.9\%$

6.6.2. TX LPT blade test case: Turbulence generated by a grid (3.2%)

The working conditions at a turbulence intensity of 3.2% are displayed in table 6.14. The area-averaged kinetic losses (see figure 6.51) and the area-averaged outlet flow angle (see figure 6.52) are given. The reference for the non-dimensionalization is the corresponding experimental value at $Re_{2, is} = 104000$. The predictions are in good agreement with the experimental trends. This time, the numerical investigation was not extended to higher $Re_{2, is}$. It was done for the low turbulence intensity case in order to understand and define the bursting region as long bubble

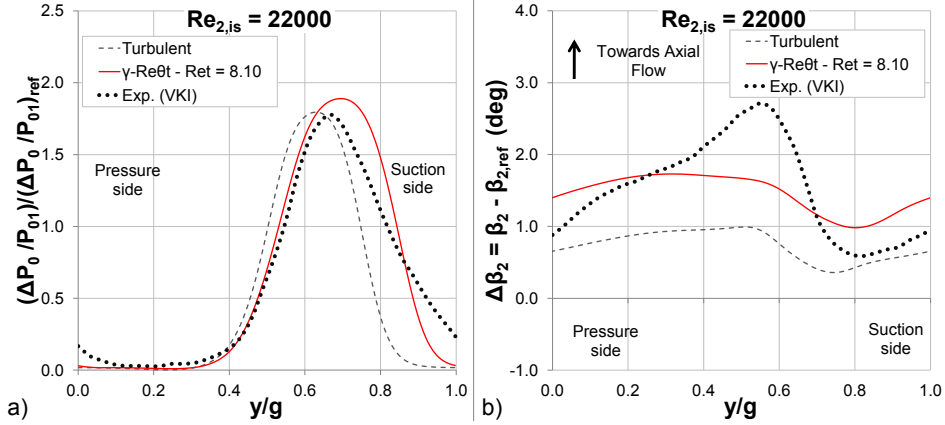


Figure 6.50.: TX wake profile (a) and outlet flow angle profile (b) at $Re_{2,is} = 22000$ and $Tu_{l,e.} = 0.9\%$

Table 6.14.: TX LPT blade working conditions at a turbulence intensity of 3.2%

Blade	TX
Ψ	0.95
g/c	N/A
Loading	Aft
D_R	0.50
$M_{2,is}$	0.6
$Re_{2,is} (\times 10^3)$	[30 ; 104]
$Tu_{l,e.} (\%)$	3.2
Re_t	[28.2 ; 99.1]
Facility	S1

and massive separation are expected. Instead, at high turbulence intensity level, one would expect a by-pass transition with a short bubble type.

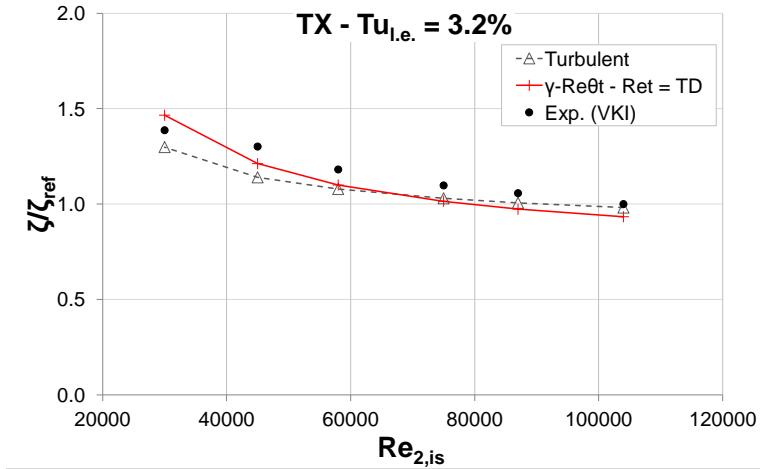


Figure 6.51.: TX area-averaged kinetic losses at $Tu_{l,e.} = 3.2\%$

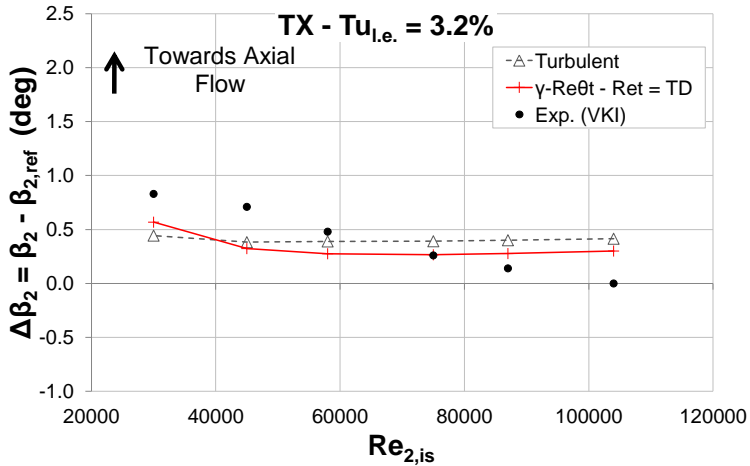


Figure 6.52.: TX area-averaged outlet flow angle at $Tu_{l,e.} = 3.2\%$

The wake and the outlet flow angle profiles downstream of the cascade are provided for two $Re_{2,is}$ (104000, see figure 6.53 and 30000, see figure 6.54). The non-dimensionalization of the wake is done by dividing $\Delta P_0/P_{01}$ by its maximum measured value at $Re_{2,is} = 104000$.

At $Re_{2,is} = 104000$, the predicted wake width is smaller than the experimental one.

As already pointed out for the low turbulence intensity case, there is a separation bubble extending up to 50% of the pressure side curvilinear abscissa (this was assessed by the numerical wall shear stress, not presented here). Moreover, the transition process is hastened by this separation phenomenon associated to the concave surface of the pressure side. At $Re_{2,is} = 30000$, the agreement between the numerical prediction and the experimental result is good for both the wake profile and the outlet flow angle. The width and the depth of the wake are acceptable and the outlet flow angle profile is as expected in a wake.

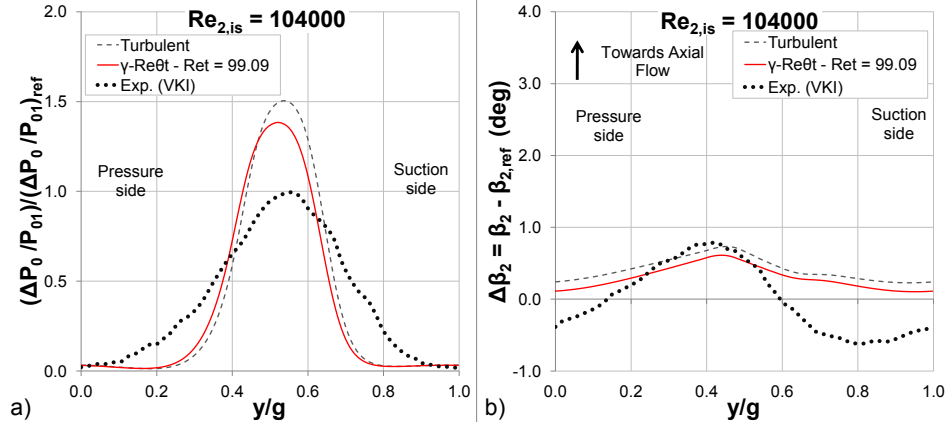


Figure 6.53.: TX wake profile (a) and outlet flow angle profile (b) at $Re_{2,is} = 104000$ and $Tu_{l.e.} = 3.2\%$

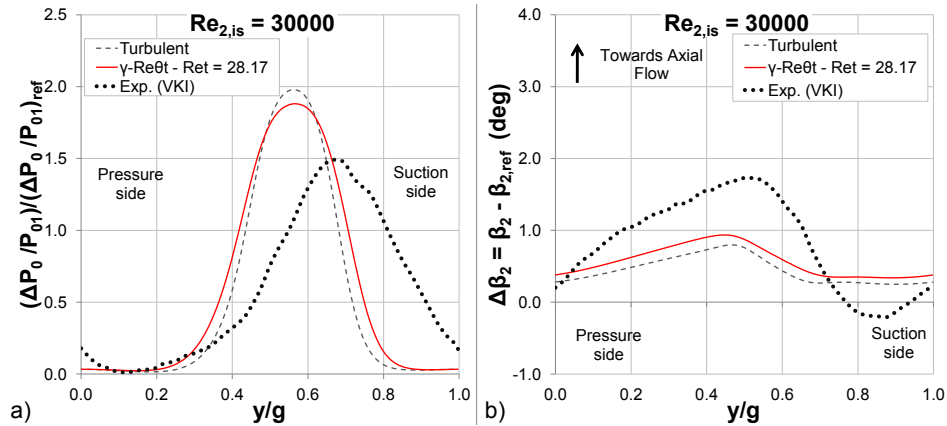


Figure 6.54.: TX wake profile (a) and outlet flow angle profile (b) at $Re_{2,is} = 30000$ and $Tu_{l.e.} = 3.2\%$

6.7. Summary

This chapter constitutes the evaluation of an innovative approach to predict transition with a RANS equation model. The framework of the new transition model ($\gamma\text{-}\widetilde{Re}_{\theta t}$) is well known in the literature and was extensively studied for different types of aerospace applications (both external and internal aerodynamics). However, to the best knowledge of the author, this model has not been studied on a large number of LPT blades. Indeed, one has to remember that the transition model was not calibrated for HL-LPT blades. From the comparisons with the experiments and the fully turbulent predictions, the present CFD methodology gives predictions that are in good agreement with what was measured.

One can conclude that this methodology is reliable in predicting transitional flows on HL-LPT blades with mild diffusion rate. However, it turned out that for HL-LPT blades with high diffusion rate, the predictions are underestimated. Consequently, an adjustment of the methodology was done to predict laminar separation and massive separation that may happen in HL-LPT blade configurations. This adjustment allows to get satisfactory predictions.

Chapter 7.

Investigation of the flow topology with the γ - $\widetilde{Re}_{\theta t}$ transition model

The γ - $\widetilde{Re}_{\theta t}$ transition model turns out to be interesting to predict with a certain confidence experimental measurements at the expenses of an adjustment of the boundary conditions in specific cases.

To better understand the influence of the separation on transition, an investigation of the flow topology is carried out. The main parameters in this study are the transition onset and the separation locations. This information can be extracted from both the numerical and experimental data. The way to define those flow topology parameters is illustrated in section 3.2.

However, the momentum thickness Reynolds number is only accessible via the numerical predictions. That is why, one can compare the momentum thickness Reynolds number at separation and at transition onset with correlations of the open literature.

For separated-flow transition at low turbulence intensity and with uniform upstream boundary conditions (at the natural freestream turbulence intensity of the facility), the correlation of Hatman and Wang [30] is, at the time of writing and to the best knowledge of the author, the most comprehensive correlation for this type of transition. It is an interesting tool to characterise the bursting Reynolds number from the outcomes of the present work predictions and to validate and corroborate the analysis of the experimental database carried out in chapter 4.

For by-pass transition at high turbulence intensities (above 3%) generated by a turbulence grid, the correlations of Abu-Ghannam and Shaw [1], Mayle [52], Hourmouziadis [35] and Steelant and Dick [71] are used to assess the predictions of the γ - $\widetilde{Re}_{\theta t}$ transition model.

7.1. Separated-flow transition at the natural (low) freestream turbulence intensity

In the following plots, the curves designated as “*Onset-Re_t*” represent the numerical transition onset information and the curves designated as “*Sep-Re_t*” represent the numerical separation information while the symbols designated as “*Onset-Exp.*” and “*Sep-Exp.*” represent the experimental transition onset and separation information.

7.1.1. T108 LPT blade test case

The T108 blade predictions were within the measurement uncertainty range in terms of kinetic losses when applying the expected $Re_t = TD$ approach. Again, a break is intentionally present in the plots (see section 3.3). The corresponding transition onset and separation locations through the isentropic outlet Reynolds number range are displayed in figure 7.1. When looking at the separation positions, the predictions follow the trend of the experimental results. Indeed, when decreasing the isentropic outlet Reynolds number, the separation location moves upstream. Moreover, the predictions are slightly underestimated, even though the hot-film sensors discretization over the blade suction side is around 4% of the suction side TE curvilinear abscissa. One can conclude that the predictions are satisfactory. There is a good confidence on the transition onset location as well. As expected, when decreasing the isentropic outlet Reynolds number, the transition onset location, first, moves downstream, then the transition still happens in the free shear layer but moves upstream due to the effect of the earlier separation.

From the investigation of the momentum thickness Reynolds number at separation, one can compare the present predictions with the correlation of Hatman and Wang [30] (see figure 7.2). The intersection between the $Re_{\theta,sep}$ trend and the $Re_{\theta,sep} = 240$ line defines the isentropic outlet Reynolds number at bursting (Re_{2,is_B}). The T108 blade Re_{2,is_B} prediction, assessed with the Hatman and Wang correlation [30], is 115000.

7.1.2. T106C LPT blade test case

The T106C blade predictions were within the measurement uncertainty range in terms of kinetic losses when applying the expected $Re_t = TD$ approach for $Re_{2,is} \geq 120000$ and the $Re_t = 0.01$ approach for $Re_{2,is} < 120000$. The corresponding transition onset and separation locations through the isentropic outlet Reynolds number range are displayed in figure 7.3. When looking at the separation position, the predictions follow the trend of the experiments. Indeed, when

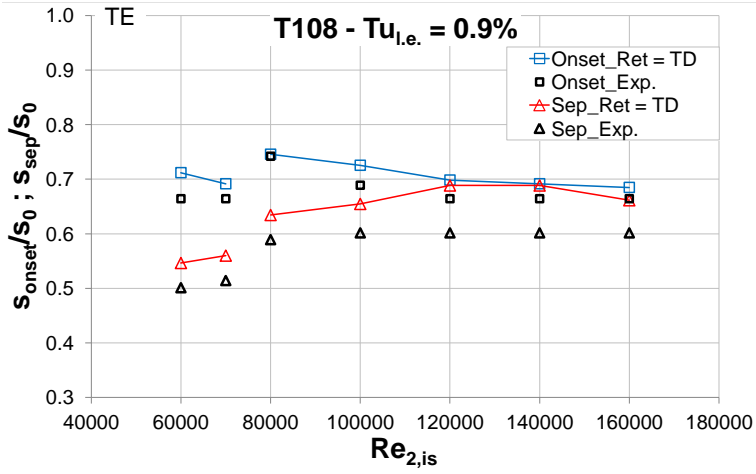


Figure 7.1.: T108 transition onset (s_{onset}/s_0) and separation (s_{sep}/s_0) positions through the $Re_{2,is}$ range at $Tu_{l.e.} = 0.9\%$

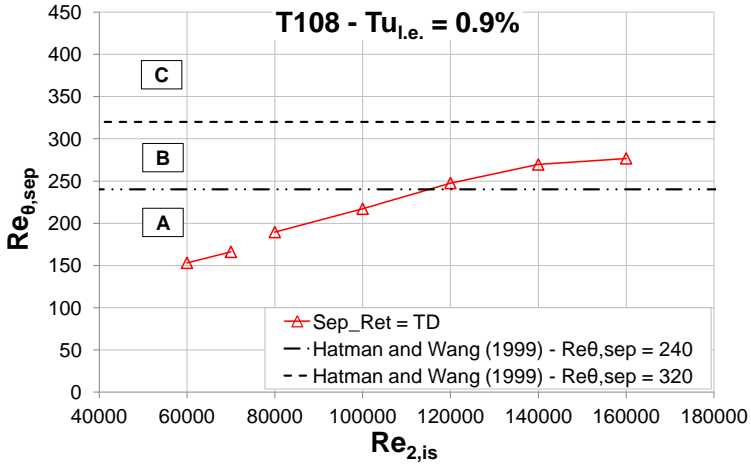


Figure 7.2.: T108 momentum thickness Reynolds number at separation ($Re_{\theta,sep}$) through the $Re_{2,is}$ range at $Tu_{l.e.} = 0.9\%$ - A: Laminar separation - Long bubble region ($Re_{\theta,sep} < 240$); B: Laminar separation - Short bubble region ($240 < Re_{\theta,sep} < 320$); C: Laminar separation - Dominant transitional / Transitional separation region ($Re_{\theta,sep} > 320$)

decreasing the isentropic outlet Reynolds number, the separation location moves upstream. The predictions are satisfactory as they are within the spatial uncertainty range of the hot-film sensors (around 4% of the curvilinear TE suction side abscissa). There is a good confidence on the transition onset locations as well. As expected, when decreasing the isentropic outlet Reynolds number, the transition onset location, first, moves downstream, then the transition still happens in the free shear layer but moves upstream due to the effect of the earlier separation.

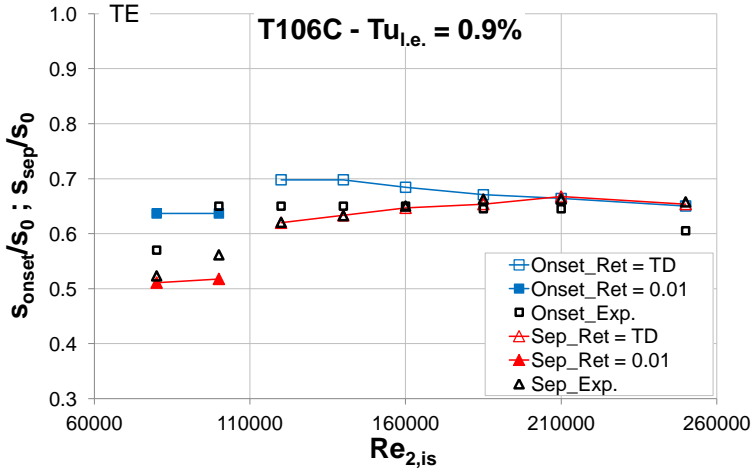


Figure 7.3.: T106C transition onset (s_{onset}/s_0) and separation (s_{sep}/s_0) positions through the $Re_{2,is}$ range at $Tu_{l,e.} = 0.9\%$

The T106C blade Re_{2,is_B} prediction, assessed with the Hatman and Wang correlation [30], is 170000 (see figure 7.4).

7.1.3. T2 LPT blade test case

The T2 blade predictions approach the experimental trend of the kinetic losses only when applying the $Re_t = 0.01$ method for the $Re_{2,is}$ range. The corresponding transition onset and the separation locations through the isentropic outlet Reynolds number range are displayed in figure 7.5. When looking at the separation position, the predictions follow the trend of the experiments. Indeed, when decreasing the isentropic outlet Reynolds number, the separation location moves upstream. The predictions are satisfactory as they are within the spatial uncertainty range of the hot-film sensors (around 4% of the curvilinear TE suction side abscissa). The transition onset location is clearly affected by the separation location as the former moves upstream when decreasing the isentropic outlet

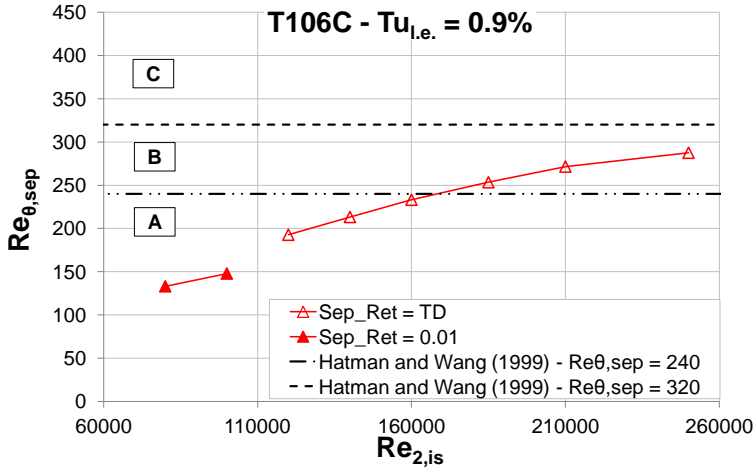


Figure 7.4.: T106C momentum thickness Reynolds number at separation ($Re_{\theta,sep}$) through the $Re_{2,is}$ range at $Tu_{l.e.} = 0.9\%$ - A: Laminar separation - Long bubble region ($Re_{\theta,sep} < 240$) ; B: Laminar separation - Short bubble region ($240 < Re_{\theta,sep} < 320$) ; C: Laminar separation - Dominant transitional / Transitional separation region ($Re_{\theta,sep} > 320$)

Reynolds number. In contrary to the two former cases, the transition onset location does not move downstream when decreasing $Re_{2,is}$ then upstream when decreasing $Re_{2,is}$ further. This illustrates the effect of the massive separation and long bubble types on the transition onset. However, the predictions underestimate the experimental locations (difference of 15% of the curvilinear TE suction side abscissa). Unfortunately, the information, necessary for the evaluation of the transition onset location from the experiments, was not available for $Re_{2,is} > 160000$. Moreover, the evaluation of the transition onset from the experiments is open to discussion. Indeed, for $Re_{2,is} \leq 160000$, the transition onset location is ahead of the separation location. However, they are within the spatial uncertainty of the hot-film sensors. They may be close to each other. One reason might be the tremendous influence of the massive separation at those isentropic outlet Reynolds numbers that induces step disturbances at the inception of the boundary layer separation. Consequently, these disturbances are the roots of the transition. As a comparison, the T106C (see figure 7.3) experiences a slightly similar behaviour at $Re_{2,is} = 80000$ (where massive separation was encountered). The transition onset location moved closer to the separation location.

The T2 blade Re_{2,is_B} prediction, assessed with the Hatman and Wang correlation [30], is 240000 (see figure 7.6).

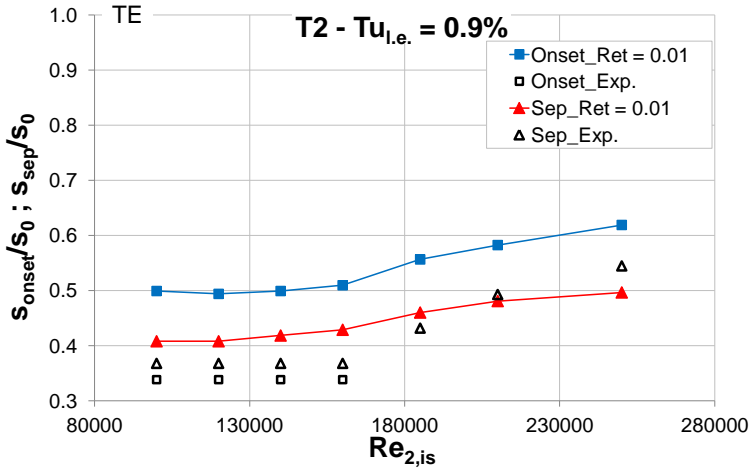


Figure 7.5.: T2 transition onset (s_{onset}/s_0) and separation (s_{sep}/s_0) positions through the $Re_{2,is}$ range at $Tu_{l.e.} = 0.9\%$

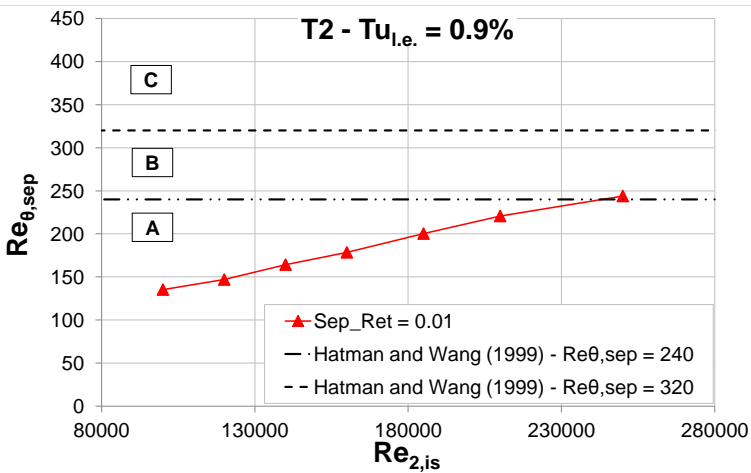


Figure 7.6.: T2 momentum thickness Reynolds number at separation ($Re_{\theta,sep}$) through the $Re_{2,is}$ range at $Tu_{l.e.} = 0.9\%$ - A: Laminar separation - Long bubble region ($Re_{\theta,sep} < 240$) ; B: Laminar separation - Short bubble region ($240 < Re_{\theta,sep} < 320$) ; C: Laminar separation - Dominant transitional / Transitional separation region ($Re_{\theta,sep} > 320$)

7.1.4. HIVK_LS LPT blade test case

The HIVK_LS blade predictions were within the measurement uncertainty range in terms of kinetic losses when applying the expected $Re_t = TD$ approach for $Re_{2,is} \geq 110000$ and the $Re_t = 0.01$ approach for $Re_{2,is} < 110000$. The corresponding transition onset and separation locations through the isentropic outlet Reynolds number range are displayed in figure 7.7. When looking at the separation position, the predictions follow the trend of the experiments. Indeed, when decreasing the isentropic outlet Reynolds number, the separation location moves upstream. One has to stress that the separation positions were determined thanks to the pressure coefficient distributions. Consequently, the evaluation may not be as precise as the hot-film sensors information. The predictions are satisfactory as they are within the spatial uncertainty range of the pressure taps (around 4% of the curvilinear TE suction side abscissa) for $Re_{2,is} \geq 110000$. For $Re_{2,is} < 110000$, the predictions are overestimated as they are predicted earlier than the experiments. However, considering the technique to evaluate the separation location from the experiments, one has to put more emphasis on the trend. Indeed, the trend is satisfying. The transition onset location could not be determined from the experiments as there is no reliable information. Instead, the predictions still feature the typical effect of the separation which is the upstream movement of the transition onset.

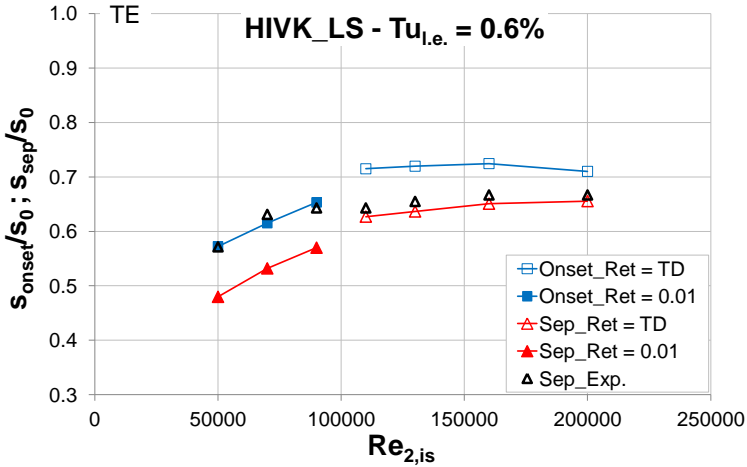


Figure 7.7.: HIVK_LS transition onset (s_{onset}/s_0) and separation (s_{sep}/s_0) positions through the $Re_{2,is}$ range at $Tu_{l.e.} = 0.6\%$

The HIVK_LS blade Re_{2,is_B} prediction, assessed with the Hatman and Wang correlation [30], is 100000 (see figure 7.8). The results of Coton [16] are displayed as “*Sep_Coton (2003)*”. The integral parameters (particularly the momentum

thickness at separation) could not be measured in the facility because of the reduced dimensions of the blade passage. The integral parameters were then obtained from a boundary layer code which input was the measured velocity distribution [16]. When comparing the predictions of Coton [16] and the predictions of the present work, they match well at low isentropic outlet Reynolds numbers ($Re_{2,is} \leq 90000$). For $Re_{2,is} > 90000$, there is an overestimation of the momentum thickness Reynolds number at separation predicted in the present work. However, the offset is constant and the trend is correct.

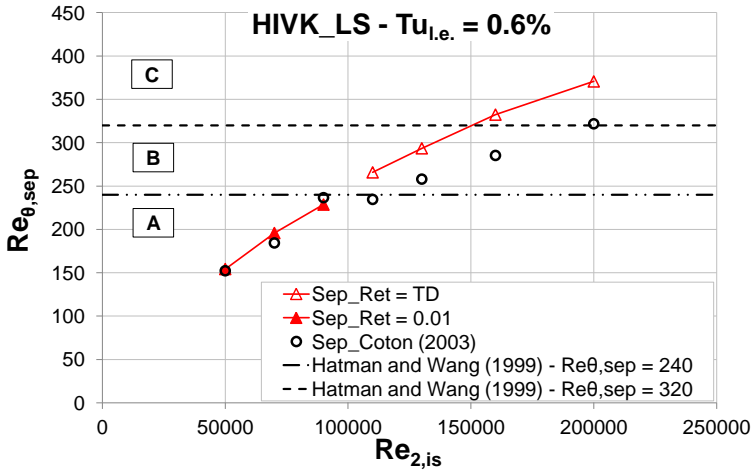


Figure 7.8.: HIVK_LS momentum thickness Reynolds number at separation ($Re_{\theta,sep}$) through the $Re_{2,is}$ range at $Tu_{l.e.} = 0.6\%$ - A: Laminar separation - Long bubble region ($Re_{\theta,sep} < 240$) ; B: Laminar separation - Short bubble region ($240 < Re_{\theta,sep} < 320$) ; C: Laminar separation - Dominant transitional / Transitional separation region ($Re_{\theta,sep} > 320$)

7.1.5. HIVK_HS LPT blade test case

The HIVK_HS blade predictions were able to describe the kinetic losses trend when applying the $Re_t = 0.01$ approach for the $Re_{2,is}$ range. The corresponding transition onset and separation locations through the isentropic outlet Reynolds number range are displayed in figure 7.9. When looking at the separation positions, the predictions follow the trend of the experiments. Indeed, when decreasing the isentropic outlet Reynolds number, the separation location moves upstream. The predictions are satisfactory as they are within the spatial uncertainty range of the thin films (around 4% of the curvilinear TE suction side abscissa). The transition onset location is clearly affected by the separation location as the former

moves upstream when decreasing the isentropic outlet Reynolds number. This was already seen with the T2 blade. This illustrates the effect of the massive separation and long bubble types on the transition onset. Moreover, the evaluation of the transition onset from the experiments is open to discussion as it is not based on the thin films signal RMS but on the averaged heat transfer coefficient. This might be an explanation of the constant offset seen on the predictions (the transition onset is predicted 10% of the curvilinear TE suction side abscissa later than the experimental value). Anyway, bearing in mind this offset, the trends are more of interest as they are similar.

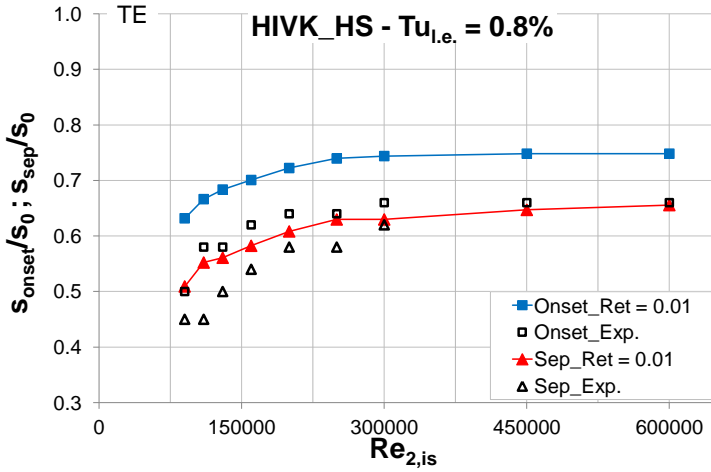


Figure 7.9.: HIVK_HS transition onset (s_{onset}/s_0) and separation (s_{sep}/s_0) positions through the $Re_{2,is}$ range at $Tu_{l,e} = 0.8\%$

The HIVK_HS blade Re_{2,is_B} prediction, assessed with the Hatman and Wang correlation [30], is 140000 (see figure 7.10).

7.1.6. TX LPT blade test case

The TX blade numerical simulations were able to predict the experimental kinetic losses trend when applying the expected $Re_t = TD$ approach. The corresponding transition onset and separation locations through the isentropic outlet Reynolds number range are displayed in figure 7.11. Unfortunately, there is no surface instrumentation on the blade that allows to define the flow topology parameters. When decreasing the isentropic outlet Reynolds number, the separation location moves upstream. About the transition onset location, when decreasing the isentropic outlet Reynolds number, as expected, the transition onset location only moves downstream. Indeed, this blade has a mild diffusion rate and a mid Zweifel

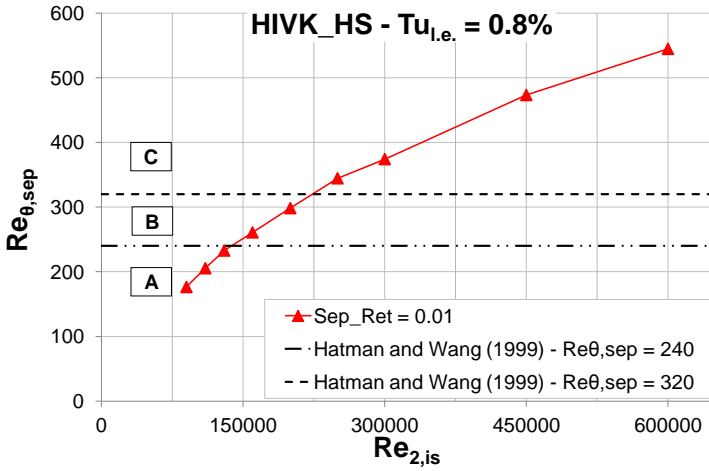


Figure 7.10.: HIVK_HS momentum thickness Reynolds number at separation ($Re_{\theta,sep}$) through the $Re_{2,is}$ range at $Tu_{l.e.} = 0.8\%$ - A: Laminar separation - Long bubble region ($Re_{\theta,sep} < 240$) ; B: Laminar separation - Short bubble region ($240 < Re_{\theta,sep} < 320$) ; C: Laminar separation - Dominant transitional / Transitional separation region ($Re_{\theta,sep} > 320$)

loading coefficient. Consequently, the separation process on the aft part of the blade suction side is not as harsh as on the T2 and HIVK_HS test cases.

The TX blade $Re_{2,isB}$ prediction, assessed with the Hatman and Wang correlation [30], is 135000 (see figure 7.12).

7.1.7. TD LPT blade test case

The TD blade predictions were able to describe the kinetic losses trend when applying the $Re_t = 0.01$ approach for the $Re_{2,is}$ range. However, the $Re_t = TD$ approach seems to be more reasonable for such a mild diffusion rate blade at mid and high $Re_{2,is}$. That is why both approaches are presented for the flow topology parameters. The corresponding transition onset and separation locations through the isentropic outlet Reynolds number range are displayed in figure 7.13. For the $Re_t = 0.01$ approach, the predicted separation location moves upstream while decreasing the isentropic outlet Reynolds number. The experiments feature only one separation location which is well predicted by the corresponding Re_t approach at $Re_{2,is} = 190000$. That prediction is satisfactory as it is within the spatial uncertainty range of the thin films (around 4% of the curvilinear TE suction side abscissa). In contrast, the $Re_t = TD$ approach predicts only one separation at

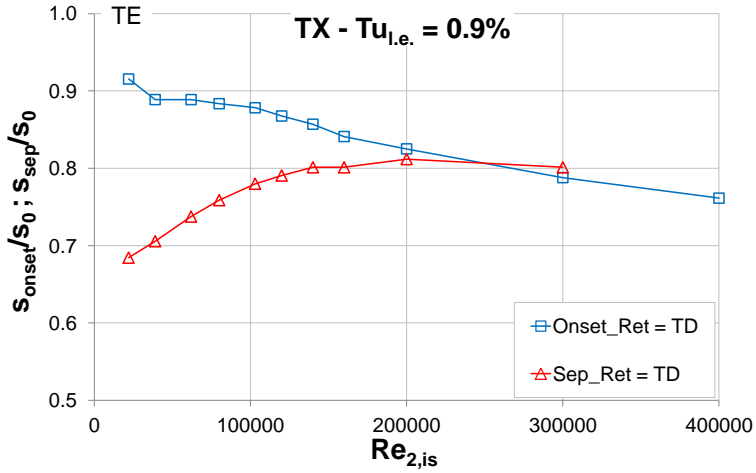


Figure 7.11.: TX transition onset (s_{onset}/s_0) and separation (s_{sep}/s_0) positions through the $Re_{2,is}$ range at $Tu_{l.e.} = 0.9\%$

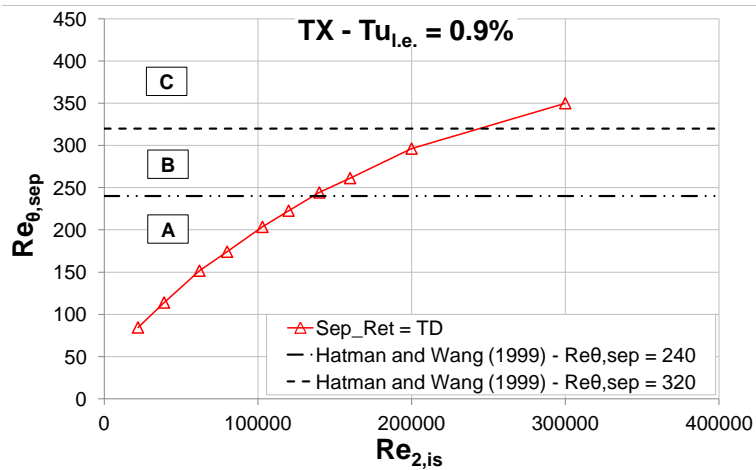


Figure 7.12.: TX momentum thickness Reynolds number at separation ($Re_{\theta,sep}$) through the $Re_{2,is}$ range at $Tu_{l.e.} = 0.9\%$ - A: Laminar separation - Long bubble region ($Re_{\theta,sep} < 240$) ; B: Laminar separation - Short bubble region ($240 < Re_{\theta,sep} < 320$) ; C: Laminar separation - Dominant transitional / Transitional separation region ($Re_{\theta,sep} > 320$)

$Re_{2,is} = 80000$. In addition, the $Re_t = 0.01$ predictions of the transition onset are farther than the $Re_t = TD$ predictions with respect to the experimental results. Indeed, the $Re_t = TD$ predictions follow the experiments like the typical downstream movement of the transition onset when decreasing the isentropic outlet Reynolds number.

Nevertheless, the evaluation of the transition onset and separation positions from the experiments is open to discussion as it is based only on the averaged heat transfer coefficient. This might be an explanation of the difficulty to compare the experiments and the predictions.

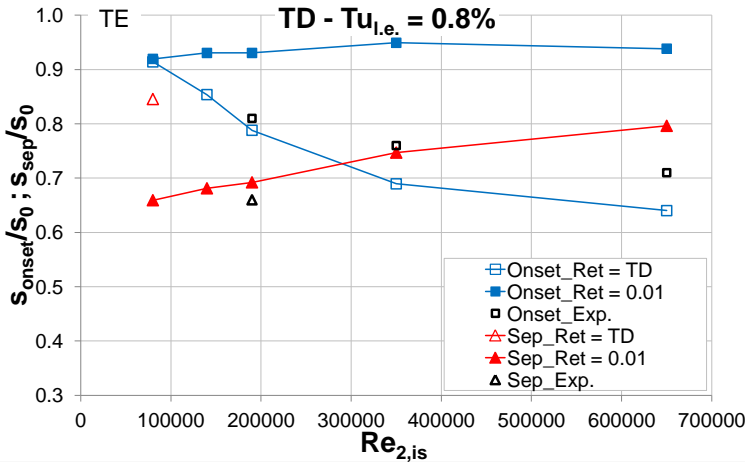


Figure 7.13.: TD transition onset (s_{onset}/s_0) and separation (s_{sep}/s_0) positions through the $Re_{2,is}$ range at $Tu_{l.e.} = 0.8\%$

The TD blade Re_{2,is_B} prediction, assessed with the Hatman and Wang correlation [30] and with the $Re_t = 0.01$ approach, is 140000 (see figure 7.14). The value is submitted to discussion as the $Re_t = TD$ approach does not predict a separation-induced transition through the isentropic outlet Reynolds number range (except at $Re_{2,is} = 80000$). Consequently, at this $Re_t = TD$ approach, the bursting might be lower because the flow passes by a separation-induced transition state (at $Re_{2,is} = 80000$) to a by-pass transition state (at $Re_{2,is} = 140000$).

7.1.8. TF LPT blade test case

The TF blade predictions were able to describe the kinetic losses trend when applying the $Re_t = 0.01$ approach for the $Re_{2,is}$ range. The corresponding transition onset and separation locations through the isentropic outlet Reynolds number

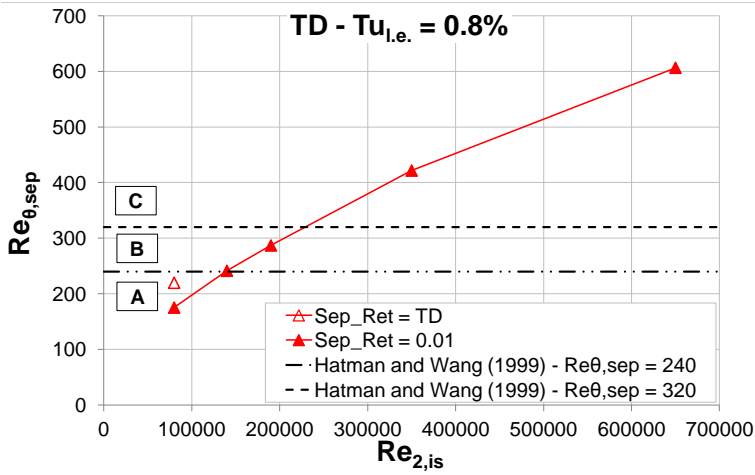


Figure 7.14.: TD momentum thickness Reynolds number at separation ($Re_{\theta,sep}$) through the $Re_{2,is}$ range at $Tu_{l,e.} = 0.8\%$ - A: Laminar separation - Long bubble region ($Re_{\theta,sep} < 240$) ; B: Laminar separation - Short bubble region ($240 < Re_{\theta,sep} < 320$) ; C: Laminar separation - Dominant transitional / Transitional separation region ($Re_{\theta,sep} > 320$)

range are displayed in figure 7.15. The predicted separation location moves upstream while decreasing the isentropic outlet Reynolds number. The experiments feature a constant separation location. This is corroborated by the predictions for the $Re_{2,is} \geq 190000$ range. The transition onset location is slightly affected by the separation location from both the experiments and the predictions, except at low $Re_{2,is}$.

Nevertheless, the evaluation of the transition onset and separation positions from the experiments is open to discussion as it is based only on the averaged heat transfer coefficient. This might be an explanation of the difficulty to compare the experiments and the predictions.

The TF blade $Re_{2,isB}$ prediction, assessed with the Hatman and Wang correlation [30], is 140000 (see figure 7.16).

7.1.9. TG LPT blade test case

The TG blade predictions were able to describe the kinetic losses trend when applying the $Re_t = 0.01$ approach for the $Re_{2,is}$ range. The corresponding transition onset and separation locations through the isentropic outlet Reynolds number

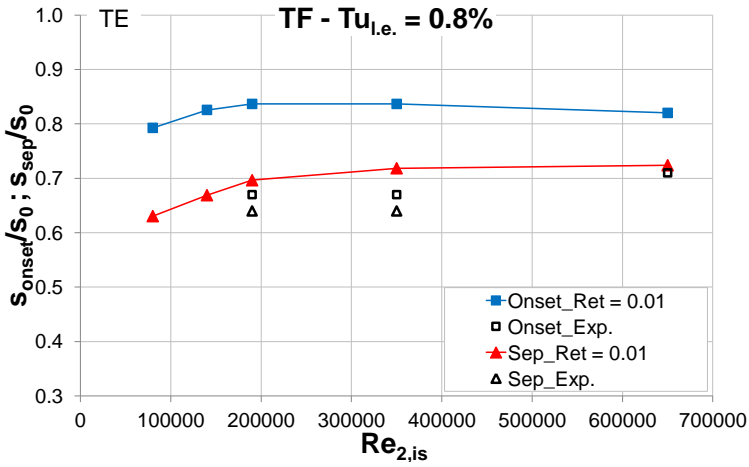


Figure 7.15.: TF transition onset (s_{onset}/s_0) and separation (s_{sep}/s_0) positions through the $Re_{2,is}$ range at $Tu_{l.e.} = 0.8\%$

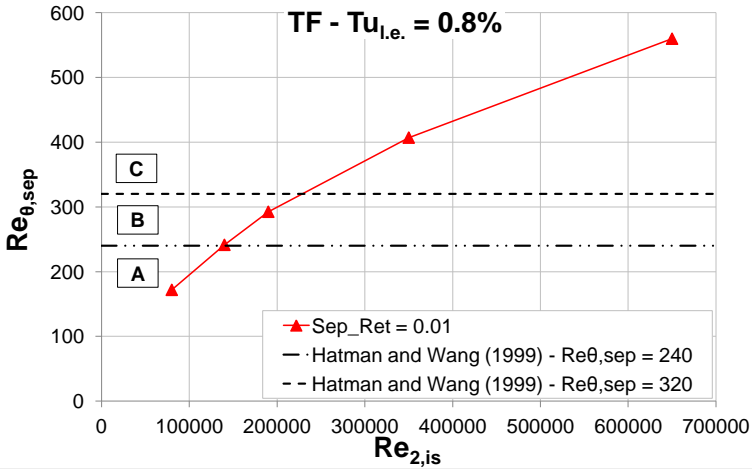


Figure 7.16.: TF momentum thickness Reynolds number at separation ($Re_{\theta,sep}$) through the $Re_{2,is}$ range at $Tu_{l.e.} = 0.8\%$ - A: Laminar separation - Long bubble region ($Re_{\theta,sep} < 240$) ; B: Laminar separation - Short bubble region ($240 < Re_{\theta,sep} < 320$) ; C: Laminar separation - Dominant transitional / Transitional separation region ($Re_{\theta,sep} > 320$)

range are displayed in figure 7.17. The predicted separation location moves upstream while decreasing the isentropic outlet Reynolds number. This trend is visible from the experiments. The transition onset location is affected by the separation location from both the experiments and the predictions. Indeed, the transition onset location moves upstream when decreasing the isentropic outlet Reynolds number.

Nevertheless, the evaluation of the transition onset and separation positions from the experiments is open to discussion as it is based only on the averaged heat transfer coefficient. This might be an explanation of the difficulty to compare the experiments and the predictions.

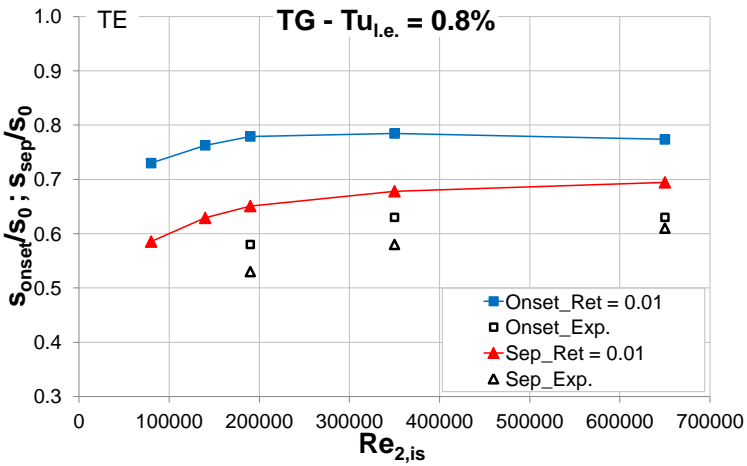


Figure 7.17.: TG transition onset (s_{onset}/s_0) and separation (s_{sep}/s_0) positions through the $Re_{2,is}$ range at $Tu_{l,e} = 0.8\%$

The TG blade Re_{2,is_B} prediction, assessed with the Hatman and Wang correlation [30], is 135000 (see figure 7.18).

7.1.10. Bursting characterization

Previously, the bursting characterization of each numerical test case investigation was done in association with the Hatman and Wang correlation [30]. This process is really delicate. The bursting characterization of the experimental database, done in chapter 4, was based on several criteria, such as the kinetic losses and outlet flow angle evolutions through the isentropic outlet Reynolds number range and coupled with the local information around the blade such as the isentropic Mach number, wall-shear stress and heat transfer distributions. That is why, this process is open to a certain uncertainty. Consequently, it was not of interest to

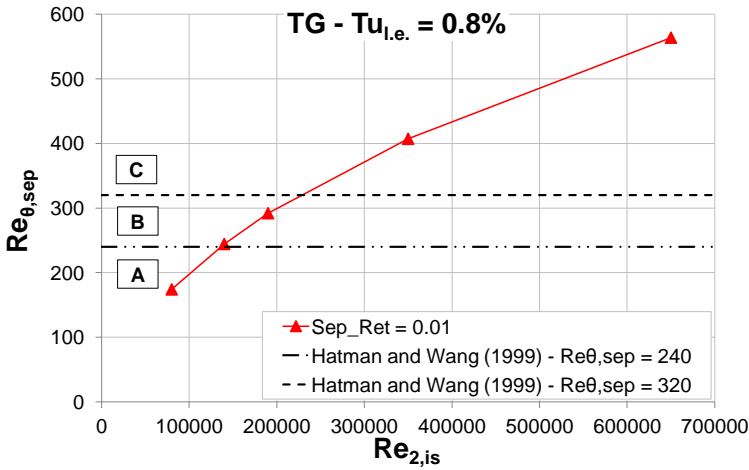


Figure 7.18.: TG momentum thickness Reynolds number at separation ($Re_{\theta,sep}$) through the $Re_{2,is}$ range at $Tu_{l.e.} = 0.8\%$ - A: Laminar separation - Long bubble region ($Re_{\theta,sep} < 240$) ; B: Laminar separation - Short bubble region ($240 < Re_{\theta,sep} < 320$) ; C: Laminar separation - Dominant transitional / Transitional separation region ($Re_{\theta,sep} > 320$)

carry out the same investigation with the predictions of the present work. Indeed, since the agreement between the experiments and the predictions was generally good, the bursting characterization of the numerical predictions would not have given much more insights. Instead, what is more of interest is to try to define a correlation that could provide the limits between the different types of separation bubble.

The Hatman and Wang correlation [30] has this purpose as it gives a limit for the bursting in terms of momentum thickness Reynolds number at separation ($Re_{\theta,sep} = 240$). Thus, to assess the experimental findings, the predictions can be used, and particularly the integral parameter of the boundary layer (i.e. Re_{θ}), to conclude on the reliability of the Hatman and Wang correlation for LPT blades.

Figure 7.19 depicts this investigation. An effort was made to define the experimental information by plain symbols and the numerical information by empty symbols. One can see that the T108, TX and T106C blades predictions fall into a linear trend. However, the slope is too steep for higher diffusion rate blades. The isentropic outlet Reynolds number difference between these predictions and the experiments is high (35000 to 60000). The T2 blade prediction is pretty high, even though this test case experiences a massive separation up to $Re_{2,is} = 185000$. In contrast both HIVK_LS and HIVK_HS present a good agreement where the

isentropic outlet Reynolds number difference between the predictions and the experiments is within 10000 to 20000.

It may be understood that the isentropic outlet Reynolds number at bursting increases while increasing the diffusion rate (see figure 7.19). Both the experiments and the predictions confirm this statement. However, this increase might be limited by a threshold, as illustrated by the HIVK_HS value.

At this stage, those conclusions are the only ones that could be drawn. Indeed, as done by several researchers who have built correlations, a large number of test cases are necessary in order to reduce the data scattering. Moreover, they need to cover the same range in terms of isentropic outlet Reynolds number for instance. The TX, TD, TF and TG blades are examples of these out-of-range investigations. Their isentropic outlet Reynolds number at bursting was either at a higher out-of-range $Re_{2,is}$ (TX blade) or at a lower out-of-range $Re_{2,is}$ (TD, TF and TG blades).

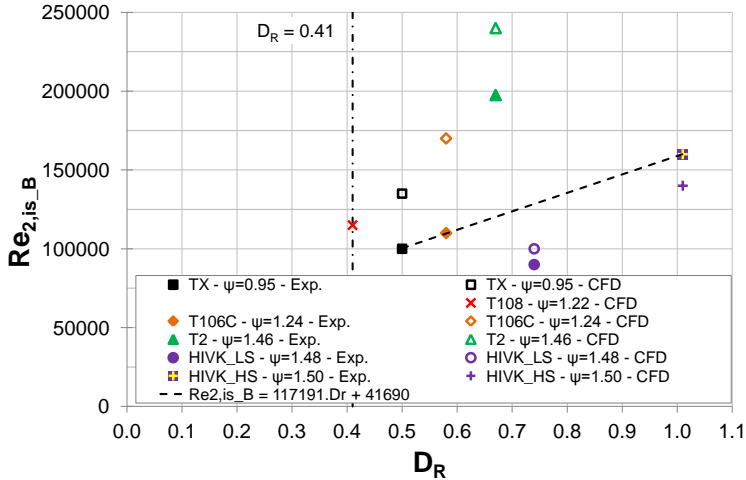


Figure 7.19.: Re_{2,is_B} against D_R at the natural (low) freestream turbulence intensity - Bursting correlation updated with the CFD predictions used with the Hatman and Wang correlation [30]

7.2. Transition at the freestream turbulence intensity generated by a turbulence grid

To illustrate the by-pass transition mode, numerical investigations were carried out on the T106C and the TX blades, where the turbulence intensity at the leading

edge plane is extrapolated at 3.2%. At this turbulence intensity, one will expect to have by-pass transition, even though for highly loaded blade, such as the T106C, separation-induced transition may happen at low $Re_{2, is}$.

The correlations of Abu-Ghannam and Shaw [1], Mayle [52], Hourmouziadis [35] and Steelant and Dick [71] constitutes good examples of by-pass transition correlations.

Abu-Ghannam and Shaw correlation [1] It constitutes the most comprehensive correlation on transition for LPT blade. It is illustrated in section 2.4.1. At high turbulence levels (above 3%), the effect of the pressure gradient is less significant (see figure 2.15). Consequently, two $Re_{\theta, onset}$ limits could be defined for the present work investigations with the corresponding turbulence intensity input. The first one is defined by the laminar separation pressure gradient condition ($\lambda_{\theta} = -0.09$) as taken by U.K. Singh, cited by Abu-Ghannam and Shaw [1]. The corresponding transition onset is determined by $Re_{\theta, onset} = 192$. The second one is defined by the zero-pressure gradient condition. The corresponding transition onset is determined by $Re_{\theta, onset} = 204$.

Mayle correlation [52] This correlation is intended for flow with zero-pressure gradient. In fact, the expression is only a function of the turbulence intensity. However, as pointed out in the former paragraph, the effect of the pressure gradient is less significant when increasing the turbulence level. Consequently, one can assume that this Mayle correlation is applicable to by-pass transition occurring on LPT blades (i.e. with non-zero pressure gradient).

$$Re_{\theta t} = 400 \cdot Tu^{-5/8} \quad (7.1)$$

Hourmouziadis correlation [35] This correlation of Hourmouziadis [35] is similar to the former correlation of Mayle [52].

$$Re_{\theta t} = 1000 \left[\frac{Tu}{0.3} \right]^{-0.65} = 457 \cdot Tu^{-0.65} \quad (7.2)$$

Steelant and Dick correlation [71] This correlation takes into account the compressibility effect in addition to the turbulence intensity level as pointed out previously. Indeed, they showed that the compressibility effect is necessary to assure a correct prediction of both transition onset and length. It was observed that with increasing Mach number, all experiments indicate that the transition onset shifts

downstream at any given turbulence level. This correlation (equation 7.3) is suggested by R. Narasimha, cited by Steelant and Dick [71], and features a correlation of Steelant and Dick [71] (equation 7.4).

$$Re_{\theta t, comp} = Re_{\theta t, incomp} \sqrt{1 + 0.38 \cdot M^{0.6}} \quad (7.3)$$

$$Re_{\theta t, incomp} = 0.664 \sqrt{400094 \cdot Tu_{l.e.}^{-1.38} - 105254 \cdot Tu_{l.e.}^{-7/8}} \quad (7.4)$$

7.2.1. T106C LPT blade test case

The T106C blade features a separation bubble at low isentropic outlet Reynolds numbers (at least up to $Re_{2, is} = 120000$). This evaluation was done only with the isentropic Mach number distribution (not presented here) as there was no wall-shear stress information available. As a consequence, the pressure plateau visible from the isentropic Mach number distribution was considered as an illustration of the presence of a separation bubble, though they are most likely of the transitional separation bubble mode (see section 2.1.2.1) The predictions did not show a separation bubble except at $Re_{2, is} = 80000$ (not presented here).

Thus, the evolution of the momentum thickness Reynolds number at transition onset in function of the isentropic outlet Reynolds number is represented in figure 7.20 with the aforementioned correlations of the literature. One can see that the Mayle correlation and the Abu-Ghannam and Shaw correlation (for both pressure gradient conditions) predicts similar levels. Instead, the Hourmouziadis correlation predicts a higher level of momentum thickness Reynolds number whereas the Steelant and Dick correlation gives a lower level. When comparing the numerical predictions of the present work with the correlations of the literature, one can see that for the highest isentropic outlet Reynolds numbers (where there is more confidence about the by-pass transition type and the transitional separation bubble mode), the agreement is acceptable with the Mayle and Abu-Ghannam and Shaw correlations.

7.2.2. TX LPT blade test case

The TX blade was tested at a low isentropic outlet Reynolds number range ($35000 \leq Re_{2, is} \leq 104000$). The numerical investigations predicts a separation bubble up to $Re_{2, is} = 58000$ (not presented here). Figure 7.21 still displays the aforementioned correlations of the literature. Again, the lowest isentropic outlet Reynolds number cases do not present the characteristics of a by-pass transition according to the numerical investigations and the isentropic outlet Reynolds number level. Instead, at the highest isentropic outlet Reynolds numbers, the momentum

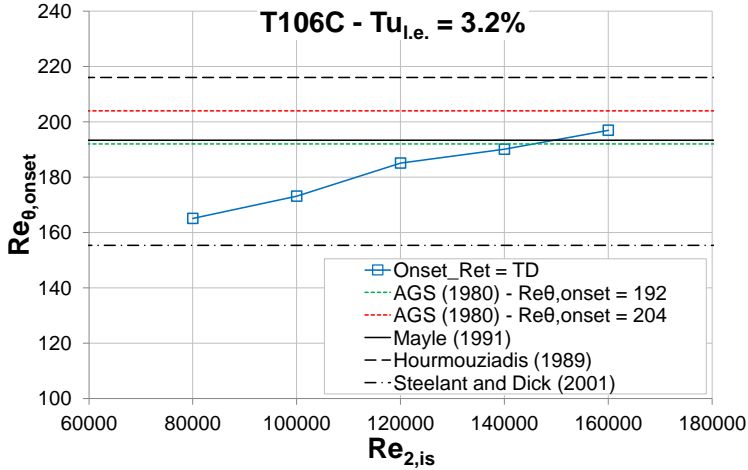


Figure 7.20.: T106C momentum thickness Reynolds number at transition onset ($Re_{\theta, onset}$) through the $Re_{2, is}$ range at $Tu_{l.e.} = 3.2\%$

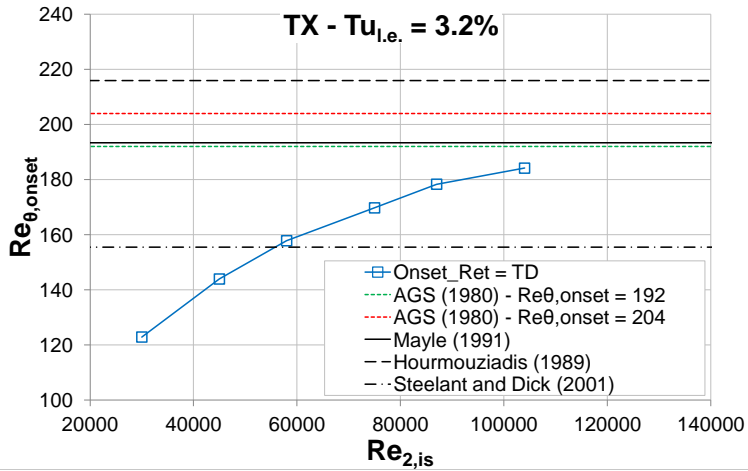


Figure 7.21.: TX momentum thickness Reynolds number at transition onset ($Re_{\theta, onset}$) through the $Re_{2, is}$ range at $Tu_{l.e.} = 3.2\%$

thickness Reynolds number at transition onset tends towards the level of the Mayle and Abu-Ghannam and Shaw correlations.

7.3. Summary

An effort was done to investigate the flow topology parameters from the predictions and to confront them to the experiments. The general conclusion is a fairly good agreement of the characteristic positions between the predictions and the experiments in terms of trend. Indeed, there are some offsets but this is due to the spatial uncertainty range of the sensors.

Otherwise, the comparisons with correlations of the literature provide interesting information such as the determination of the isentropic outlet Reynolds number at bursting for low turbulence level test cases. However, it is based on Hatman and Wang [30] criteria and may necessitate an adjustment as it was meant for incompressible flat plate flows. Indeed, the evaluation of the present work correlation shows some discrepancy with the predictions.

Likewise, for by-pass transition, the predictions fall within the correlations of the literature and particularly the one of Abu-Ghannam and Shaw [1] ($Re_{\theta,onset} = 192$) and the one of Mayle [52]. However, there is a dependency on the isentropic outlet Reynolds number visible from the predictions that was not included in the literature correlations and which should be taken into account for future works.

Chapter 8.

Investigation of the local roughness-induced transition with the Chimera technique

The UTAT european programme partly investigated the effectiveness of a local roughness passive control device. The design was a wavy-shaped wire. The wavy wire is similar to a sawtooth spanwise forward-backward facing step (see figure 8.1). During the test campaigns, only measurements at midspan were performed. As a first approach to assess the design numerically, it is suggested to set the wavy wire as a straight forward-backward facing step extending in the spanwise direction. The yellow lines illustrate the spanwise layers used to delimit the domain to mesh (see figure 8.1). Again, as described in section 5.2, the spanwise mesh extension is restricted to 5 layers for a CFD time-saving reason. This configuration will be called “straight forward-backward facing step” or “straight FB” in the following. Similarly, the TATMo european programme in the continuity of the UTAT programme partly investigated the effectiveness of a local roughness passive control device. The design was a transversal cylindrical wire. The geometry was set numerically as a Gaussian shape in order to take into account the fillet radius due to the glue used to stick the wire on the surface. Indeed, the cylinder diameter is pretty small (0.2 mm) (see figure 8.2). This configuration will be called “cylindrical wire” in the following.

To understand the impact of the local roughness on the numerical predictions, the $\gamma\text{-}\widetilde{Re}_{\theta t}$ transition model will be used, even though, it was not meant for this kind of configuration. What will be interesting to investigate is the boundary layer information (and particularly the transition onset) that come from the calculations and see if the correlative process could be extended to local roughness passive control devices. To ease the introduction of the local roughness on the suction side surface, the Chimera technique will be used. The aim of this investigation is to get more insight on the use of the Chimera technique for the introduction of geometrical artifacts in a LPT environment and in association with the $\gamma\text{-}\widetilde{Re}_{\theta t}$ transition model. To the best knowledge of the author, there is no application of the aforementioned technique for such configurations. That is why the purpose is to assess the feasibility of that technique as a prediction tool for the designer. This study has been performed with the active collaboration of Juan Ramón Llobet

Gómez [48, 47] during the period of his Research Master at the von Karman Institute.

At last, there exists a transition model to take into account the presence of a local roughness in *elsA*. The required information about the local roughness are its location and its height. This technique uses its own transition criterion. The criterion is based on the calculation of a critical Reynolds number based on the local roughness height. As soon as the criterion reaches a value of 500, the transition is triggered. Consequently, the model introduces an over-thickening of the boundary layer simulating the presence of the local roughness. This over-thickening is produced by injecting a small amount of fluid across the wall over a small length. However, when predicting the flow field around the blade, this approach cannot determine the presence of recirculation bubbles ahead and after the local roughness and then the expected overshoot in isentropic Mach number. As a consequence, this approach will not be discussed in this thesis as the real effect of the local roughness is intended here for the understanding of the phenomenon and evaluation of the γ - $\widetilde{Re}_{\theta t}$ transition model associated to the Chimera technique.

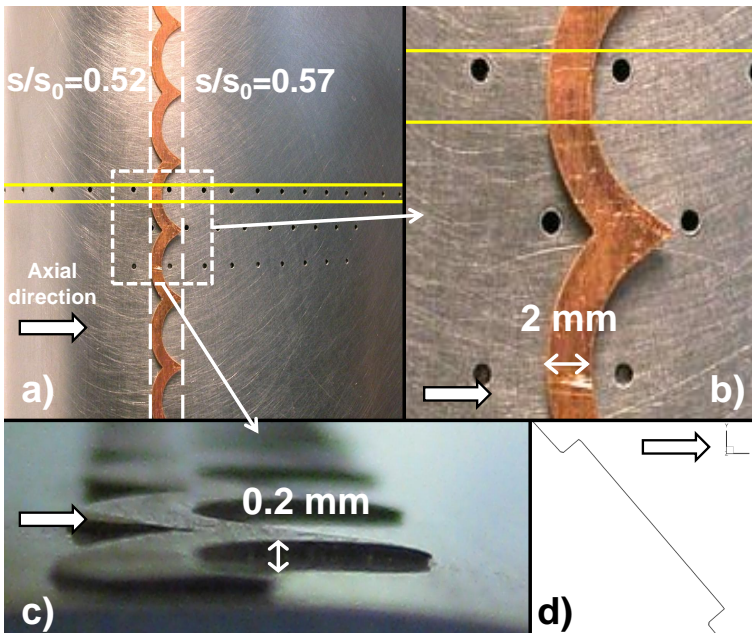


Figure 8.1.: T106C blade suction side with wavy wire passive control device - UTAT programme - a) View from the top of the blade suction side, b) Zoom of the view from the top of the blade suction side, c) Transversal view from the edge of the blade suction side, d) Straight FB geometry used for the mesh generation

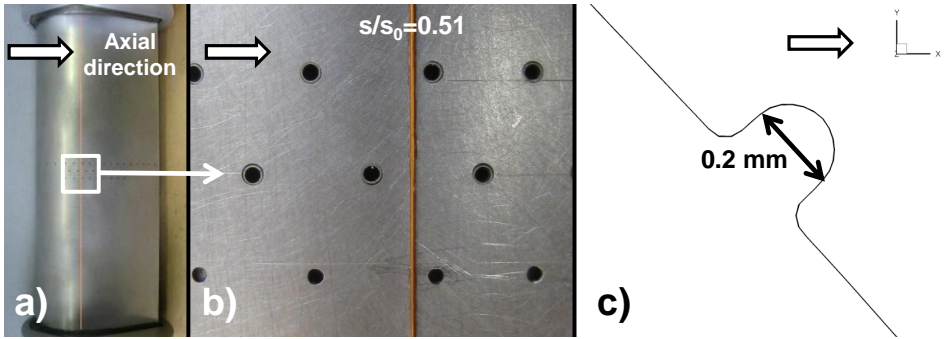


Figure 8.2.: T106C blade suction side with cylindrical wire passive control device - TATMo programme - a) View from the top of the blade suction side, b) Zoom of the view from the top of the blade suction side, c) Cylindrical wire geometry used for the mesh generation

8.1. Incorporation of the local roughness geometry with the Chimera technique

As briefly highlighted previously in section 5.1, the Chimera technique is used to simplify the meshing of complicated objects or the addition of new features in the mesh. This method lies within the scope of the resolution of the equations of Navier-Stokes on overlapping multi-domain 3D grids. Therefore, it allows overlapping different mesh blocks in order to add new features to an already existing meshed geometry. This method consists in the transfer of the solution from overlapping grids by interpolation [59].

For that purpose, a new mesh (see figures 8.3, 8.4 and 8.6) was generated for the surroundings of the local roughness and overlapped on the existing original mesh of the smooth blade configuration (see table 6.3 and figure 5.1). This new mesh (overlapping) is a standard H-type mesh. It allows extracting the geometry of the blade suction side and generating the strip with the following parameters:

- Straight FB
 - Blade O-type mesh data file
 - $\frac{x}{c_{ax}}; \frac{s}{s_0}$ for start of mesh, start of step, end of step and end of mesh
 - Step height
 - Mesh height in the perpendicular direction away from the blade surface
- Cylindrical wire

- Blade O-type mesh data file
- $\frac{x}{c_{a,x}}; \frac{s}{s_0}$ for start of mesh, center of the wire and end of mesh
- Diameter of the wire
- Diameter of the fillet radius (simulation of the glue)
- Mesh height in the perpendicular direction away from the blade surface

To have a good overlap of the background mesh, the overlapping mesh resolution has to be higher than the overlapped mesh. This was done in both streamwise direction and perpendicular direction away from the blade surface and can be seen in figures 8.5 and 8.7 where the red mesh corresponds to the overlapped mesh whereas the black mesh refers to the overlapping mesh.

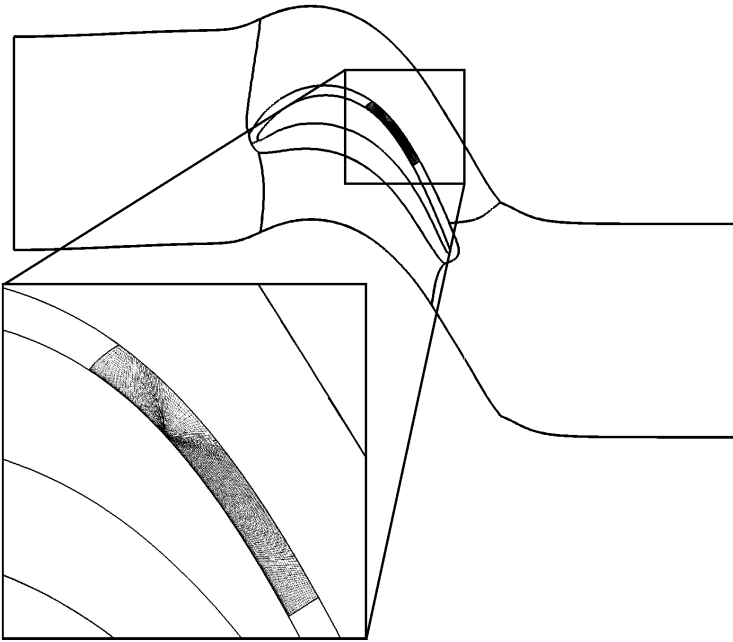


Figure 8.3.: T106C original mesh (overlapped mesh) including the overlapping mesh

A study of the mesh independence was carried out for the local roughness blocks. The parameters varied for this study were the length of the mesh upstream and downstream of the local roughness location and the density of the mesh. More insights are provided in section 8.2.3. Table 8.1 sums up the meshing information of the overlapping mesh.

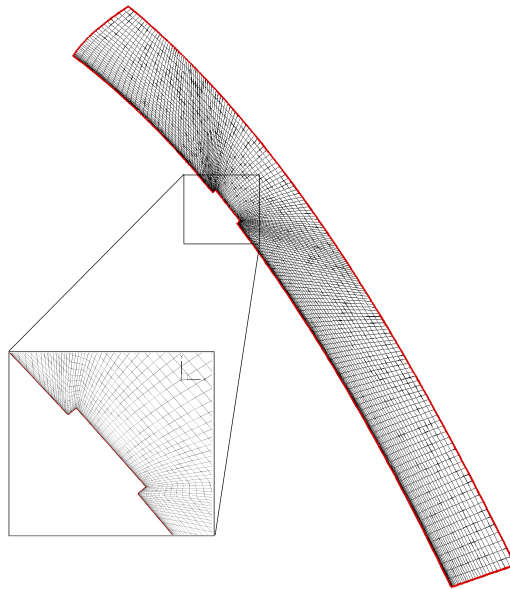


Figure 8.4.: T106C overlapping mesh: Straight FB

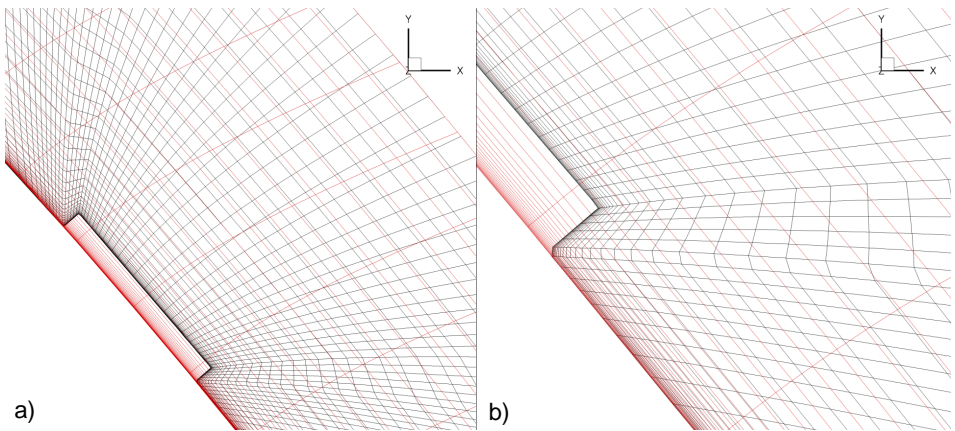


Figure 8.5.: T106C overlapping mesh: Straight FB meshes resolution - a) Standard view and b) zoom

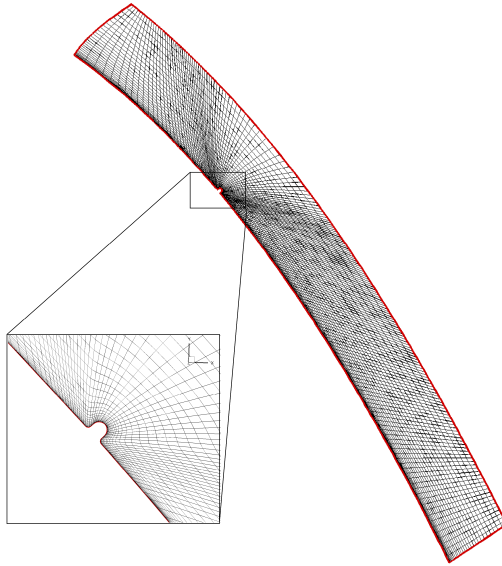


Figure 8.6.: T106C overlapping mesh: Cylindrical wire

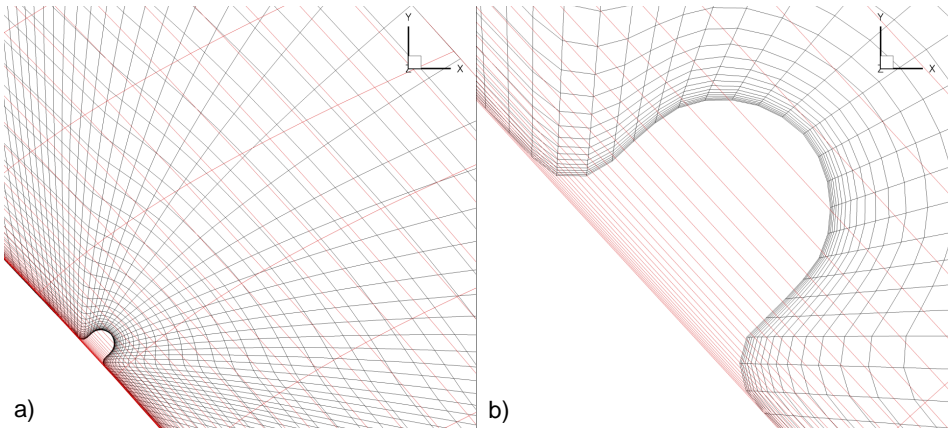


Figure 8.7.: T106C overlapping mesh: Cylindrical wire meshes resolution - a) Standard view and b) zoom

Table 8.1.: T106C LPT blade overlapping mesh information

Blade	T106C		
	Local roughness configuration	Straight FB	Straight FB (Long)
Number of {nodes ; cells} in one streamwise layer	{6765 ; 6560}	{7257 ; 7040}	{7093 ; 6880}
Minimum orthogonality (deg)	34.2	35.6	31.1
Number of cells in orthogonality interval: [27 deg ; 36 deg] in one streamwise layer	3	1	46
Maximum expansion ratio	1.47	1.44	1.33
Maximum y^+	0.22	0.14	0.23
Number of nodes in the stream-wise direction	165	177	173
Number of nodes in the perpendicular direction away from the blade surface	41	41	41
Overlapping mesh upstream extension from the local roughness	$50.h_r$	$50.h_r$	$50.h_r$
Overlapping mesh downstream extension from the local roughness	$100.h_r$	$130.h_r$	$100.h_r$

Three different zones status are created for the overlapping and are illustrated with the current local roughness geometry:

- **Blanked zone:** This is a non-calculated zone which is located in the overlapped mesh (see figure 8.8b). As a consequence, the calculation of this zone is performed in the corresponding area of the overlapping mesh. In this region, the features of the overlapping mesh substitute the features of the overlapped mesh. In the present case, the overlapped mesh corresponds to the smooth blade, whereas the overlapping mesh introduces the strip geometry.
- **Interpolated zone:** This zone is situated at the limit of the overlapped and overlapping meshes. It is where the information is transferred between meshes (see figure 8.8). The overlapping mesh will get its boundary conditions through this area (see figure 8.8a). In the same way, the overlapped mesh will retrieve the information of the flow inside the overlapping zone through these regions (see figure 8.8b).
- **Calculated zone:** This zone is calculated normally.

The blanking of the overlapped zones can be done, either manually, defining the regions within the code, or automatically, using one of the implemented algorithms in *elsA*. For the present project two different automatic blanking algorithms are used and tested: the Implicit Hole Cutting (IHC) and the Patch Assembly (PA).

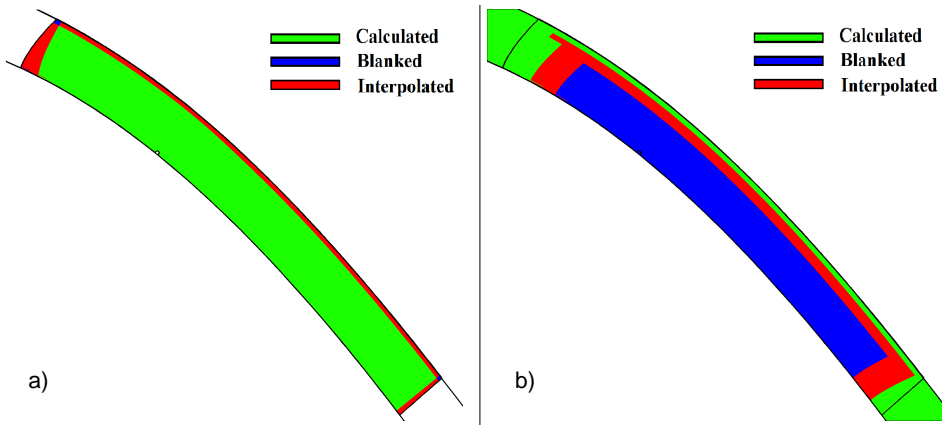


Figure 8.8.: Zones status at overlapping - Cylindrical wire with the implicit hole cutting algorithm - a) Overlapping mesh status, b) Overlapped mesh status

Implicit hole cutting The implicit hole cutting algorithm is a cell selection process where only the “best” cells located in a multiple overlapping region are used for the calculation. Different quality criteria can be used to select the most suitable cells to perform the calculation among the meshes present in the same zone. The cheapest and the easiest criterion is the cell volume one. By these means, the algorithm selects the cells to be calculated (overlapping zone) and the blanked cells (overlapped zone). A minimal interpolation zone is always respected, even if an overlapping mesh presents preferable cells than the overlapped mesh for all its extension. On its boundaries the calculation will be performed in the overlapped mesh in order to provide an interpolation zone, where the boundary conditions required for the overlapping mesh will be transferred [59].

Patch assembly The patch assembly algorithm is based on the designation of different priorities for the multiple overlapping meshes. For this method, the user has to define the higher priority to the mesh where the calculation must be done. By these means, the algorithm automatically assigns the blanking zones to avoid calculation in the overlapped mesh and forces it to be done in the overlapping one. It also generates the zone of interpolation, where the higher and lower priority meshes share the required information to calculate the domain as a whole [59].

8.2. Evaluation of the Chimera technique methodology

Before showing the results of the local roughness-induced transition with the Chimera technique, it is important to evaluate the chosen Chimera technique methodology. Two tests are carried out to illustrate this evaluation. A first comparison of the automatic blanking algorithms is provided. This is followed by the use of the Chimera technique with an overlapping mesh that does not feature any local roughness element or artifact, i.e. with a smooth blade suction side surface. This last approach aims at evaluating the transfer of information between the different overlapping mesh blocks.

8.2.1. Comparison between the implicit hole cutting and the patch assembly automatic blanking algorithms

To start the evaluation of the Chimera technique methodology, the comparison between two automatic blanking algorithms is provided. In figure 8.9, the comparison between the implicit hole cutting (IHC) algorithm and the patch assembly (PA) algorithm is illustrated with the isentropic Mach number distribution, the suction side wall-shear stress and the downstream wake profile. From the comparison, one can see that the difference is tiny except for the wall-shear stress where the reattachment region differs slightly. However, the levels are still of the same order. As a conclusion, it seems that the choice of the automatic blanking algorithm does not affect the results for the straight FB case.

However, the blanking definitions are different for the two algorithms in the overlapped mesh.

Patch assembly Concerning the PA algorithm, it reduces the blanked zone to a minimum. This means that most of the overlapped zone is calculated both in the overlapped and overlapping meshes. The overlapping mesh contains the geometry of the straight FB and the overlapped mesh corresponds to the original smooth blade. Only the zones near the geometrical difference between both meshes are blanked in the overlapped mesh and calculated only in the overlapping one, as observed in figure 8.10. In these contours, the overlapping mesh (figure 8.10a) gets its boundary conditions through the interpolated zones on its limits and the flow is calculated on all the rest of its volume. In the case of the overlapped mesh (figure 8.10b), the flow is calculated in almost all its volume. It is only interpolated near the straight FB location, where it gets the information from the overlapping mesh. The blanking takes place only in the interior part of the straight FB. This reduces the effective part of the overlapping mesh to the small region near the straight FB. Indeed, the only information transmitted to the rest of the

domain, coming from the overlapping mesh, is reduced to the interpolated zones in the overlapped mesh. The main drawback is that introducing an overlapping mesh optimised for the newly introduced geometry is of no effect, as the only data transmitted to the overlapped mesh will come just from a confined region near the straight FB. Moreover, the prediction of the separation bubble is performed in the overlapped mesh. This mesh is not optimised for the calculation of this phenomenon. Nevertheless, this bubble develops close to the wall and the higher gradients are in the direction normal to it. Near the wall, the refinement of the overlapped mesh in the direction normal to the wall is high, allowing good results even if the mesh is not specifically adapted for the separated flow. This is the reason for which the results with both the PA and the IHC algorithms do not differ substantially. An important drawback of this method is that, if the local roughness is smaller than the size of two cells of the overlapped mesh, it may not be detected and the overlapping mesh would not transfer any information to the rest of the domain. This is the case for the cylindrical wire geometry, where the PA algorithm cannot be used (see figures 8.5 and 8.7). An advantage of the presented approach is that it facilitates the extraction of the data with respect to the IHC algorithm. The interpolated zones may present deviations from the correct value. These zones act as an information exchange area and the values may not correspond to the solution. The higher gap between interpolated zones of both meshes always allows to have a calculated area in one of the meshes far from any interpolation. This avoids any spurious value due to the proximity of interpolated zones between meshes, as may happen for the IHC as will be described below.

Implicit hole cutting The IHC algorithm is dependent on a mesh quality criterion and not on a geometrical difference like the PA algorithm. Generally, the overlapping mesh that introduces a geometrical difference will be optimised for this new feature. This method will always respect the zones of better quality grid. The calculation will be always performed on the best fitted cells. Hence, the calculation will be performed on the overlapping mesh as long as the quality criterion for its cells is better than for the overlapped mesh cells. In the present case, the overlapping mesh contains cells of smaller volume than the overlapped mesh in all its extension. As the used quality criterion was the cell volume, the calculation will be performed as long as possible in the overlapping mesh, respecting a minimum interpolation area and blanking the overlapped mesh. This, can be observed in figure 8.11. This methodology allows to introduce new geometry features of any size, as the overlapped mesh is blanked where the overlapping mesh is finer. In particular, it allows to introduce the cylindrical wire geometry and to perform the calculation in the overlapping mesh, where the grid is optimised for the flow around this obstacle. The only drawback of this approach is that in some cases, a slightly spurious value can be extracted in the region between interpolated zones in both meshes.

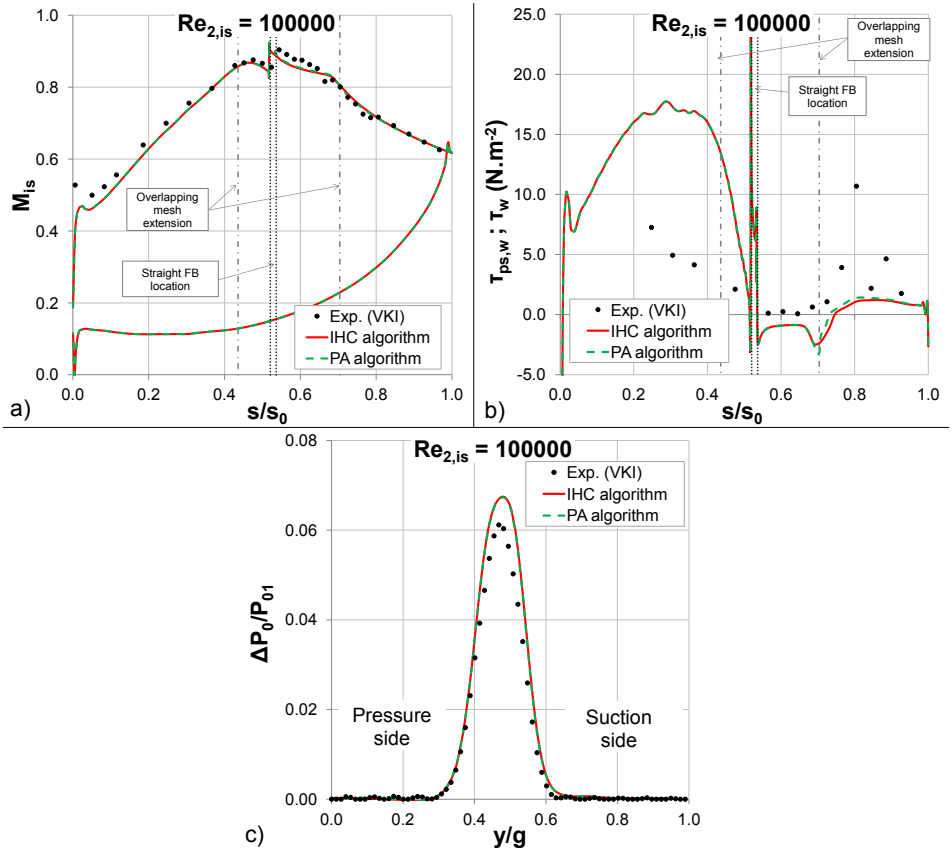


Figure 8.9.: Comparison between the Implicit hole cutting and the Patch assembly automatic blanking algorithms - T106C at $Re_{2,is} = 100000$ and at $Tu_{l.e.} = 0.9\%$ - a) Isentropic Mach number distribution, b) Pseudo-wall-shear stress ($\tau_{ps,w}$ from experiment) and wall-shear stress (τ_w from CFD calculation) distributions on the SS, c) Wake profile

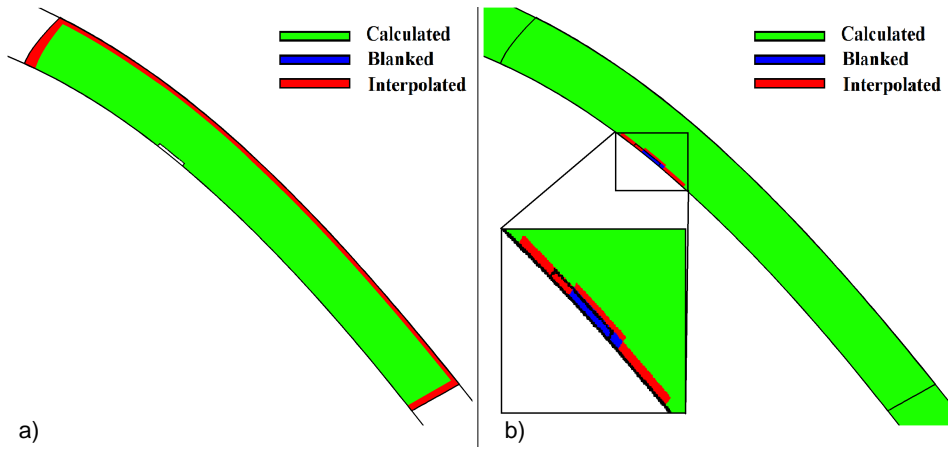


Figure 8.10.: Zones status at overlapping - Straight FB with the patch assembly algorithm - a) Overlapping mesh status, b) Overlapped mesh status

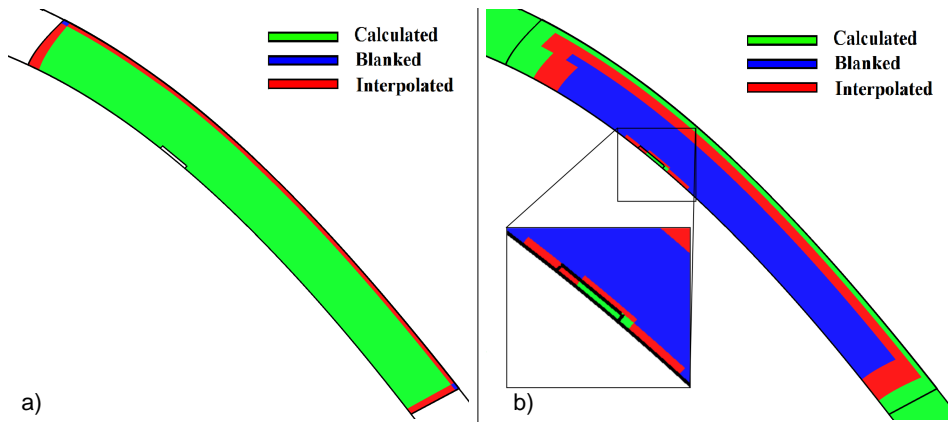


Figure 8.11.: Zones status at overlapping - Straight FB with the implicit hole cutting algorithm - a) Overlapping mesh status, b) Overlapped mesh status

8.2.2. Evaluation of the Chimera technique with a smooth blade suction side overlapping mesh

The evaluation of the transfer of information is assessed with an overlapping mesh that does not feature any local roughness. Thus, the configuration is a smooth blade. The aim is to see if the Chimera technique affects the prediction on a simple smooth blade. The standard O4H mesh calculation is at disposal for comparison (see section 6.2.1). At first sight, figure 8.12 shows no real difference in the isentropic Mach number distribution. However, tiny differences exist in the wall-shear stress and the wake profile but are still negligible. The reason might be due to the higher resolution of the overlapping mesh.

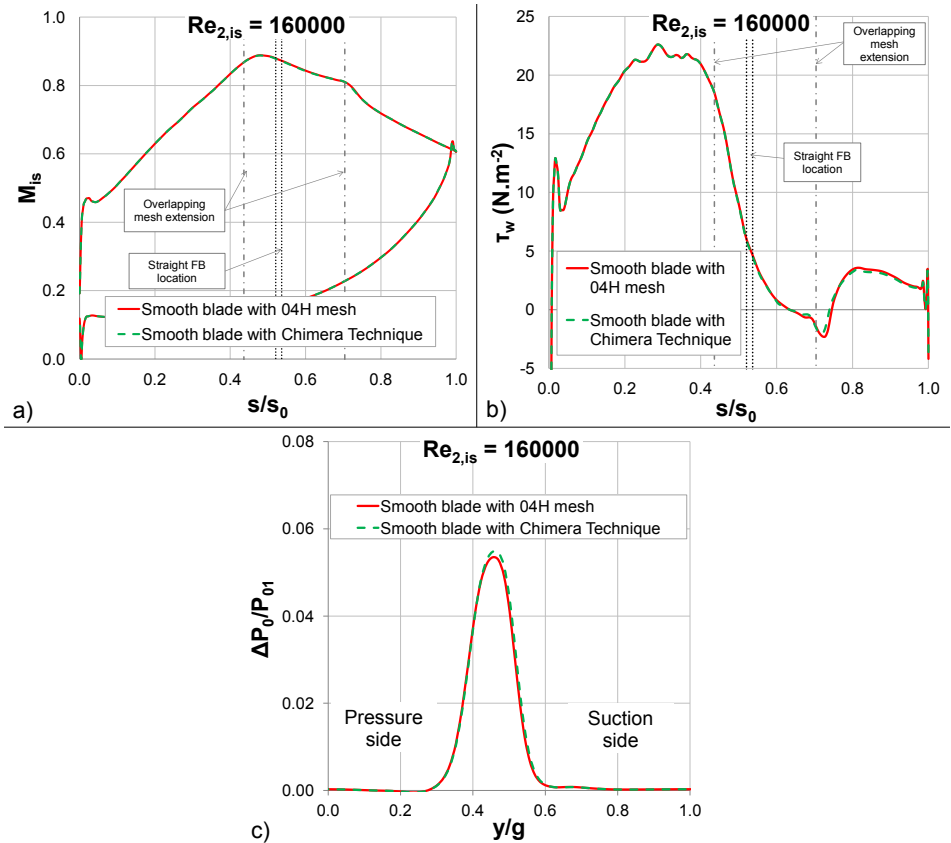


Figure 8.12.: Evaluation of the Chimera technique with a smooth blade suction side overlapping mesh - T106C at $Re_{2,is} = 160000$ and at $Tu_{l.e.} = 0.9\%$ - a) Isentropic Mach number distribution, b) Wall-shear stress, c) Wake profile

8.2.3. Evaluation of the overlapping mesh extensions upstream and downstream of the straight forward-backward facing step

The extensions of the overlapping mesh upstream and downstream of the straight FB were evaluated in order to assess their influence in the separation prediction.

The most relevant conclusions are that the upstream and downstream lengths of the mesh have to cover the recirculation zones generated by the local roughness. This means that the upstream length can be relatively small, as the recirculation bubble on the front part of the local roughness is localised close to the front foot of the local roughness. On the contrary, the length downstream of the local roughness needs to be much longer, as the separation bubble generated downstream of it can be very large (see figure 8.13).

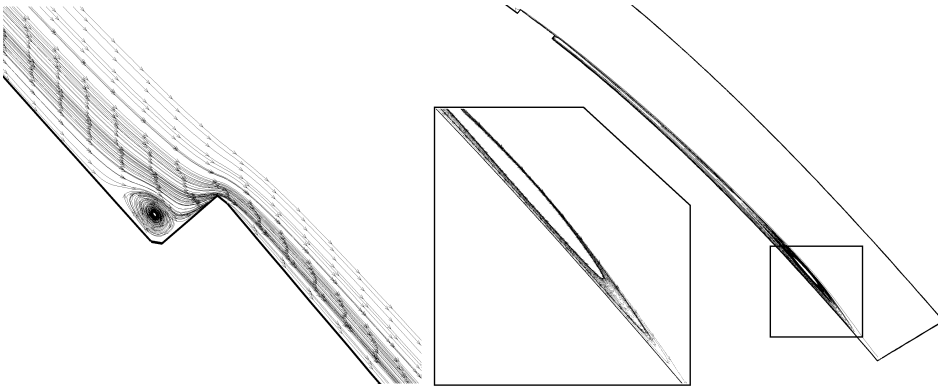


Figure 8.13.: Recirculation zones upstream and downstream of the straight FB on the T106C suction side at $Re_{2, is} = 100000$ with the patch assembly algorithm

From the observation of figure 8.13, the upstream recirculation bubble size is comparable to the straight FB height (h_r). However, it is advisable to extend the length of the mesh much more upstream in order to allow a good area of overlapping between meshes. This allows the Chimera technique to interpolate far from the area of interest. The recirculation bubble downstream of the straight FB was found to be around 50 to 100 times the height of this straight FB. Following this reasoning, the selected mesh for the calculations has an upstream length of $50.h_r$ and a downstream length of $100.h_r$ for the cases from $Re_{2, is} = 120000$ to $Re_{2, is} = 185000$ and $130.h_r$ for $Re_{2, is} = 80000$ and $Re_{2, is} = 100000$. An investigation, focusing at an isentropic outlet Reynolds number of 100000 with two downstream mesh extensions from the straight FB end ($100.h_r$ and $130.h_r$), was carried out to illustrate those findings. These positions are marked on figure 8.14

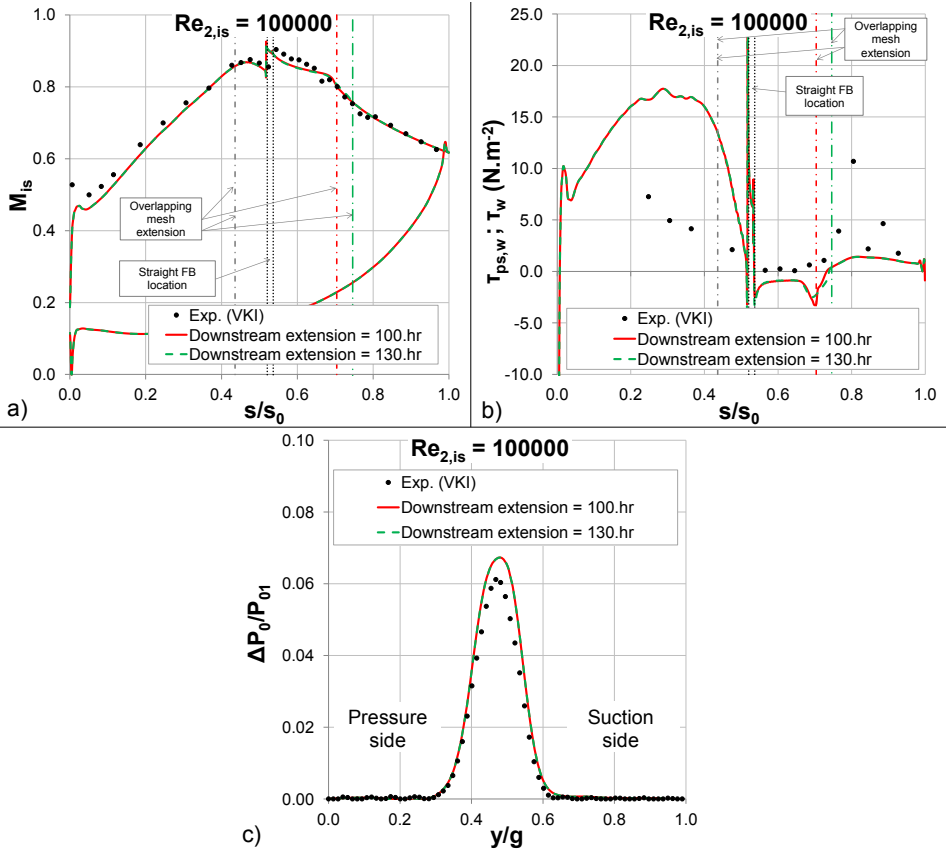


Figure 8.14.: Evaluation of the overlapping mesh extension downstream of the straight FB - T106C at $Re_{2,is} = 100000$ and at $Tu_{l.e.} = 0.9\%$ - a) Isentropic Mach number distribution, b) Pseudo-wall-shear stress ($\tau_{ps,w}$ from experiment) and wall-shear stress (τ_w from CFD calculation) distributions on the SS, c) Wake profile

by vertical lines. This figure does not show major differences between the standard downstream overlapping mesh extension (100.hr) and the longer one (130.hr). Only the wall-shear stress illustrates a minor difference even though the levels are still the same. That is why, one can conclude that the downstream extension does not influence the separation prediction as long as the separation bubble is mostly captured.

Table 8.2.: T106C LPT blade working conditions at the natural freestream turbulence intensity and with the local roughness

Blade	T106C
Ψ	1.24
g/c	0.95
Loading	Aft
D_R	0.58
$M_{2,is}$	0.65
$Re_{2,is} (\times 10^3)$	[80 ; 185]
$Tu_{l.e.}(\%)$	0.9
Re_t	[6.7 ; 16.4]
Facility	S1

8.3. Straight forward-backward facing step investigations

The straight FB case was performed with the PA algorithm for $Re_{2,is}$ ranging from 80000 to 185000. Table 8.2 sums up the geometrical and working conditions.

8.3.1. Evaluation of the $\gamma\text{-}\widetilde{Re}_{\theta t}$ transition model on the straight forward-backward facing step configuration

The mass-averaged kinetic losses (see figure 8.15) and the mass-averaged outlet flow angle (see figure 8.16) are predicted with a good confidence. Indeed, it was expected as the straight FB provides disturbances in the boundary layer and consequently hastens the transition. Moreover, the behaviour of the $\gamma\text{-}\widetilde{Re}_{\theta t}$ model with such a configuration (which is supposed to be out of the scope of this model) is satisfactory. This is even confirmed from the isentropic Mach number distribution, the wake profile and the wall-shear stress distribution on the suction side at two isentropic outlet Reynolds numbers (185000, see figures 8.17 to 8.19 and 80000, see figures 8.20 to 8.22). From the isentropic Mach number distributions, one can see the pressure drop associated to the local acceleration induced by the local roughness. In addition, there a good prediction of the pressure recovery for both $Re_{2,is}$. This confirms the good prediction of the separation bubble downstream of the local roughness with the corresponding pressure plateau and from the wall-shear stress information.

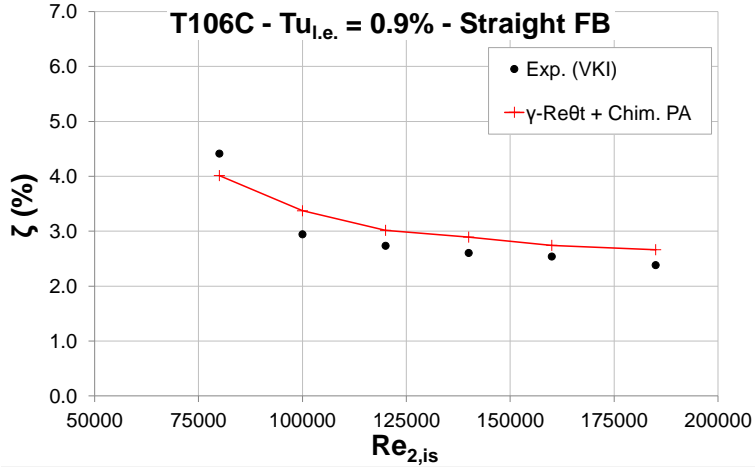


Figure 8.15.: T106C mass-averaged kinetic losses at $Tu_{l,e} = 0.9\%$ with the straight FB

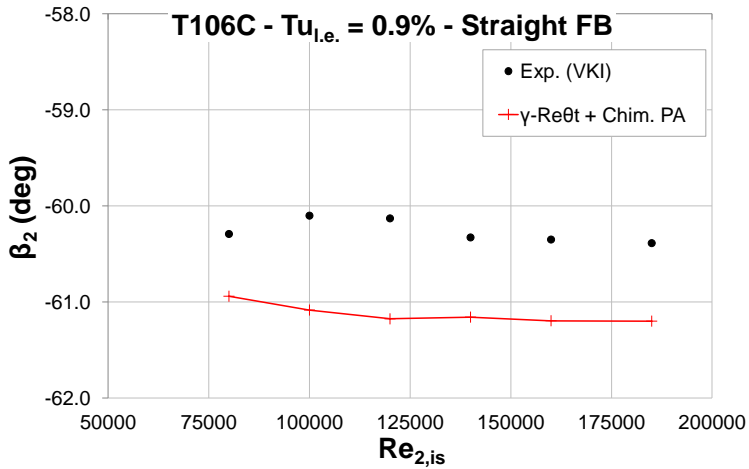


Figure 8.16.: T106C mass-averaged outlet flow angle at $Tu_{l,e} = 0.9\%$ with the straight FB

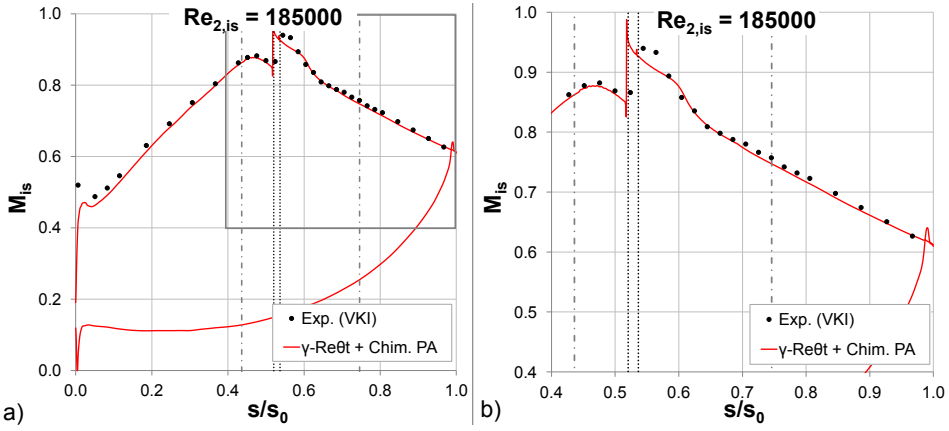


Figure 8.17.: T106C isentropic Mach number distribution at $Re_{2,is} = 185000$, $Tu_{l.e.} = 0.9\%$ and with the straight FB - a) Full scale, b) Zoom in the aft region

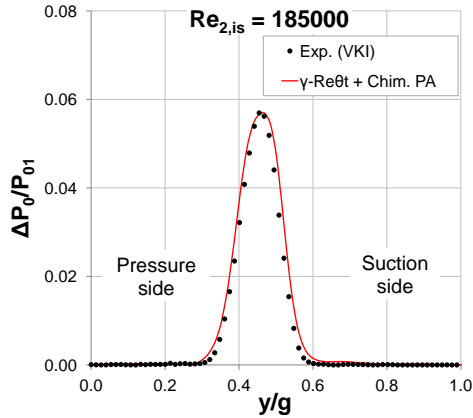


Figure 8.18.: T106C wake profile at $Re_{2,is} = 185000$, $Tu_{l.e.} = 0.9\%$ and with the straight FB

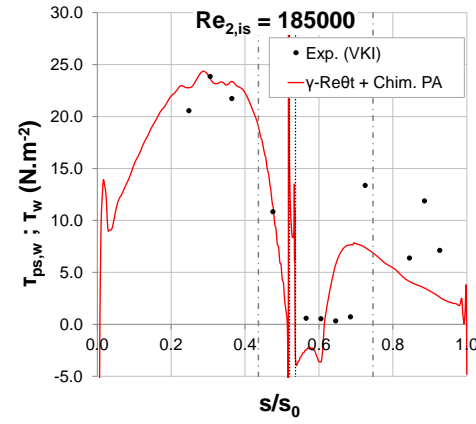


Figure 8.19.: T106C pseudo-wall-shear stress ($\tau_{ps,w}$ from experiment) and wall-shear stress (τ_w from CFD calculation) distributions on the SS at $Re_{2,is} = 185000$, $Tu_{l.e.} = 0.9\%$ and with the straight FB

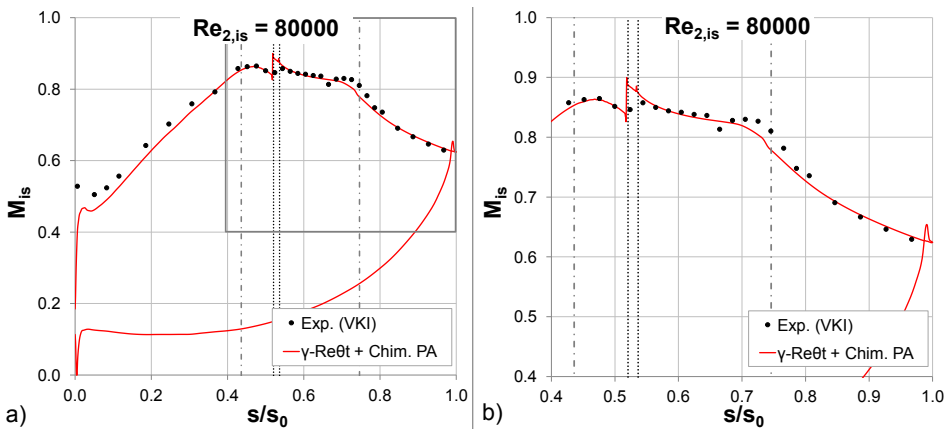


Figure 8.20.: T106C isentropic Mach number distribution at $Re_{2,is} = 80000$, $Tu_{l.e.} = 0.9\%$ and with the straight FB - a) Full scale, b) Zoom in the aft region

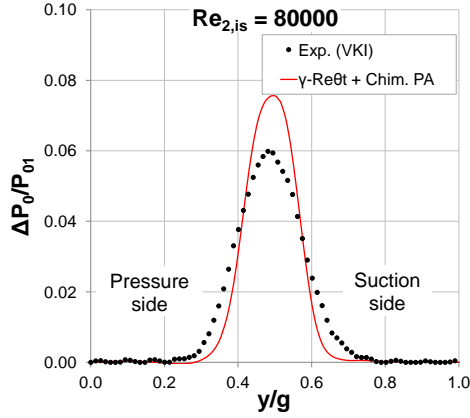


Figure 8.21.: T106C wake profile at $Re_{2,is} = 80000$, $Tu_{l.e.} = 0.9\%$ and with the straight FB

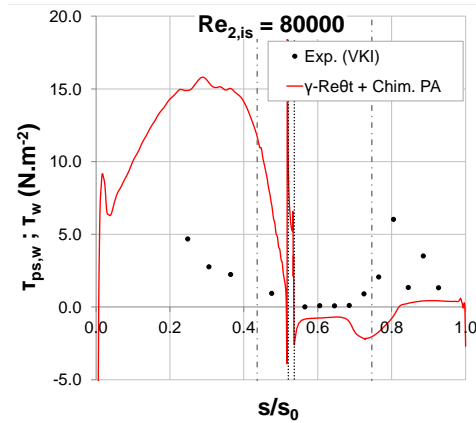


Figure 8.22.: T106C pseudo-wall-shear stress ($\tau_{ps,w}$ from experiment) and wall-shear stress (τ_w from CFD calculation) distributions on the SS at $Re_{2,is} = 80000$, $Tu_{l.e.} = 0.9\%$ and with the straight FB

8.3.2. Investigation of the flow topology parameters with the $\gamma\widetilde{Re}_{\theta t}$ transition model on the straight forward-backward facing step configuration

After evaluating the information measured during the test campaigns (isentropic Mach number distribution, wake profile, wall-shear stress distribution), it is of interest to investigate the transition onset information, even though, as it was stressed previously, the correlation-based transition model ($\gamma\widetilde{Re}_{\theta t}$) is not meant for local roughness configuration but for smooth configurations. Moreover, this transition model was calibrated to cover natural transition (low turbulence intensity), separated-flow transition and by-pass transition. In this local roughness configuration, it is not really obvious if this configuration could be classified in one of the aforementioned categories. Indeed, natural transition is by definition discarded as well as by-pass transition since the freestream level of turbulence is low (around 1%). Besides, the disturbances are embedded in the boundary layer since the local roughness introduces a discontinuity in the flowfield (sort of forward-backward facing step). Since the local roughness induces a separation of the flow downstream, this type of transition may be associated to separation-induced transition, even though the level of disturbances is expected to be higher in the local roughness configuration due to the physical obstacle. However, the type of the separation bubble is expected to be short according to the classification illustrated in section 2.1.2.1. Indeed, the peak Mach number is not affected as long as the local roughness location is close to the suction side peak Mach number location.

The local roughness-induced transition is of interest in this study of transition in an LPT environment, as it constitutes a way to cope with massive separation occurring at low $Re_{2,is}$. Indeed, it seems to be a good trade-off to tremendously reduce the kinetic losses at low $Re_{2,is}$ and to keep reasonable level at high $Re_{2,is}$ (see figures 3.9 and 3.10).

During the UTAT programme, the T106C blade with the wavy wire (approximated as a forward-backward facing step in the CFD approach) was instrumented with hot-film sensors. Consequently, the transition onset information is available. Figure 8.23 shows a good matching between the experimental transition onset positions and the CFD predictions. What is interesting to see is that the transition starts downstream of the local roughness location and move downstream at low $Re_{2,is}$. The presence of the local roughness has an impact on the development of the separation bubble process as it avoids to have a massive separation at low $Re_{2,is}$ (in comparison to the smooth blade case, see figure 6.17). Indeed, the local roughness induces a separation bubble that extends further at low $Re_{2,is}$ but still belongs to the short bubble type (see section 2.1.2.1). As a consequence, the boundary layer is able to withstand the strong adverse pressure gradient, which explains the gain in performance when looking at the kinetic losses (see figure 3.9).

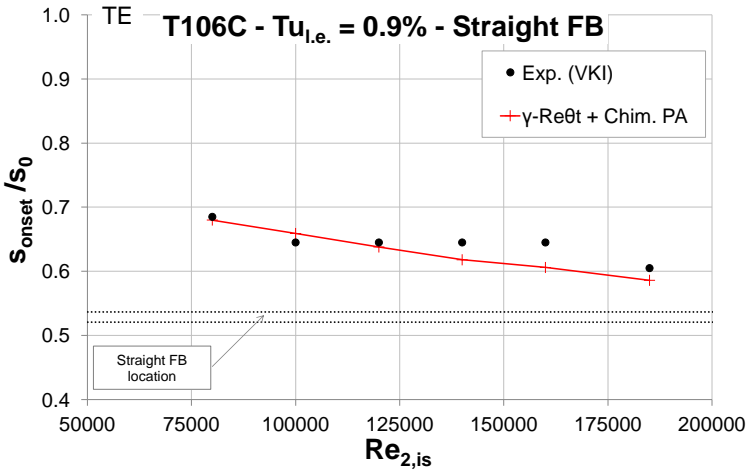


Figure 8.23.: Transition onset (s_{onset}/s_0) through the $Re_{2,is}$ range for the T106C at $Tu_{l.e.} = 0.9\%$ with the straight FB

8.4. Cylindrical wire investigations

The cylindrical wire case was performed with the IHC algorithm for the $Re_{2,is}$ ranging from 80000 to 185000. Table 8.2 sums up the geometrical and working conditions.

Similarly to the straight FB case, the mass-averaged kinetic losses (figure 8.24) and the mass-averaged outlet flow angle (figure 8.25) are predicted with a good confidence and particularly when looking at the trends. The isentropic Mach number distribution and the wake profile at two isentropic outlet Reynolds numbers (160000, see figures 8.26 and 8.27 and 100000, see figures 8.28 and 8.29) show interesting predictions. Indeed, the pressure drop caused by the local roughness blockage is retrieved on the suction side as well as the pressure recovery. Moreover, the wake profile is correctly predicted and illustrates the good boundary layer development occurring on the both sides of the blade. However, during the TATMo programme, no hot-film sensors were implemented on the blade featuring the cylindrical wire. Therefore, no information concerning the flow topology parameters such as the transition onset cannot be investigated.

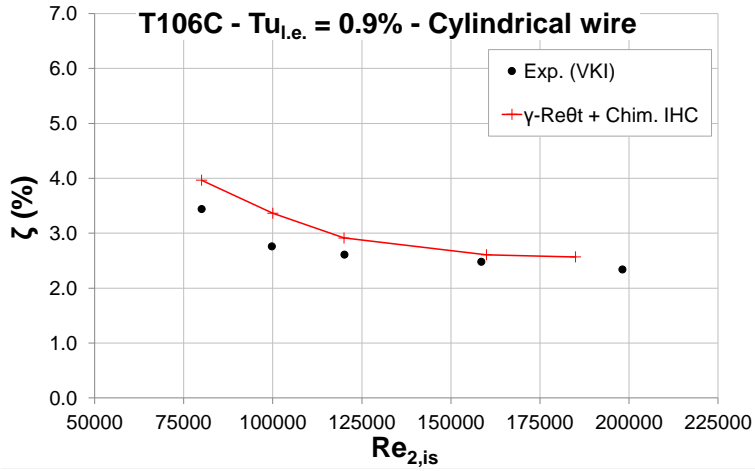


Figure 8.24.: T106C mass-averaged kinetic losses at $Tu_{l.e.} = 0.9\%$ with the cylindrical wire

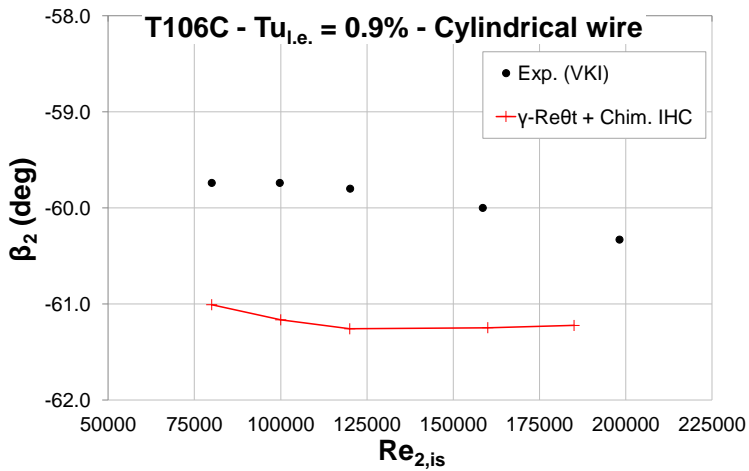


Figure 8.25.: T106C mass-averaged outlet flow angle at $Tu_{l.e.} = 0.9\%$ with the cylindrical wire

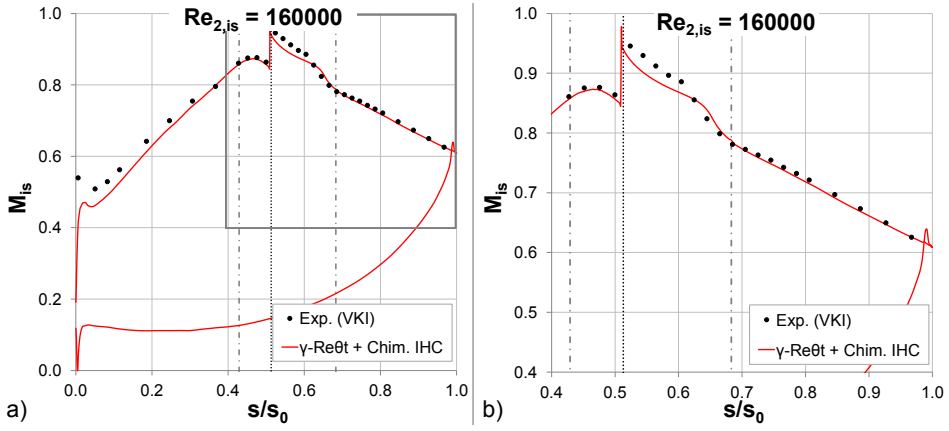


Figure 8.26.: T106C isentropic Mach number distribution at $Re_{2,is} = 160000$, $Tu_{l.e.} = 0.9\%$ and with the cylindrical wire - a) Full scale, b) Zoom in the aft region

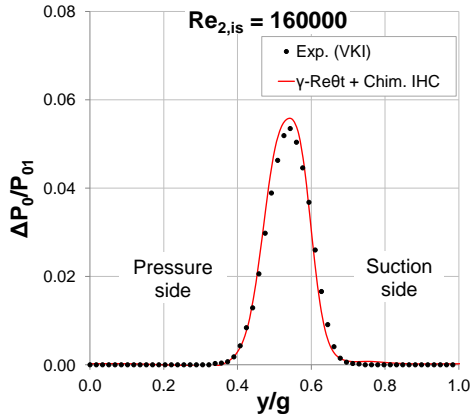


Figure 8.27.: T106C wake profile at $Re_{2,is} = 160000$, $Tu_{l.e.} = 0.9\%$ and with the cylindrical wire

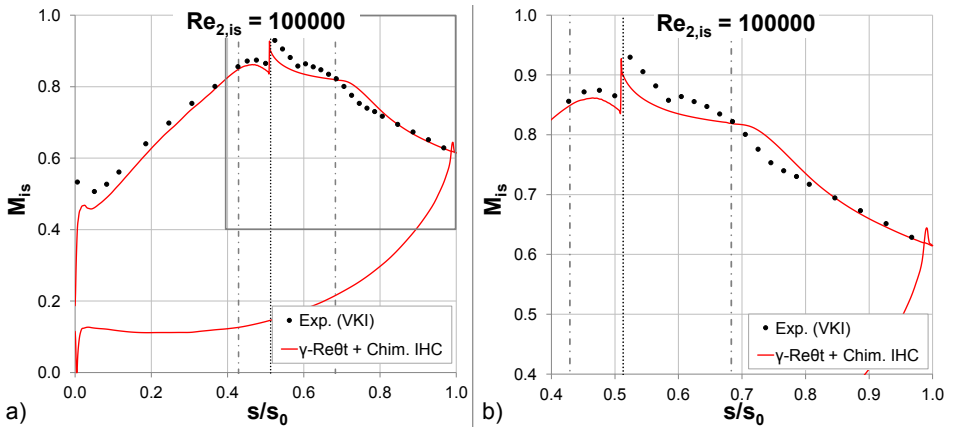


Figure 8.28.: T106C isentropic Mach number distribution at $Re_{2,is} = 100000$, $Tu_{l.e.} = 0.9\%$ and with the cylindrical wire - a) Full scale, b) Zoom in the aft region

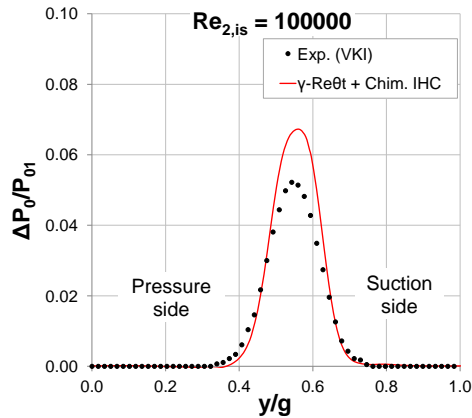


Figure 8.29.: T106C wake profile at $Re_{2,is} = 100000$, $Tu_{l.e.} = 0.9\%$ and with the cylindrical wire

8.5. Summary

This final chapter illustrates the investigation of passive control devices to improve the performance of HL-LPT blades at low isentropic outlet Reynolds number. The aim was to set a methodology to incorporate easily and with reliability a local roughness geometry in the CFD methodology presented in chapter 5.

The use of the Chimera technique coupled with the $\gamma\text{-}\widetilde{Re}_{\theta t}$ transition model gives great confidence in the flow topology prediction around the obstacle and the prediction of the onset of transition, even though the transition model was not calibrated for local roughness-induced transition.

In addition to the methodology, the passive control devices seem promising for the reduction of losses but should be evaluated with other working condition parameters (extended $Re_{2, is}$ range, different turbulence intensity levels representative of real machine environment, incoming wakes, ...).

Chapter 9.

Conclusions and recommendations

This thesis has presented the investigation of the separation-induced transition phenomenon occurring in a LPT environment. The study was primarily numerical, using CFD prediction tools, and relied as well on the analysis of data from experimental test campaigns.

9.1. Conclusions and contributions

Previous experimental campaigns, carried out in several VKI facilities in the frame of several programmes, feature nine LPT blades tested at different isentropic outlet Reynolds numbers, isentropic outlet Mach numbers, inlet turbulence intensity levels, with or without incoming wakes generated by the bars of a rotating disk and with two local roughness configurations. The LPT blades belong to different types of families from aft- to front-loaded, normal- and high-lift designs. These cases constitute a large and unique database.

Separation-induced transition: Bursting characterization

The main outcome of the experimental database analysis is the importance of the isentropic outlet Reynolds number on the performance. The LPT blade performance is quantified from the kinetic losses (resulting from the total pressure deficit in the wake downstream of the cascade). It is well-known that the deterioration of the performance at low $Re_{2,is}$ is associated to an increase in profile losses. At low $Re_{2,is}$, the profile losses are mainly driven by the occurrence of a separation bubble that will be detrimental. The bursting condition (where the separation bubble status changes from short to long) is a very important criterion for the designer. Consequently, the aim is to decrease as much as possible the isentropic outlet Reynolds number at bursting. As every blade of the database was tested at a low turbulence intensity (around 1%) and with homogeneous inlet conditions, the present work mainly looked into those conditions. Moreover, it seemed more reasonable to study the blade aerodynamic performance in a decoupled way. Indeed, from the database analysis, the increase of the turbulence level as well as incoming wakes tend to prevent the massive separation and the long bubble types

existing at low $Re_{2, is}$ and consequently improve the performance. This means that between two wake impingements the boundary layer is still prone to laminar separation and particularly in the case of high pitch-to-chord ratio (reduction of blade number policy). Moreover, in a purpose of comparison with a CFD RANS approach, the simulation of the incoming wakes is still questionable as the vortex shedding associated with the rotating bars might not be well reproduced since only the total pressure deficit and the turbulence scales could be set. Indeed, the flow around a bar is known to be difficult to solve with a RANS approach. It was observed that the separation bubble type affects the transition onset. The stronger the separation bubble is (long bubble and massive separation), the earlier is the transition onset. A correlation linking the isentropic outlet Reynolds number at bursting and the diffusion rate was established and features a linear relationship for the most comprehensive test cases.

Methodology to predict LPT flows

To get more insight into the flow topology with a prediction tool and to evaluate it, one needs to define a methodology accordingly. This was set thanks to the available measured turbulence information. Indeed, the turbulence scales condition the laminar separation process as seen from the database analysis. As a consequence, a determination of the decay of turbulence was carried out. The latter was the input of the CFD calculation and the predictions revealed to be in a good agreement with the experiments. This contributed to confirm the good calibration of the turbulence model used. A mesh investigation stressed the importance of the discretization of critical regions, such as the wake. Likewise, the transition modelling techniques were assessed and it emphasised the need for local models (such as the innovative $\gamma\text{-}\widetilde{Re}_{\theta t}$ transport equation model) in comparison to the conventional non-local transition criteria (such as the well known Abu-Ghannam and Shaw correlation or any other technique using a prescribed intermittency function).

Flow topology parameters for separated-flow transition

The methodology being set, the evaluation of the $\gamma\text{-}\widetilde{Re}_{\theta t}$ transition model revealed to be quite satisfactory. Indeed, the model behaved very well for mild diffusion rate LPT blades (such as the T108 and TX blades). Instead, for stronger diffusion rate LPT blades (such as the T106C, T2 and HIVK.HS blades), an adjustment of the turbulence scales at the inlet of the domain was necessary. As the laminar separation-induced transition could not be retrieved with the standard decay of turbulence, the aim was to trigger the laminar separation by lowering the turbulence intensity and consequently increasing the dissipation (ω) of the turbulent kinetic energy (k). This approach was successful as it allowed to simulate a long bubble and a massive separation with the expected influence on the transition onset. Attention was drawn to the investigation of the flow topology and the agreement was good while considering the evolution of the separation and

transition onset positions with respect to the isentropic outlet Reynolds number. Moreover, the predictions generally fell within the spatial uncertainty range of the sensors. In addition, the determination of the bursting condition from the predictions with correlations of the literature was a good procedure to assess existing correlations. Nevertheless, it turned out that the bursting condition extracted from this assessment was not totally satisfactory as these correlations were meant for incompressible flows over a flat plate.

Reliability and robustness of the Chimera technique

The defined methodology has demonstrated to be reliable and robust in comparison to the standard way of tackling transition with RANS equations. That is why a straightforward way to improve the performance of LPT blades with local roughness was investigated. Based on the aforementioned methodology, the investigation of the Chimera technique to ease the introduction of local roughness was studied and resulted to be reliable and robust in predicting the flow over a local obstacle, and more precisely the separation downstream of this obstacle as well as the local acceleration induced by this obstacle.

9.2. Recommendations and prospects

The purposes of the investigation were to define a reliable and robust numerical methodology to predict steady transition in a LPT environment and to get more insight into the flow topology with the help of detailed numerical information. The limits of the present numerical approach allow to provide recommendations for further work. Two types of recommendations are stressed. One deals with the numerical approach and the roots of the transition modelling implementation. The other one focuses on the topic and particularly on the correlation extension.

Numerical approach - Transition modelling

It has to be reminded that the CFD code used was provided by ONERA and was not open for implementation. Therefore the constants of the transition model could not be changed. Even though the job done by the ONERA is not questionable, it would be of interest to adjust the transition modelling for LPT cases or add new extra weighting functions. It was shown that the γ - $\widetilde{Re}_{\theta t}$ transition model was reliable in predicting flows for mild diffusion rate LPT blades but needed an adjustment of the inlet boundary conditions for stronger diffusion rates. Even though it constitutes a good alternative to predict the laminar separation-induced transition, it should not be in contradiction with the real flow characteristics measured in the facility. As the study focused more on the steady transition process, no incoming wakes calculation was performed. Even though the drawbacks of simulating the

incoming wakes was previously stressed, an attempt to assess the correlation process for multimode transition applications might be tried. The Chimera technique for the introduction of an overlapping mesh including an obstacle is a reliable tool. That is why investigating the benefits of innovative passive controls such as local roughness or cavity is definitely of interest for the designer in order to understand as a first approach which design performs better and where is the optimal location prior to the manufacturing of a mock-up. Moreover, this could be eased by the use of an optimization process. Investigations were done on elevated local roughness. However, depressed local roughness might be of interest as they allow to contain the separation bubble and reduce the thickening of the boundary layer. In addition, it is well-known that they allow to control shock-boundary layer interaction. Channels that connect the pressure side to the suction side are an alternative technique to generate jets and could then be investigated in the frame of boundary layer separation and transition control.

Correlation extension

About the correlation extension, there is an obvious need for more investigations of the momentum thickness. It was observed that most of the information lies in this parameter. Investigating this information in a high-speed cascade configuration turns out to be tricky particularly with the curvature of the blade. Moreover, one needs to have a probe which head diameter is smaller than the boundary layer thickness (at least one order of magnitude smaller) in order to get a good discretization of the velocity profile for integration. That is why a flattened total pressure probe could be considered even though it will introduce a higher blockage in the flow than a hot wire sensor. Still the hot wire supports are sources of disturbance. The advantage of the hot wire is its thickness (in the order of magnitude of the micron) which allows to explore the boundary layer whereas a conventional total pressure probe inner head size diameter is around 0.1 mm. Those two techniques could be used in a cascade configuration with the appropriate traversing mechanism. One major disadvantage of the aforementioned measurement techniques is their intrusive character. That is why non-intrusive techniques such as Particle Image Velocimetry and Laser Doppler Velocimetry are more convenient. However, one needs to set appropriately the optics and the optical access to the test section (lenses, glass endwall, ...). Another alternative is to reproduce a LPT blade pressure gradient with a flat plate and a diverged outer wall. This type of configuration was extensively used to build correlations at low-speed conditions (Abu-Ghannam and Shaw work and Hatman and Wang work). However, the effect of curvature on the boundary layer development is not negligible for LPT blades. Most likely, the use of the same measurement techniques would be eased in the latter configuration. However, an investigation with blades would provide more insights as no curvature effect was introduced in the correlations below the $\gamma-Re_{\theta t}$ transition model. The purpose of these recommended wind tunnel investigations is to extend the existing correlation of Abu-Ghannam and Shaw. Indeed,

this correlation constitutes the most comprehensive investigation of LPT blades and is still a reliable frame for further investigations and extensions. That is why investigations on more loaded LPT blades would be of interest in order to cover the laminar separation region that was not addressed in their work.

Appendix A.

Evaluation of the $\gamma\text{-}\widetilde{Re}_{\theta t}$ transition model: Additional LPT blade test cases

In addition to the test cases presented in chapter 6, three other LPT blades were studied in the CT2 facility (TD, TF and TG). These blades were investigated with similar conditions as the HIVK_HS (see section 6.5) by the same experimentalists. Consequently, the comment on the offsets present in both the kinetic losses and the outlet flow angle are still seen for the TD, TF and TG blades [4]. These blades were designed to operate with the same velocity triangulation, outlet Mach number and for a nominal Reynolds number of 190000 [16]. However, their pitch-to-chord ratio was gradually increased from the TD blade to the TG blade. Consequently, the profile losses are expected to increase in association to detrimental separation. In order to get more insight at the separation/transition phenomenon occurring at low $Re_{2,is}$, the numerical investigations were extended towards low $Re_{2,is}$ (80000 and 140000). Indeed, it helps understanding the influence of the separation bubble on the kinetic losses and on the outlet flow angle. The kinetic losses and the outlet flow angle are non-dimensionalised with respect to the experimental value at $Re_{2,is} = 650000$. The heat transfer coefficient distributions on the suction side do not exhibit the ordinate for confidentiality reasons imposed by the industrial partner. For each blade, the heat transfer coefficient distribution at two isentropic outlet Reynolds numbers are provided (650000 and 190000). What is more of interest in the present work is the separation effect on the transition process. That is why, the trends of the plots are sufficient for the present analysis.

A.1. TD LPT blade test case

The TD blade is the less loaded of the three aforementioned blades. In the database, this blade is characterised by a low Zweifel loading coefficient with a mild diffusion (see table 3.1). The mesh information is provided in table A.1.

The TD blade was assessed at the natural freestream turbulence intensity of the facility as well as at a higher turbulence intensity generated by a grid (3.5%). However, it turned out that the high turbulence intensity predictions did not

Table A.1.: TD LPT blade mesh information

Blade	TD
Number of {nodes ; cells} in one streamwise layer	{54581 ; 53408}
Minimum orthogonality (deg)	21.9
Number of cells in orthogonality intervals: {[18 deg ; 27 deg[; [27 deg ; 36 deg]} in one streamwise layer	{395 ; 818}
Maximum expansion ratio	1.55
Maximum y^+ on the blade {SS ; PS}	{1.47 ; 1.25}
Number of nodes around the blade	361
Number of nodes on the blade SS	256

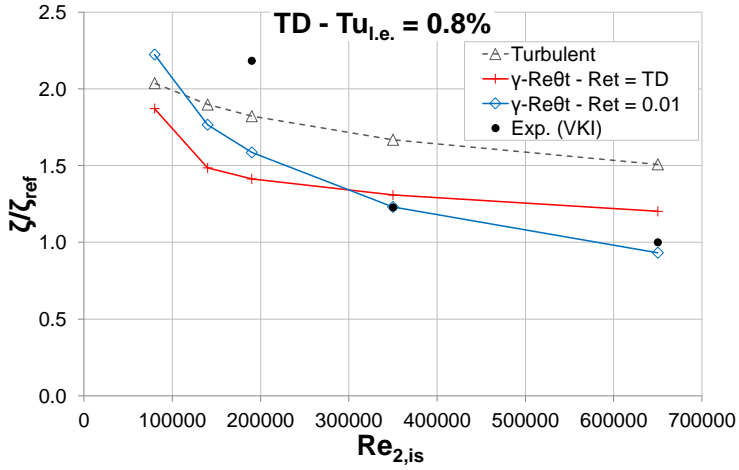
inspire confidence as at this high turbulence intensity, the transition was triggered too early (see the following discussion in section A.4). Moreover, some information were missing to have a complete assessment of the test matrix (kinetic losses, outlet flow angle or heat transfer coefficient). The working conditions at which the TD blade was evaluated are displayed in table A.2.

Table A.2.: TD LPT blade working conditions at the natural freestream turbulence intensity

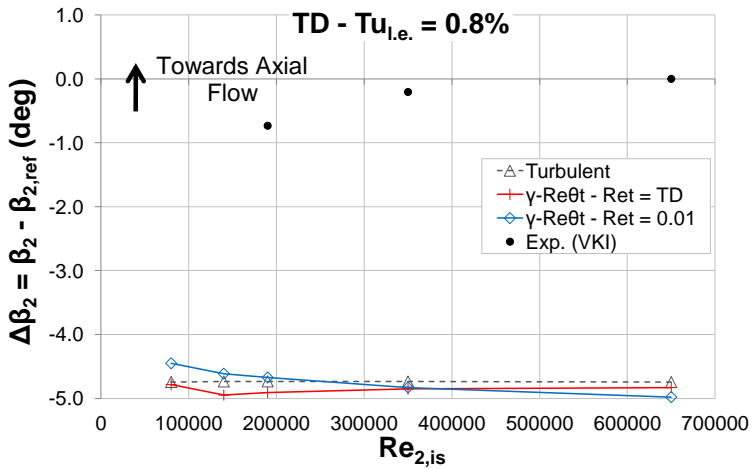
Blade	TD
Ψ	1.07
g/c	N/A
Loading	Aft
D_R	N/A
$M_{2,is}$	0.8
$Re_{2,is} (\times 10^3)$	[190 ; 650]
$Tu_{l.e.}(\%)$	0.8
Re_t	[33.2 ; 113.4]
Facility	CT2

The numerical predictions of the kinetic losses (see figure A.1) present a good agreement with the measurements and particularly when using the $Re_t = 0.01$ approach. Indeed, this trend follows the increase of the kinetic losses at low isentropic outlet Reynolds numbers as depicted by the experimental results.

Concerning the outlet flow angle (see figure A.2), the numerical predictions show a slight reduction of the turning at low $Re_{2,is}$ (around 0.5 degree). Instead, the experimental outlet flow angle illustrates a slight increase of the turning at low $Re_{2,is}$ (around 0.5 degree as well). This behaviour is not really expected. However, one has to remind that the angle measurement uncertainty is a bit more than 0.5

Figure A.1.: TD area-averaged kinetic losses at $Tu_{l.e.} = 0.8\%$

degree (see section 3.2.2). Consequently, a flat evolution of the outlet flow angle is rather consistent for this isentropic outlet Reynolds number range.

Figure A.2.: TD area-averaged outlet flow angle at $Tu_{l.e.} = 0.8\%$

The heat transfer coefficient h for two isentropic outlet Reynolds numbers (650000 and 190000) are presented in figure A.3 and allow to have a look in more details at the flow topology. The $Re_t = 0.01$ approach predicts a separation bubble for both $Re_{2,is}$. For the $Re_{2,is} = 650000$, the presence of a separation bubble is open to discussion. Indeed, at such a high isentropic Reynolds number, no

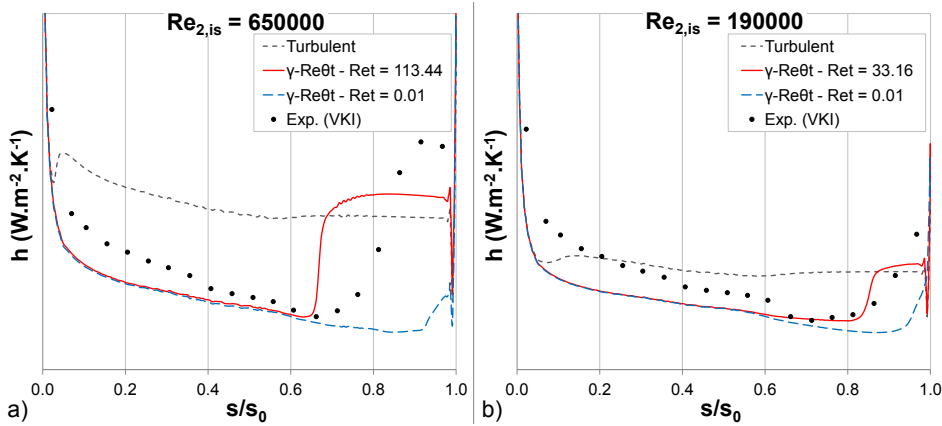


Figure A.3.: TD heat transfer coefficient on the blade suction side at $Tu_{l.e.} = 0.8\%$
 - a) $Re_{2,is} = 650000$ and b) $Re_{2,is} = 190000$

separation is expected. Moreover, the level of the minimum heat transfer coefficient (at $s/s_0 = 0.66$) is still high to conclude on the absence of separation. Instead, the $Re_{2,is} = 190000$ features a lower minimum heat transfer coefficient level (at $s/s_0 = 0.71$) and an inflectional point close to the minimum heat transfer coefficient that allow to conclude on the presence of a separation. In contrast, the $Re_t = TD$ approach predicts level of heat transfer coefficient similar to the experimental results but does not predict any separation (from the investigation of the numerical prediction of the wall-shear stress, not presented here). In addition, the level of the heat transfer coefficient for the $Re_t = 0.01$ approach in the aft part has not recovered as the level of the experimental results whereas the $Re_t = TD$ approach has recovered. This is due to the massive separation (for $Re_{2,is} = 190000$) and long bubble extension (for $Re_{2,is} = 650000$) predicted by the $Re_t = 0.01$ approach.

A.2. TF LPT blade test case

The TF blade has a mid Zweifel loading coefficient with a mild diffusion (see table 3.1). The mesh information is provided in table A.3 and the working conditions at which the TF blade was evaluated are displayed in table A.4.

The conclusions on the kinetic losses (see figure A.4) and the outlet flow angle (see figure A.5) are the same as the ones already stressed for the TD blade.

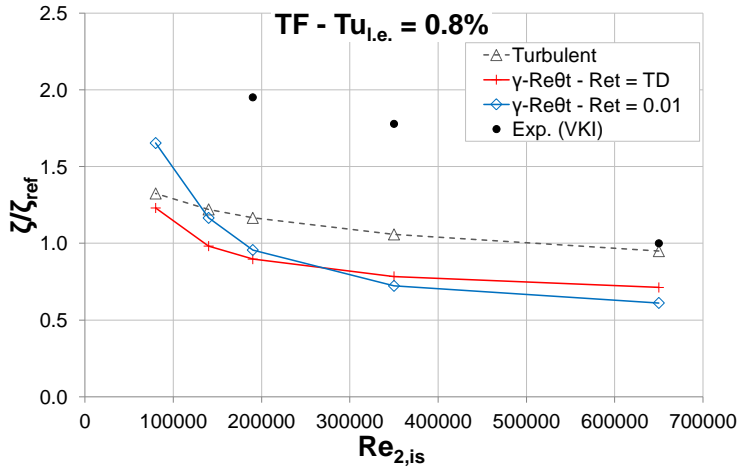
Concerning the heat transfer coefficient analysis (see figure A.6), the conclusions are again the same except that for the $Re_t = 0.01$ approach, the heat transfer coefficient experiences a recovery which is corroborated by the wall-shear stress

Table A.3.: TF LPT blade mesh information

Blade	TF
Number of {nodes ; cells} in one streamwise layer	{54581 ; 53408}
Minimum orthogonality (deg)	20.4
Number of cells in orthogonality intervals: {[18 deg ; 27 deg[; [27 deg ; 36 deg[} in one streamwise layer	{577 ; 844}
Maximum expansion ratio	1.56
Maximum y^+ on the blade {SS ; PS}	{1.46 ; 1.40}
Number of nodes around the blade	361
Number of nodes on the blade SS	256

Table A.4.: TF LPT blade working conditions at the natural freestream turbulence intensity

Blade	TF
Ψ	1.19
g/c	N/A
Loading	Aft
D_R	N/A
$M_{2,is}$	0.8
$Re_{2,is} (\times 10^3)$	[190 ; 650]
$Tu_{l.e.} (\%)$	0.8
Re_t	[33.2 ; 113.4]
Facility	CT2


Figure A.4.: TF area-averaged kinetic losses at $Tu_{l.e.} = 0.8\%$

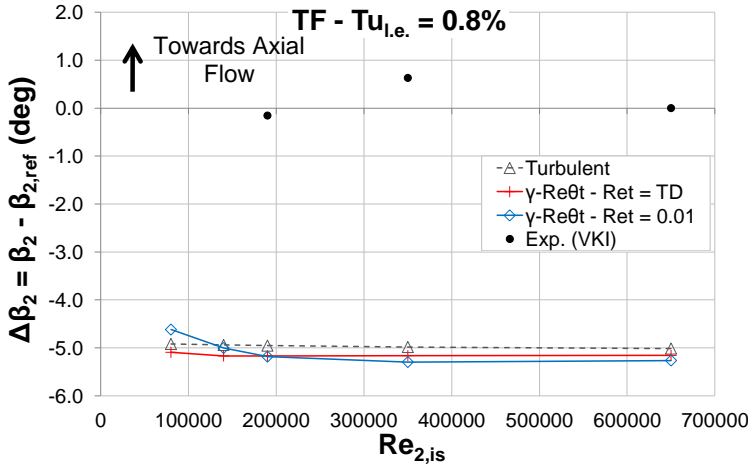


Figure A.5.: TF area-averaged outlet flow angle at $Tu_{i.e.} = 0.8\%$

numerical prediction (not presented here) where for both $Re_{2, is}$, a close separation bubble exists. What is more interesting from this $Re_t = 0.01$ approach is that the level of the heat transfer coefficient, in the aft region, is similar to the experimental results level and the gradients are comparable.

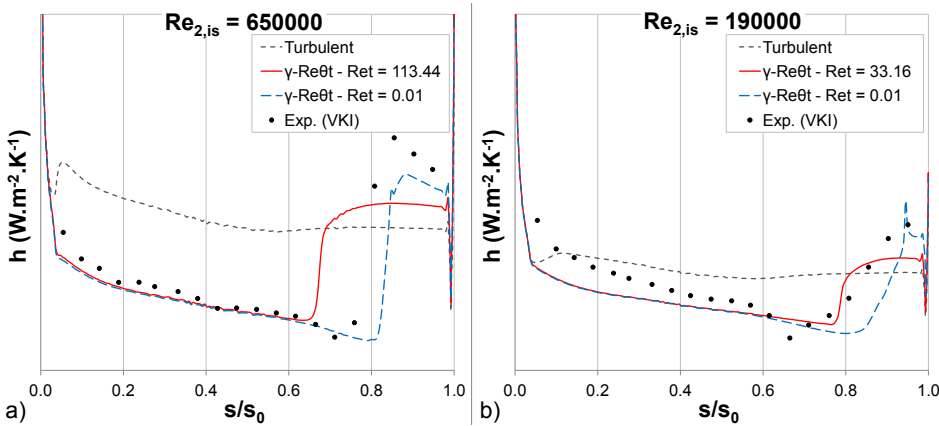


Figure A.6.: TF heat transfer coefficient on the blade suction side at $Tu_{i.e.} = 0.8\%$
 - a) $Re_{2, is} = 650000$ and b) $Re_{2, is} = 190000$

A.3. TG LPT blade test case

The TG blade has a high Zweifel loading coefficient with a strong diffusion (see table 3.1). The mesh information is provided in table A.5 and the working conditions at which the TG blade was evaluated are displayed in table A.6.

Table A.5.: TG LPT blade mesh information

Blade	TG
Number of {nodes ; cells} in one streamwise layer	{54581 ; 53408}
Minimum orthogonality (deg)	25.0
Number of cells in orthogonality intervals: {[18 deg ; 27 deg] ; [27 deg ; 36 deg]} in one streamwise layer	{126 ; 1348}
Maximum expansion ratio	1.71
Maximum y^+ on the blade {SS ; PS}	{1.45 ; 1.36}
Number of nodes around the blade	361
Number of nodes on the blade SS	256

Table A.6.: TG LPT blade working conditions at the natural freestream turbulence intensity

Blade	TG
Ψ	1.35
g/c	N/A
Loading	Aft
D_R	N/A
$M_{2,is}$	0.8
$Re_{2,is} (\times 10^3)$	[190 ; 650]
$Tu_{i.e.} (%)$	0.8
Re_t	[33.2 ; 113.4]
Facility	CT2

The kinetic losses (see figure A.7) experience a strong increase at low $Re_{2,is}$. It is corroborated by the heat transfer coefficient at $Re_{2,is} = 190000$ where the separation position is moved upstream (at $s/s_0 = 0.53$) and the increase in h is smoother thereafter (see figure A.9). This latter fact may be an indication of a massive separation.

Concerning the outlet flow angle (see figure A.8), the experimental results show an increase of the turning from $Re_{2,is} = 650000$ to $Re_{2,is} = 350000$ and a decrease of the turning from $Re_{2,is} = 350000$ to $Re_{2,is} = 190000$. The variation is pretty small (around 1 degree). Again, one could consider this variation as a measurement

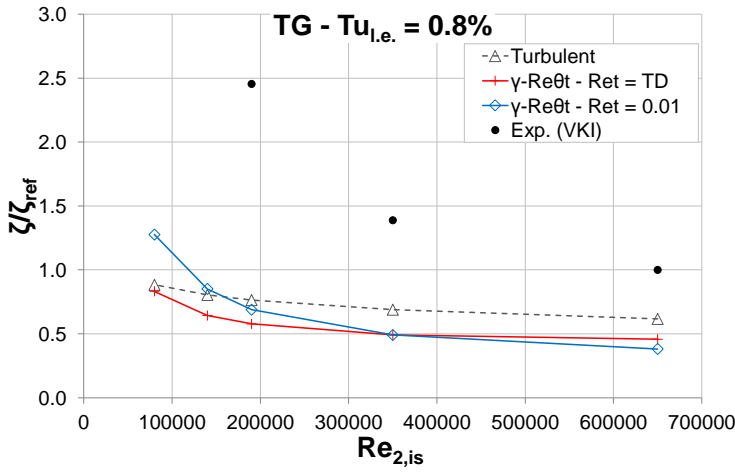


Figure A.7.: TG area-averaged kinetic losses at $Tu_{l.e.} = 0.8\%$

uncertainty fact. Otherwise another explanation might be that at high isentropic outlet Reynolds number, the boundary layer on the suction side has fully developed as a turbulent boundary layer which thickness has an impact on the turning.

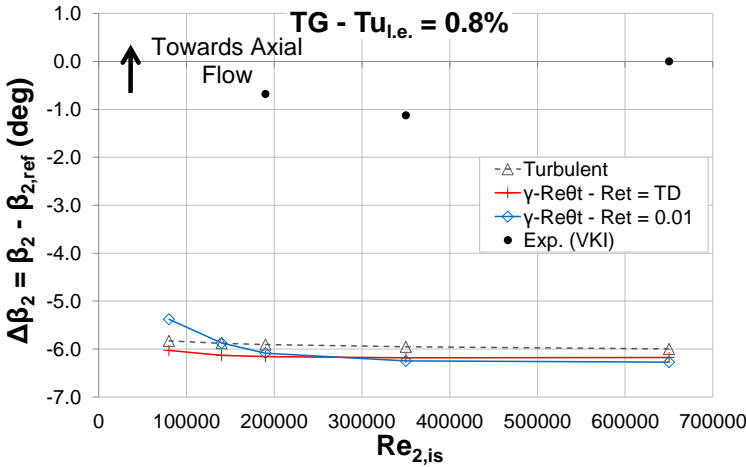


Figure A.8.: TG area-averaged outlet flow angle at $Tu_{l.e.} = 0.8\%$

About the heat transfer coefficient distribution (see figure A.9), one can see again the good level prediction in the aft region of the $Re_t = 0.01$ approach as well as the separation prediction.

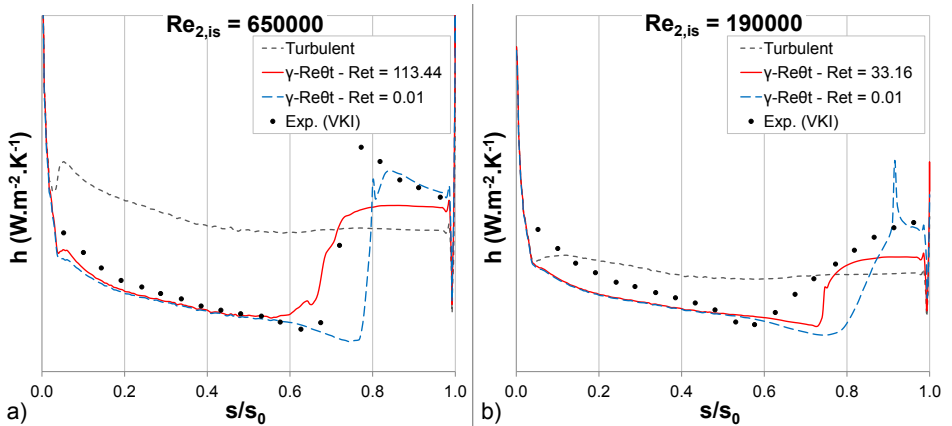


Figure A.9.: TG heat transfer coefficient on the blade suction side at $Tu_{l.e.} = 0.8\%$
 - a) $Re_{2,is} = 650000$ and b) $Re_{2,is} = 190000$

A.4. Comments about the numerical predictions at a turbulence intensity generated by a grid (3.5%)

As briefly indicated in sections 6.5 and A.1, the numerical predictions of the heat transfer coefficient at a turbulence intensity generated by a grid (3.5%) did not succeed to catch the boundary layer evolution on the blade suction side according to the analysis of the measurements of h .

The heat transfer coefficient distributions at $Tu_{l.e.} = 3.5\%$ and $Re_{2,is} = 190000$ for the TD and TG blades are presented in figure A.10. The experimental results feature a separation for both configurations. This is visible from the level of h as well as the inflection point before the minimum level of h . In contrast, the numerical predictions do not present a separation as the level of h is higher than the experimental results and the transition starts earlier. This is verified in the numerical wall-shear stress distributions (not presented here).

Similarly, the heat transfer coefficient distribution at $Tu_{l.e.} = 3.5\%$ and $Re_{2,is} = 90000$ for the HIVK_HS blade is presented in figure A.11 on the blade suction side. At this low isentropic outlet Reynolds number, it is expected to have a glimpse at the separation phenomenon. Instead, the prediction reveals no presence of a separation (which is corroborated from the wall-shear stress information, not presented here). Indeed, the predicted boundary layer transitions around $s/s_0 = 0.4$. As the prediction at the lowest isentropic outlet Reynolds number does not feature a separation, there is no confidence in the high turbulence intensity predictions on the whole $Re_{2,is}$ range.

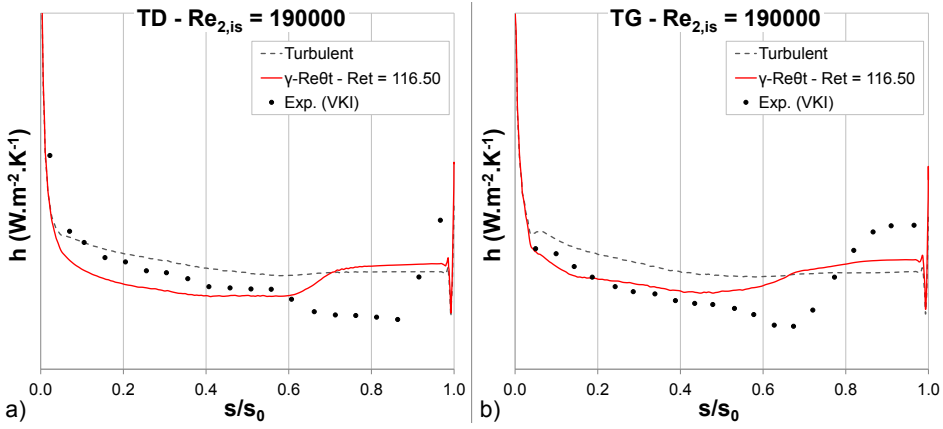


Figure A.10.: Heat transfer coefficient on two blades suction side at $Re_{2,is} = 190000$ and $Tu_{l.e.} = 3.5\%$ - a) TD and b) TG

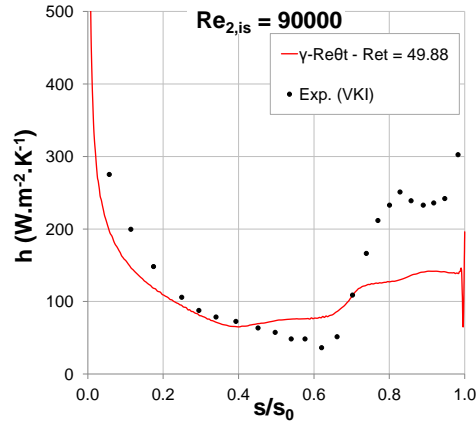


Figure A.11.: HIVK_HS heat transfer coefficient on the blade suction side at $Re_{2,is} = 90000$ and $Tu_{l.e.} = 3.5\%$

Consequently, the evaluation and the investigation of the test cases, assessed in the CT2 facility where the turbulence intensity level is 3.5%, will not be discussed in this work as the predictions are not satisfactory for the aim of separation-induced transition.

Bibliography

Each reference is followed by the list of the pages where it is cited.

- [1] B. J. Abu-Ghannam and R. Shaw. Natural Transition of Boundary Layers - The Effects of Turbulence, Pressure Gradient and Flow History. *Journal Mechanical Engineering Science*, 22(5):213–228, 1980. xxii, xxiii, 23, 34, 35, 36, 37, 39, 100, 101, 111, 145, 162, 165
- [2] D. G. Ainley and G. C. R. Mathieson. A Method of Performance Estimation for Axial-Flows Turbines. Reports and Memoranda 2974, British Aeronautical Research Council, December 1951. 64, 67
- [3] D. G. Ainley and G. C. R. Mathieson. An Examination of the Flow and Pressure Losses in Blade Rows of Axial-Flow Turbines. Reports and Memoranda 2891, British Aeronautical Research Council, March 1951. 64
- [4] T. Arts. Private Communications. September 2012. 134, 199
- [5] T. Arts and M. Monaldi. Private Communications. September 2010. 46
- [6] J. Babajee. Modeling and Analysis of the Laminar to Turbulent Transition in a Low-Pressure Turbine. In *2nd VKI PhD Symposium*, Rhode-saint-Genèse, Belgium, March 1-3, 2011. 100
- [7] J. Baumann, M. Rose, T. Ries, S. Staudacher, and U. Rist. Actuated Transition in a LP Turbine Laminar Separation: An Experimental Approach. In *ASME Turbo Expo 2011: Power for Land, Sea and Air*, number GT2011-45852, Vancouver, British Columbia, Canada, June 6-10, 2011. 28
- [8] A. Benyahia, L. Castillon, and R. Houdeville. Prediction of Separation-Induced Transition on High Lift Low Pressure Turbine Blade. In *ASME Turbo Expo 2011: Power for Land, Sea and Air*, number GT2011-45566, Vancouver, British Columbia, Canada, June 6-10, 2011. 109, 112, 113
- [9] A. Binder, W. Förster, H. Kruse, and H. Rogge. An Experimental Investigation Into the Effect of Wakes on the Unsteady Turbine Rotor Flow. *ASME Journal of Engineering for Gas Turbines and Power*, 107(2):458–466, April 1985. 19

- [10] L. Cambier and J.-P. Veillot. Status of the elsA CFD software for flow simulation and multidisciplinary applications. In *46th AIAA Aerospace Science Meeting and Exhibit*, number AIAA 2008-664, Reno, Nevada, USA, January 7-10, 2008. 87
- [11] P. Chassaing. *Turbulence en mécanique des fluides - Analyse du phénomène en vue de sa modélisation à l'usage de l'ingénieur*. Cépaduès-Éditions, 1st edition, August 2000. 93
- [12] S. Chen. A Loss Model for the Transonic Flow Low-Pressure Steam Turbine Blades. *IMEchE*, C269:145–155, 1987. 65
- [13] C. Content and R. Houdeville. Application of the γ - R_θ laminar-turbulent transition model in Navier-Stokes computations. In *AIAA 40th Fluid Dynamics Conference and Exhibit*, number AIAA 2010-4445, Chicago, Illinois, USA, June 28 - July 4, 2010. 38, 39
- [14] T. C. Corke. Dielectric Barrier Discharge Plasma Actuators. *von Karman Institute for Fluid Dynamics Lecture Series*, 2011-02, February 21-24, 2011. 28
- [15] R. Corral and F. Gisbert. Prediction of Separated-Induced Transition Using a Correlation-Based Transition Model. In *ASME Turbo Expo 2010: Power for Land, Sea and Air*, number GT2010-23239, Glasgow, UK, June 14-18, 2010. 40, 109
- [16] T. Coton. *Unsteady Wake-Boundary Layer Interaction on Advanced High Lift Low Pressure Turbine Airfoils*. PhD thesis, Université Libre de Liège, December 2003. 9, 20, 47, 48, 49, 50, 55, 57, 91, 128, 130, 131, 133, 134, 151, 152, 199
- [17] E. M. Curtis, H. P. Hodson, M. R. Banieghbal, J. D. Denton, R. J. Howell, and N. W. Harvey. Development of Blade Profiles for Low Pressure Turbine Applications. *ASME Journal of Turbomachinery*, 119(3):531–538, July 1997. 8
- [18] P. de la Calzada. Aerothermodynamic design of low pressure turbines. *von Karman Institute for Fluid Dynamics Lecture Series*, 2008-03, March 3-7, 2008. xxi, 3, 5
- [19] X. de Saint-Victor. Sensitivity of Numerical Simulations of Low-Reynolds Number Flow over the T106 Turbine Blade. In *ASME Turbo Expo 2010: Power for Land, Sea and Air*, number GT2010-22903, Glasgow, UK, June 14-18, 2010. 88
- [20] E. Dick. Eddy Viscosity Models for Turbulence and Transition. *von Karman Institute for Fluid Dynamics Lecture Series*, 2009-08, September 21-25, 2009. 29, 30, 40

-
- [21] A. J. Dietz and R. W. Ainsworth. Unsteady Pressure Measurements on the Rotor of a Model Turbine Stage in a Transient Flow Facility. In *ASME International Gas Turbine & Aeroengine Congress & Exposition*, number 92-GT-156, Cologne, Germany, June 1-4, 1992. xxi, 19, 20
- [22] J. Dunham and P. M. Came. Improvements to the Ainley-Mathieson Method of Turbine Performance Prediction. *ASME Journal of Engineering for Power*, 92(3):252–256, July 1970. 64, 65, 67
- [23] W. Elsner, W. Piotrowski, and P. Warzecha. Transition Modelling with Intermittency Transport Equations. In *ERCOFTAC Bulletin 80*, pages 49–52, 2009. 38
- [24] H. W. Emmons. The Laminar-Turbulent Transition in a Boundary Layer - Part I. *Journal of Aeronautical Sciences*, 18:490–498, July 1951. xxi, 13, 14, 15
- [25] S. Farokhi. *Aircraft Propulsion*. John Wiley & Sons, 2009. 1
- [26] M. Gaster. The Structure and Behaviour of Laminar Separation Bubbles. Technical Report NPL Aero Report 1181, ARC 28 226, National Physical Laboratory, August 1966. xxi, 17
- [27] A. Hatman and T. Wang. Separated-Flow Transition. Part 1 - Experimental Methodology and Mode Classification. In *ASME International Gas Turbine & Aeroengine Congress & Exhibition*, number 98-GT-461, Stockholm, Sweden, June 2-5, 1998. 18, 70, 75
- [28] A. Hatman and T. Wang. Separated-Flow Transition. Part 2 - Experimental Results. In *ASME International Gas Turbine & Aeroengine Congress & Exhibition*, number 98-GT-462, Stockholm, Sweden, June 2-5, 1998. 18, 70, 75
- [29] A. Hatman and T. Wang. Separated-Flow Transition. Part 3 - Primary Modes and Vortex Dynamics. In *ASME International Gas Turbine & Aeroengine Congress & Exhibition*, number 98-GT-463, Stockholm, Sweden, June 2-5, 1998. 18, 70, 75
- [30] A. Hatman and T. Wang. A Prediction Model for Separated-Flow Transition. *ASME Journal of Turbomachinery*, 121(3):594–602, July 1999. xxvii, 18, 70, 75, 145, 146, 148, 149, 151, 153, 154, 156, 157, 159, 160, 161, 165
- [31] C. G. Himmel and H. P. Hodson. Modifying Ultra-High Lift Low Pressure Turbine Blades for Low Reynolds Number Applications. In *12th International Symposium on Unsteady Aerodynamics, Aeroacoustics & Aeroelasticity of Turbomachines (ISUAAAT12)*, number I12-S7-3, Imperial College London, UK, September 1-4, 2009. xxi, 25, 26, 27
-

- [32] C. G. Himmel and H. P. Hodson. Passive Air Jets for Loss Reductions in High Lift Low Pressure Turbines. In *ISABE*, number 1295, 2009. 26
- [33] C. Hirsch. Numerical Methods in Turbomachinery: Fundamentals. *von Karman Institute for Fluid Dynamics Lecture Series*, 2009-08, September 21-25, 2009. 88
- [34] H. P. Hodson and R. J. Howell. The Role of Transition in High Lift Low Pressure Turbines. *von Karman Institute for Fluid Dynamics Lecture Series*, 2005-03 (2005), April 25-29, 2005. 5, 6
- [35] J. Hourmouziadis. Aerodynamic Design of Low Pressure Turbines. *AGARD Lecture Series*, 167 (1989), 1989. xxi, 6, 7, 8, 145, 162
- [36] R. Houtermans, T. Coton, and T. Arts. Aerodynamic Performance of a Very High Lift LP Turbine Blade with Emphasis on Separation Prediction. In *ASME Turbo Expo 2003: Power for Land, Sea and Air*, number GT2003-38802, Atlanta, Georgia, USA, June 16-19, 2003. 47
- [37] R. J. Howell, O. N. Ramesh, H. P. Hodson, N. W. Harvey, and V. Schulte. High Lift and Aft-Loaded Profiles for Low-Pressure Turbines. *ASME Journal of Turbomachinery*, 123(2):181–188, April 2001. 8
- [38] J. Huang, T. C. Corke, and F. O. Thomas. Plasma Actuators for Separation Control of Low-Pressure Turbine Blades. *AIAA Journal*, 44(1):51–57, January 2006. 28
- [39] D. Jackson and B. Launder. Osborne Reynolds and the Publication of His Papers on Turbulent Flow. *The Annual Review of Fluid Mechanics*, 39:19–35, 2007. 29
- [40] D. Japikse. Turbomachinery Performance Modeling. In *SAE World Congress and Exhibition 2009*, number 2009-01-0307, Detroit, Michigan, United States, April 20, 2009. 63, 64, 65
- [41] S. C. Kacker and U. Okapuu. A Mean Line Prediction Method for Axial Flow Turbine Efficiency. *ASME Journal of Engineering for Power*, 104(1):111–119, January 1982. 64, 65, 67
- [42] J. Kurzke. Preliminary Design. *von Karman Institute for Fluid Dynamics Lecture Series*, 2008-03, March 3-7, 2008. xxi, 5
- [43] R. B. Langtry. *A Correlation-Based Transition Model using Local Variables for Unstructured Parallelized CFD codes*. PhD thesis, Universität Stuttgart, May 31, 2006. 36, 39, 40, 47
- [44] R. B. Langtry and F. R. Menter. Correlation-Based Transition Modeling for Unstructured Parallelized Computational Fluid Dynamics Codes. *AIAA Journal*, 47(12):2894–2906, December 2009. 9, 34, 36, 38, 39, 93

-
- [45] R. B. Langtry, F. R. Menter, S. R. Likki, Y. B. Suzen, P. G. Huang, and S. Völker. A Correlation-Based Transition Model Using Local Variables - Part II: Test Cases and Industrial Applications. *ASME Journal of Turbomachinery*, 128(3):423–434, July 2006. 36
- [46] S. Lardeau, N. Li, and M. A. Leschziner. Large Eddy Simulation of Transitional Boundary Layers at High Free-Stream Turbulence Intensity and Implications for RANS Modeling. *ASME Journal of Turbomachinery*, 129(2):311–317, April 2007. 34, 40
- [47] J. R. Llobet, J. Babajee, and T. Arts. Investigation of the Roughness Strip Effects on the Separation-Induced Transition with the $\gamma\text{-}\widetilde{Re}_{\theta t}$ Transition Model on a High-Lift Low-Pressure Turbine Rotor Blade at Steady Conditions. In *10th European Conference on Turbomachinery Fluid Dynamics and Thermodynamics*, Lappeenranta, Finland, April 15-19, 2013. 168
- [48] J. R. Llobet Gómez. Low Reynolds Prediction of the Flow in Low Pressure Turbines. Project report 2012-23, von Karman Institute for Fluid Dynamics, June 2012. 168
- [49] P. Malan, K. Suluksna, and E. Juntasaro. Calibrating the $\gamma\text{-}Re_{\theta}$ Transition Model. In *ERCRAFTAC Bulletin 80*, pages 53–57, 2009. 38
- [50] E. Malkiel and R. E. Mayle. Transition in a Separation Bubble. *ASME Journal of Turbomachinery*, 118(4):752–759, October 1996. 16
- [51] R. E. Mayle. Fundamental Aspects of Boundary Layers and Transition in Turbomachines. *von Karman Institute for Fluid Dynamics Lecture Series*, 1991-06 (1991), September 2-6, 1991. 24
- [52] R. E. Mayle. The Role of Laminar-Turbulent Transition in Gas Turbine Engines. *ASME Journal of Turbomachinery*, 113(4):509–537, October 1991. xxi, 15, 22, 23, 24, 34, 145, 162, 165
- [53] R. E. Mayle and A. Schulz. The Path to Predicting Bypass Transition. *ASME Journal of Turbomachinery*, 119(3):405–411, July 1997. 40
- [54] F. R. Menter. Two-Equation Eddy-Viscosity Turbulence Models for Engineering Applications. *AIAA Journal*, 32(8):1598–1605, August 1994. 32
- [55] F. R. Menter, R. B. Langtry, S. R. Likki, Y. B. Suzen, P. G. Huang, and S. Völker. A Correlation-Based Transition Model Using Local Variables - Part I: Model Formulation. *ASME Journal of Turbomachinery*, 128(3):413–422, July 2006. 36, 38, 39, 111
- [56] J. Michálek, A. Ilikan, and T. Arts. A Comparison of High and Low Speed Aerodynamic Performance of a Very High Lift Low-Pressure Turbine Airfoil
-

- (T108) at Low Reynolds Numbers: Experimental Analysis and Numerical Prediction. In *9th European Conference on Turbomachinery Fluid Dynamics and Thermodynamics*, Istanbul, Turkey, March 21-25, 2011. 46
- [57] J. Michálek, M. Monaldi, and T. Arts. Aerodynamic Performance of a Very High Lift Low Pressure Turbine Airfoil (T106C) at Low Reynolds and High Mach Number with Effect of Free Stream Turbulence Intensity. In *ASME Turbo Expo 2010: Power for Land, Sea and Air*, number GT2010-22884, Glasgow, UK, June 14-18, 2010. 45, 46, 47, 91, 93, 94
- [58] ONERA. *elsA User's Reference Manual, v.3.3*, December 2009. 88, 89
- [59] ONERA. *elsA Theoretical Manual, v.2.1*, February 2010. 33, 34, 87, 88, 90, 169, 174
- [60] R. Pacciani, M. Marconcini, A. Arnone, and F. Bertini. A CFD Study of Low Reynolds Number Flow in High Lift Cascades. In *ASME Turbo Expo 2010: Power for Land, Sea and Air*, number GT2010-23300, Glasgow, UK, June 14-18, 2010. 109, 113
- [61] H. Pfeil, R. Herbst, and T. Schröder. Investigation of the Laminar-Turbulent Transition of Boundary Layers Disturbed by Wakes. *ASME Journal of Engineering for Power*, 105(1):130–137, January 1983. xxi, 13, 14, 19, 21
- [62] W. Piotrowski, W. Elsner, and S. Drobniak. Transition Prediction on Turbine Blade Profile with Intermittency Transport Equation. In *ASME Turbo Expo 2008: Power for Land, Sea and Air*, number GT2008-50796, Berlin, Germany, June 9-13, 2008. 38
- [63] P. Pucher and R. Göhl. Experimental Investigation of Boundary Layer Separation with Heated Thin-Film Sensors. *ASME Journal of Turbomachinery*, 109(2):303–309, April 1987. 47
- [64] R. B. Rivir, J. P. Johnston, and J. K. Eaton. Heat Transfer on a Flat Surface Under a Region of Turbulent Separation. *ASME Journal of Turbomachinery*, 116(1):57–62, January 1994. 49
- [65] W. B. Roberts. *A Study of the Effect of Reynolds number and Laminar Separation Bubbles on the Flow through Axial Compressor Cascades*. PhD thesis, Université Libre de Bruxelles, May 1973. xxi, 16, 17
- [66] Rolls-Royce plc. *The Jet Engine*. 2005. ISBN 0 902121 2 35. 1, 2, 4
- [67] G. B. Schubauer and P. S. Klebanoff. Contributions on the Mechanics of Boundary-Layer Transition. Technical Report 1289, National Advisory Committee for Aeronautics, 1956. xxi, 13
- [68] C. H. Sieverding. Private Communications. June 2005. 122

-
- [69] C. H. Sieverding, C. Bagnera, A. C. Boege, J. A. Cordero Antòn, and V. Luère. Investigation of the Effectiveness of Various Types of Boundary Layer Transition Elements of Low Reynolds Number Turbine Bladings. In *ASME Turbo Expo 2004: Power for Land, Sea and Air*, number GT2004-54103, Vienna, Austria, June 14-17, 2004. xxi, 27, 28
- [70] P. R. Spalart and C. L. Rumsey. Effective Inflow Conditions for Turbulence Models in Aerodynamic Calculations. *AIAA Journal*, 45(10):2544–2553, October 2007. 93, 100
- [71] J. Steelant and E. Dick. Modeling of Laminar-Turbulent Transition for High Freestream Turbulence. *ASME Journal of Fluids Engineering*, 123:22–30, March 2001. 145, 162, 163
- [72] R. D. Stieger. *The Effects of Wakes on Separating Boundary Layers in Low Pressure Turbines*. PhD thesis, University of Cambridge, 2002. 9
- [73] E. R. van Driest and C. B. Blumer. Boundary Layer Transition: Freestream Turbulence and Pressure Gradient Effects. *AIAA Journal*, 1(6):1303–1306, June 1963. 36
- [74] M. Vera, X. F. Zhang, H. P. Hodson, and N. Harvey. Separation and Transition Control on an Aft-Loaded Ultra-High-Lift LP Turbine Blade at Low Reynolds Numbers: High-Speed Validation. *ASME Journal of Turbomachinery*, 129(2):340–347, April 2007. 24, 27, 28
- [75] R. J. Volino, O. Kartuzova, and M. B. Ibrahim. Experimental and Computational Investigations of Low-Pressure Turbine Separation Control Using Vortex Generator Jets. In *ASME Turbo Expo 2009: Power for Land, Sea and Air*, number GT2009-59983, Orlando, Florida, USA, June 8-12, 2009. 28
- [76] D. K. Walters and D. Cokljat. A Three-Equation Eddy-Viscosity Model for Reynolds-Averaged Navier-Stokes Simulations of Transitional Flow. *ASME Journal of Fluids Engineering*, 130(12):121401.1–121401.14, December 2008. 34, 40
- [77] F. M. White. *Viscous Fluid Flow*. McGraw-Hill, 2nd edition, 1991. xxi, 12
- [78] D. C. Wilcox. *Turbulence Modeling for CFD*. DCW Industries, Inc., La Cañada, 1993. 29, 30, 31, 32, 34
- [79] G. Wilfert. Geared Fan. *von Karman Institute for Fluid Dynamics Lecture Series*, 2008-03, March 3-7, 2008. 3, 4
- [80] D. C. Wisler. The Technical and Economical Relevance of Understanding Blade Row Interactions Effects in Turbomachinery. *von Karman Institute for Fluid Dynamics Lecture Series*, 1998-02, February 9-12, 1998. 8
-

- [81] X. F. Zhang, A. Mahallati, and S. A. Sjolander. Hot-Film Measurements of Boundary Layer Transition, Separation and Reattachment on a Low-Pressure Turbine Airfoil at Low Reynolds Numbers. In *38th AIAA/ASME/SAE/ASEE Joint Propulsion Conference and Exhibit*, number AIAA 2002-3643, Indianapolis, Indiana, USA, July 7-10, 2002. 47
- [82] X. F. Zhang, M. Vera, H. P. Hodson, and N. Harvey. Separation and Transition Control on an Aft-Loaded Ultra-High-Lift LP Turbine Blade at Low Reynolds Numbers: Low-Speed Investigation. *ASME Journal of Turbomachinery*, 128(3):517–527, July 2006. 28

List of Publications

J. Babajee. Modelling and Analysis of the Laminar to Turbulent Transition in a Low-Pressure Turbine. In *1st VKI PhD Symposium*, Rhode-saint-Genèse, Belgium, March 1-3, 2010.

Reference used in Chapters 1 and 2.

J. Babajee. Modelling and Analysis of the Laminar to Turbulent Transition in a Low-Pressure Turbine. In *2nd VKI PhD Symposium*, Rhode-saint-Genèse, Belgium, March 1-3, 2011.

Reference used in Chapters 2, 4 and 5.

J. Babajee. Modelling and Analysis of the Laminar to Turbulent Transition in a Low-Pressure Turbine. In *3rd VKI PhD Symposium*, Rhode-saint-Genèse, Belgium, March 5-7, 2012.

Reference used in Chapters 6 and 7.

J. Babajee and T. Arts. Investigation of the Laminar Separation-Induced Transition with the $\gamma\text{-}\widetilde{Re}_{\theta t}$ Transition Model on One Very High-Lift Low-Pressure Turbine (T2) and One Engine-like Scale Low-Pressure Turbine (TX) Rotor Blades at Steady Conditions and Freestream Turbulence. In *47th Applied Aerodynamics Symposium*, Paper No. FP27-2012, Paris, France, March 26-28, 2012.

Reference used in Chapters 6 and 7.

J. Babajee and T. Arts. Investigation of the Laminar Separation-Induced Transition with the $\gamma\text{-}\widetilde{Re}_{\theta t}$ Transition Model on Low-Pressure Turbine Rotor Blades at Steady Conditions. In *ASME Turbo Expo 2012: Power for Land, Sea and Air*, Paper No. GT2012-68687, Copenhagen, Denmark, June 11-15, 2012.

Reference used in Chapters 6 and 7.

J. Babajee and T. Arts. Investigation of the Laminar Separation-Induced Transition on Two Low-Pressure Turbine Rotor Blades. *International Journal of Engineering Systems Modelling and Simulation*, Vol.5, Nos.1/2/3, February 2013.

Reference used in Chapters 6 and 7.

J. R. Llobet, J. Babajee and T. Arts. Investigation of the Roughness Strip Effects on the Separation-Induced Transition with the $\gamma\text{-}\widetilde{Re}_{\theta t}$ Transition Model on a High-Lift Low-Pressure Turbine Rotor Blade at Steady Conditions. In *10th European Conference on Turbomachinery Fluid Dynamics and Thermodynamics*, Lappeenranta, Finland, April 15-19, 2013.

Reference used in Chapter 8.

Jayson Babajee

Born: November 2, 1985 in Paris, France

Nationality: French

Email: jayson.babajee@yahoo.fr

EDUCATIONAL BACKGROUND

Ph.D. von Karman Institute for Fluid Dynamics, Belgium Turbomachinery and Propulsion Department Ecole Centrale de Lyon, France Ecole Doctorale MEGA LMFA	Mar. 2009 - Nov. 2013
M.Sc. in Aerospace Dynamics Cranfield University, United Kingdom	Oct. 2007 - Sept. 2008
M.Sc. in Mechanical Engineering and Energetics ENSIAME, France	Sept. 2005 - June 2008

WORK EXPERIENCE

Aerodynamics Engineer ALSTOM Power, United Kingdom	June 2013 - ...
Research Engineer SNECMA, France	June 2009 - May 2012
Aerodynamicist as an intern Institut AéroTechnique, France	Sept. 2006 - Jan. 2007

REFERENCES

Prof. Tony Arts
Head, Turbomachinery and Propulsion Department
von Karman Institute for Fluid Dynamics, Belgium
arts@vki.ac.be

Dr. Nicholas Lawson
Reader & Pilot
National Flying Laboratory Centre
Cranfield University, United Kingdom
n.lawson@cranfield.ac.uk